THÈSE

Pour obtenir le grade de

DOCTEUR DE L'UNIVERSITÉ GRENOBLE ALPES

École doctorale : STEP - Sciences de la Terre de l'Environnement et des Planètes
Spécialité : Sciences de la Terre et de l'Environnement
Unité de recherche : Institut des Sciences de la Terre

Reconstruction de l'épaisseur de la glace de mer par inversion de forme d'onde d'icequakes et tomographie

Sea Ice Thickness Reconstruction Using Icequake Waveform Inversion and Tomorgraphy

Présentée par :

Hooshmand ZANDI

Direction de thèse :

Ludovic MOREAU Enseignant-chercheur, UGA	Directeur de thèse
Ludovic METIVIER DIRECTEUR DE RECHERCHE, CNRS DELEGATION ALPES	Co-encadrant de thèse
Romain BROSSIER MAITRE DE CONFERENCES HDR, UNIVERSITE GRENOBLE ALPES	Co-encadrant de thèse

Rapporteurs :

Fabrice LEMOULT
MAITRE DE CONFERENCES HDR, ESPCI Paris
Arnaud MESGOUEZ
PROFESSEUR DES UNIVERSITES, Avignon Université

Thèse soutenue publiquement le **17 décembre 2025**, devant le jury composé de :

Jérôme WEISS, DIRECTEUR DE RECHERCHE, CNRS délégation Alpes	Président
Ludovic MOREAU, MAITRE DE CONFERENCES HDR, Université Grenoble Alpes	Directeur de thèse
Ludovic METIVIER, DIRECTEUR DE RECHERCHE, CNRS délégation Alpes	Co-directeur de thèse
Romain BROSSIER, MAITRE DE CONFERENCES HDR, UNIVERSITE GRENOBLE ALPES	Co-directeur de thèse
Fabrice LEMOULT, MAITRE DE CONFERENCES HDR, ESPCI Paris	Rapporteur
Arnaud MESGOUEZ, PROFESSEUR DES UNIVERSITES, Avignon Université	Rapporteur
Gregor HILLERS, FULL PROFESSOR, Helsingin Yliopisto	Examinateur

Acknowledgements

This thesis was made possible thanks to the guidance, patience, and insightful feedback of many people, and I am deeply grateful for their support throughout this journey.

First and foremost, I would like to express my heartfelt gratitude to my supervisors, Ludovic Moreau, Ludovic Métivier, and Romain Brossier. Their mentorship, thoughtful guidance, and constructive criticism were instrumental in shaping this work. I am particularly thankful for their patience during the most challenging moments of my PhD, and for encouraging me to pursue new ideas, even when the path forward was uncertain.

I would also like to thank my friends and colleagues, who have made this journey far more enjoyable and memorable. Marc, Arthur, Lahcene, Amine, Federica, Fabio, Bruno, Dominik, Fandy, Jian, Alizia, Goulven, Philippe, Giuseppe, Pauline, Sam, and specially dear Laura — thank you for your support, your laughter, and the many wonderful moments we shared along the way. Bruno, be sure to keep the SEISCOPE table after me… and then pass on the tasks to the next lucky colleague!

My time at ISTerre has been exceptional, filled with rich experiences and inspiring colleagues. Grenoble, with its stunning mountains, provided a beautiful backdrop to both the highs and the inevitable challenges of this PhD, and it will always hold a special place in my memory.

I am also grateful to the SEISCOPE team and its sponsors, whose support and resources made this research possible. Special thanks to all team members for the lively discussions, valuable advice, and daily support that enriched my work.

Finally, I want to extend my deepest gratitude to my family, particularly my parents, and friends from afar, whose unwavering support, encouragement, and belief in me carried me through the ups and downs of this journey. Without them, this PhD would have been far more difficult, and certainly less joyful.

Résumé

La glace de mer joue un rôle crucial dans le système climatique terrestre, agissant à la fois comme moteur et comme indicateur sensible des changements environnementaux — en particulier dans les régions polaires et subpolaires. Cette étude vise à améliorer notre compréhension de la structure de la glace de mer et de sa variabilité temporelle en réponse aux forçages environnementaux, en reconstruisant l'épaisseur de la glace de mer par inversion d'onde sismique et tomographie, à partir de données sismiques passives et actives. L'objectif plus large est de contribuer à une meilleure compréhension des changements climatiques.

Nous utilisons la modélisation directe de la propagation des ondes sismiques dans la glace de mer pour générer des formes d'ondes synthétiques, en utilisant la méthode des éléments spectraux (SEM). Ces formes d'ondes synthétiques sont ensuite intégrées dans un cadre d'inversion qui les compare aux ondes observées, enregistrées par des capteurs sismiques placés sur la glace. En minimisant l'écart entre les données synthétiques et les données observées à l'aide d'une approche stochastique combinée à une recherche sur grille, nous estimons l'épaisseur de la glace le long des trajets source-récepteur et déterminons les localisations des icequakes. Cette stratégie d'inversion est appliquée aux données issues à la fois de sources sismiques passives et actives. Une fois les estimations d'épaisseur obtenues, elles sont utilisées comme entrée pour une deuxième étape d'inversion : la tomographie sismique. Ce processus permet d'obtenir des cartes de l'épaisseur de la glace de mer avec une résolution spatiale.

L'approche est validée par des tests synthétiques, puis appliquée à plusieurs ensembles de données de terrain. L'ensemble principal, acquis sur le lac Vallunden, au Svalbard (Norvège), entre le 28 février et le 26 mars 2019, comprend des enregistrements passifs continus ainsi que deux expériences à sources actives, à partir de 247 capteurs. Les icequakes quotidiens, extraits des données passives à l'aide d'algorithmes d'apprentissage automatique, constituent la base de notre inversion. Des ensembles de données supplémentaires provenant d'expériences à sources actives à petite échelle menées au Québec (Canada), en mars 2024 et février 2025, permettent une validation supplémentaire de notre approche. Dans tous les cas, les résultats de la tomographie sismique sont cohérents avec les observations de terrain, y compris les mesures in situ, processus hydrodynamiques, et les relevés de température.

Les cartes quotidiennes de l'épaisseur de la glace, dérivées des données du Svalbard, révèlent un schéma spatial clair, avec une glace plus fine au centre du lac et plus épaisse vers les bords. Elles capturent également les variations quotidiennes de croissance et de fonte de la glace au fil du temps, montrant des corrélations significatives avec les observations et les fluctuations de température. Ces résultats démontrent la robustesse et la sensibilité de notre méthode, qui combine une modélisation numérique efficace avec des stratégies d'inversion efficaces. En capturant l'évolution quotidienne de la structure de la glace de mer, ce travail apporte des éléments précieux sur l'épaisseur et l'évolution de la glace, et introduit un outil novateur pour observer et comprendre les changements climatiques affectant les environnements cryosphériques.

Abstract

Sea ice plays a crucial role in the Earth's climate system, serving both as a driver of and a sensitive indicator for environmental change—particularly in polar and subpolar regions. This study seeks to improve our understanding of sea ice structure and its temporal variability in response to environmental forces by reconstructing sea ice thickness through seismic waveform inversion and tomography, using both passive and active seismic datasets. The broader goal is to contribute to a better understanding of climate changes.

We use forward modeling of seismic wave propagation in sea ice to generate synthetic waveforms, employing the Spectral Element Method (SEM). These synthetic waveforms are then used in an inversion framework that compares them to observed waveforms recorded by seismic receivers deployed on the ice. By minimizing the misfit between synthetic and observed data through a stochastic approach combined with grid search, we estimate ice thickness along source-receiver paths and determine icequake locations. This inversion strategy is applied to both passive and active seismic source data. Once ice thickness estimates are obtained, they are used as input for a second inversion step: seismic tomography. This process yields spatially resolved maps of sea ice thickness.

The approach is validated through synthetic tests and applied to several field datasets. The primary dataset, acquired on Lake Vallunden, Svalbard (Norway) between 28 February and 26 March 2019, includes continuous passive recordings as well as two active-source experiments, from 247 sensors. Daily icequakes extracted from passive data using machine learning algorithms form the basis for our inversion. Additional datasets from small-scale active-source experiments conducted in Québec, Canada, in March 2024 and February 2025 provide further validation of our approach. In all cases, seismic tomography results are consistent with field observations, including in-situ measurements, hydrodynamic processes, and temperature records.

The daily ice thickness maps derived from the Svalbard data reveal a clear spatial pattern, with thinner ice at the center of the lake and thicker ice toward the edges. They also capture daily changes in ice growth and thinning over time, showing meaningful correlations with observations and temperature fluctuations. These results demonstrate the robustness and sensitivity of our method, which combines effective numerical modeling with efficient inversion strategies. By capturing the daily evolution of sea ice structure, this work offers valuable insights into the structure and evolution of sea ice thickness, and introduces a novel tool for observing and understanding climate-driven changes in cryospheric environments.

CONTENTS

1 General Introduction **1**
- 1.1 Arctic Sea Ice and Its Significance . . . 1
- 1.2 Methods for Measuring Sea Ice Extent and Thickness . . . 5
  - 1.2.1 Seismic Methods . . . 6
- 1.3 Field Data . . . 10
  - 1.3.1 St. Lawrence Estuary, Quebec, Canada . . . 11
  - 1.3.2 Svalbard, Norway . . . 13
- 1.4 Outline of the Thesis . . . 14

2 Modeling Seismic Wave Propagation in Sea Ice **17**
- 2.1 Analytical and Asymptotic Modeling of Wave Propagation in Floating Plates . . . 18
  - 2.1.1 Analytical Formulation . . . 18
  - 2.1.2 Asymptotic Approximation . . . 24
  - 2.1.3 Comparison and Validation . . . 29
- 2.2 Spectral Element Modeling for Wave Propagation in Sea Ice Sheets . 32
  - 2.2.1 Physical Model . . . 33
  - 2.2.2 Governing Equations for the Ice–Sea System . . . 34
  - 2.2.3 Discretization . . . 35
  - 2.2.4 Numerical Implementation . . . 38
  - 2.2.5 Comparison With Analytical Solutions . . . 46
- 2.3 Perspectives: Exploring SEM Capabilities with Snow Cover and Varying Ice Thickness . . . 49
  - 2.3.1 Snow Cover Impact . . . 49
  - 2.3.2 Linearly Changing Thickness . . . 51

3 Inverse Methods for Ice Thickness Estimation and Icequake Localization **53**
- 3.1 Overview of Inversion Methods . . . 54
  - 3.1.1 Traditional Earthquake Location Methods . . . 54
  - 3.1.2 Challenges Specific to Icequake Inversion . . . 54
  - 3.1.3 Inversion Strategy Overview . . . 54

3.2 Inversion Approach for Icequake Localization and Ice Thickness Estimation . . . 55
3.2.1 Simulated Annealing . . . 55
3.2.2 Synthetic Data Generation Using SEM . . . 58
3.2.3 Cost Function Visualization and Selection . . . 59
3.3 Validation of the Inversion Strategy Using Synthetic Test . . . 69
3.4 Field Data Application . . . 73
3.5 Perspectives . . . 78
3.5.1 Particle Swarm Optimization . . . 78
3.5.2 Sensitivity of Inversion to the Choice of Forward Model, Heterogeneity, and Layer Geometry . . . 79

4 Ice Thickness Reconstruction Using Tomography: Methods and Applications 81
4.1 Introduction . . . 81
4.2 Methodology . . . 82
4.3 Synthetic Test . . . 87
4.3.1 Uncertainty Analysis . . . 89
4.3.2 Checkerboard Test . . . 92
4.4 Field Data Application . . . 94
4.4.1 Tomographic Inversion of Sea Ice in the St. Lawrence Estuary, Quebec, Canada . . . 94
4.4.2 Tomographic Inversion of Sea Ice in Svalbard . . . 104
4.5 Perspectives . . . 115
4.5.1 Impacts of the Number and Configuration of Stations . . . 115
4.5.2 Adaptive Mesh Stratgey . . . 118

5 Conclusions and Perspectives 125
5.1 Conclusions . . . 125
5.2 Perspectives . . . 126
5.2.1 Technical Refinements and Expanded Inversions . . . 126
5.2.2 Applications and Integration . . . 127

A Zero-Lag Correlation in the Frequency Domain 129

B Synthetic Tests In Svalbard 131

Bibliography 135

Glossary

$\mathbf{u}$ Displacement vector

λ_s, μ_s Lamé parameters for a solid

ρ_s Density of a solid (e.g., ice) in kg/m^3

c_P, c_S Compressional (P) and shear (S) wave velocities in a solid

c_L, c_T Longitudinal and transverse wave velocities in a plate

ϕ_s, Ψ_s Scalar and vector displacement potentials for a solid

σ_{ij} Components of the stress tensor

ϵ Strain tensor

h Plate thickness

$h_{\mathbf{ice}}$ Ice thickness

$A_n^{\pm}, B_n^{\pm}$ Amplitudes of wave potentials

k Horizontal wavenumber

q_z, r_z Vertical wavenumbers for P and S waves

ω Angular frequency in rad/s

c_{ph} Phase velocity in a plate

ϕ_f Displacement potential in a fluid

ρ_f Density of a fluid (e.g., water, air) in kg/m^3

c_f Compressional wave speed in a fluid

c_w, c_a Compressional wave speeds in water and air

E Young's modulus

ν Poisson's ratio

D Flexural rigidity of a plate, $D = \frac{Eh^3}{12(1-\nu^2)}$

u_z Out-of-plane displacement (vertical deflection)

g Acceleration due to gravity

$l_i(\xi)$ Lagrange polynomial of degree N

H Water depth

t_0 Source activation time (time lag)

$\mathbf{A}$ Forward operator or matrix in tomography

$\mathbf{h_{obs}}$ Observed ice thickness data vector

$\hat{\mathbf{h}}$ Pixel-wise ice thickness model

α, β Regularization parameters

$\mathbf{L}$ First-order derivative (gradient) operator

$\mathbf{R}_m$ Model resolution matrix

$\mathbf{C}_M$ Posterior model covariance matrix

$\boldsymbol{\rho}$ Correlation matrix

$\mathbf{W}_d, \mathbf{W}_m$ Data and model weighting matrices

$\mathbf{I}$ Identity matrix

$\mathbf{D}_x, \mathbf{D}_y$ Derivative matrices in x and y directions

$\mathbf{J}_e$ Jacobian matrix

$\mathbf{f}_s$ Body force vector in solid

$\mathbf{P}_f$ Pressure source in fluid

κ Bulk modulus of fluid

Ω_f, Ω_s Fluid and solid domains

Γ_{fs} Fluid-solid interface

CHAPTER 1

GENERAL INTRODUCTION

Contents

1.1 Arctic Sea Ice and Its Significance 1

1.2 Methods for Measuring Sea Ice Extent and Thickness . . 5

1.2.1 Seismic Methods 6

1.3 Field Data 10

1.3.1 St. Lawrence Estuary, Quebec, Canada 11

1.3.2 Svalbard, Norway 13

1.4 Outline of the Thesis 14

In this chapter, we introduce the significance of sea ice at both global and local scales and describe the changes it has undergone, along with their ecological, climatic, and societal consequences. We then review common methods for measuring and monitoring sea ice, highlighting their strengths and limitations. Finally, we focus on seismic approaches, discussing their potential to provide high-resolution, small-scale observations of ice thickness and structure, and explain how this thesis contributes to improving the monitoring and understanding of sea ice dynamics through seismic modeling and inversion techniques.

1.1 Arctic Sea Ice and Its Significance

Sea ice forms as a mushy layer, a porous two-phase, two-component system comprising a rigid ice matrix and interstitial brine. Its growth is governed by both thermal processes, such as freezing and melting, and mechanical processes, including wind forcing, ocean currents, and internal stresses (Feltham et al., 2006). During formation, salts are progressively expelled from the ice through processes like brine drainage and diffusion, resulting in desalination and a low-salinity ice structure (Notz and Worster, 2009). Furthermore, a snow cover can insulate the ice, reducing heat flux and thereby affecting the growth rate and overall thickness of the ice (Liston et al., 2020). Together, these processes govern the thermodynamic and mechanical

properties of sea ice, which are fundamental for understanding this dynamic and complex system.

Over the past decades, Arctic sea ice has declined dramatically in both extent and thickness, primarily due to climate warming. The greatest absolute and relative losses occur in late summer and early autumn. Between 2010 and 2019, the average Arctic sea ice area from August to October was about 25% smaller than in 1979–1988, while ice volume fell by roughly 72% from 1979 to 2016. Thinning is widespread across the central Arctic and key regions, including Fram Strait, northern Canada, and Svalbard, largely driven by human-caused greenhouse gas emissions. Satellite observations suggest that practically ice-free Arctic summers could occur before 2050, earlier than many climate models had predicted. The combined reduction in ice area and volume, along with the lengthening of the open-water season, indicates that Arctic summer sea ice is retreating faster than most models project (Rampal et al., 2011; Stroeve et al., 2012; Stroeve and Notz, 2018; Comiso et al., 2017; Schweiger et al., 2019).

This rapid loss of sea ice is closely linked to Arctic amplification (AA), the accelerated warming observed in the Arctic relative to the global average. Both model simulations and observational studies show that a key driver of AA is the changing extent of sea ice, which modulates heat fluxes between the atmosphere and ocean, influences water vapor and cloud cover, and alters heat transport within the climate system. Regions experiencing substantial sea ice loss exhibit a more pronounced AA effect, while areas where sea ice remains relatively stable or melts entirely show a weaker response. Sea ice melting therefore plays a central role in enabling other processes that contribute to AA (Serreze and Barry, 2011; Dai et al., 2019).

Figure 1.1 illustrates changes in Arctic sea ice extent over recent decades, highlighting the record low in September 2012 and the notably low daily extent in 2024, clearly demonstrating this ongoing decline. Figure 1.2 compares Arctic sea ice extent and concentration between 1990 and 2012, showing seasonal growth and melt, with the yellow outlines indicating the 1981–2010 median extent. The figure highlights the overall decline in summer minima and winter maxima in recent decades.

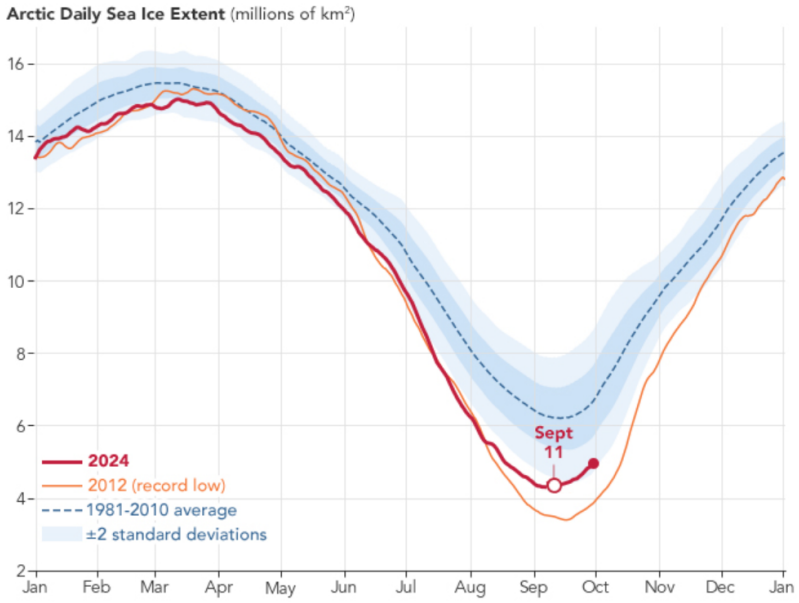

Figure 1.1: Changes in Arctic sea ice extent over recent decades, illustrating the ongoing decline (NASA Earth Observatory, 2025).

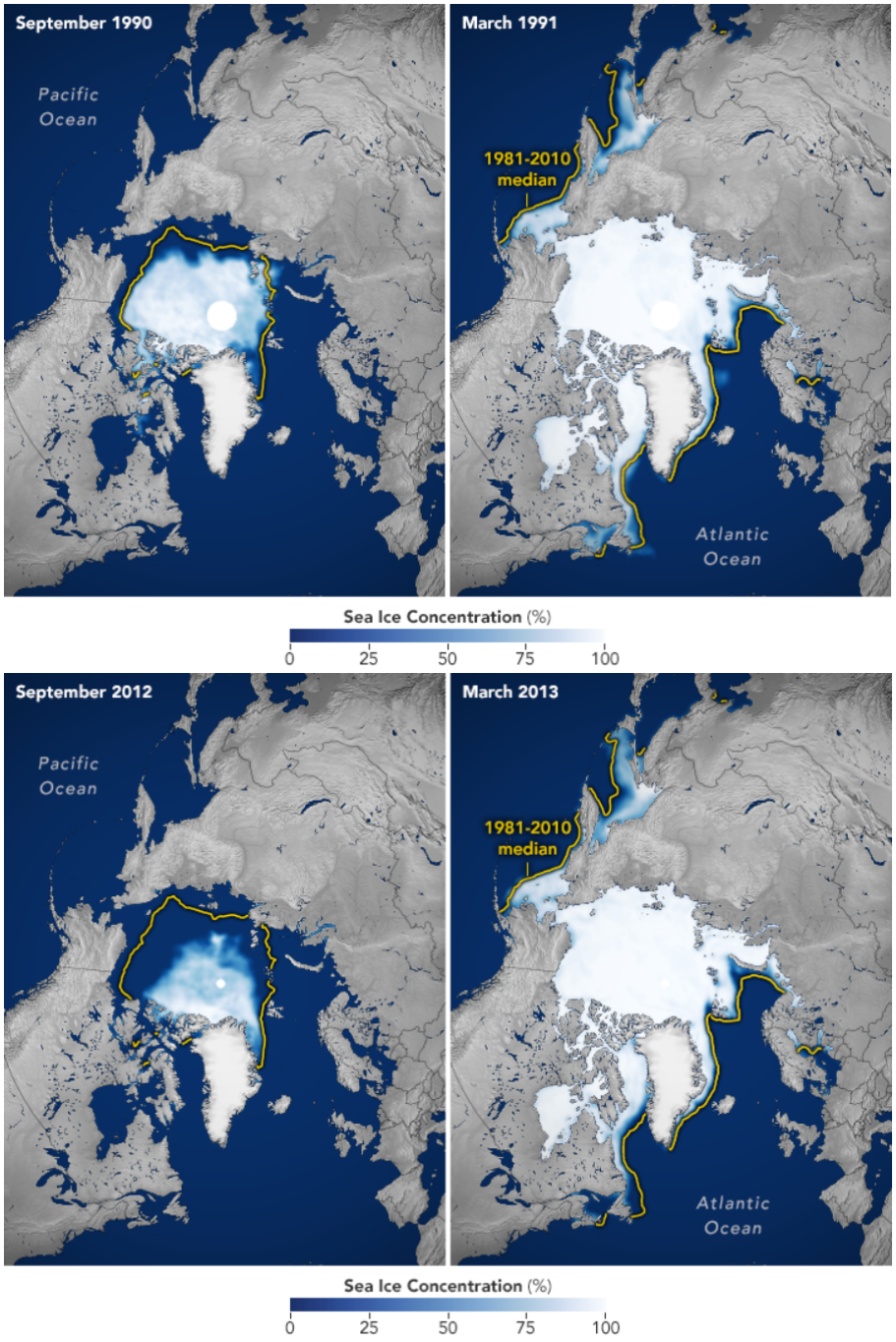

Figure 1.2: Sea ice extent in the Arctic, illustrating its role in climate regulation and human activities (NASA Earth Observatory, 2025).

In recent years, increasing attention has been directed toward the Marginal Ice Zone (MIZ), where understanding wave–ice interactions is essential for describing the coupled ocean–ice–climate system. In this context, accurate estimation of sea-ice thickness has become particularly important, as it governs how waves propagate, attenuate, and induce ice breakup. Early modelling work by Williams et al. (2013) demonstrated that ice thickness and mechanical strength strongly influence wave transmission and fracturing, with thinner ice allowing deeper wave penetration and

enhanced fragmentation. More recently, Kuchly et al. (2025) conducted a comprehensive multi-instrument field campaign in the MIZ of the St. Lawrence Estuary, Canada, integrating geophones, wave buoys, smartphones, and UAVs to measure ice thickness, mechanical properties, wave characteristics, and ice motion under natural forcing conditions. Their results show strong agreement across independent measurement methods, confirming that local ice properties strongly influence wave dispersion, attenuation, and ice breakup dynamics. Such wave-induced fragmentation increases open-water fraction and reduces surface albedo, thereby enhancing melt through greater solar absorption and ocean–atmosphere heat exchange. These feedbacks highlight the climatic significance of MIZ processes and the central role of reliable sea-ice thickness measurements in understanding and modelling polar climate evolution (e.g., Zhang et al., 2015; Boutin et al., 2021).

Beyond its climatic role, sea ice is essential for Arctic ecosystems and human societies. Its rapid decline has increased sunlight penetration and open water, altering ocean conditions, enhancing vertical mixing, and enabling not only the traditional spring phytoplankton bloom but also the emergence of a new fall bloom in some regions. These ecological shifts signal a move from a polar system with a single short growing season to a more temperate-like regime with two productive periods, affecting marine food webs and key species such as polar bears, seals, walruses, and seabirds. At the same time, the loss of sea ice drives profound societal impacts: Indigenous and local communities experience changes in wildlife, livelihoods, culture, and infrastructure, while reduced ice also opens new opportunities for shipping and resource development, creating challenges that require adaptation.. (Post et al., 2013; Ford et al., 2021; Ardyna et al., 2014).

Despite advances in observations and modeling, significant uncertainties remain, highlighting the urgent need for improved forecasting and adaptation strategies. Studying Arctic sea ice extent and thickness is therefore critical, both for understanding Arctic warming in response to rising CO_2 and for informing practical ecological and socio-economic decision-making.

1.2 Methods for Measuring Sea Ice Extent and Thickness

Field data play a crucial role in studying the dynamics and properties of sea ice. Such data can be acquired using remote or indirect measurement techniques. One highly accurate approach is ice-profiling sonar, which allows the estimation of ice thickness, drift, and topography (Fissel et al., 2008). However, these measurements are often limited in spatial and temporal coverage and come at a high operational cost. Another widely used technique is ground-penetrating radar (GPR), which provides estimates of both ice and snow thickness (Matsumoto et al., 2019). Similar to ice-profiling sonar, GPR surveys are typically short-term and expensive, restricting their application to limited field campaigns.

Due to the harsh and inaccessible conditions in polar regions, in situ observations remain sparse, making satellite remote sensing the primary tool for large-scale monitoring of sea ice. Sea ice thickness (SIT) is a critical climate variable because

it influences heat exchange between the ocean and atmosphere, contributes to sea ice volume and mass balance, and affects freshwater fluxes (Mäkynen et al., 2020). Satellites, including radar and laser altimeters, provide extensive coverage and long-term records, allowing the detection of trends and fine-scale features. Traditional monthly-averaged SIT maps, however, neglect sea ice motion and short-term dynamics, introducing spatial blurring and regional biases. Drift-aware approaches (DA-SIT) improve these products by accounting for ice motion and dynamic changes, providing more accurate daily maps and better regional representation (Ricker et al., 2025).

Despite these advances, estimating ice thickness remains challenging due to factors such as snow cover, ice roughness, and ice–water interactions, which introduce uncertainties and biases (Guerreiro et al., 2017). While satellites and large-scale observations are indispensable for broad coverage, they are limited in resolving small-scale variations and local dynamics. This highlights the need for alternative approaches, such as seismic and other in situ methods, which can provide higher-resolution information on ice thickness and structure at local scales, complementing large-scale satellite observations.

At smaller scales, laboratory and field studies have explored ice structure and sub-layer characteristics. X-ray computed tomography Crabeck et al. (2016); Kawamura (1988) allowed detailed imaging of brine channels and air inclusions but focused on small ice cores rather than thickness. Ground-based SAR tomography has been used to resolve snow and ice interfaces at centimeter-scale resolution in Tromsø, Norway Yitayew et al. (2014, 2015), but such studies primarily characterized ice structure rather than providing quantitative ice thickness over extended areas. Similarly, Karvonen and Cheng (2024) and Wang et al. (2022) explored operational and simulated methods to retrieve sea ice thickness and snow depth using SAR or GNSS-IR, demonstrating potential but often limited to specific regions or simulations. Xing et al. (2022) combined GPR and ice core acoustic measurements to model the vertical structure and acoustic velocity of Arctic ice, highlighting the role of density and salinity variations, yet these approaches are typically limited to short-term campaigns. Laboratory point measurements using a time-domain electromagnetic induction (EMI) sensor have also been explored to estimate ice thickness at discrete heights above seawater Hills et al. (2025).

Seismic methods provide an alternative approach for estimating ice thickness at small scales and over local areas. By recording and analyzing elastic waves in the ice, these techniques can infer ice properties and thickness with high resolution, and they can be deployed for continuous monitoring. This makes them a valuable complement to satellite and large-scale in situ observations, which are often limited in spatial or temporal coverage.

1.2.1 Seismic Methods

Seismic methods provide a powerful tool to investigate the physical properties of sea ice by analyzing the propagation of elastic waves within the ice sheet. Within the frequency range of natural seismic sources, three types of waves are typically observed in floating ice (Moreau et al., 2017): longitudinal waves, shear-horizontal

(SH) waves, and flexural waves. The velocities of longitudinal and SH waves are directly used to estimate the elastic constants of the ice, including the elastic moduli and Poisson's ratio. Flexural waves, in contrast, are sensitive to both the mechanical properties and the thickness of the ice, and are therefore used for ice-thickness estimation.

The development of seismic methods for sea ice characterization can be traced through three main phases: early theoretical and experimental foundations, the introduction of numerical modeling and inversion techniques, and the recent emergence of passive seismic approaches for continuous monitoring.

Early Theoretical and Experimental Foundations. Early studies focused on developing the theory of wave propagation in ice and validating it through field experiments. Ewing et al. (1934) explored the elastic properties of ice through laboratory experiments on ice rods and field measurements on lake ice. Their field results for longitudinal wave velocity, obtained using blasting caps as the source and recorded with geophones, showed close agreement with theoretical predictions relating wave speed in a rod to that in an infinite plate.

Building on their foundational work, Ewing and Crary (1934) used explosion-generated seismic waves to investigate wave propagation in lake ice. They observed highly dispersive flexural waves, for which they derived a characteristic equation and an empirical group velocity formula. The study also directly measured the velocity of horizontally polarized shear (SH) waves, validating their earlier lab results. Multi-component recordings revealed the flexural wave motion was complex, dominated by a vertical component but with significant horizontal energy.

Press and Ewing (1951) extended these results with theoretical developments on air-coupled flexural waves (ACFWs) in floating ice sheets excited by impulsive sources in air or water. His analysis demonstrated that coupling with compressional waves in air introduces additional branches in the flexural dispersion curve. Using group and phase velocity calculations, he predicted the sequence and amplitudes of waves arriving at distant locations, and field data from Lake Superior and Lake Cayuga confirmed these predictions. Building on this and previous studies, Press (1951) adopted a different approach to formulate the characteristic equation for wave propagation in floating ice, showing how phase velocities behave for very large and very small wavelengths. Unlike a plate in vacuum or fluid, the ice–water–air system does not reduce to purely symmetric and antisymmetric modes. This work extended earlier treatments by Lamb (1917) for a plate in vacuum and Osborne and Hart (1945) for a plate in fluid.

Thanks to these pioneering studies and the theory of ACFWs, Oliver et al. (1954) used velocities of longitudinal and SH waves, together with density data, to estimate the elastic constants of ice and applied ACFWs to derive ice thickness in the Beaufort Sea, Arctic Ocean. Hunkins (1960) adopted a similar strategy to determine elastic properties and ice thickness in sea ice near Drifting Station Alpha in the central Arctic Ocean, also analyzing seasonal variations in wave velocities, elastic constants, and density.

In another study, Dugan et al. (1992) further improved the understanding of wave propagation. They distinguished several wave modes in multiyear pack ice and identified their dominant frequency ranges: gravity waves below 0.05 Hz, wind-driven

motions up to 0.3 Hz, flexural waves from 0.1 to 10 Hz, and combined acoustic–flexural modes above 10 Hz.

Introduction of Numerical Modeling and Inversion. The first numerical analyses and inversion methods were applied in the 1980s and 1990s to determine the physical properties of sea ice, and have been further developed in subsequent decades. Miller and Schmidt (1991) conducted experiments on first- and multi-year pack ice. Geophone recordings of seismic waves from under-ice explosions revealed unexpected SH waves alongside longitudinal and flexural waves. Using numerical modeling and inverting the flexural wave's dispersion curve (extracted via short-time Fourier transform), the authors determined the best-fitting compressional wave speed, shear wave speed, and ice thickness. Their results showed compressional and shear wave speeds consistent with previous studies, but attenuation values were up to four times higher. In a similar way, Wang (1995) applied numerical modeling and inversion to first-year ice. They used wavelet transforms to extract dispersion curves, and by matching synthetic and observed dispersion curves, the authors derived ice thickness and elastic constants.

Expanding on wave propagation analysis, Yang and Giellis (1994) applied frequency-wavenumber analysis to hammer-blow data from a geophone array on sea-ice. Their results confirmed that longitudinal and SH waves are nondispersive at the measured frequencies. Conversely, flexural waves showed strong dispersion. A key finding was the observation of a second, unexpected family of flexural wave dispersion curves. The study also provided estimates of attenuation coefficients for these wave types.

Yang and Yates (1995) further developed a forward model using fluid-loaded thin elastic plate theory to simulate flexural waves in floating ice sheets excited by a vertical hammer blow. The ice response was computed in the frequency domain and converted to time-domain waveforms for comparison with field data, successfully capturing waveform shapes and flexural wave dispersion, and enabling estimation of frequency-dependent ice attenuation. Stein (1986) developed an inversion method to estimate Arctic sea ice mechanical properties, including thickness, by analyzing low-frequency longitudinal, SH, and flexural waves using a uniform elastic plate model (Stein et al., 1998) and 3C geophone data.

Furthermore, studies on air-coupled flexural waves (ACFWs) offered practical methods for monitoring ice thickness. Romeyn et al. (2021) built on early work on ACFWs, which travel ahead of air pressure waves over floating ice. Field experiments on first-year sea ice using explosive sources and geophone arrays in Svalbard showed that ACFW frequency decreases as ice thickness increases. The study developed a theoretical framework based on linear filter theory and Fourier methods, providing a formula to estimate ice thickness and demonstrating that ACFWs are a reliable feature for monitoring ice. Romeyn and Hanssen (2023) further showed that inexpensive microphones with simple artificial and natural sources could reliably provide thickness measurements on a lake consistent with drilled values.

Other studies focused on the spatial variability and heterogeneity of ice. Rajan et al. (1993) used crosshole tomography with high-frequency pulses to measure compressional (P) and shear (S) wave velocities in multi-year sea ice. The results revealed significant spatial variability, including low-velocity zones likely associated with high brine content, and these measurements were used to estimate material

properties such as Poisson's ratio, salinity, elastic moduli, and attenuation coefficients. Xie and Farmer (1994) investigated the influence of ice ridges and impact angles on the damping, spatial variability of P- and S-wave velocities, and directional acoustic radiation, emphasizing energy dissipation through ice damage rather than wave propagation. Xu et al. (2025) used high-resolution cross-hole acoustic tomography to map the internal structure of summer Arctic sea ice, revealing a vertically heterogeneous, multilayered structure with high near-surface attenuation due to partial melting, and showing how temperature and ocean cooling affect sound speed, improving understanding of acoustic wave behavior in Arctic ice.

In parallel, theoretical and modeling studies provided insights into ice behavior under dynamic loads. Squire et al. (1996) presented a theoretical and experimental framework for how moving loads interact with floating ice, modeling the ice as a thin elastic or viscoelastic plate on an inviscid fluid, and identifying a critical speed at which wave energy accumulates, causing large deflections. Landschulze (2018) used finite-element simulations to model the full seismic wavefield in a floating ice sheet. The model captured the fundamental guided waves—flexural and longitudinal modes—alongside their higher modes. A comparison with analytical plate-theory models demonstrated that the numerical approach more accurately captures high-frequency effects, wave interactions, and mode conversions. In another study, Johansen et al. (2019) investigated seismic acquisition setups for Arctic surveys using full-waveform modeling validated against field data. The objective was to identify source–receiver configurations that minimize unwanted wave energy. Flexural waves, often treated as coherent noise, dominate when both sources and receivers are placed on the ice surface, although these signals are particularly valuable for sea ice studies. Alternative setups reduce flexural energy but enhance other modes, such as Scholte and waterborne waves. The study offers practical recommendations for Arctic acquisition strategies aimed at geological targets, while also providing important insights into wave propagation in sea ice.

Emergence of Passive Seismic Approaches. All the aforementioned studies rely on active sources, requiring human presence. However, an alternative approach involves utilizing passive ambient noise data, eliminating the need for active sources and resulting in cost-effective and less labor-intensive operations. Marsan et al. (2012) and Marsan et al. (2019) used ambient noise correlations, based on noise interferometry (Shapiro and Campillo, 2004; Sabra et al., 2005), to measure ice thickness from flexural waves and to study flexural and SH waves, respectively.

Building upon the laboratory-scale research conducted by Moreau et al. (2017), making it possible to obtain dispersion curves of guided waves in a floating layer of ice through array processing, Moreau et al. (2020a) apply the method to field data acquired on sea ice to estimate ice thickness and mechanical properties. They obtain dispersion curves from both noise correlation functions (NCFs) and icequakes, which they use to derive the Young's modulus and Poisson's ratio from non-dispersive waves (longitudinal and shear waves), knowing the densities of ice and water. To estimate ice thickness, the observed dispersion curves for the flexural wave are compared to those obtained from forward modeling based on the Finite Element method (FEM). In a follow-up study, Moreau et al. (2020b) introduced a method that significantly reduces instrumentation requirements by an order of magnitude. They

first utilized NCFs to estimate elastic constants from the dispersion curves of non-dispersive waves. They then inferred ice thickness from passive data recorded on 3–5 receivers, using Bayesian inversion in which the waveforms of recorded icequakes were compared with those obtained from the forward model provided in Stein (1986), allowing monitoring of ice thickness from passive data. Similarly, Serripierri et al. (2021) used ambient noise correlations to derive the dispersion curves of these waves, from which they jointly inverted for elastic constants, density, and thickness of fast ice, facilitating the monitoring of these parameters using passive data.

Moreau et al. (2023) analyzed microseismicity recorded on fast ice in Svalbard. The study first used a deep convolutional neural network to cluster thousands of icequakes, successfully isolating the flexural mode. Following the methodology of Moreau et al. (2020b), Bayesian inversion of these waveforms was then applied to determine icequake source locations and the average ice thickness along the source–receiver paths. The results show that icequakes occur along the fjord shoreline roughly every 24 hours, and that ice thickness increased by approximately 15 cm over the first two weeks.

Overall, the literature provides a solid foundation for characterizing sea ice using seismic methods. Theoretical developments, supported by laboratory experiments and field campaigns, have deepened our understanding of the ice–sea system. Early studies relied on simplified models, while later work combined numerical modeling with inversion techniques to extract valuable information on sea ice elastic properties and thickness. The advent of passive methods has further facilitated data acquisition, enabling continuous and cost-effective monitoring.

Despite these advances, current inversion approaches still have limitations. For example, passive seismic studies such as Serripierri et al. (2021) estimate elastic constants while assuming a uniform ice thickness over the array area (e.g., Vallunden Lake using noise correlation functions), providing a single daily value for both elastic constants and thickness. Similarly, Kuchly et al. (2025) uses active-source data and retrieves constant values of ice thickness and elastic constants over the array area. More recent work Moreau et al. (2023) uses icequakes to derive a constant ice thickness between a source and receivers, providing path-specific estimates.

While these path-specific estimates represent an important step forward, they do not capture the full spatial variability of ice thickness within the array. This thesis extends such path-specific estimates to reconstruct high-resolution spatial maps of ice thickness, capturing both spatial heterogeneity and temporal evolution. This addresses the growing need for accurate, non-invasive monitoring in polar and subpolar regions. Such high-resolution imaging offers a powerful tool not only for studying sea ice dynamics but also for understanding the associated climatological and environmental changes.

1.3 Field Data

To investigate ice thickness and its spatial variability using seismic methods, we employ two field datasets acquired in distinct regions. The first dataset comes from

active-source campaigns in the St. Lawrence Estuary, Quebec, Canada, while the second consists of both passive and active-source recordings from Svalbard, Norway. Both datasets are used to estimate ice thickness along source–receiver paths and to construct tomographic maps, as discussed in the following chapters.

1.3.1 St. Lawrence Estuary, Quebec, Canada

The ANR-funded MSIM project (Multi-scale Monitoring of Sea Ice Parameters with Passive Seismology and Deep Learning, funded by the National Agency for Research) pursues two main objectives. First, it aims to develop high-resolution techniques for monitoring sea ice thickness, stiffness, and density using passive seismology, distributed acoustic sensing (DAS), and deep learning. Second, it advances field and laboratory methods to better understand wave-induced sea ice breakup in MIZ. Ultimately, the project seeks to improve the representation of sea ice in climate models with a level of accuracy and spatial resolution that current satellite-based imaging methods cannot provide.

A representative case within the MSIM project is the work of Kuchly et al. (2025), which presents a multi-instrument dataset from a field campaign conducted in the Marginal Ice Zone of the St. Lawrence Estuary, Canada. The deployment included geophone arrays, UAV imaging, wave buoys, and smartphones used as motion sensors, enabling observation of wave–ice interactions from the retrieval of mechanical properties through to the initiation of fracture. Seismic analyses were used to infer ice thickness and elastic parameters (e.g. Young's modulus, Poisson's ratio, density), with reliable results except in highly attenuating or partially consolidated ice. UAV and buoy data provided remote measurements of hydroelastic wave behaviour with sub-centimetre sensitivity, allowing extraction of key parameters such as dispersion, attenuation, and wavelength across different ice conditions. By combining field observations with inversion techniques and numerical modeling, the study provides a quantitative framework for understanding MIZ dynamics and lays the foundation for improved sea ice parameterizations in forecasting and climate models.

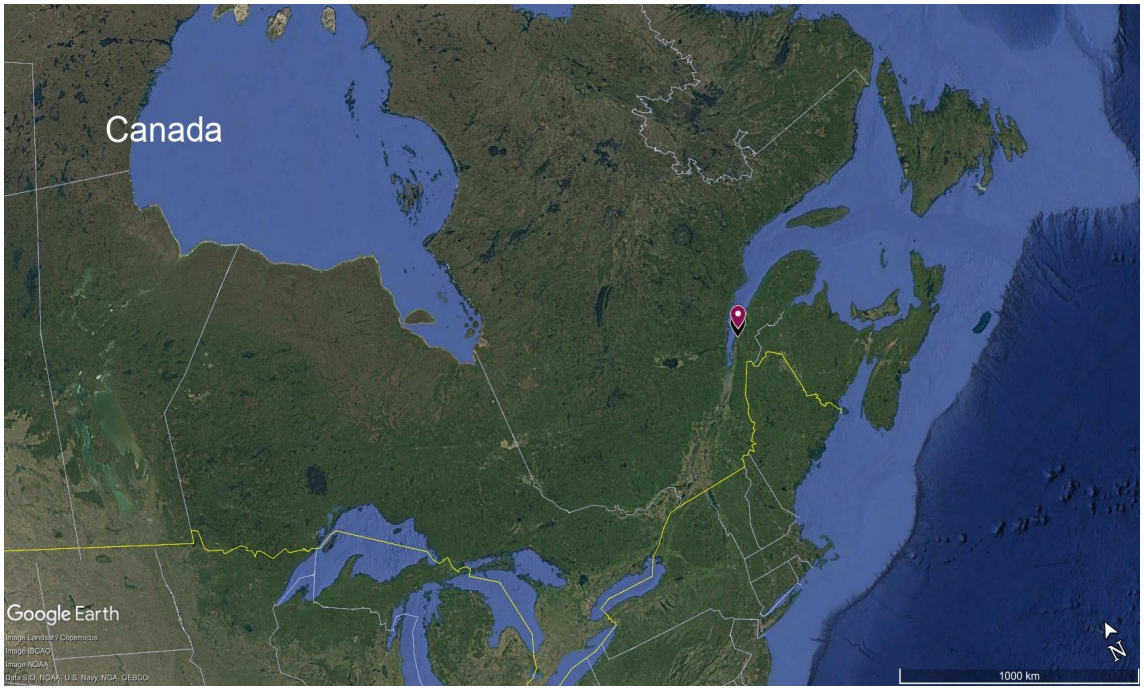

Figure 1.3: Locations of the surveys in the St. Lawrence Estuary, Quebec.

In this work, we focus on four surveys from the active seismic experiments conducted in this region for our subsequent analyses. These surveys correspond to four distinct experiments, as illustrated in Figure 1.3, which shows the array locations relative to the St. Lawrence Estuary. Figure 1.4 provides a zoomed-in view highlighting the four arrays (S1–S4) along with their corresponding source-receiver configurations, where sources are indicated by black stars and receivers by blue filled circles. The first experiment (S1), conducted in 2024 on a small inland lake, is located nearly 25 km from the three experiments performed in 2025 on the St. Lawrence River. Array sizes range from approximately 120×120 m^2 to 160×160 m^2. For this study, we consider only the vertical component of the recorded displacement.

- **6 March 2024** (S1): 21 active sources, including 16 three-component sources
- **6 February 2025** (S2): 33 active sources, 16 3C stations
- **10 February 2025** (S3): 21 active sources, 16 3C stations
- **24 February 2025** (S4): 20 active sources, 16 3C stations

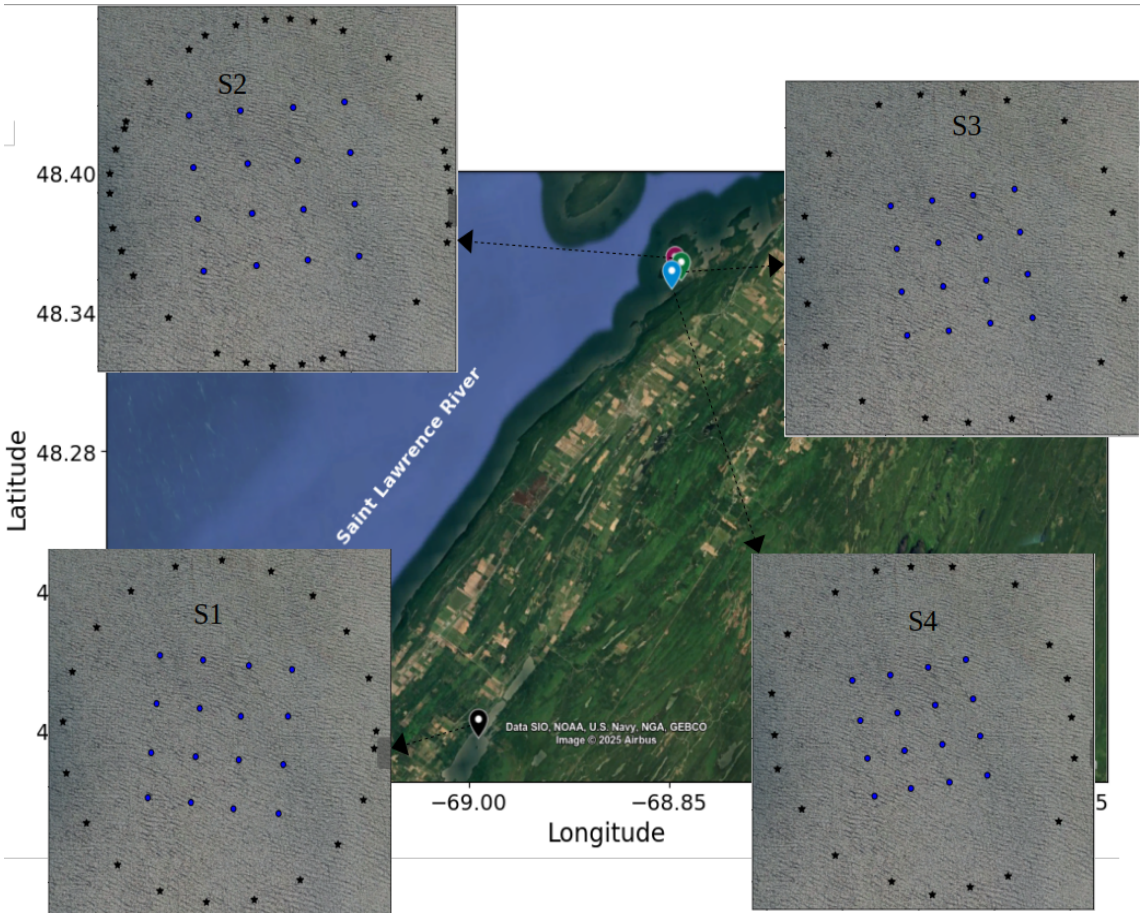

Figure 1.4: Zoomed-in view of the seismic survey locations, showing source-receiver configurations for each case (sources: black stars; receivers: blue filled circles).

1.3.2 Svalbard, Norway

The ICEWAVEGUIDE project, funded by ANR, aims to advance passive seismic techniques for in situ monitoring of sea ice properties. The approach relies on guided seismic waves propagating within the ice, which are sensitive to its geometry and elastic characteristics. Analysis of these waves enables the characterization of mechanical properties of ice. Following successful laboratory experiments, the methodology has been extended to real-scale field data, providing a framework for robust passive monitoring and characterization of sea ice.

A representative dataset from the project consists of 27 days of continuous ambient noise recordings collected with 247 geophones on Vallunden Lake, Van Mijen Fjord, Svalbard, in February–March 2019, supplemented by two days of active-source measurements. Among the instruments, 100 were three-component (3C) geophones, and the remaining were single-component (1C) units. Analyses of this dataset have demonstrated that passive seismic monitoring can reliably estimate ice thickness and elastic properties using array processing, noise interferometry, forward modeling, and Bayesian inversion. More recent developments have further shown that temporal and spatial variations in ice properties can be tracked continuously while minimizing the number of sensors required. Collectively, these studies confirm

that passive seismology provides a reliable and efficient approach for characterizing the mechanical behavior of sea ice (Moreau et al., 2020a,b; Serripierri et al., 2021; Moreau et al., 2023).

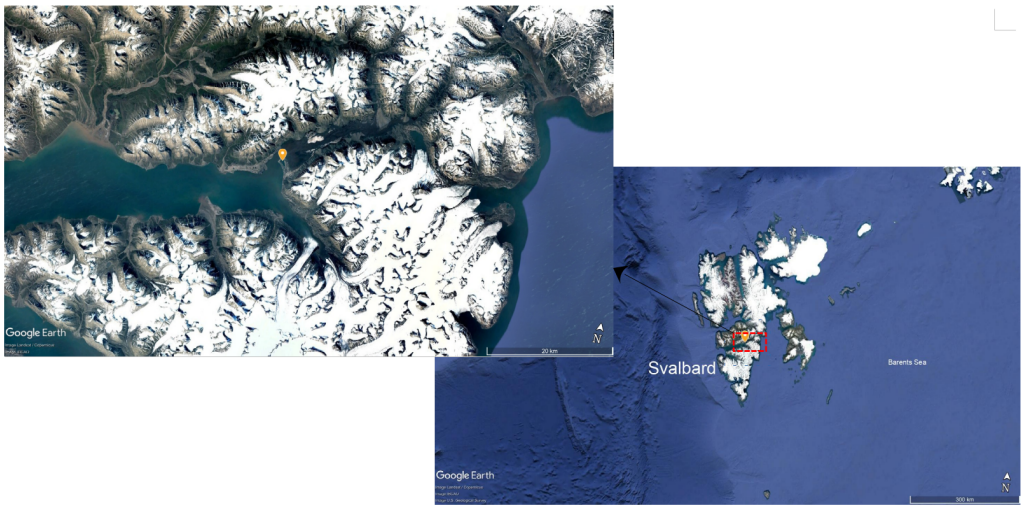

Figure 1.5: Survey location in Svalbard, Norway, indicated by an orange icon.

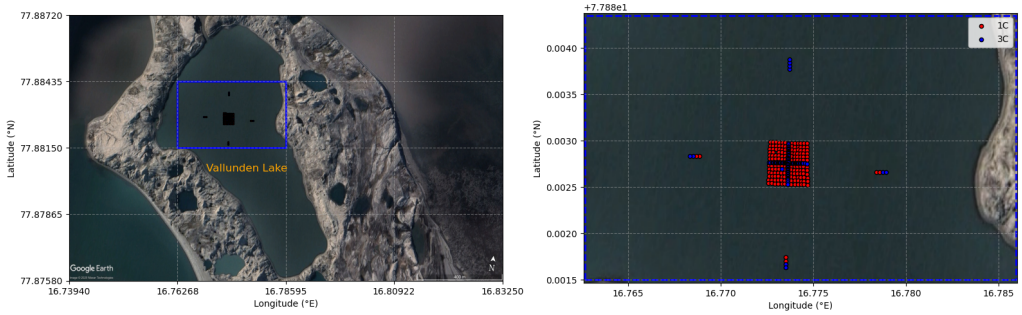

Figure 1.6: Positions of the deployed stations: 1-component geophones in red and 3-component geophones in blue.

Figure 1.5 shows the survey location, while Figure 1.6 provides a zoomed-in view of the receiver deployment in the center of Vallunden Lake. The array consists of 1C (red) and 3C (blue) receivers. The deployment includes a dense core of 231 stations arranged over an area of approximately 50×50 m^2, surrounded by 16 additional stations, with four stations positioned on each side (east, west, south, and north) positioned to the east, west, south, and north. These outer stations are located roughly 100 m from the center of the dense array.

1.4 Outline of the Thesis

Sea ice plays a critical role in regulating heat exchange between the ocean and atmosphere, yet current climate models underestimate its rapid decline. This discrepancy arises because most sea ice models operate at large scales and cannot

resolve small-scale processes within the Atmosphere-Ice-Ocean system, which are increasingly important as sea ice becomes thinner, younger, and more fragile. One key small-scale process is the breakup of ice by waves in the Marginal Ice Zone, which significantly influences ice-ocean interactions.

Understanding and modeling these interactions requires precise observations of small-scale sea ice properties, particularly its thickness and rigidity. This thesis aims to develop a methodology to reconstruct spatially resolved maps of sea ice thickness from seismic recordings. By combining forward modeling of elastic wave propagation with inversion techniques, ice thickness is estimated along individual source–receiver paths and then integrated into a tomographic framework to generate high-resolution maps. This approach is applied to both controlled-source and passive seismic datasets collected in the St. Lawrence Estuary (Canada) and Svalbard (Norway), providing a pathway for continuous, local-scale monitoring of sea ice properties essential for improving future sea ice models. This novel framework establishes a foundation for future studies in which seismic imaging techniques can be further developed to extract detailed spatio-temporal changes in ice properties.

This manuscript is structured to guide the reader from forward modeling to final ice thickness mapping. Chapter 2 develops and validates a Spectral Element Method (SEM) framework for accurately simulating seismic wave propagation in sea ice, addressing the limitations of the analytical and asymptotic models. Building on this forward engine, Chapter 3 introduces a three-step inversion strategy that jointly estimates icequake locations and path-specific ice thicknesses from natural-source seismic data. These pathwise estimates are then integrated in Chapter 4 into a tomographic inversion framework to reconstruct high-resolution spatial maps of ice thickness, capturing both its distribution and daily evolution. Finally, Chapter 5 summarizes the key findings and outlines future directions.

CHAPTER 2

MODELING SEISMIC WAVE PROPAGATION IN SEA ICE

Contents

2.1 Analytical and Asymptotic Modeling of Wave Propagation in Floating Plates 18

2.1.1 Analytical Formulation 18

2.1.2 Asymptotic Approximation 24

2.1.3 Comparison and Validation 29

2.2 Spectral Element Modeling for Wave Propagation in Sea Ice Sheets 32

2.2.1 Physical Model 33

2.2.2 Governing Equations for the Ice–Sea System 34

2.2.3 Discretization 35

2.2.4 Numerical Implementation 38

2.2.5 Comparison With Analytical Solutions 46

2.3 Perspectives: Exploring SEM Capabilities with Snow Cover and Varying Ice Thickness 49

2.3.1 Snow Cover Impact 49

2.3.2 Linearly Changing Thickness 51

The study of seismic wave propagation in sea ice has been the focus of numerous investigations due to its importance in understanding and monitoring this dynamic system. As interest in the Arctic grows—driven both by climate change and the exploration of natural resources—accurately characterizing how seismic energy travels through floating ice sheets becomes increasingly crucial. Early experiments relied on active seismic sources, while later approaches incorporated passive seismology techniques to measure wave velocities in sea ice, laying the groundwork for further theoretical and experimental studies. On the theoretical side, considerable effort

has been devoted to understanding the behavior of seismic waves and their various modes of propagation.

Initial research focused on wave propagation in elastic plates in a vacuum, followed by studies involving plates submerged in fluid on one or both sides. Sea ice represents a particular case within this framework, where the ice layer is bounded by air above and water below. The presence of water further influences wave propagation characteristics, making it a critical factor in modeling efforts. Both analytical and asymptotic approaches have been proposed to describe wave behavior under these conditions, alongside the development of numerical methods that account for more complex geometries and boundary conditions.

In Section 2.1, we describe analytical and asymptotic solutions for wave propagation in a floating ice layer. Analytical solutions provide an exact description in the homogeneous case, while asymptotic solutions offer simplified expressions that are widely used in the literature for their practicality. Comparing the two highlights the conditions where asymptotic solutions accurately describe wave behavior and where they fail.

In Section 2.2, we present our numerical approach based on the Spectral Element Method (SEM) and explain why it is particularly useful for heterogeneous media, where analytical solutions are not easily available. We begin by recalling the governing fluid–solid equations, then describe the discretization procedure used in SEM. To verify its accuracy, we first compare SEM simulations with analytical solutions in the homogeneous case. This validation demonstrates that SEM is a reliable tool, which we then use to model wave propagation in floating ice layers for the remainder of our analysis.

2.1 Analytical and Asymptotic Modeling of Wave Propagation in Floating Plates

In this section, we first present the theory of analytical and asymptotic solutions for wave propagation in a floating plate, and conclude by identifying the conditions under which asymptotic solutions are valid and where they fail to accurately describe wave behavior.

2.1.1 Analytical Formulation

Analytical solutions provide an exact description of wave propagation in homogeneous ice layers.

In a 3D elastic plate of finite thickness, internal stresses and displacements arise whenever the material is subjected to external forces or boundary constraints. For a plate of thickness h, the stress and displacement components are illustrated in Figure 2.1.

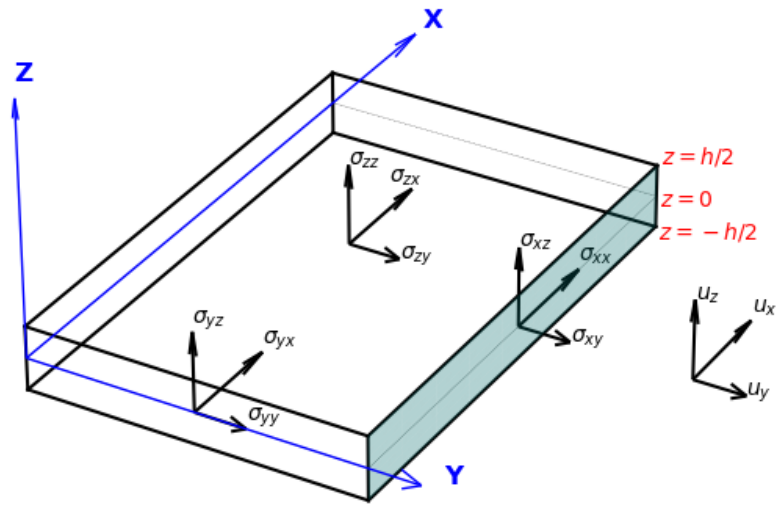

Figure 2.1: Stress and displacement components in an elastic plate of thickness h.

The displacement field includes both in-plane (u_x, u_y) and out-of-plane (u_z) components.

The simplest case is the case of a plate in vacuum. Lamb (1917) solved the problem of elastic wave propagation in a homogeneous, isotropic, infinite elastic plate in vacuum, which acts as a waveguide. His analysis describes two-dimensional wave propagation in a plate of finite thickness, where the wavelength is larger than the thickness, while the plate is considered infinite in the in-plane directions.

The plate surfaces are traction-free. In this case, we consider wave propagation primarily in the x-direction and neglect the y-components of stress and displacement. The traction-free boundary conditions in vacuum are therefore:

$$\sigma_{zz} = \sigma_{xz} = 0 \quad \text{at } z = \pm h/2.$$

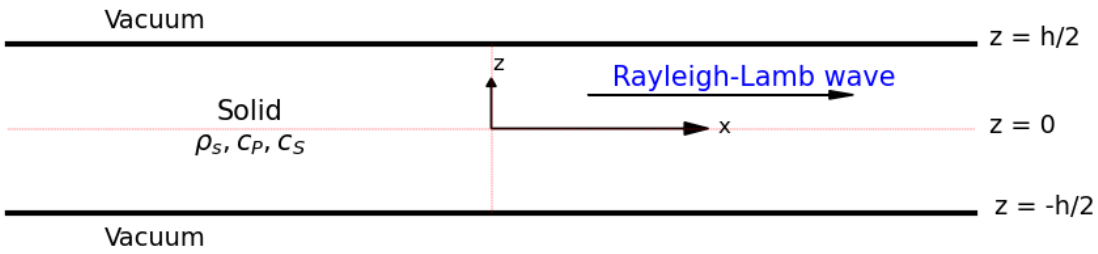

Figure 2.2: Rayleigh–Lamb wave propagating in the x-direction in an infinite elastic plate of thickness h surrounded by vacuum. The solid plate has density ρ_s and supports compressional and shear waves with speeds C_P and C_S, respectively.

Wave modes in a plate are formed by the repeated reflections of compressional (P) and shear (SV) waves within the plate. When these waves interfere constructively, they create guided waves called Rayleigh–Lamb waves.

To quantitatively describe these wave modes and determine their dispersion characteristics, we start from the fundamental equations of motion for a continuous elastic medium. The equations of motion are derived from Newton's second law:

$$\partial_j \sigma_{ij} = \rho_s \frac{\partial^2 u_i}{\partial t^2}, \tag{2.1}$$

where $\mathbf{u}$ is the displacement vector, σ_{ij} the stress tensor, and ρ_s the solid density. The stress is related to strain via the linear isotropic constitutive relation:

$$\sigma_{ij} = \lambda_s \delta_{ij}\, \partial_k u_k + \mu_s(\partial_i u_j + \partial_j u_i), \tag{2.2}$$

with λ_s and μ_s the Lamé parameters.
Using a Helmholtz decomposition, the displacement is expressed in terms of scalar and vector potentials:

$$\mathbf{u} = \nabla \phi_s + \nabla \times \mathbf{\Psi}_s, \tag{2.3}$$

which satisfy separate wave equations for compressional and shear waves. If we substitute this form into the equations of motion, we obtain two uncoupled wave equations: one for the scalar potential ϕ_s, associated with compressional motion, and one for the vector potential $\mathbf{\Psi}_s$, associated with shear motion. The characteristic velocities of these wave equations are:

$$C_P = \sqrt{\frac{\lambda_s + 2\mu_s}{\rho_s}} = \sqrt{\frac{E(1-\nu)}{\rho_s(1+\nu)(1-2\nu)}}, \quad C_S = \sqrt{\frac{\mu_s}{\rho_s}} = \sqrt{\frac{E}{2\rho_s(1+\nu)}}, \tag{2.4}$$

with C_P and C_S denoting compressional and shear wave speeds, respectively.

In a plate, compressional and shear waves generally propagate at different angles with respect to the interfaces. However, in the derivation of Rayleigh–Lamb modes, it is assumed (as in Equation 2.5) that they share the same horizontal wavenumber k. This assumption ensures they have the same phase velocity in the propagation direction, allowing their interference to form Rayleigh–Lamb modes.

Assuming 2D motion in the x–z plane simplifies the vector potential, leaving only one component Ψ_s^y. In this case, the wave solutions are taken as combinations of upward and downward traveling waves across the plate:

$$\phi_s = \left(A_2^+ e^{iq_z z} + A_2^- e^{-iq_z z}\right) e^{i(kx-\omega t)}, \quad \Psi_s^y = \left(B_2^+ e^{ir_z z} + B_2^- e^{-ir_z z}\right) e^{i(kx-\omega t)}, \tag{2.5}$$

where q_z and r_z are vertical wavenumbers, k the horizontal wavenumber, and $A_2^\pm, B_2^\pm$ the amplitudes. From these potentials, displacements u_x, u_z and stresses σ_{zz}, σ_{xz} are obtained.

The boundary conditions at the plate surfaces ($z = \pm h/2$) are applied to determine the amplitudes. For a plate in vacuum, the surfaces are traction-free:

$$\sigma_{zz} = 0, \quad \sigma_{xz} = 0. \tag{2.6}$$

The four boundary conditions at the plate surfaces can be written as a linear system for the unknown amplitudes:

$$\mathbf{MX} = \mathbf{0}, \tag{2.7}$$

where the vector of unknowns is defined in terms of symmetric and antisymmetric combinations of the upward and downward traveling wave amplitudes (Lohne et al., 2008):

$$A_{2,1} = A_2^+ + A_2^-, \quad A_{2,2} = A_2^+ - A_2^-, \tag{2.8}$$
$$B_{2,1} = B_2^+ + B_2^-, \quad B_{2,2} = B_2^+ - B_2^-. \tag{2.9}$$

Solving this matrix system yields the Rayleigh–Lamb wave modes:

$$\begin{bmatrix} \cos\left(q_z\frac{h}{2}\right) & \frac{-2kr_z\cos\left(r_z\frac{h}{2}\right)}{2k^2-r^2} & i\sin\left(q_z\frac{h}{2}\right) & \frac{-i2kr_z\sin\left(r_z\frac{h}{2}\right)}{2k^2-r^2} \\ \frac{i2kq_z\sin\left(q_z\frac{h}{2}\right)}{2k^2-r^2} & i\sin\left(r_z\frac{h}{2}\right) & \frac{2kq_z\cos\left(q_z\frac{h}{2}\right)}{2k^2-r^2} & \cos\left(q_z\frac{h}{2}\right) \\ \cos\left(q_z\frac{h}{2}\right) & \frac{-2kr_z\cos\left(r_z\frac{h}{2}\right)}{2k^2-r^2} & -i\sin\left(q_z\frac{h}{2}\right) & \frac{i2kr_z\sin\left(r_z\frac{h}{2}\right)}{2k^2-r^2} \\ \frac{-i2kq_z\sin\left(q_z\frac{h}{2}\right)}{2k^2-r^2} & -i\sin\left(r_z\frac{h}{2}\right) & \frac{2kq_z\cos\left(q_z\frac{h}{2}\right)}{2k^2-r^2} & \cos\left(r_z\frac{h}{2}\right) \end{bmatrix} \begin{bmatrix} A_{2,1} \\ B_{2,2} \\ A_{2,2} \\ B_{2,1} \end{bmatrix} = \begin{bmatrix} 0 \\ 0 \\ 0 \\ 0 \end{bmatrix}. \tag{2.10}$$

Here wavenumbers are defined as:

$$q_z = \begin{cases} \sqrt{q^2-k^2}, & \text{if } q \geq k \\ i\sqrt{k^2-q^2}, & \text{if } q < k \end{cases}, \quad r_z = \begin{cases} \sqrt{r^2-k^2}, & \text{if } r \geq k \\ i\sqrt{k^2-r^2}, & \text{if } r < k \end{cases}, \tag{2.11}$$

where $k = \frac{\omega}{c_{ph}}$, $q = \frac{\omega}{C_P}$, $r = \frac{\omega}{C_S}$, with ω denoting the angular frequency of the wave, and c_{ph} the phase velocity of the Rayleigh–Lamb mode in the x-direction.
After simplifying the matrix system, nontrivial wave amplitudes occur when the determinant vanishes. The matrix can be arranged in two independent 2×2 blocks along the diagonal, corresponding to symmetric and antisymmetric modes. Evaluating the determinant of each block separately gives the two dispersion relations:
Symmetric mode:

$$\frac{\tan\left(r_z\frac{h}{2}\right)}{\tan\left(q_z\frac{h}{2}\right)} = -\frac{4k^2q_zr_z}{(2k^2-r^2)^2}. \tag{2.12}$$

Antisymmetric mode:

$$\frac{\tan\left(r_z\frac{h}{2}\right)}{\tan\left(q_z\frac{h}{2}\right)} = -\frac{(2k^2-r^2)^2}{4k^2q_zr_z}. \tag{2.13}$$

An infinite number of guided modes can exist, with their velocities governed by the relation between wavelength and plate thickness. Lamb waves are dispersive, being symmetric/antisymmetric about the midplane ($z = 0$) (see Figure 2.3) with no particle motion in the y-direction.

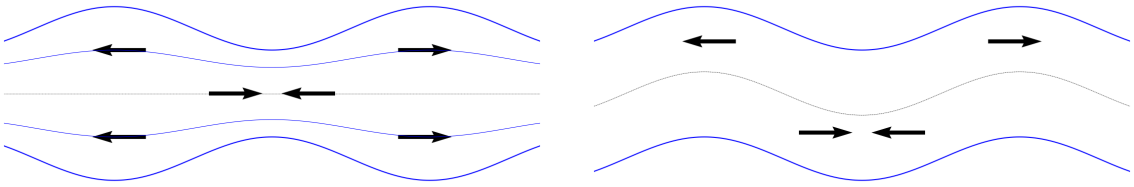

(a) (b)

Figure 2.3: (a) Example of symmetric (a) and antisymmetric (b) deformations of the plate.

Generalization of Rayleigh–Lamb Waves to Floating Ice Sheets

When an elastic plate is in contact with a surrounding fluid, the resulting wave modes are known as Rayleigh–Lamb waves. These waves can radiate energy into the fluid, giving rise to leaky Rayleigh–Lamb waves.

When an elastic plate is loaded with fluid on one or both of its surfaces, the supported wave modes are referred to as leaky Rayleigh–Lamb waves due to their capacity to radiate energy into the adjacent fluid medium. The setup is illustrated in Figure 2.4.

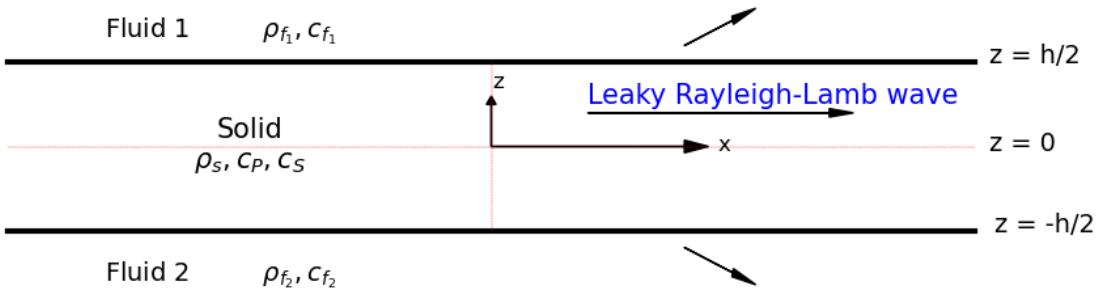

Figure 2.4: Leaky Rayleigh-Lamb wave propagating in the x-direction in the same plate surrounded by two different fluids. The upper fluid has density ρ_{f1} and sound speed C_{f1}, the lower fluid has density ρ_{f2} and sound speed C_{f2}. Wave propagation is along the x-direction, with vertical displacement indicated by u_z.

Generalizing the classical work of Lamb (1917), Osborne and Hart (1945) reformulated the wave propagation problem for an infinite elastic plate in vacuum to the case of a plate submerged in a fluid. Similarly, Press (1951) developed a theoretical model for elastic wave propagation in a floating, homogeneous, isotropic ice sheet over an inviscid, irrotational fluid half-space, with a vacuum above the ice. They derived general dispersion relations: for short wavelengths (much smaller than the ice thickness), the solutions reduce to Rayleigh-type waves, including Scholte waves at the ice-water interface; for long wavelengths (much larger than the thickness), flexural and longitudinal waves dominate; at intermediate wavelengths—when the phase velocity exceeds the speed of sound in the fluid—flexural waves radiate energy into the liquid and become attenuated.

Numerous studies have investigated the propagation of guided waves in plates interacting with various fluids. A comprehensive overview, including both Rayleigh–Lamb and leaky Rayleigh–Lamb waves, can be found in Rose (2014); Shuvalov et al. (2006). In the following, we present the generalized case of a plate bounded by two distinct fluid media (e.g., water and air) as discussed in Lohne et al. (2008).

For a plate immersed in fluid, the surrounding fluids support only outward-propagating waves: in the upper half-space ($z \geq +h/2$) waves move downward, while in the lower half-space ($z \leq -h/2$) waves move upward. These are described by scalar displacement potentials:

$$\phi_{f_1} = A_1^- e^{-iq_{z,f_1}z}, \quad \phi_{f_2} = A_3^+ e^{iq_{z,f_2}z}, \tag{2.14}$$

where the vertical wavenumbers q_{z,f_n} are defined as:

$$q_{z,f_n} = \begin{cases} \sqrt{\dfrac{\omega^2}{c_{f_n}^2} - k^2}, & \dfrac{\omega}{c_{f_n}} \geq k, \\ i\sqrt{k^2 - \dfrac{\omega^2}{c_{f_n}^2}}, & \dfrac{\omega}{c_{f_n}} < k, \end{cases} \qquad n = 1 \text{ or } 2. \tag{2.15}$$

The wave speeds c_{f_n} are given by:

$$c_{f_n} = \sqrt{\frac{\lambda_{f_n}}{\rho_{f_n}}}. \tag{2.16}$$

The normal displacement and stress in each fluid follow from the potentials:

$$u_z = \frac{\partial \phi_{f_n}}{\partial z}, \quad \sigma_{zz} = -p_n = -\rho_{f_n}\omega^2\phi_{f_n}.$$

At the fluid–plate interfaces ($z = \pm h/2$), continuity of normal displacement (u_z), normal stress (σ_{zz}), and zero shear stress (σ_{xz}) are enforced. These boundary conditions couple the fluid potentials to the plate's solid potentials, increasing the number of unknown amplitudes and resulting in a larger matrix system compared to the free plate. Solving this system yields the dispersion relations for fluid-loaded Lamb waves (Lohne et al., 2008):

$$\begin{bmatrix} a_{11} & a_{12} & a_{13} & a_{14} & a_{15} & 0 \\ a_{21} & a_{22} & a_{23} & a_{24} & a_{25} & 0 \\ 0 & a_{32} & a_{33} & a_{34} & a_{35} & 0 \\ 0 & -a_{12} & -a_{13} & a_{14} & a_{15} & a_{16} \\ 0 & a_{22} & a_{23} & -a_{24} & -a_{25} & a_{26} \\ 0 & -a_{32} & -a_{33} & a_{34} & a_{35} & 0 \end{bmatrix} \begin{bmatrix} A_1^- \\ A_{2,1} \\ B_{2,2} \\ A_{2,2} \\ B_{2,1} \\ A_3^+ \end{bmatrix} = \begin{bmatrix} 0 \\ 0 \\ 0 \\ 0 \\ 0 \\ 0 \end{bmatrix}, \tag{2.17}$$

where:

$$
\begin{aligned}
a_{11} &= iq_{z,f_1} e^{iq_{z,f_1}\frac{h}{2}}, & a_{23} &= -2\mu_s k r_z \cos\left(r_z\tfrac{h}{2}\right)\\
a_{12} &= q_z \sin\left(q_z\tfrac{h}{2}\right), & a_{24} &= -i\mu_s(2k^2-r^2)\sin\left(q_z\tfrac{h}{2}\right)\\
a_{13} &= k \sin\left(r_z\tfrac{h}{2}\right), & a_{25} &= i2\mu_s k r_z \sin\left(r_z\tfrac{h}{2}\right)\\
a_{14} &= iq_z \cos\left(q_z\tfrac{h}{2}\right), & a_{26} &= \rho_{f_2}\omega^2 e^{iq_{z,f_2}\frac{h}{2}},\\
a_{15} &= ik \cos\left(r_z\tfrac{h}{2}\right), & a_{32} &= -i2kq_z \sin\left(q_z\tfrac{h}{2}\right)\\
a_{16} &= -iq_{z,f_2} e^{iq_{z,f_2}\frac{h}{2}}, & a_{33} &= -i(2k^2-r^2)\sin\left(r_z\tfrac{h}{2}\right)\\
a_{21} &= \rho_{f_1}\omega^2 e^{iq_{z,f_1}\frac{h}{2}}, & a_{34} &= 2kq_z \cos\left(q_z\tfrac{h}{2}\right)\\
a_{22} &= \mu_s(2k^2-r^2)\cos\left(q_z\tfrac{h}{2}\right), & a_{35} &= (2k^2-r^2)\cos\left(r_z\tfrac{h}{2}\right).
\end{aligned}
$$

The dispersion relations for both symmetrical and antisymmetrical leaky Rayleigh-Lamb waves are obtained by setting the determinant of the matrix on the left-hand side of Equation 2.17 to zero.
A closed-form solution can be expressed as follows (Lohne et al., 2008):
Symmetric case:

$$
(2k^2-r^2)^2 \frac{\tan\left(r_z\frac{h}{2}\right)}{\tan\left(q_z\frac{h}{2}\right)} + 4k^2 q_z r_z = i\frac{\rho_{f1} r^4 q_z}{\rho_s q_{z,f1}} \tan\left(r_z\frac{h}{2}\right). \tag{2.18}
$$

Asymmetric case:

$$
(2k^2-r^2)^2 \frac{\tan\left(q_z\frac{h}{2}\right)}{\tan\left(r_z\frac{h}{2}\right)} + 4k^2 q_z r_z = -i\frac{\rho_{f1} k^4 q_z}{\rho_s q_{z,f1}} \frac{1}{\tan\left(r_z\frac{h}{2}\right)}. \tag{2.19}
$$

When k exceeds the vertical wavenumber in the fluid, q_{z,f_n}, the vertical component q_{z,f_n} becomes purely imaginary, corresponding to evanescent waves that decay exponentially away from the solid-fluid interface. On the other hand, when k is smaller than the fluid's vertical wavenumber, q_{z,f_n} is real, leading to propagating waves in the fluid.

Examples of the full set of modes for both a free plate in vacuum and a fluid-loaded plate are provided in (Lohne et al., 2008), where the dispersion relations are obtained by solving Equations 2.10 and 2.17 over a wide frequency range. This is done by identifying the roots of the system, i.e., the values for which the determinant of the matrix vanishes.

In the present study, we consider the specific case of a floating ice layer, where the upper medium is air (or as vacuum). Under this assumption, Equation 2.17 simplifies accordingly. We solve the resulting system over a limited frequency range relevant to our application. The computed dispersion curves reveal several propagating modes, as illustrated in Figure 2.6.

2.1.2 Asymptotic Approximation

Asymptotic solutions offer simplified expressions that are widely used in the literature for their practicality. In the analytical solution based on full 3D elasticity,

plates support an infinite number of Lamb modes, whose velocities depend on the frequency–thickness product. These modes are found by zeroing the determinant of a frequency- and wavenumber-dependent matrix derived from 3D elasticity under traction-free boundary conditions. Given the material properties (elastic constants and density), roots of the dispersion equation are computed numerically for each frequency by sweeping over wavenumber values, yielding symmetric and antisymmetric modes (e.g., A0, S0). However, tracking these roots across frequencies is challenging, as the equation is transcendental and admits multiple real and complex solutions at each frequency, making it difficult to consistently identify individual modes (Gong and Chen, 2023). The challenge is further compounded when multiple sets of model parameters (e.g., plate thickness, elastic constants, density) must be considered, since roots must be tracked separately for each parameter set, greatly increasing the computational and analytical complexity. This motivates the use of simplified models and approximate solutions, which allow a more simple analysis of wave behavior.

For plate waves, the full 3D problem can be reduced to a set of 2D equations. This asymptotic solution is valid in the thin-plate or long-wavelength limit, where the wavelength is much larger than the plate thickness. In this regime, only the fundamental Lamb modes are captured, greatly simplifying the analysis.

In thin plates under the Kirchhoff–Love assumptions ($h \ll \lambda$), the longitudinal (in-plane) and flexural (out-of-plane) motions are decoupled. The Kirchhoff–Love theory, or classical plate theory (CPT), applicable to thin plates, assumes that straight lines initially normal to the mid-surface remain straight and normal after deformation and the plate thickness does not change (Reddy, 2006) (see Figure 2.5).

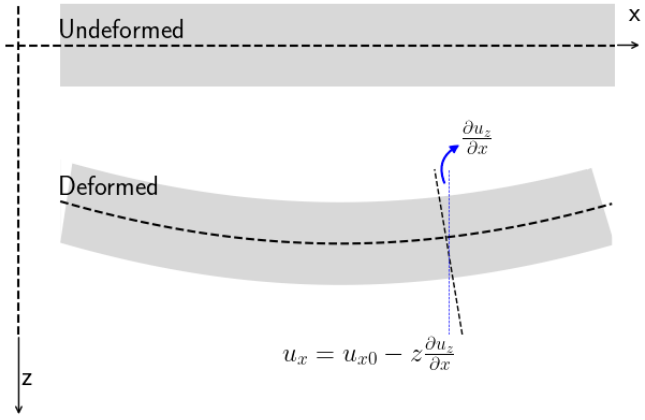

Figure 2.5: Plate deformation in classical plate theory. Here the displacement in the x-direction, u_x, is shown.

The displacement field is defined as:

$$u_x = u_{x0} - z\,\frac{\partial u_z}{\partial x}, \quad u_y = u_{y0} - z\,\frac{\partial u_z}{\partial y}, \quad u_z = u_z. \tag{2.20}$$

where u_{x0}, u_{y0} are in-plane displacements and u_z is the out-of-plane displacement.

Using the displacement field in Equation 2.20, linearized strain–displacement relations yield strains that can be separated into z-independent (stretching) and z-linear (bending) components. The corresponding stresses similarly split.

Starting from the equations of motion (Equation 2.1), and inserting these stresses and strains followed by integration through the plate thickness, one obtains separate governing equations for in-plane and out-of-plane motions.

- In-plane motion (longitudinal and shear-horizontal waves): For 1D propagation along x, in-plane displacements satisfy wave equations:

$$\begin{aligned} \frac{\partial^2 u_{x0}}{\partial t^2} &= C_L^2 \frac{\partial^2 u_{x0}}{\partial x^2}, \quad C_L = \sqrt{\frac{E}{\rho_s(1-\nu^2)}}, \\ \frac{\partial^2 u_{y0}}{\partial t^2} &= C_T^2 \frac{\partial^2 u_{y0}}{\partial x^2}, \quad C_T = \sqrt{\frac{E}{2\rho_s(1+\nu)}}, \end{aligned} \tag{2.21}$$

Comparing these equations with those in Equation 2.4, we see that the shear wave velocity in a plate, C_S, is the same as the shear wave velocity in a 3D medium, C_T. On the other hand, the longitudinal wave speed in the plate, C_L, is smaller than the P-wave speed in the 3D medium, C_P, for Poisson's ratio in the range $0 < \nu < 0.5$.

- Out-of-plane motion (flexural waves): In the case of flexural waves, multiplying the equations of motion by z and integrating through the plate thickness gives the bending moments, which represent the restoring forces generated by the plate curvature. Inserting these bending moments into the out-of-plane equation of motion then leads to the governing equation for flexural waves:

$$D\frac{\partial^4 u_z}{\partial x^4} + \rho_s h \frac{\partial^2 u_z}{\partial t^2} = 0, \quad D = \frac{Eh^3}{12(1-\nu^2)}. \tag{2.22}$$

Assuming a plane wave $u_z(x,t) = e^{i(kx-\omega t)}$, the flexural wave phase velocity is

$$c_{ph} = \omega^{1/2}\left(\frac{D}{\rho_s h}\right)^{1/4} = \left(\frac{Eh^2\omega^2}{12\rho_s(1-\nu^2)}\right)^{1/4}. \tag{2.23}$$

Here D is flexural stiffness the plate, also called flexural rigidity, a measure of its resistance to bending.
Equation 2.23 shows that flexural waves in thin plates are strongly dispersive: higher-frequency components travel faster, and the speed is highly sensitive to thickness ($D \sim h^3$), unlike in-plane longitudinal and shear waves, which are essentially thickness-independent.

Generalizing Plate Theory for Ice Sheets Interacting with Fluids

When studying wave propagation in sea ice, the interaction between the ice layer and the surrounding fluid must be considered.

The fluid pressure in an irrotational, inviscid fluid can be expressed using the linearized Bernoulli–Euler equation, which separates the pressure into dynamic and hydrostatic components (Landau and Lifshitz, 1987):

$$p = -\rho_f \frac{\partial \phi_f}{\partial t} - \rho_f g z, \tag{2.24}$$

where ϕ_f is the velocity potential of the fluid, p is the fluid pressure, ρ_f is the fluid density, and g is the acceleration due to gravity. The first term represents the dynamic pressure due to fluid motion, while the second term corresponds to the hydrostatic pressure arising from gravity (buoyancy force).

In general, two types of fluids are considered in this context. The first type is an ideal, incompressible fluid, which is assumed to be irrotational and inviscid. In this case, the velocity potential satisfies the Laplace equation:

$$\nabla^2 \phi_f = 0.$$

The second type is a compressible fluid, which is also assumed to be irrotational and inviscid, but allows for small, linearized perturbations in density, pressure, and velocity. These perturbations are described by the acoustic wave equation:

$$\frac{\partial^2 \phi_f}{\partial t^2} = c^2 \nabla^2 \phi_f.$$

Depending on the assumptions about the fluid, the presence of air above the water, and whether buoyancy forces are included, various asymptotic models have been developed. These models are briefly outlined in the following sections.
The general plate equation for a floating ice layer, given in Equation 2.25, can be extended by including terms that account for the interaction of the plate with the surrounding air and water, resulting in (Squire et al., 1996):

$$D\nabla^4 u_z(x,t) + \rho_s h \frac{\partial^2 u_z(x,t)}{\partial t^2} + \delta p(x, z = -\frac{h}{2} \text{ and } \frac{h}{2}, t) = f(x,t). \tag{2.25}$$

The pressure at the ice interface denoted by $\delta p(x, z = -h/2 \text{ and } h/2, t)$ is a result of the interaction between ice and air ($z = -h/2$) and ice and water ($z = h/2$), for a given source of $f(x,t)$.

Ewing and Crary (1934) developed the theory of flexural waves in a floating ice layer based on classical plate theory, assuming the ice to be homogeneous and isotropic, and resting on water that is inviscid and irrotational. They account for the interaction between the ice and the water, and derive the dispersion relation for flexural waves. Their work extends that of Greenhill (1886), where the water is assumed incompressible ($c_w = \infty$, where c_w is the compressional wave speed in water), and the flexural rigidity is computed using E instead of the expression $\frac{E}{1-\nu^2}$. They consider both incompressible and compressible fluids to derive the governing equations. For incompressible water ($c_w = \infty$), the flexural-gravity dispersion relation is defined as:

$$\omega^2 = \frac{Dk^4 + g\rho_w}{\rho_s h + \frac{\rho_w}{k} \coth(kH)}. \tag{2.26}$$

Here, H denotes the water depth, ρ_w is the water density, and k is the wavenumber.

Note that when the ice thickness $h = 0$, it reduces to the classical expression for wave propagation under gravity:

$$\omega^2 = \frac{gk}{\coth(kH)}.$$

In the compressible case, the dispersion relation becomes:

$$\omega^2 = \frac{Dk^4 + g\rho_w}{\rho_s h + \frac{\rho_w}{\gamma_1 k}\coth(\gamma_1 kH)}. \tag{2.27}$$

Here $\gamma_1 = \sqrt{1 - \frac{c_{ph}^2}{c_w^2}}$.
Note that when $c_{ph} > c_w$, the term $\gamma_1 k$ becomes imaginary, indicating that energy propagates vertically as an acoustic wave in the water. In contrast, when $c_{ph} < c_w$, $\gamma_1 k$ is real, and the solution becomes a hyperbolic function whose amplitude decays exponentially with depth—characteristic of an evanescent wave.

Motivated by observations of atmospheric-ocean coupling (e.g., following the Krakatoa eruption), Press and Ewing (1951) developed a theory for air-coupled flexural waves (ACFW) in a floating ice sheet (a thin plate with fluid and air loading), considering point sources located in either the air or water (both water and air are modeled as acoustic half-spaces). Dispersion relation for the ice-air-water system can be written as:

$$\omega^2 = \frac{Dk^4 + g\rho_w}{\rho_s h + \frac{\rho_w}{\gamma_1 k} - \frac{\rho_a}{\gamma_2 k}}. \tag{2.28}$$

Here c_a is the compressional wave speed in air, ρ_a is the air density, and $\gamma_2 = \sqrt{1 - \frac{c_{ph}^2}{c_a^2}}$. Note that this equation reduces to Equation 2.27 when the air is treated as a vacuum ($\rho_a = 0$) and the water depth is assumed to be infinite ($H = \infty$), in which case $\coth(kH) \approx 1$.

Stein (1986) derived a similar equation to that of Equation 2.28, where they assume that ice is bounded by water below and vacuum top, and defined as:

$$\omega^2 = \frac{Dk^4 + g\rho_w}{\rho_s h + \frac{\rho_w}{\gamma_1 k}}. \tag{2.29}$$

On the other hand, using a distinct approach, Yang and Yates (1995) combined theory and field data to study flexural wave propagation in floating ice sheets with fluid-loaded thin plate theory. The response to vertical point and line forces was analyzed using integral transforms. The resulting characteristic equation is the same as Equation 2.29, but without the buoyancy term $g\rho_w$, since for the frequency–thickness range considered in their analysis the bending contribution Dk^4 dominates $g\rho_w$ by orders of magnitude. Thus, Equations 2.26-2.29 describe flexural-gravity waves, while the formulation of Yang and Yates (1995) corresponds to flexural waves in a floating plate, as the buoyancy term is neglected. This assumes higher-frequency regimes, rather than very low frequencies (approximately 1 Hz or less).

The dispersion relation given by Equation 2.26 also emerges from the study of moving loads on floating ice, as demonstrated by Squire et al. (1996). Modeling the ice as a thin elastic plate overlying an inviscid, incompressible fluid, they derived a dispersion relation analogous to Equation 2.26 in the context of flexural-gravity waves generated by a moving load. Within this framework, the air-coupled flexural wave phenomenon can be seen as a special case of moving loads on floating plates, where the load speed equals the speed of sound in air. Studies of vehicles traveling on ice show that when the vehicle speed reaches the critical load speed—matching both the flexural phase and group velocities—ice deflections can grow significantly over time, increasing the risk of ice breakage and raising important safety concerns. They provide a review of behavior of a floating ice layer on freshwater and sea ice in response to moving loads. It examines dynamic ice deformation and develops predictive models that incorporate elasticity, inhomogeneity, and viscoelasticity. Based on this work, Romeyn et al. (2021) show that airborne sources generate monochromatic waves in the ice that travel at the speed of sound in air (c_a), arriving before the direct air wave. This coupling depends primarily on ice thickness, due to the h^3 scaling of flexural rigidity. Measuring the phase velocity ($= c_a$) and wave frequency therefore enables ice thickness to be estimated using a closed-form relation. In contrast, waterborne sources generate flexural-gravity waves whose phase velocities remain below c_a, resulting in minimal coupling between ice and air.

To simplify terminology, we will hereafter refer to the (leaky) Rayleigh–Lamb wave formulation as the **analytical solution**, and to the plate-theory approximations as the **asymptotic solution**.

2.1.3 Comparison and Validation

Asymptotic solutions have been widely used to estimate sea-ice thickness due to their simplicity (e.g., Moreau et al., 2020a,b; Serripierri et al., 2021; Moreau et al., 2023; Romeyn and Hanssen, 2023). For the same reason, several authors have also studied the response of floating plates to different types of sources, such as a harmonic point source in air (Press and Ewing, 1951) or vertical point and line forces (Yang and Giellis, 1994). However, in this section we demonstrate that asymptotic approximations are accurate only at low-frequency regimes.

For analytical solutions, the solution is obtained by zeroing the determinant of a frequency- and wavenumber-dependent matrix given in Equation 2.17, as shown in in Figure 2.6.

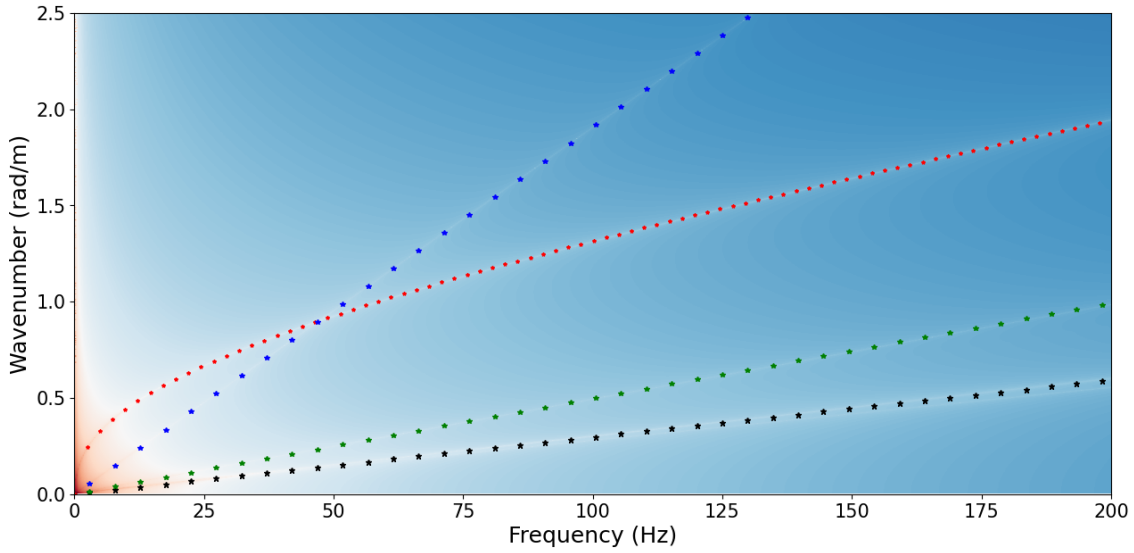

Figure 2.6: Frequency–wavenumber representation for a 1 m thick elastic ice plate over water with air above. The red stars indicate the flexural mode, and the black stars correspond to the longitudinal mode, a non-dispersive mode with a constant velocity of 2122 m/s. Two additional branches are observed: a non-dispersive mode with a velocity of approximately 1266 m/s (green stars), slightly slower than the compressional wave speed in water and likely associated with a Scholte-type interface wave, and a slow mode with a velocity of approximately 330 m/s (blue stars) arising from coupling with the air layer—absent when the upper medium is vacuum. The red region at low frequency and wavenumber indicates strong coupling between the air, ice, and water layers. The flexural and longitudinal dispersion branches remain unchanged when the air layer is removed.

For the asymptotic solutions, we use Equation 2.27 (with water depth $H = 100$ m and an incompressible fluid, $\gamma_1 = 1$) and Equation 2.29, referred to as Ewing model and Stein model, respectively. These are solved numerically using the Newton method to obtain dispersion curves. In these cases, the longitudinal wave speed (c_L, denoted as QS0) is constant and computed from Equation 2.21, matching the slope of the black stars shown in Figure 2.6.

In this study, we focus on flexural waves. The following compares dispersion curves of flexural waves from different models: those extracted from F-K plots of the analytical solution, as well as the Ewing and Stein models. Comparisons are performed for two ice thicknesses, 50 cm and 100 cm, with results shown in Figures 2.7 and 2.8.

The dispersion curve from leaky Rayleigh–Lamb waves (EL-Water-Vacuum) is plotted for comparison with the asymptotic solutions. In addition, the Rayleigh–Lamb curve (EL-Vacuum) is included to illustrate the effect of water on phase velocities. Figures 2.7 and 2.8 show that the presence of water reduces the flexural wave phase velocities.

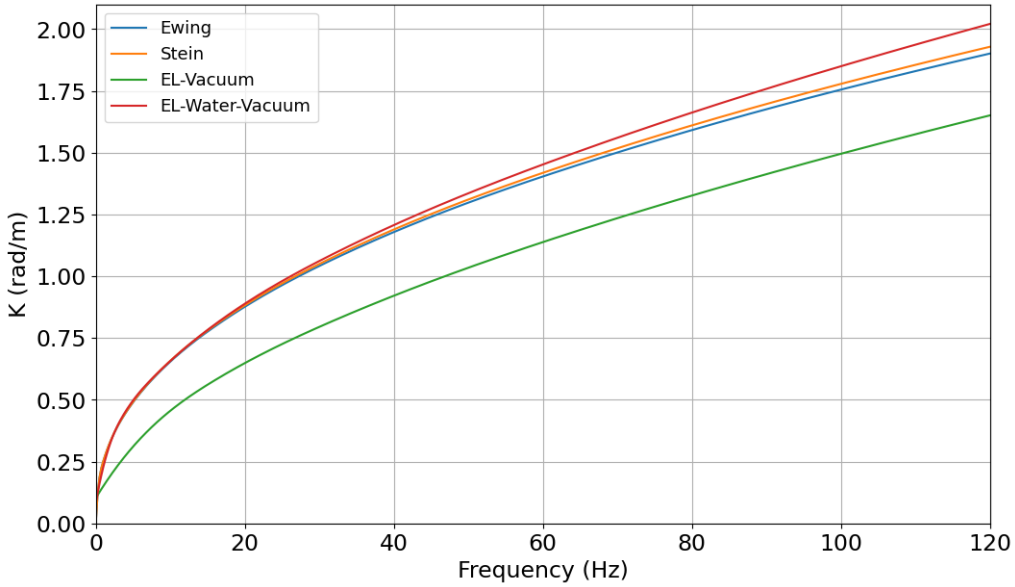

Figure 2.7: Dispersion curves obtained from different modeling tools for an ice layer of 50 cm.

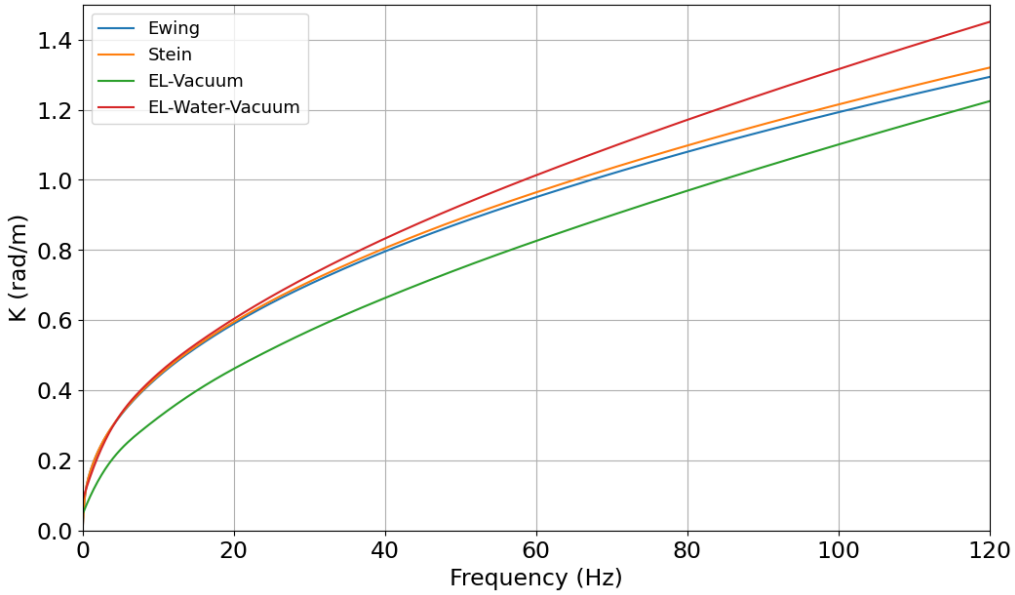

Figure 2.8: Dispersion curves obtained from different modeling tools for an ice layer of 100 cm.

As expected, phase velocity increases with both frequency and thickness. While analytical dispersion relations derived from leaky Rayleigh–Lamb theory (e.g., by zeroing the determinant in Equation 2.17) provide exact solutions in principle, isolating individual modes in practice is challenging. At higher frequency–thickness values, multiple dispersion branches coexist and intersect, complicating mode tracking and making it difficult to extract curves consistently across different thicknesses. Furthermore, for more realistic scenarios involving complex geometries, boundary

conditions, or heterogeneous ice structures, analytical solutions are either unavailable or prohibitively cumbersome to derive.

For these reasons, asymptotic solutions are often preferred as a simplified alternative. In the long-wavelength limit, leaky Rayleigh–Lamb waves reduce to thin-plate bending theory (asymptotic approximation), yielding closed-form expressions for phase velocity. These asymptotic models are computationally efficient, easier to extend to complex boundary conditions, and generally sufficient when only the fundamental flexural mode is of interest—as is commonly the case in sea-ice systems. Several studies have successfully applied such formulations under various source mechanisms to compute synthetic waveforms at given distances (e.g., vertical point force (Yang and Giellis, 1994)).

However, the validity of asymptotic solutions deteriorates at higher frequencies and increasing ice thickness. As shown in Figures 2.7 and 2.8, asymptotic models increasingly overestimate phase velocities relative to full Rayleigh–Lamb theory, with the Stein formulation performing slightly better but still diverging (the Stein model is valid only when the flexural wave phase velocity c_{ph} is smaller than the sound speed in water, c_w). These deviations are non-negligible: in inversions using flexural waves to estimate icequake source locations and ice thickness along source–receiver paths, they introduce systematic biases in inferred parameters, as shown in Section 3.5.2.

To address these limitations, we adopt a numerical approach based on the Spectral Element Method (SEM), as described in the next section. SEM enables direct simulation of full wavefields generated by arbitrary source wavelets without requiring explicit dispersion-curve extraction or mode identification, producing solutions that closely approximate the analytical results. Moreover, SEM naturally accommodates complex geometries, boundary conditions, and heterogeneous ice models, making it a versatile tool for current analyses and future studies of more realistic or complex sea-ice environments.

2.2 Spectral Element Modeling for Wave Propagation in Sea Ice Sheets

As shown, asymptotic solutions deteriorate at high frequencies (Landschulze, 2018; Moreau et al., 2020a; Johansen et al., 2019) and with increasing ice thickness (see Figures 2.7 and 2.8). Analytical solutions, in contrast, provide exact results but are challenging to obtain even in homogeneous media due to complex mode tracking. In heterogeneous media, analytical solutions are generally unavailable, requiring numerical approximations.

Classical numerical approaches for stratified media include the Thomson–Haskell propagator matrix method (Thomson, 1950; Haskell, 1953), which propagates displacement–stress vectors across layers using transfer matrices and is widely employed to compute dispersion relations and modal properties in horizontally layered elastic systems. Related approaches in seismology and acoustics, such as the reflectivity method and the wavenumber integration method (e.g., Müller, 1985; Olson et al., 1984; Jensen et al., 2000), achieve similar results by decomposing the wavefield into

plane waves or modal contributions, but they are inherently limited to laterally invariant structures.

To model more realistic sea ice environments, including horizontal heterogeneities or variable ice thickness profiles, we instead employ discretization methods, which solve the governing wave equations on a spatially discretized domain. Finite-element methods (FEM) have been applied in this context (Landschulze, 2018; Moreau et al., 2020a), and here we use the spectral element method (SEM), a high-order variant of FEM that provides high accuracy for wave propagation problems. Although this study focuses on homogeneous validation cases, this choice establishes a foundation for future investigations involving more complex geometries and material variations.

In this section, we investigate the use of the SEM for simulating wave propagation in the ice–sea system. We first present the physcial model, the governing equations, the discretization used in SEM, then validate the numerical model by comparing its results with the analytical solution for a homogeneous plate, using the dispersion curves of flexural waves.

2.2.1 Physical Model

Fracturing in the ice, caused by natural phenomena such as ocean currents, wind forces, internal stresses, and collisions, gives rise to icequakes that propagate within the ice. To model this process, we consider a 2D physical setup shown in Figure 2.9: a floating ice layer, assumed infinite in the x (propagation) direction, overlying a water half-space (i.e., an infinitely deep layer beneath the ice). Sources are placed within the ice to represent icequakes, while receivers on the surface record both the vertical and horizontal components of displacement.

For the frequencies and ice thicknesses considered here, only longitudinal and flexural waves are observed; the SH0 mode, with displacement normal to the plane, does not appear. Following Moreau et al. (2017), the flexural wave is referred to as the quasi-Scholte (QS) wave and the longitudinal wave as the fundamental symmetric mode (QS0).

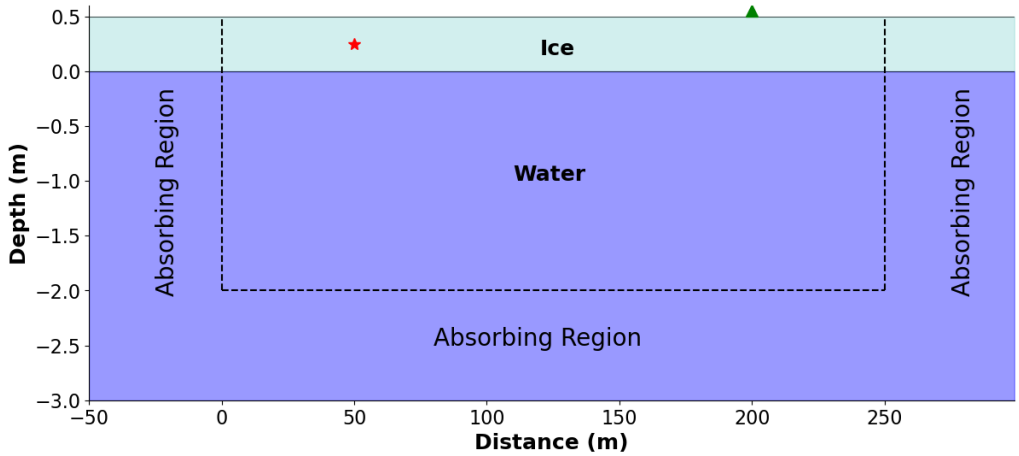

Figure 2.9: Schematic of the simulation medium used in Section 2.2.4. The absorbing region shown is illustrative; its actual size in the x-direction depends on the model parameters and source wavelet and is around 70 m in the example, while in the y-direction the medium extends approximately 300 m. The source is represented by a red star located within the ice layer, and receivers are placed along the ice surface, indicated by green triangles.

2.2.2 Governing Equations for the Ice–Sea System

SEM has gained significant recognition in seismology due to its ability to accurately model seismic wave propagation in complex 2D and 3D geometries of heterogeneous media. SEM employs a mathematical model that is similar to the classical Finite Element Method (FEM), utilizing the weak form of the equation of motion. It combines the flexibility of FEM in handling intricate geometries with the accuracy of pseudospectral methods Komatitsch and Tromp (1999).

We have a medium consisting of water and ice, where the assumptions of linear elasticity for the solid and inviscidity and irrotationality for the fluid are considered. In the solid part we solve the elastic wave equation, while in the fluid, we solve the acoustic wave equation derived from the equations of dynamics (Euler) and conservation (continuity). So we have a coupled system of equations, for which the continuity of traction at the interface of fluid-solid needs to be ensured. The strong formulation, together with the boundary conditions, can be expressed as follows, where it involves the use of displacement potential in the fluid and displacement in the solid, allowing for the accurate representation of the interaction between the fluid and solid components (Cao et al., 2021):

$$\begin{aligned}
&\frac{1}{\kappa}\ddot{\phi}_f = \nabla \cdot \left(\frac{1}{\rho_f}\nabla\phi_f\right) + \frac{1}{\kappa}\boldsymbol{P}_f, && \text{in} \quad \Omega_f \\
&\rho_s \ddot{\boldsymbol{u}} = \nabla.\boldsymbol{\sigma} + \boldsymbol{f}_s, \quad \boldsymbol{\sigma} = \boldsymbol{C} : \boldsymbol{\epsilon}, && \text{in} \quad \Omega_s \\
&\boldsymbol{u}_s.\boldsymbol{n} = \frac{1}{\rho_f}\nabla\phi_f.\boldsymbol{n}, \quad \boldsymbol{\sigma}_s.\boldsymbol{n} = \ddot{\phi}_f \boldsymbol{n}. && \text{on} \quad \Gamma_{fs}
\end{aligned} \tag{2.30}$$

Here, $\boldsymbol{u}_s$, $\boldsymbol{f}_s$, $\boldsymbol{\sigma}$, and $\boldsymbol{\epsilon}$ denote the displacement vector, body force vector, stress tensor, and strain tensor in the solid, respectively. The bulk modulus κ measures

the compressibility of the fluid and is related to the density ρ and the sound speed in fluid c_f by $\kappa = \rho\, c_f^2$. $\boldsymbol{C}$ is the fourth-order stiffness tensor (the constitutive relation is shown in Equation 2.2). The symbols ρ_f and ρ_s refer to the densities of the fluid and solid, respectively, the scalar field ϕ_f represents the displacement potential in the fluid, and $\boldsymbol{P}_f$ is the pressure source in fluid. The domains Ω_f and Ω_s correspond to the fluid and solid regions, while Γ_{fs} denotes their shared interface.

2.2.3 Discretization

These strong-form equations describe wave propagation in both the solid and fluid domains, as well as the coupling conditions at their interface. To implement these equations numerically using SEM, we reformulate them in their weak form. This involves multiplying each equation by test functions and integrating over the respective domains. The weak form facilitates the handling of complex geometries and boundary conditions while ensuring the incorporation of the fluid–solid interface conditions. In the weak formulation, the free-surface boundary condition is implicitely satisfied because the boundary integral of the traction term vanishes.

Let w be a test function for the fluid potential and $\boldsymbol{w}$ a test function for the solid displacement. The weak form of the system in Equation (2.30) is written as (Cao et al., 2021; Komatitsch and Tromp, 1999):

$$\begin{aligned}
\int_{\Omega_f} w\, \frac{1}{\kappa} \ddot{\phi}_f \, d\Omega + \int_{\Omega_f} \frac{1}{\rho_f} \nabla w \cdot \nabla \phi_f \, d\Omega &= \int_{\Omega_f} w\, \frac{1}{\kappa} \boldsymbol{P}_f \, d\Omega + \int_{\Gamma_{fs}} w\, (\boldsymbol{u}_s \cdot \boldsymbol{n})\, d\Gamma \\
&\quad + \int_{\Gamma^f_{\text{abs}}} w\, \frac{1}{\rho_f c_f} \dot{\phi}_f \, d\Gamma, \\
\int_{\Omega_s} \boldsymbol{w} \cdot \rho_s \ddot{\boldsymbol{u}}_s \, d\Omega + \int_{\Omega_s} \nabla \boldsymbol{w} : \boldsymbol{C} : \nabla \boldsymbol{u}_s \, d\Omega &= \int_{\Omega_s} \boldsymbol{w} \cdot \boldsymbol{f}_s \, d\Omega + \int_{\Gamma_{fs}} \boldsymbol{w} \cdot (\ddot{\phi}_f \boldsymbol{n})\, d\Gamma \\
&\quad + \int_{\Gamma^s_{\text{abs}}} \boldsymbol{w} \cdot (\boldsymbol{\sigma} \cdot \boldsymbol{n})\, d\Gamma.
\end{aligned} \tag{2.31}$$

Here, Γ^f_{abs} and Γ^s_{abs} denote the terms related to absorbing boundary conditions in the fluid and solid, respectively. The medium's material heterogeneity is incorporated through spatial variations in model parameters (e.g., ρ, c_f, $\boldsymbol{C}$), which are directly accounted for in the weak formulation.

To discretize the weak form for numerical computation, the domain is divided into non-overlapping hexahedral elements. Within each element, the wavefield is represented using high-order polynomial basis functions, typically Lagrange polynomials, defined on Gauss–Lobatto–Legendre (GLL) points. Each element Ω_e is mapped to a reference domain $\Lambda = [-1, 1]^{n_d}$ (for a 2D medium, $n_d = 2$, so Λ is a square) via an invertible local mapping $\mathcal{F}_e : \Lambda \to \Omega_e$ such that $\mathbf{x}(\boldsymbol{\xi}) = \mathcal{F}_e(\boldsymbol{\xi})$. This allows the SEM to naturally handle complex, heterogeneous media while preserving the accuracy of the numerical solution.

On the reference element Λ, we use a set of local basis functions of degree N. In each direction (ξ, η), there are $N+1$ GLL points. The basis functions are products of

$(N+1)$ 1D Lagrange interpolants $l_p(\xi)$ with the property (Komatitsch and Tromp, 1999):

$$l_p(\xi_q) = \delta_{pq},$$

where the Lagrange basis polynomials are defined as:

$$l_i(\xi) = \prod_{\substack{j=0 \\ j \neq i}}^{N} \frac{\xi - \xi_j}{\xi_i - \xi_j}, \quad i = 0, 1, \ldots, N.$$

Typically, the polynomial degree is chosen between 4 and 8: degrees lower than 4 lead to numerical dispersion, while degrees higher than 8 greatly increase computational cost (Chaljub et al., 2007). Integrals are computed using GLL quadrature. Figure 2.10 shows an example of a Lagrange polynomial of degree 4 mapped on GLL points. Each polynomial is zero at all points except one, e.g., $l_0(\eta)$ is 1 at the first GLL point $\eta = -1$ and zero elsewhere.

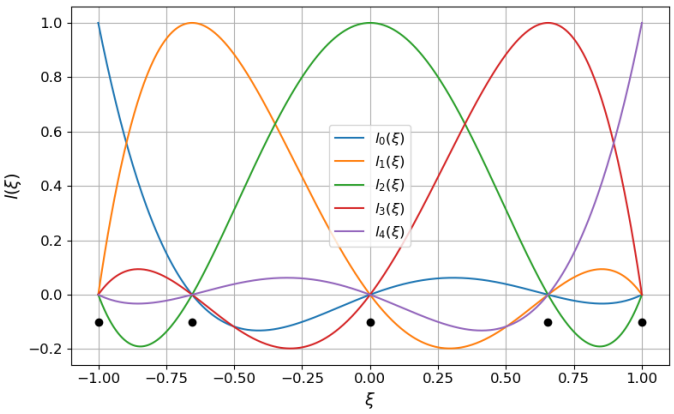

Figure 2.10: Lagrange polynomial $l_i(\xi)$ of degree 4, defined on GLL points in the reference element $\xi \in [-1, 1]$. The polynomial equals 1 at its corresponding GLL point and 0 at all others.

Any field within an element Ω_e can be interpolated from its nodal values at the GLL points. For the displacement field (Komatitsch and Tromp, 1999):

$$u^e(\xi, \eta) = \sum_{p=0}^{N} \sum_{q=0}^{N} u^e(\xi_p, \eta_q)\, l_p(\xi)\, l_q(\eta).$$

Spatial derivatives are obtained analytically by differentiating the basis functions:

$$\frac{\partial u^e}{\partial \xi}(\xi, \eta) = \sum_{p=0}^{N} \sum_{q=0}^{N} u^e(\xi_p, \eta_q)\, l'_p(\xi)\, l_q(\eta), \quad \frac{\partial u^e}{\partial \eta}(\xi, \eta) = \sum_{p=0}^{N} \sum_{q=0}^{N} u^e(\xi_p, \eta_q)\, l_p(\xi)\, l'_q(\eta),$$

where the derivative matrices $l'_p(\xi)$ and $l'_q(\eta)$ are precomputed once on the reference element. Physical gradients are then obtained via the Jacobian of the mapping $\mathcal{F}_e$:

$$\mathbf{J}_e = \frac{\partial \mathbf{x}}{\partial \boldsymbol{\xi}} = \begin{bmatrix} \frac{\partial x}{\partial \xi} & \frac{\partial x}{\partial \eta} \\ \frac{\partial z}{\partial \xi} & \frac{\partial z}{\partial \eta} \end{bmatrix}, \qquad \det(\mathbf{J}_e) = |J_e|.$$

Using the chain rule, the gradient in physical space is:

$$\nabla u^e = \mathbf{J}_e^{-T} \nabla_{\boldsymbol{\xi}} u^e.$$

All integrals in the weak formulation (Equation 2.31) are approximated using GLL quadrature. As an example, the first term of the solid weak form is expressed as:

$$\begin{aligned} \int_{\Omega_s} \boldsymbol{w} \cdot \rho_s \ddot{\boldsymbol{u}}_s \, d\Omega &= \sum_{e=1}^{n_{\text{el}}} \int_{\Omega_e} \boldsymbol{w}^e \cdot \rho_s \ddot{\boldsymbol{u}}^e \, d\Omega \\ &\simeq \sum_{e=1}^{n_{\text{el}}} \sum_{i=0}^{N} \mathfrak{w}_i \sum_{j=0}^{N} \boldsymbol{w}^e(\xi_i, \eta_j) \, \rho^e(\xi_i, \eta_j) \, \ddot{\boldsymbol{u}}^e(\xi_i, \eta_j) \, |J_e(\xi_i, \eta_j)| \, \mathfrak{w}_j, \end{aligned} \tag{2.32}$$

where $\mathfrak{w}_i, \mathfrak{w}_j > 0$ indicate the weights of GLL integration rule, and they are independent of the element and can be computed numerically.

The spatially semi-discretized form of the coupled acoustic–elastic weak formulation can be written as (Cao et al., 2021):

$$\begin{pmatrix} M_f & \mathbf{0} \\ \mathbf{A}^{\mathrm{T}} & \mathbf{M}_s \end{pmatrix} \begin{pmatrix} \ddot{\phi} \\ \ddot{\mathbf{u}}_s \end{pmatrix} + \begin{pmatrix} D_f & \mathbf{0} \\ \mathbf{0} & \mathbf{D}_s \end{pmatrix} \begin{pmatrix} \dot{\phi} \\ \dot{\mathbf{u}}_s \end{pmatrix} + \begin{pmatrix} K_f & \mathbf{A} \\ \mathbf{0} & \mathbf{K}_s \end{pmatrix} \begin{pmatrix} \phi \\ \mathbf{u}_s \end{pmatrix} = \begin{pmatrix} \phi_f \\ \mathbf{f}_s \end{pmatrix}. \tag{2.33}$$

Here, $\mathbf{M}_f$ and $\mathbf{M}_s$ are the mass matrices, $\mathbf{A}$ is the fluid–solid coupling matrix, $\mathbf{D}_f$ and $\mathbf{D}_s$ implement absorbing boundary conditions, and $\mathbf{K}_f$ and $\mathbf{K}_s$ are the stiffness matrices. The terms ϕ_f and $\mathbf{f}_s$ denote the external sources in the fluid and solid domains.
Then, time discretization is performed using finite differences as follows:

$$M_f \frac{\phi^{n+1} - 2\phi^n + \phi^{n-1}}{\Delta t^2} + D_f \frac{\phi^{n+1} - \phi^{n-1}}{2\Delta t} + K_f \phi^n + \mathbf{A}\mathbf{u}_s^n = \phi_f^n, \tag{2.34}$$

$$\mathbf{M}_s \frac{\mathbf{u}_s^{n+1} - 2\mathbf{u}_s^n + \mathbf{u}_s^{n-1}}{\Delta t^2} + \mathbf{D}_s \frac{\mathbf{u}_s^{n+1} - \mathbf{u}_s^{n-1}}{2\Delta t} + \mathbf{K}_s \mathbf{u}_s^n + \mathbf{A}^\top \frac{\phi^{n+1} - 2\phi^n + \phi^{n-1}}{\Delta t^2} = \mathbf{f}_s^n. \tag{2.35}$$

The fluid potential ϕ^{n+1} is first updated from Equation 2.34, followed by the solid displacement $\mathbf{u}_s^{n+1}$ from Equation 2.35.

To emulate an infinite domain, absorbing boundary conditions are enforced through the matrices $\mathbf{D}_f$ and $\mathbf{D}_s$, which combine a radiative boundary condition (Lysmer and Kuhlemeyer, 1969) with a sponge layer (Cerjan et al., 1985).

A key advantage of SEM arises from the use of Lagrange polynomials at GLL points together with GLL quadrature, which renders the mass matrices $\mathbf{M}_f$ and $\mathbf{M}_s$ diagonal. This enables fully explicit time integration without costly matrix

inversions, in contrast to classical FEM or Chebyshev-based SEM. This enables efficient implementation of explicit time schemes on parallel hardware (Komatitsch and Tromp, 1999; Tromp et al., 2008). Forward modeling is carried out using a 2D spectral element package for coupled acoustic–elastic wave propagation. The coupled system of Equations 2.34 and 2.35 is solved explicitly using a Newmark time-marching scheme in prediction–correction form (see Cao et al. (2021)).

In addition, to improve computational efficiency, we employ an adaptive mesh: elements in the physical ice domain maintain a fixed size, while elements in the absorbing boundary region gradually increase in size. This approach significantly reduces the total number of elements compared to using uniformly sized elements, which would lead to rapidly growing computational costs in large simulations, without compromising accuracy. The implementation details are discussed in the next section.

In summary, SEM offers spectral accuracy, efficient explicit time-stepping, accurate treatment of fluid–solid coupling, and flexible handling of complex geometries. The following section presents a practical implementation example.

2.2.4 Numerical Implementation

In this section, we present a test case illustrating the numerical modeling setup used for SEM simulations. This example covers the choice of model parameters, the computational domain, the mesh and absorbing boundary design, source and receiver configuration, simulation parameter choices, and finally, sample results of longitudinal and flexural wave simulations.

The model parameters utilized in the following examples of SEM simulations are presented in Table 2.1. Values are adopted from Serripierri et al. (2021) for ice and from Sidler (2015) for dry snow, while water is modeled as an acoustic medium with a density of $1000\,\mathrm{kg\,m^{-3}}$ and a compressional wave speed of $1440\,\mathrm{m\,s^{-1}}$.

Table 2.1: Model parameters for 2D SEM simulations.

Parameters	**Ice**	**Snow**
Density (ρ)	910 kg/m^3	140 kg/m^3
Poisson's ratio (ν)	0.27	0.08
Young's modulus (E)	3.8 GPa	5 MPa
V_p	2284 m/s	190 m/s
V_s	1282 m/s	129 m/s

The computational domain extends horizontally from 0 to 250 m, with absorbing regions added to both sides to mimic an infinite medium. Vertically, the domain consists of an ice layer overlying water, followed by an absorbing region that mimics the water half-space.

The estimated flexural wave phase velocities and wavelengths for the three ice thicknesses are presented in Table 2.2, based on the asymptotic solution. This provides an approximate understanding of the phase velocities across different frequencies and ice thicknesses. In the simulations, we use a vertical point source

represented by a 15 Hz Ricker wavelet placed within the ice at $x = 50$ m, with receivers from $x = 51$ m to $x = 250$ m at 1 m spacing (the Ricker wavelet spectrum extends up to about $2.7 f_{\text{peak}}$; see Figure 2.11).

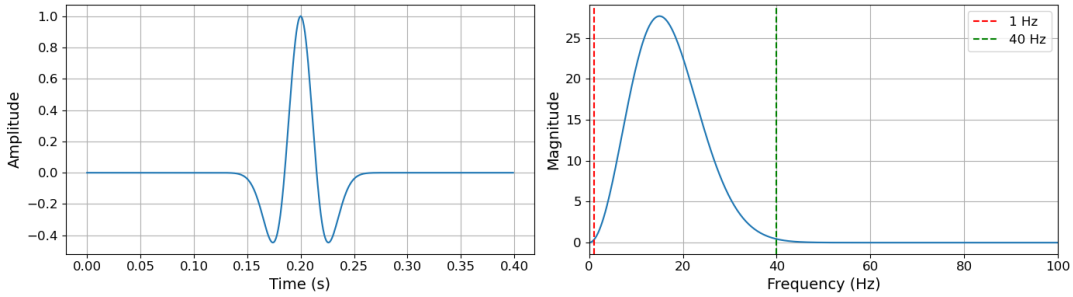

Figure 2.11: An example of a Ricker wavelet with $f_{\text{peak}} = 15$ Hz. On the left is the wavelet signal in the time domain, and on the right is the associated spectrum.

Table 2.2: Estimated flexural wave phase velocities and wavelengths, obtained by solving Equation 2.26 numerically.

Thickness	Frequency (Hz)	Phase Velocity (m/s)	Wavelength (m)
20 cm	40	126.1	3.2
	15	71.2	4.7
	1	14.6	14.5
50 cm	40	213.3	5.3
	15	121.2	8.1
	1	24.8	24.8
100 cm	40	316.0	7.9
	15	180.6	12.0
	1	37.2	37.2

Maintaining numerical accuracy requires minimizing numerical dispersion, which occurs when the number of grid points per minimum wavelength is insufficient. To reduce dispersion, the element size h_e should satisfy $(N + 1)\,\lambda_{\text{min}}/h_e \gtrsim 5$, where N is the polynomial order and λ_{min} the shortest wavelength (Chaljub et al., 2007). Elements in the physical domain have a fixed size, while elements in the absorbing boundaries gradually increase in size, reducing the total number of elements.

Given the polynomial order ($N = 4$) and the minimum wavelengths in each domain—determined by the maximum source frequency and the ice thickness in the ice, and by the maximum source frequency in the water—the element sizes are chosen accordingly. Inside the domain, the number of points per wavelength is higher, while in the absorbing region it gradually decreases toward the boundaries, reaching roughly 5 points per wavelength. Thus, the choice of element size depends on the ice thickness and the source frequency for a given set of elastic constants and densities.

The physical ice domain is discretized with a fixed element size of 1 m in the x-direction. Vertically, the entire ice thickness is represented by a single element, which in the example below is 50 cm. The water domain is discretized with an initial element size of 10 m at the ice–water interface, gradually increasing within the absorbing region.

In the water absorbing boundary region, the width is set to approximately three times the dominant wavelength (corresponding to the peak frequency) to ensure effective attenuation of outgoing waves. Within this region, the element size increases linearly from 10 m to the dominant wavelength (based to Equation 2.37). This configuration, using only five elements, was found to minimize reflections and maintain numerical accuracy for the source wavelength considered.

For dispersive flexural waves, the optimal absorbing boundary cannot be determined solely from the dominant wavelength, since phase velocities vary not only with frequency but also with ice thickness. To address this, we design two separate tests: the first identifies the optimal width of the absorbing boundary region, and the second determines the maximum element size within that region. This approach ensures that reflections are minimized while maintaining numerical accuracy.

As an example, we consider a floating ice layer of thickness $h_{\text{ice}} = 50\,\text{cm}$, using elements of 0.5 m vertically and 1 m horizontally, to determine the minimum absorbing region size. The model includes absorbing layers on both sides with the same element size of 1 m. We vary the boundary width in x direction from 10 m to 150 m (i.e., 10 to 150 elements on each side, in 5 m steps) and compare each case to a reference model with a 200 m-wide boundary region.

The source is placed at 50 m inside the ice layer, and waveforms are recorded from 51 m to 250 m, resulting in 200 seismograms per simulation. To evaluate the simulation accuracy, we select 20 recordings from the reference model (with 10 m interstation spacing) and compute the waveform misfit for each test case using a mean correlation error:

$$\text{Mean Correlation Error} = \frac{1}{20}\sum_{i=1}^{20}\Big(1 - \text{corr}(S_{\text{ref},i}, S_i)\Big). \tag{2.36}$$

Here, $S_{\text{ref},i}$ and S_i represent the i-th waveform from the reference and test models, respectively.

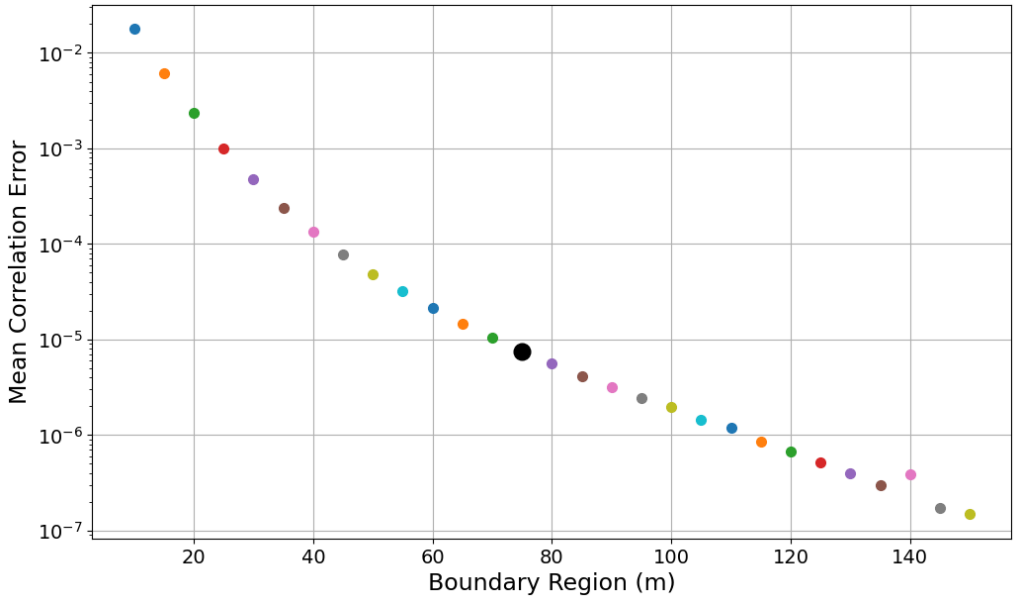

Figure 2.12: Waveform misfit computed across 20 selected recordings, representing the error associated with each tested boundary region size.

As illustrated in Figure 2.12, boundary regions larger than 60 m significantly reduce error. We select a 75 m-wide absorbing boundary, approximately three times the wavelength at 1 Hz. However, using 75 uniformly sized elements significantly increases the computational cost, particularly in large-scale simulations. To enhance efficiency, a second test is conducted in which the element size within the absorbing region increases linearly, defined as:

$$h_i = h_0 + i \times \frac{h_{\max} - h_0}{N_{\text{abc}}}. \tag{2.37}$$

Here, h_0 is the element size in the x-direction within the physical domain, $h_{\max}$ is the maximum element size in the absorbing region, N_{abc} is the number of absorbing elements, and h_i is the linearly increasing element size, starting from h_0 and growing away from the physical domain.

Based on Figure 2.12, we fix the boundary width at 75 m in the x-direction and vary the maximum element size $h_{\max}$ from 1 m to 15 m in 1 m increments. While the boundary width remains nearly the same ($\approx$ 75 m), increasing $h_{\max}$ reduces the number of elements, reducing computational cost.

To determine the optimal maximum element size in the absorbing region, we proceed similarly and compute the waveform misfit between each test model and the reference model. This allows us to identify the optimal element size ($h_{\max}$), achieving a trade-off between numerical accuracy and computational efficiency, as shown in Figure 2.13.

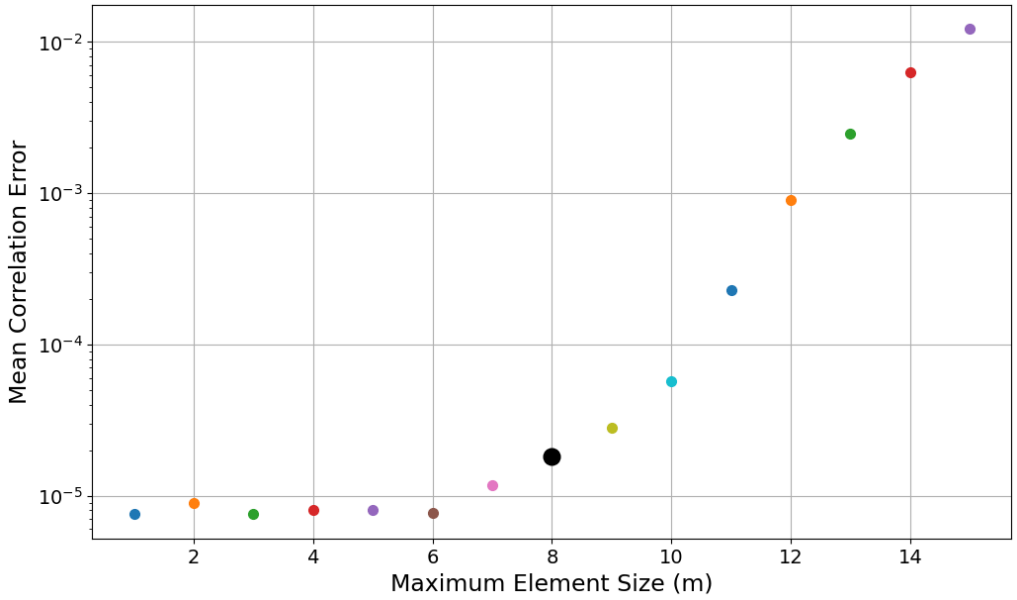

Figure 2.13: Waveform misfit computed across 20 selected recordings for different maximum element sizes in the absorbing boundary region. As the maximum element size increases, the number of elements required in the boundary decreases accordingly, following the sequence $(75, 50, 37, 29, 24, 21, 18, 16, 14, 13, 12, 11, 10, 9, 8)$.

From Figure 2.13, we observe that setting the maximum element size equal to the dominant wavelength of the flexural wave (8.1 m from Table 2.2)—corresponding to 15 elements—provides an optimal trade-off between numerical accuracy and computational efficiency. For instance, on the Dahu cluster at ISTerre using 32 cores, increasing $h_{\max}$ from 1 m (75 elements) to 8 m (16 elements) in the absorbing region reduces the simulation time from 4 min 30 s to 3 min 20 s.

The computational mesh is shown in Figure 2.14. The yellow region represents the physical domain, which includes a light-blue ice layer at the top (visible in the zoomed-in view) and a single water layer beneath it. The remaining area corresponds to the absorbing region.

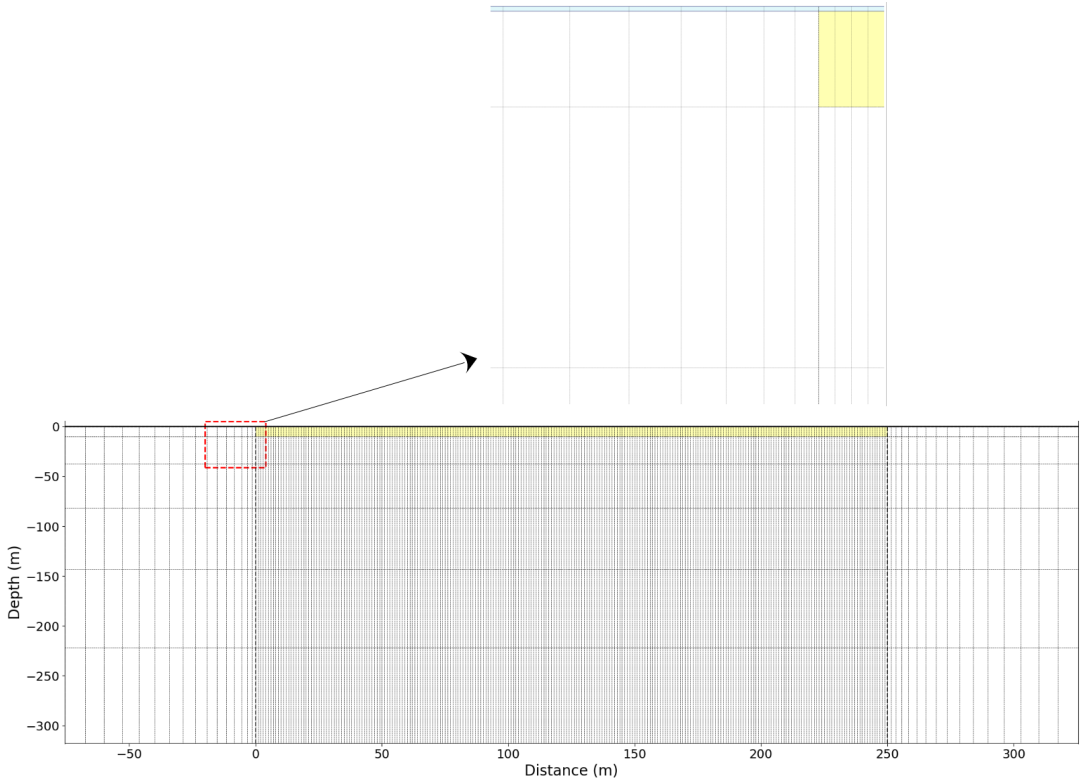

Figure 2.14: Example mesh used in the simulations for $h_{\text{ice}} = 50\,\text{cm}$ with a zoomed-in view of the red dashed area. The ice layer is shown in light blue, and below is water. In the horizontal (x) direction, the element size is 1 m in the physical domain (yellow region with overlying ice layer) and increases linearly to 8.1 m in the absorbing region. Vertically, the element size starts at 10 m (in the physical domain) and increases linearly to 96 m in the absorbing layer. The aspect ratio of the main plot is not to scale; the vertical dimension is compressed by approximately a factor of 3 for clarity.

The simulation duration should ideally be based on the slowest phase velocity to ensure all energy has propagated; however, this is often difficult to estimate precisely. As a practical choice, we set the duration to at least twice the travel time of the dominant wave, which ensures that the main energy reaches the farthest receivers while keeping computational costs reasonable. For example, for a 200 m propagation distance and a dominant flexural wave velocity of 121.2 m/s (for a 15 Hz Ricker wavelet, in 50 cm ice), the simulation duration is about 3.3 s.

Finally, the time step Δt in wave propagation simulations must satisfy the Courant–Friedrichs–Lewy (CFL) condition to ensure numerical stability and minimize dispersion. The CFL condition is expressed as (Virieux, 1986):

$$\text{CFL} = V_{max}\Delta t\sqrt{\frac{1}{\Delta x^2} + \frac{1}{\Delta z^2}} < 1.$$

Solving for Δt, we obtain:

$$\Delta t = \frac{\text{CFL}}{V_{\max}\sqrt{\frac{1}{\Delta x^2} + \frac{1}{\Delta z^2}}}$$

The maximum wave speed is the compressional velocity in ice, $V_{\max} = V_p = 2284\,\mathrm{m/s}$, and the smallest vertical grid spacing occurs in the ice layer, for which $\Delta z = 0.0863$ m and $\Delta x = 0.173$. However, in our code, the CFL condition is computed using only the smallest grid spacing. We therefore choose CFL = 0.5: in the case where $\Delta x_{\min} = \Delta z_{\min}$, this ensures that the CFL value does not exceed 1, satisfying the stability requirement. Thus, corresponding time step size is 1.89×10^{-5} s. Dividing the simulation duration by Δt yields the number of time steps needed.

The time step in our SEM simulations is constrained by the Courant – Friedrich – Lewy (CFL) condition, which ensures stability of explicit time integration by linking Δt to the minimum spacing between GLL grid points and the maximum wave speed in the model. For a polynomial degree $N = 4$, and the smallest grid spacings $\Delta x_{\min} = 0.173$ m, $\Delta z_{\min} = 0.0863$ m corresponding to element sizes of 1 m and 0.5 m, the stable time step is given by:

$$\Delta t = \frac{\mathrm{CFL}}{V_{\max}\sqrt{1/\Delta x_{\min}^2 + 1/\Delta z_{\min}^2}}. \tag{2.38}$$

Using $V_{\max} = V_p = 2284$ m/s, this formula gives $\Delta t \approx 1.69 \times 10^{-5}$ s.

However, in our code, the CFL condition is computed using only the smallest horizontal grid spacing $\Delta x_{\min}$. This is why we choose CFL = 0.5: in the extreme case where $\Delta x_{\min} = \Delta z_{\min}$, the maximum CFL will not exceed 1, which satisfies the necessary stability condition. Based on this approach, the actual time step used in the simulations is

$$\Delta t \approx 1.89 \times 10^{-5}\ \mathrm{s}. \tag{2.39}$$

Figure 2.15 shows SEM waveforms recorded at 50, 100, 150, and 200 m from the source, illustrating the dispersive nature of flexural waves, which becomes increasingly pronounced with distance.

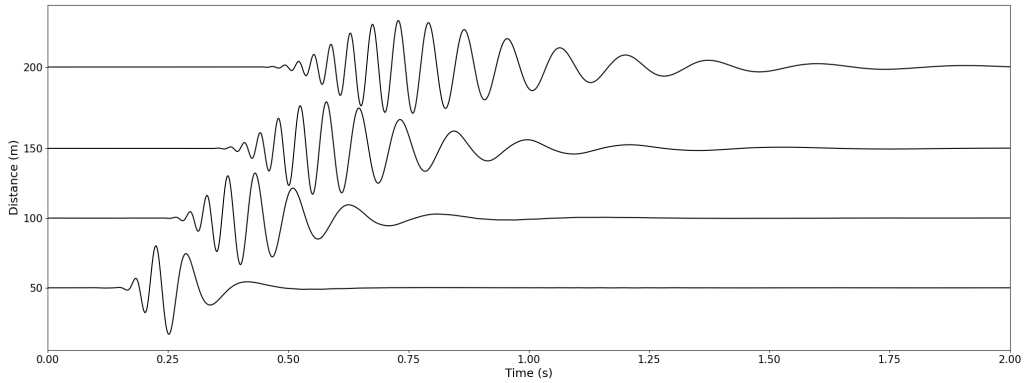

Figure 2.15: SEM simulations for a floating ice layer of 50 cm thickness. Recordings are taken at 50, 100, 150, and 200 m from the source on the vertical channel, where most of the energy comes from the flexural wave. The dispersive nature of these waves is evident. The source is a vertical point force with a 15 Hz Ricker wavelet.

To illustrate the effect of ice thickness on flexural wave propagation, Figure 2.16 presents SEM simulations for ice layers of 20, 50, and 100 cm. As the ice thickness increases, the phase velocity of the flexural wave increases, while the longitudinal

wave velocity remains constant. Using a vertical point source with a 15 Hz Ricker wavelet, most of the energy on the vertical channel comes from flexural waves, while the horizontal channel records both flexural waves with large amplitude and longitudinal waves with smaller amplitude.

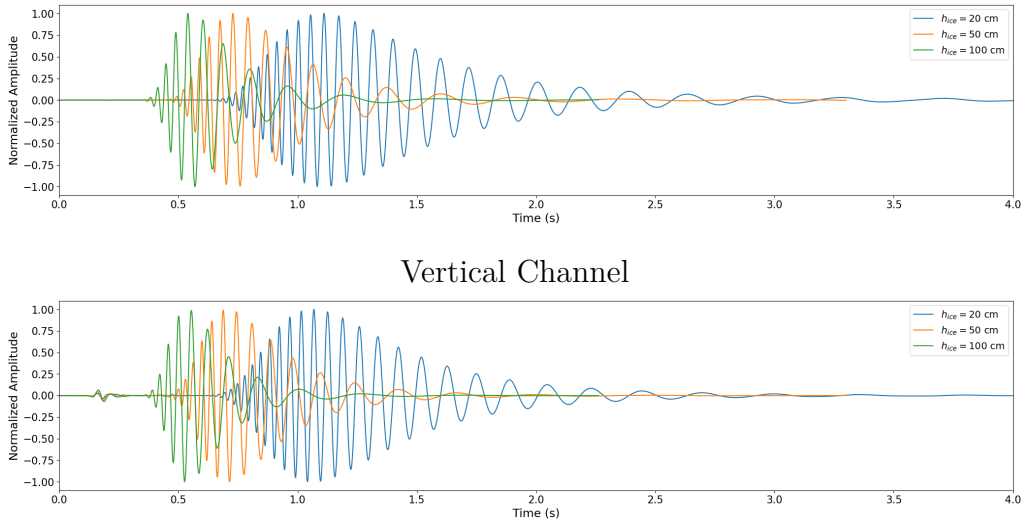

Vertical Channel

Horizontal Channel

Figure 2.16: SEM simulations are performed for ice thicknesses of 20 cm, 50 cm, and 100 cm, recorded at 200 m from the source. On the vertical channel, only flexural (QS) waves are observed, exhibiting dispersive behavior. The horizontal channel shows consistent low-amplitude arrivals of the longitudinal (QS0) wave across all cases. The source is a vertical point force with a 15 Hz Ricker wavelet.

In this frequency range, a vertical point source generates very weak longitudinal waves on the horizontal channel, justifying the use of a boundary layer optimized for flexural waves. However, with a horizontal point source, the longitudinal wave amplitude becomes significant on the horizontal channel, requiring an adapted boundary layer. We retain the same profile (same number of elements and maximum element size corresponding to the dominant wavelength of the flexural wave) but increase the number of elements to extend the boundary region until it reaches approximately 1–2 times the dominant wavelength of the longitudinal wave. For example, a velocity of 2122 m/s at 15 Hz corresponds to a wavelength of about 140 m. Accordingly, we use 70, 45, and 30 elements for ice thicknesses of 20, 50, and 100 cm, respectively, resulting in boundary regions over 200 m, which effectively minimizes reflections. Figure 2.17 presents SEM simulations for a horizontal point source in ice layers with thicknesses of 20, 50, and 100 cm. The vertical channel shows longitudinal waves with small amplitudes, while the horizontal channel is dominated by longitudinal wave arrivals.

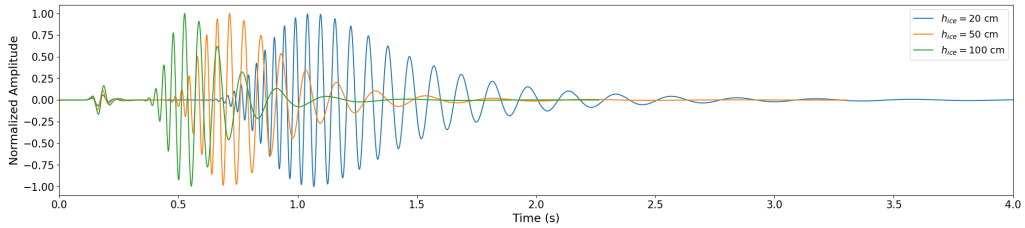

Vertical Channel

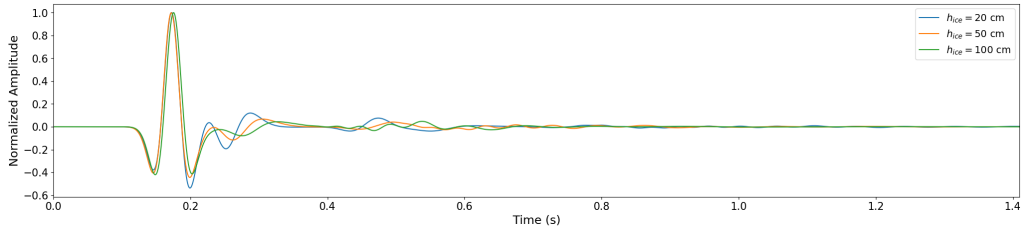

Horizontal Channel

Figure 2.17: SEM simulations are performed for ice thicknesses of 100 cm, 50 cm, and 20 cm, recorded at 200 m from the source. On the vertical channel, flexural (QS) and low-amplitude arrivals of the longitudinal (QS0) waves are observed. On the horizontal channel, the dominant wave is longitudinal, with only a very small-amplitude flexural component. The source is a horizontal point force with a 15 Hz Ricker wavelet.

2.2.5 Comparison With Analytical Solutions

In this section, we present a numerical validation of SEM by comparing simulation results with analytical solutions for wave propagation in a homogeneous medium. This comparison demonstrates the accuracy and reliability of the SEM implementation and confirms its ability to accurately reproduce wave behavior. Establishing this validation provides confidence in using SEM not only throughout this thesis but also as a robust tool for modeling more complex scenarios in future studies.

A direct comparison is best achieved through dispersion curves. Here, we compare the SEM-derived and analytical dispersion curves for ice thicknesses of 50 cm and 100 cm. For the SEM simulations, dispersion curves are extracted from frequency–wavenumber (F–K) analysis of waveforms recorded at 200 receivers spaced 1 m apart. A 50 Hz Ricker wavelet is used as the source. The force is applied as a vertical point source. Figure 2.18 shows the F–K spectrum from SEM simulations for a 100 cm thick ice layer. Waveforms recorded from 1–200 m were arranged in a matrix, and a 2D Fourier transform was applied to compute the amplitude spectrum for positive frequencies and wavenumbers.

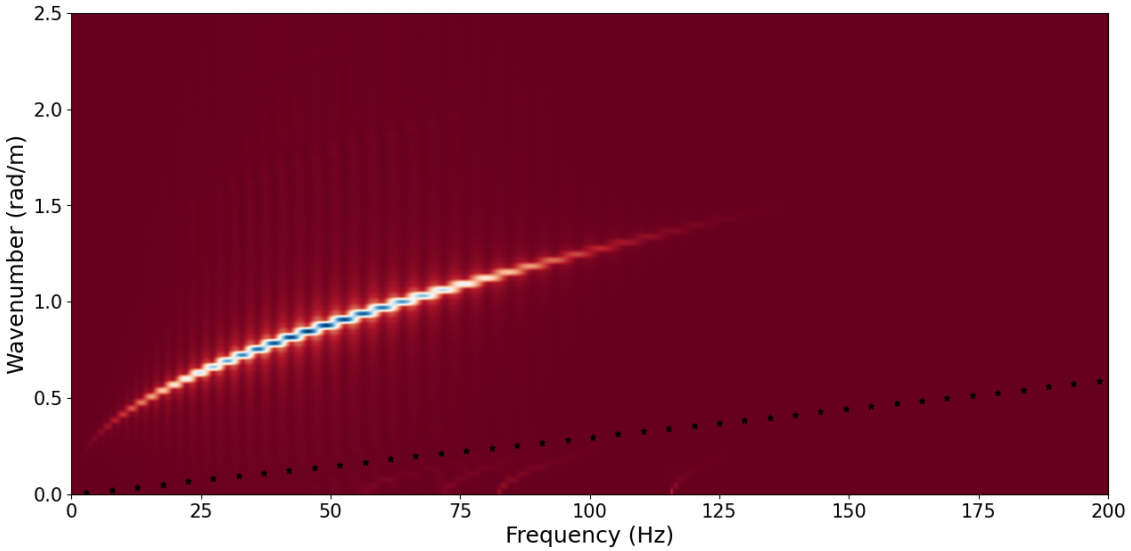

Figure 2.18: Frequency–wavenumber representation obtained from SEM simulations using a vertical point source and recorded on the horizontal channel. The flexural wave's dominant energy ridge is clearly visible. The black stars represent the longitudinal mode, which closely matches the analytical solution shown in Figure 2.6.

The representations in Figure 2.18 and Figure 2.6 (Section 2.1.3) are different because the dispersion curves are obtained using two different methods. In Figure 2.18, the curves are extracted from numerical simulations (SEM). A 2D Fourier transform is applied to the wavefield, using only the vertical component, where the flexural waves are dominant. This gives a frequency–wavenumber (f–k) representation. In Figure 2.6, the curves come from the analytical model. Here, we solve a matrix equation that depends on frequency and wavenumber (Equation 2.17). By scanning different values of frequency and wavenumber and finding where the determinant of the matrix is close to zero, we identify all possible modes in the selected frequency range.

In both cases, amplitudes are normalized. The purpose is to compare the dispersion curves of flexural waves obtained from the SEM simulation with those selected from the analytical solutions. Results for ice thicknesses of 50 cm and 100 cm are shown in Figures 2.19 and 2.20, respectively.

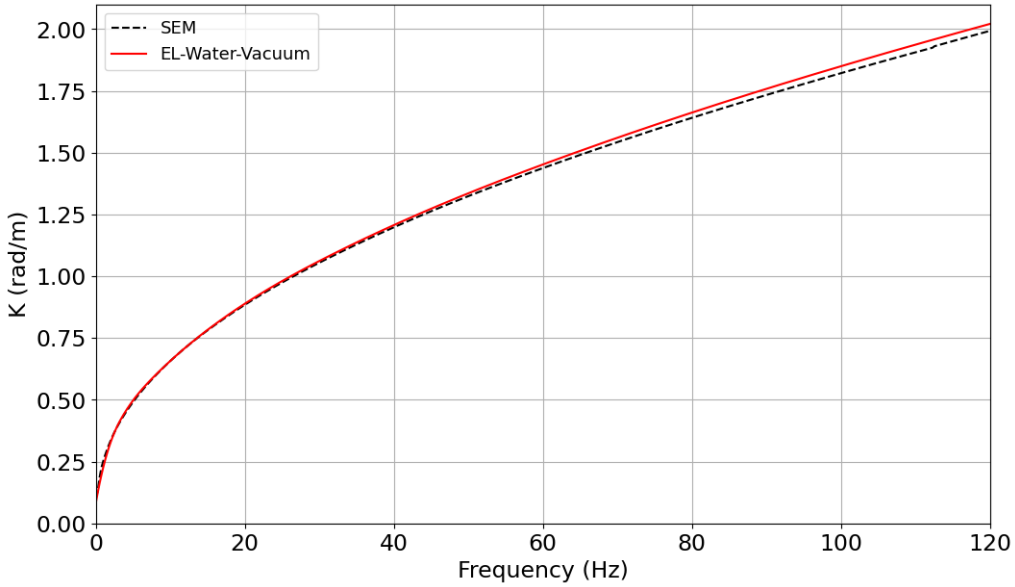

Figure 2.19: Dispersion curves of flexural wave obtained from SEM and analytical solutions for an ice layer of 50 cm thickness.

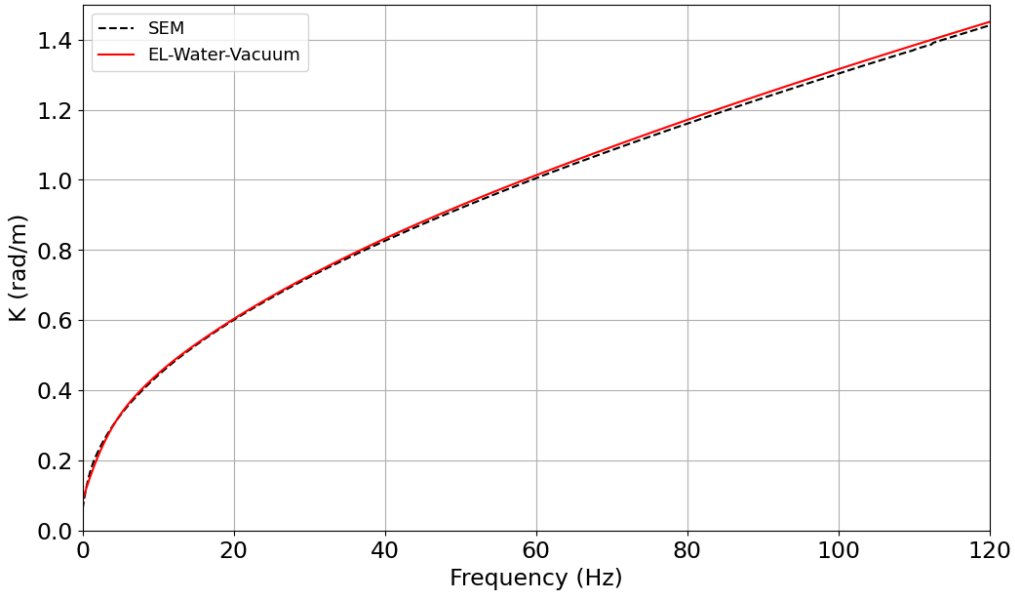

Figure 2.20: Dispersion curves of flexural wave obtained from SEM and analytical solutions for an ice layer of 100 cm thickness.

Here, the dispersion curves of flexural waves in the frequency range of interest are plotted. As shown in Figures 2.19 and 2.20, for an ice thickness (50 cm), the phase velocities obtained from SEM closely match the analytical solution, while for the larger thickness (100 cm), they nearly coincide.

SEM accurately reproduces the dispersion curves of flexural waves, performing particularly well at higher thicknesses and across the full frequency range. In both cases, the SEM results remain very close to the analytical solutions, demonstrating

its reliability and high accuracy in modeling wave propagation. Moreover, SEM provides direct access to synthetic waveforms, eliminating the need to extract dispersion curves or identify individual wave modes from the simulations.

In addition, thanks to its implementation, SEM can incorporate complex geometries, horizontal and vertical heterogeneities, anisotropy, and attenuation—capabilities that open the door for more realistic and detailed studies in future research (in the following section we illustrate two special cases highlighting SEM's ability to model heterogeneity and variations in ice thickness).

2.3 Perspectives: Exploring SEM Capabilities with Snow Cover and Varying Ice Thickness

SEM offers several advantages over analytical and asymptotic approaches. By overcoming the simplifications inherent in these methods, SEM enables the modeling of gradual property gradients in both the lateral (x) and vertical (z) directions and the use of arbitrary thickness profiles—whether increasing, decreasing, or more complex. This flexibility makes SEM a powerful tool for studying realistic sea ice conditions, which often exhibit continuous lateral and vertical heterogeneity.

Sea ice commonly features gradual thickness variations and is frequently overlain by snow, both of which can significantly affect wave propagation. To illustrate the potential of SEM for such complex studies, we present two examples. The first examines the impact of a constant snow layer—a case that, while tractable with other methods such as wavenumber integration, serves as a baseline for understanding snow effects and paves the way toward more realistic scenarios involving depth-dependent snow properties (e.g., the evolving density profile shown in Figure 2.23) or laterally varying snow thickness. The second example addresses a case with linearly varying ice thickness, which directly showcases SEM's ability to handle lateral heterogeneity—a capability beyond the reach of wavenumber-integration approaches. Together, these examples demonstrate the flexibility of SEM and its suitability for tackling even more intricate configurations in future investigations. This section explores the effects of these two factors on wave propagation in sea ice through comparisons of simulated waveforms.

2.3.1 Snow Cover Impact

Snow plays a significant role in the sea ice environment and can influence seismic waveforms. In this section, we introduce a snow layer to evaluate its impact on flexural wave. A representative snow thickness of 25 cm, based on typical observations (Moreau et al., 2020a), is considered.

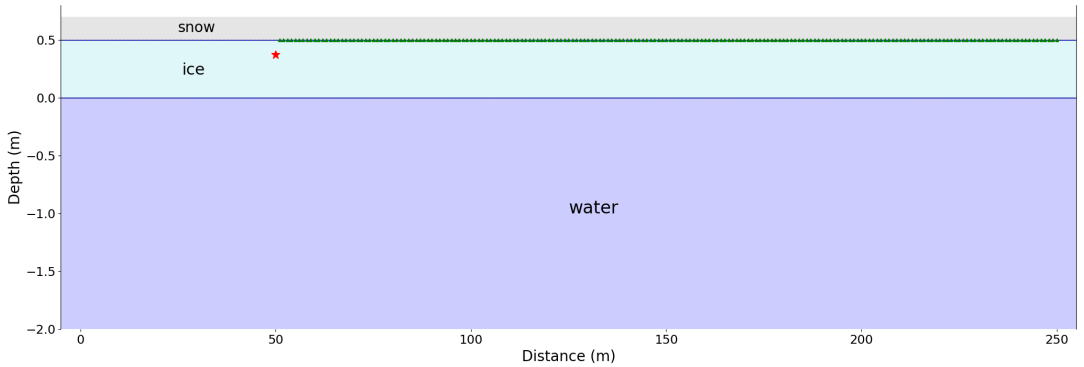

Figure 2.21: Simulation model used to assess the impact of a snow layer: a 50 cm thick floating ice layer with 25 cm of snow atop, overlying water.

To illustrate the effect of the snow layer, we perform simulations using a 15 Hz Ricker wavelet source for a 50 cm thick ice layer with varying snow thicknesses of 10 cm, 25 cm, and 50 cm. The results demonstrate shown in Figure 2.22 how increasing snow thickness influences the phase velocities of the flexural wave.

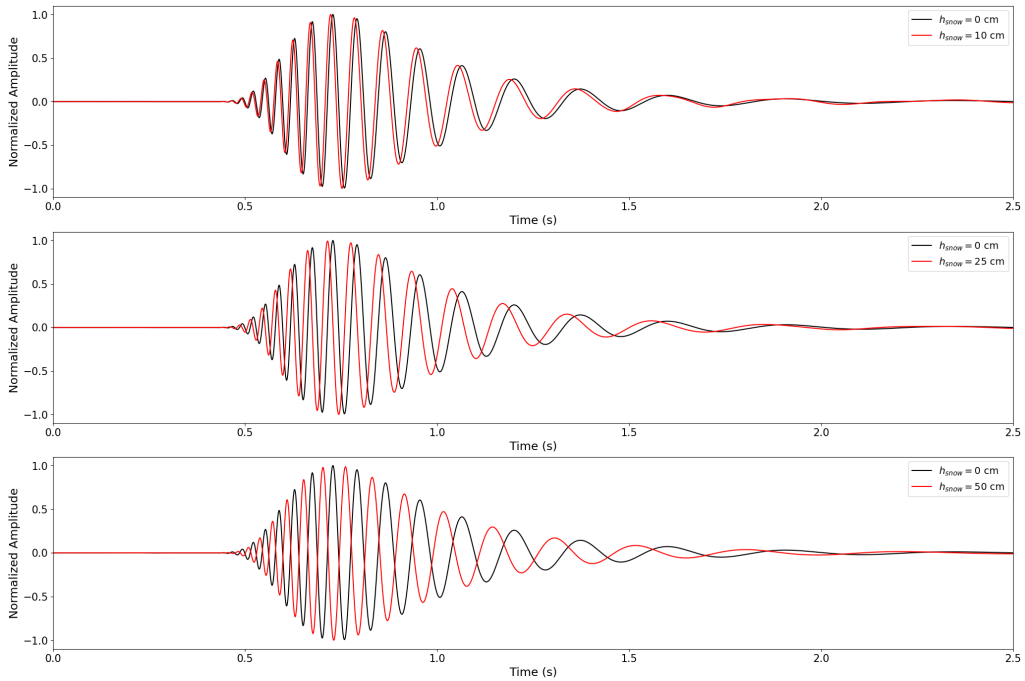

Figure 2.22: SEM simulation results showing the impact of snow layer thickness on the phase velocities of flexural waves in ice. Ice thickness is fixed at 50 cm in all cases, with a 15 Hz Ricker wavelet used as the source.

Snow properties can evolve significantly over time, with density varying at different depths due to processes such as compaction, metamorphism, and temperature fluctuations. This temporal evolution can lead to complex snow density profiles, as illustrated in Figure 2.23. Investigating the impact of such depth-dependent, time-varying snow structures on wave propagation remains an important direction for future work.

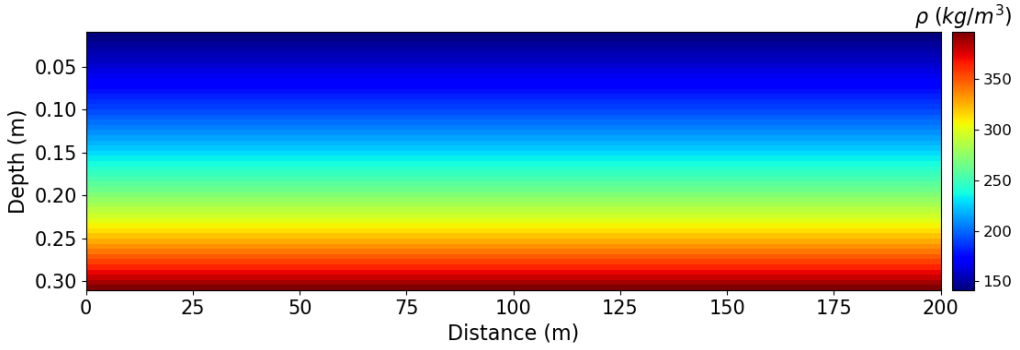

Figure 2.23: Snow density profile after 40 days of temporal evolution, starting with 50 cm of fresh snow as described in Table 2.1, under constant boundary conditions of a snow surface temperature of −15°C and an ice surface temperature of −5°C. To construct the profile, the temperature distribution is first estimated for each sub-layer of the snow (divided into layers thinner than 1 cm). From this, the sub-layer densities and thicknesses are computed, using relations for thermal gradient metamorphism from Carmagnola (2014).

2.3.2 Linearly Changing Thickness

Another experiment investigates the effect of non-uniform ice thickness. In one case, thickness decreases linearly from 70 cm at the source to 30 cm at the last receiver (200 m away); in the other, it increases from 30 cm to 70 cm. Both cases have an average thickness of 50 cm. Figure 2.24 shows the model profile with increasing/decreasing ice thickness used in the simulation.

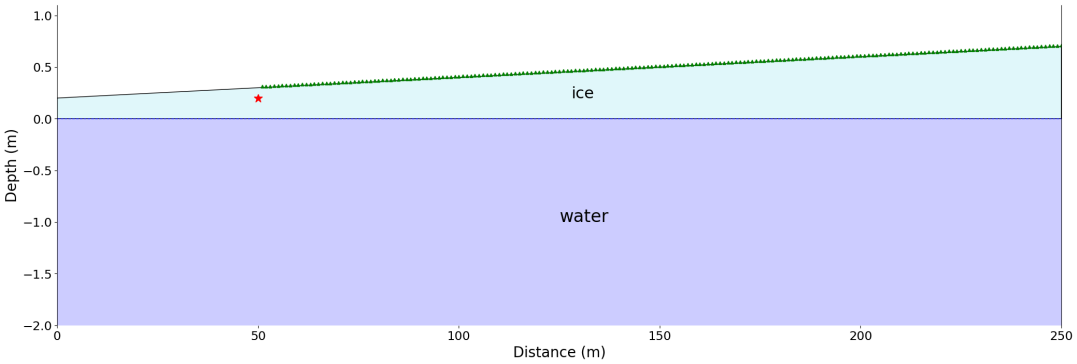

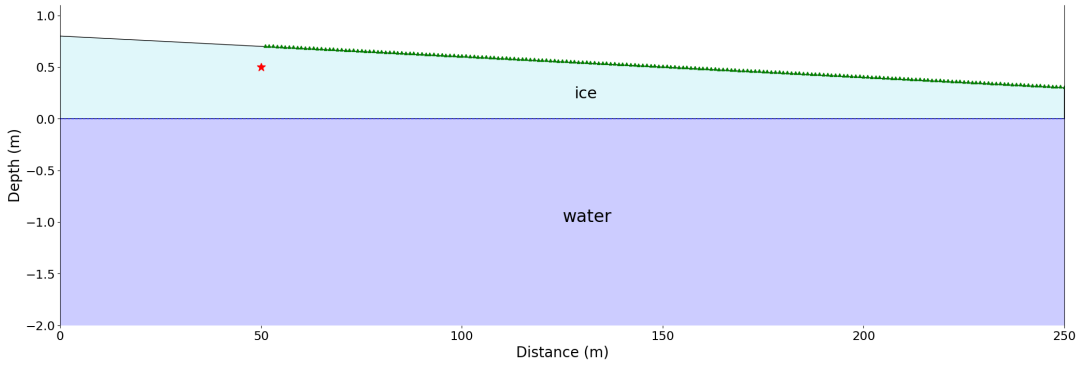

Figure 2.24: Profile with linearly increasing (top) and decreasing (bottom) ice thickness from 0.2 m to 0.7 m and 0.8 m to 0.3 m, respectively, over 250 m. Ice thickness at the source is 0.3 m for the increasing case and 0.7 m for the decreasing case; in both cases, the average thickness between source and last receiver at 200 m is 0.5 m. The receivers (green triangles) are placed along the ice surface.

Although the waveforms from the two scenarios are similar to each other, they differ from that of a constant 50 cm thickness. This suggests that the effective thickness for linearly varying profiles is not simply the average along the path.

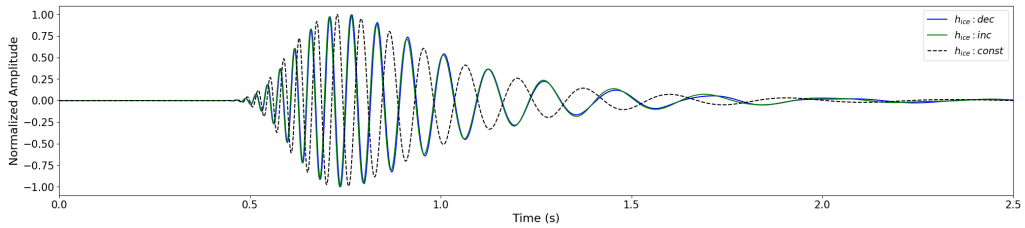

Figure 2.25: SEM simulation results for increasing, decreasing, and constant ice thickness profiles using a 15 Hz Ricker wavelet source.

The dispersive characteristics of flexural waves are influenced by both propagation distance and ice thickness. At greater distances, frequency components separate more noticeably in time due to dispersion (see Figure 2.15). Similarly, thinner ice layers exhibit more pronounced dispersive behavior (Figure 2.16) by changing phase velocities. This demonstrates a trade-off between distance and thickness, where thinner layers can produce dispersion patterns similar to those observed at longer propagation distances.

Under the adiabatic condition—when thickness changes slowly—guided waves behave locally like those in constant-thickness waveguides, with no mode conversion. This allows estimating thickness variations by analyzing wavenumber changes, given the thickness at the first receiver and evenly spaced receivers (Moreau et al., 2014). However, this assumption does not hold in our study but could be explored in future work.

CHAPTER 3

INVERSE METHODS FOR ICE THICKNESS ESTIMATION AND ICEQUAKE LOCALIZATION

Contents

3.1 Overview of Inversion Methods 54

3.1.1 Traditional Earthquake Location Methods 54

3.1.2 Challenges Specific to Icequake Inversion 54

3.1.3 Inversion Strategy Overview 54

3.2 Inversion Approach for Icequake Localization and Ice Thickness Estimation 55

3.2.1 Simulated Annealing 55

3.2.2 Synthetic Data Generation Using SEM 58

3.2.3 Cost Function Visualization and Selection 59

3.3 Validation of the Inversion Strategy Using Synthetic Test 69

3.4 Field Data Application 73

3.5 Perspectives 78

3.5.1 Particle Swarm Optimization 78

3.5.2 Sensitivity of Inversion to the Choice of Forward Model, Heterogeneity, and Layer Geometry 79

This chapter begins by outlining the inversion problem and the parameters to be estimated, namely ice thickness and icequake location. The steps of the inversion process are then presented in detail, including its implementation and the definition a cost function. Then, the method is validated using synthetic tests and subsequently applied to the field datasets introduced in Chapter 1.

3.1 Overview of Inversion Methods

3.1.1 Traditional Earthquake Location Methods

In earthquake seismology, hypocenter estimation is primarily based on P- and S-wave arrival times and their polarization, using a known or iteratively updated 1D (or simple 3D) velocity model, where travel-time residuals are minimized. Programs such as HypoInverse (which assumes a fixed 1D velocity model) (Klein, 2002), HYPOCENTER (which uses a fixed layered 1D velocity model) (Lienert and Havskov, 1995), and VELEST (which jointly inverts for earthquake locations and updates a 1D velocity model) (Kissling et al., 1995) apply linear, iterative least-squares inversion methods derived from Geiger's algorithm (Geiger, 1912). In contrast, NonLinLoc (Lomax et al., 2000) employs a nonlinear, probabilistic global search approach that uses observed travel times along with 1D or 3D velocity models to sample possible hypocenter locations, producing a full probability map of earthquake location. These methods rely on two key assumptions: (1) the existence of clear, impulsive body-wave arrivals whose travel times can be reliably picked, and (2) a known, often layered, velocity model.

3.1.2 Challenges Specific to Icequake Inversion

Icequake data pose a fundamentally different challenge compared with standard earthquake seismology. They are dominated by flexural waves—a dispersive guided mode whose phase velocity depends on both frequency and ice thickness—making traditional arrival-time picking infeasible. Furthermore, the ice thickness along the source–receiver paths is unknown yet directly controls wave speeds. Consequently, source location and ice thickness are coupled: errors in one propagate to the other, so they must be inferred simultaneously through a joint inversion.

3.1.3 Inversion Strategy Overview

Inverse methods for geophysical problems generally fall into two categories. Local methods (e.g., gradient descent, Newton-type methods) linearize the forward problem around an initial guess and iteratively refine it. They converge quickly when the initial guess is good and the cost function is convex, but they are prone to becoming trapped in local minima in nonlinear, multimodal problems. Global methods (e.g., grid search, Monte Carlo sampling, Simulated Annealing, Particle Swarm Optimization) explore the full parameter space without relying on derivatives. While computationally more demanding, they are better suited to problems with multiple local minima and provide a more complete picture of parameter trade-offs.

Given the characteristics of the icequake inversion problem—nonlinearity, multimodality, and coupling between parameters—we adopt a global optimization strategy based on Simulated Annealing (SA). SA is a stochastic method that probabilistically accepts solutions with higher cost during early iterations, allowing it to escape local minima. As the algorithm "cools," it increasingly focuses on promising regions of parameter space, converging to a close approximation of the global optimum. This behavior aligns well with our three-stage inversion strategy, where SA is

used for initial exploration (Step 1) and subsequent refinement (Step 2), followed by a final grid search (Step 3) for high precision. Alternative global methods such as Particle Swarm Optimization are discussed in the perspectives section as potential avenues for future work.

3.2 Inversion Approach for Icequake Localization and Ice Thickness Estimation

In the inversion, we compute a cost function that quantifies the misfit between synthetic and observed data for N stations. Our passive seismic dataset from Svalbard contains over 5,000 icequakes, making it essential to obtain solutions efficiently within a limited computational time. For example, when inverting for the four unknowns, i.e., [longitude, latitude, h_{ice}, t_0], if we consider a search area of 1000×1000 m for longitude and latitude (with 1 m steps), 81 values for ice thickness (1 cm steps from 20 to 100 cm), and 2500 values for origin time t_0 (from -5 to 5 s in steps of 1/250 s), a full grid search would require 2.025×10^{11} cost function evaluations, making it computationally intractable. Instead, methods such as Simulated Annealing (SA) or Markov Chain Monte Carlo (MCMC) are used, as they efficiently explore the parameter space by focusing on promising regions, significantly reducing the number of evaluations while still providing accurate approximations to the global minimum.

In this work, the inversion is implemented as a three-step procedure. In the first step, SA explores the full parameter space to identify regions containing potential solutions. The second step applies SA again, but restricted to a smaller, refined search region to improve convergence toward the global minimum. Finally, a grid search is performed within an even smaller domain to determine the optimal solution with higher precision. By progressively reducing the search area at each stage, this approach efficiently constrains ice thickness and source location within smaller regions of the parameter space. The overall strategy and its implementation are described in detail in the following sections.

3.2.1 Simulated Annealing

Simulated Annealing (SA) is a type of Markov Chain Monte Carlo (MCMC) method, based on Bayesian Inference. SA is a stochastic optimization method in which the objective function estimation is improved iteratively to find the global minimum. The method is based on an analogy between statistical mechanics and combinatorial optimization's problems (Kirkpatrick et al., 1983; Andrieu and Moulines, 2006). The SA algorithm is similar to physical annealing, where the material reaches an annealing temperature and then its temperature is gradually decreased until it reaches a desirable structure with minimum energy. Given some observation data, d, and some modelling parameters, m, used for generating synthetic data, the likelihood of the data given the model parameters, $P(d|x)$, is expressed such that (Menke, 2012):

$$P(d|x) \propto e^{-\frac{E(d,m)}{T}}, \tag{3.1}$$

where $E(d, m)$ shows the energy of the system and T is the temperature.

The objective is to reach the minimum energy. In this case, the energy of the system is the cost function, and the temperature represents the variance of the distribution. High T means that the width of distribution is larger. By cooling slowly enough, it is possible to find the global optimum. Cooling too quickly means that it is possible to get stuck in a local minimum.

For applying SA successfully, it is necessary to generate a random initial solution, from a proposal distribution which is perturbed iteratively to generate consecutive solutions, and also to build an annealing schedule, a temperature reduction function, with a specified number of iterations to go from an initial temperature T_0 to the final temperature T_f.

SA minimizes a cost function $E(d, m)$ by probabilistically accepting solutions with higher cost, enabling the algorithm to escape local minima and increase the likelihood of finding the global optimum. The acceptance probability follows the Metropolis criterion (Menke, 2012):

$$P = \begin{cases} 1 & \text{if } \Delta E < 0 \\ \exp(-\Delta E/T) & \text{if } \Delta E \geq 0 \end{cases}$$

Algorithm 1: Simulated Annealing

Input: Initial solution m_{start} , initial temperature T_0, final temperature T_f, cooling rate κ, number of iterations N

Output: Best solution found x_{best}

Initialize $m_0 \leftarrow m_{\text{start}}$, $m_{\text{best}} \leftarrow m_{\text{start}}$, $T \leftarrow T_0$, $i \leftarrow 0$
while $i < N$ **do**
  Propose new candidate m'
  Compute $\Delta E \leftarrow E(d, m') - E(d, m_i)$
  if $\min\left(1, \exp\left(-\frac{\Delta E}{T}\right)\right) > \textit{rand}(0, 1)$ **then**
    $i \leftarrow i + 1$
    $m_{i+1} \leftarrow m'$
    $T_{i+1} \leftarrow \kappa T_i$
    if $E(d, m') < E(d, m_{best})$ **then**
      $m_{\text{best}} \leftarrow m'$
    end
  end
end
return m_{best}

When the initial temperature is high, almost all candidate solutions are accepted. As the temperature decreases, the probability of accepting new candidates also decreases.

A simple choice of temperature profile is the geometric cooling schedule such as $T_{k+1} = \kappa T_k, \text{with} 0 < \kappa < 1$, where κ controls the rate of cooling. This type of schedule is often used due to its simplicity and gradual reduction of the acceptance probability. However, in our case, we employ a piecewise temperature schedule with multiple phases to allow more flexibility in controlling the acceptance behavior.

In our simulated annealing scheme, the temperature is defined using a piecewise schedule consisting of multiple phases. Each phase has an exponential decay from an initial temperature T_0 to a minimum temperature $T_{\min}$, followed by a constant plateau at $T_{\min}$.

- Exponential decay: Each phase p starts at temperature $T_0^{(p)}$ and decays exponentially to $T_{\min}^{(p)}$ over N_{decay} iterations according to

$$T_{\text{decay}}^{(p)}(k) = T_0^{(p)} \left(\frac{T_{\min}^{(p)}}{T_0^{(p)}} \right)^{\frac{k}{N_{\text{decay}}-1}}, \quad k = 0, \ldots, N_{\text{decay}} - 1$$

  where N_{decay} is the number of iterations in the exponential decay.

- Plateau: After the exponential decay, the temperature is held constant at $T_{\min}^{(p)}$ for the remainder of the phase.

- Phase continuity: The next phase begins at the minimum temperature of the previous phase, i.e.,

$$T_0^{(p+1)} = T_{\min}^{(p)}.$$

  This ensures a continuous temperature profile across phases. In our implementation, we use a total of 5 phases.

At the end of all phases, an additional constant plateau is added, using the temperature at the $T_{\min}$ of the last phase. In practice, the temperature used in the acceptance probability is T^2, which improves the convergence speed.

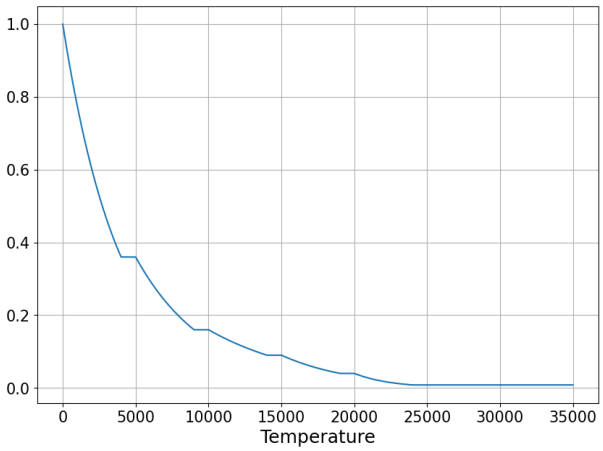

Figure 3.1: Example of the temperature profile, T^2, used in the algorithm.

As shown in Figure 3.1, the temperature schedule follows a multi-phase exponential decay pattern. Each phase shows a rapid initial decrease in temperature, followed by a constant plateau, ensuring a gradual and controlled cooling process.

In our SA algorithm, the process can terminate early if R consecutive candidate solutions are rejected. The choice of R is user-defined and can be set by trial and error.

3.2.2 Synthetic Data Generation Using SEM

The forward modeling using SEM remains expensive due to the physical domain: a very thin ice layer extending several hundred meters (Figure 2.14) requires small element sizes, which in turn necessitate a very small time step for numerical stability. For the Svalbard case, which comprises over 5,000 icequakes, a full Bayesian inversion for source location and ice thickness would require 10^4–10^5 forward simulations per event—a computationally prohibitive cost. This bottleneck directly motivates the creation of a precomputed SEM database. As shown in Table 3.1, a single simulation for a thin ice sheet (20 cm thickness) takes approximately one hour on a high-performance computing cluster. Since an inversion for a single icequake would require tens of thousands of such simulations, the total runtime is prohibitive. This motivates the creation of a precomputed SEM database.

Table 3.1: Computational cost of a single SEM simulation for the Svalbard case. Receivers at 1–620 m spacing. Mesh: 7 (vertical) × 700 (horizontal) elements. 4th-order Lagrange polynomials for interpolation. GRICAD Dahu cluster (32 cores, MPI).

Ice Thickness	**Simulation Time**
20 cm	∼1 hr
100 cm	∼5 min

For all inversions we rely on synthetic database generated with the SEM. Separate synthetic databases are created for each field dataset based on the site-specific parameters described in Chapter 1. The SEM databases are parameterized around two primary unknowns: ice thickness and source–receiver distance. This parametrization is summarized in Table 3.2.

Table 3.2: Parameter space for the precomputed SEM database.

Parameter	**Canada dataset**	**Svalbard dataset**
Distance from source (step 1 m)	1–200 m	1–620 m
Ice thickness (step 1 cm)	10–100 cm	20–100 cm
Source central frequency	40 Hz Ricker	15 Hz Ricker
Number of recorded signals	18,200	50,220

The database enables a computationally efficient inversion by eliminating the need for any forward modeling during the iterative search. The inverse problem is thus reduced to a fast look-up and comparison within the precomputed solution space.

The **source wavelet** used in the SEM simulations is a zero-phase Ricker wavelet. Its central frequency is chosen to match the dominant frequency content of the

observed icequakes in each dataset (e.g., 15 Hz for Svalbard, 40 Hz for Canada), ensuring that the wavelet's bandwidth covers the frequency range of the recorded signals. This represents a convenient choice given that we have no prior knowledge of the true source signature. As described in the following section, the cost function incorporates a spectral weighting scheme that replaces the synthetic amplitude spectrum with that of the observed data. This restricts the inversion to matching only the phase evolution of the signal—the dispersive behavior that depends on the local ice thickness and source location—while rendering the results insensitive to the unknown source amplitude spectrum.

The inversion is performed exclusively on the vertical channel, which is dominated by the flexural wave with minimal or no energy from longitudinal waves or the SH0 mode. Modeling the source as a vertical point force is therefore adequate for exciting the flexural wave in the 2D waveguide geometry. Moreover, because the ice layer acts as a guided medium in which the amplitude of the flexural wave decays rapidly with distance, 3D geometrical spreading effects are negligible. The dispersion properties that control the phase evolution are thus primarily determined by the local ice thickness along each source–receiver path, justifying the 2D waveguide approximation. While future work could investigate more complex source parameterizations, the current approach is well-suited to our goal of recovering ice thickness and source location from flexural waves.

3.2.3 Cost Function Visualization and Selection

The inversion of icequakes for localization and ice thickness estimation is based on minimizing a cost function that measures the misfit between synthetic and observed data. This cost function plays a central role in the accuracy and performance of the inversion process.

Understanding the cost function relative to model parameters is essential in designing efficient inversion methods. Specifically, we examine two types of cost functions to gain insights into their behavior, enabling us to select the most advantageous one, or a combination of both, for the design of the inversion method.

Both cost functions are correlation-based: the first uses zero-lag correlation computed in the frequency domain, while the second is based on the correlation of the short-time Fourier transforms (STFT) of the synthetic and observed data. From now on, we refer to them as the **zero-lag correlation** and **STFT-based** cost functions.

In the first case, it is essentially the conventional zero-lag correlation of two signals, but computed in the frequency domain using the correlation theorem (refer to Appendix A). It is computed as follows:

1. **Fourier transform:** Compute $D_{\text{obs}}(\omega) = \mathcal{F}\{d_{\text{obs}}(t)\}$ and $D_{\text{syn}}(\omega) = \mathcal{F}\{d_{\text{syn}}(t)\}$. Here $d_{\text{obs}}(t)$ and $d_{\text{syn}}(t)$ denote the observed and synthetic records of the flexural wave in the time domain.

2. **Time shifting:** The synthetic data are shifted in the frequency domain as:

$$D_{\text{syn}}(\omega) = D_{\text{syn}}(\omega)\ \exp(-i\omega t_0)\,,$$

where t_0 is the time-shift parameter.

3. **Spectral weighting:** Apply spectral weighting to the synthetic data using the observed data:
$$\tilde{D}_{\text{syn}}(\omega) = \frac{D_{\text{syn}}(\omega)\,|D_{\text{obs}}(\omega)|}{|D_{\text{syn}}(\omega)|}.$$
Spectral weighting is used to replace the synthetic amplitude spectrum with that of the observed data so that uncertainties in source mechanism and path effects are removed, allowing the inversion to focus solely on matching the phase (dispersion) information.

4. **Cost computation:** Compute the cost using normalized **zero-lag correlation** in the frequency domain as (based on correlation theorem, see Appendix A):
$$\text{cost} = \frac{1}{N}\sum_{k=1}^{N}\left[1 - r_0\Big(\tilde{D}_{\text{syn}}^{(k)}(\omega), D_{\text{obs}}^{(k)}(\omega)\Big)\right], \tag{3.2}$$
$$r_0\Big(\tilde{D}_{\text{syn}}^{(k)}(\omega), D_{\text{obs}}^{(k)}(\omega)\Big) = \frac{\displaystyle\int_\Omega \tilde{D}_{\text{syn}}^{(k)}(\omega)\, D_{\text{obs}}^{(k)}(\omega)\, d\omega}{\sqrt{\displaystyle\int_\Omega \left|\tilde{D}_{\text{syn}}^{(k)}(\omega)\right|^2 d\omega}\,\sqrt{\displaystyle\int_\Omega \left|D_{\text{obs}}^{(k)}(\omega)\right|^2 d\omega}}. \tag{3.3}$$
Here, $\tilde{D}_{\text{syn}}^{(k)}(\omega)$ denotes the weighted synthetic data for the k-th receiver in the frequency domain, $D_{\text{obs}}^{(k)}(\omega)$ denotes the corresponding observed data, ω is the angular frequency, Ω is the frequency range of integration, N is the total number of receivers, and $r_0(\cdot,\cdot)$ is the zero-lag correlation coefficient computed over Ω.

In the case of STFT-based cost function, each signal is divided into overlapping segments. Each segment is Fourier transformed and arranged along the vertical axis of the STFT matrix. We use the amplitude (absolute value) of each STFT to compute the cost as follows:

1. **Fourier transform:** Compute $D_{\text{obs}}(\omega) = \mathcal{F}\{d_{\text{obs}}(t)\}$ and $D_{\text{syn}}(\omega) = \mathcal{F}\{d_{\text{syn}}(t)\}$.

2. **Time shifting:** The synthetic data are shifted in the frequency domain as:
$$D_{\text{syn}}(\omega) = D_{\text{syn}}(\omega)\,\exp(-i\omega t_0)\,,$$
where t_0 is the time-shift parameter.

3. **Spectral weighting:** Apply spectral weighting to the synthetic data using the observed data:
$$\tilde{D}_{\text{syn}}(\omega) = \frac{D_{\text{syn}}(\omega)\,|D_{\text{obs}}(\omega)|}{|D_{\text{syn}}(\omega)|}.$$
Then, take the inverse Fourier transform to obtain the spectrally weighted synthetic waveform in the time domain, $\tilde{d}_{\text{syn}}(t)$.

4. **Cost computation:** Compute the cost using the normalized zero-lag correlation between the STFT magnitude matrices of $\tilde{d}_{\text{syn}}(t)$ and $d_{\text{obs}}(t)$:

$$\text{cost} = \frac{1}{N}\sum_{k=1}^{N}\left\{1 - C_{\text{STFT}}\left(|\tilde{D}_{\text{syn}}^{(k)}(\tau,\omega)|,\, |D_{\text{obs}}^{(k)}(\tau,\omega)|\right)\right\}, \tag{3.4}$$

where

$$\tilde{D}_{\text{syn}}(\tau,\omega) = \text{STFT}\{\tilde{d}_{\text{syn}}(t)\}(\tau,\omega) = \int_{-\infty}^{\infty} \tilde{d}_{\text{syn}}(t)\, w(t-\tau)\, e^{j\omega t}\, dt,$$

$$D_{\text{obs}}(\tau,\omega) = \text{STFT}\{d_{\text{obs}}(t)\}(\tau,\omega) = \int_{-\infty}^{\infty} d_{\text{obs}}(t)\, w(t-\tau)\, e^{j\omega t}\, dt.$$

Here, $w(t)$ is a window function, N is the number of stations, and C_{STFT} is the normalized zero-lag correlation in the STFT domain defined for matrices $A(\tau,\omega) = |\tilde{D}_{\text{syn}}(\tau,\omega)|$ and $B(\tau,\omega) = |D_{\text{obs}}(\tau,\omega)|$ as

$$C_{\text{STFT}}(A,B) = \frac{\sum_{i=1}^{n}\sum_{j=1}^{m}(A_{ij}-\bar{A})(B_{ij}-\bar{B})}{\sqrt{\sum_{i=1}^{n}\sum_{j=1}^{m}(A_{ij}-\bar{A})^2 \sum_{i=1}^{n}\sum_{j=1}^{m}(B_{ij}-\bar{B})^2}}. \tag{3.5}$$

Here, $\bar{A}$ and $\bar{B}$ are the mean values of A and B over all time-frequency points (τ_i, ω_j). This definition mirrors the zero-lag correlation used in the frequency-domain cost function, but applied segment-wise in the time-frequency domain.

As explained, the inversion is performed with four unknown model parameters. The observed data are flexural waves recorded on the vertical channel of seismic receivers, while the synthetic data are generated using SEM for a candidate solution of latitude, longitude, ice thickness, and time lag.

We visualize the cost function using a **grid search** method. Since the full parameter space consists of four parameters $(x, y, h_{\text{ice}}, t_0)$, we fix two of them at their true values and perform the grid search over the remaining two parameters to create a 2D slice of the cost function. For example, we may fix the ice thickness and time lag at their true values and vary the source location (x, y), or alternatively fix the source location and vary (h_{ice}, t_0). At each grid point, the cost function is computed, and the results are plotted, allowing us to understand the shape and smoothness of the cost function. These visualizations provide important insights into the behavior of different cost functions and guide the design of the inversion procedure.

First, a single flexural-wave record— at a distance of 100 m from a 15 Hz Ricker wavelet source and propagating through a 50 cm-thick ice layer—is considered, and the signal is time-shifted by $t_0 = 1$ s.

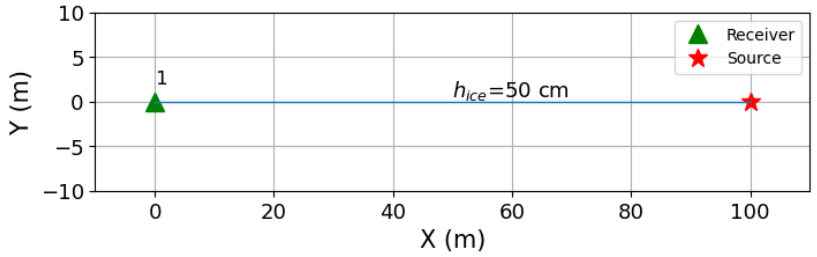

(a)

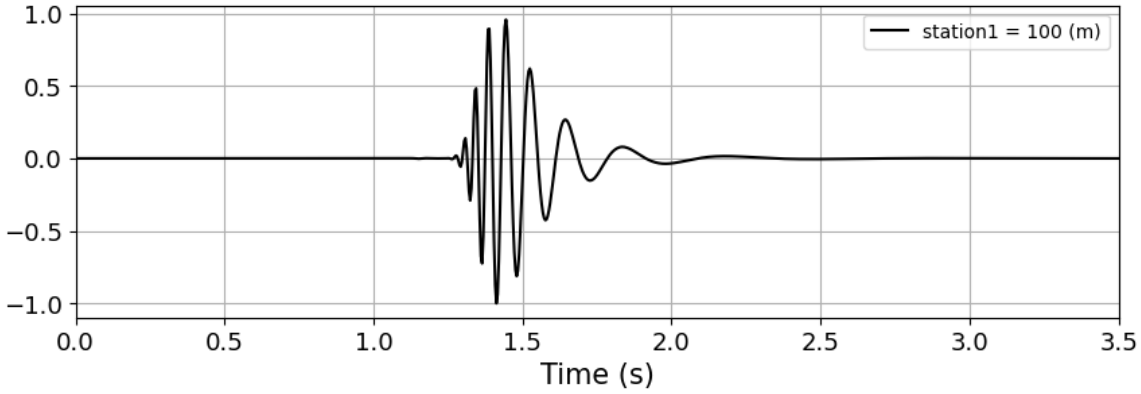

(b)

Figure 3.2: Example 1: (a) Single station at $(0, 0)$ m, with a source located at $(100, 0)$ m. (b) Recorded waveform of the flexural wave.

Given true time lag and ice thickness ($t_0 = 1$ s and $h_{\text{ice}} = 0.5$ m), we perform a grid search over the x–y plane. The results are shown below for different cost functions.

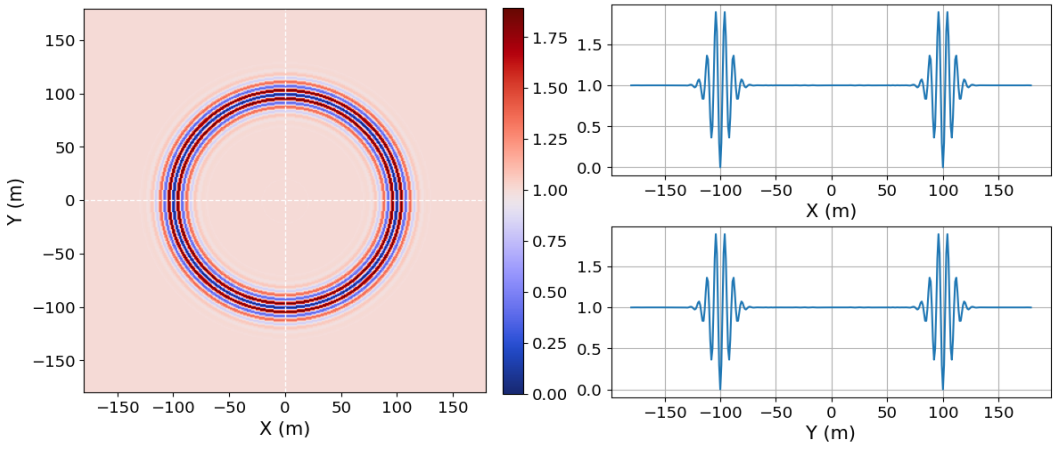

(a) Zero-lag correlation cost function

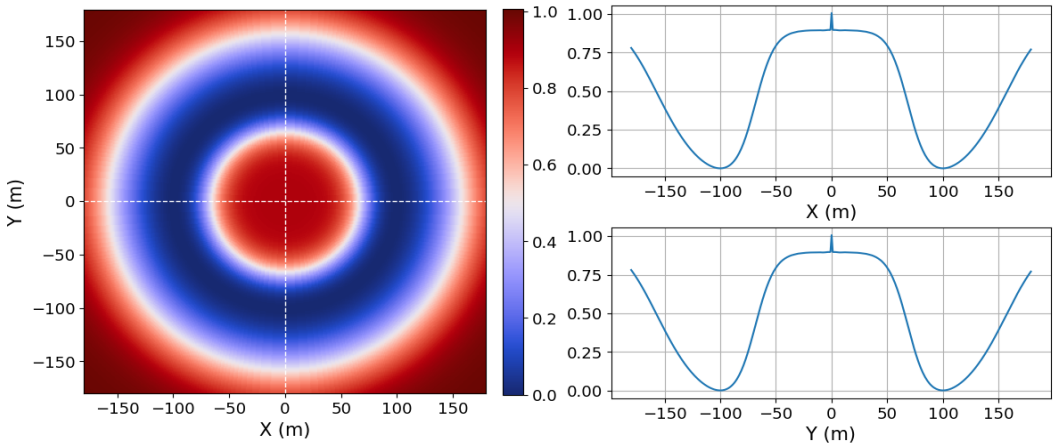

(b) STFT-based cost function

Figure 3.3: 2D view of the cost functions with horizontal and vertical cross-sections. Here, with the true ice thickness and time lag ($t_0 = 1$ s), the grid search is performed over the x and y dimensions.

Given the true source location ($x = 100$ m and $y = 0$ m), we perform a grid search over ice thickness (h_{ice}) and time lag (t_0). The results are shown below for different cost functions.

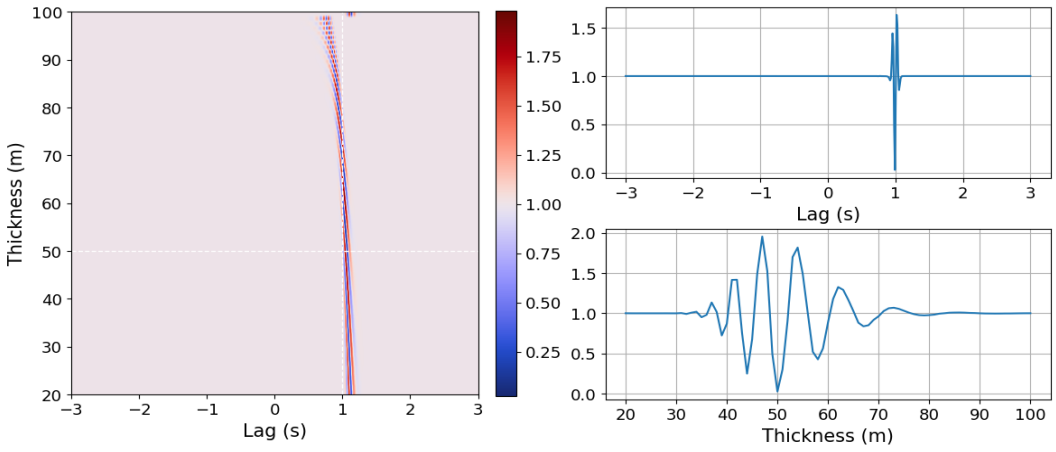

(a) Zero-lag correlation cost function

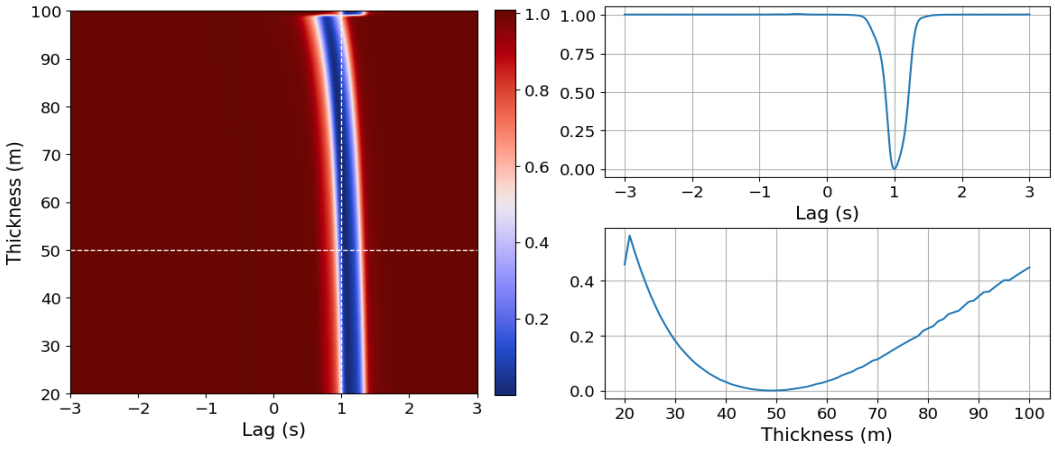

(b) STFT-based cost function

Figure 3.4: 2D view of the cost functions with horizontal and vertical cross-sections. Here, with the true source location fixed, the grid search is performed over ice thickness and time lag.

A minimum of three stations is required to localize the source via triangulation. Although the azimuthal distribution of these stations relative to the source also plays a critical role, a detailed investigation of this effect lies beyond the scope of the present study.

In the second case, three records of the flexural waves, generated by a 15 Hz Ricker wavelet as the source, propagating in a 50 cm layer of ice, are considered. The signals are shifted by $t_0 = 1$ s. Gaussian white noise, band-pass filtered within the signal's frequency band, is added so that the synthetic seismograms resemble real field data and to test method robustness. The signal-to-noise ratio (SNR) is set to 10 dB.

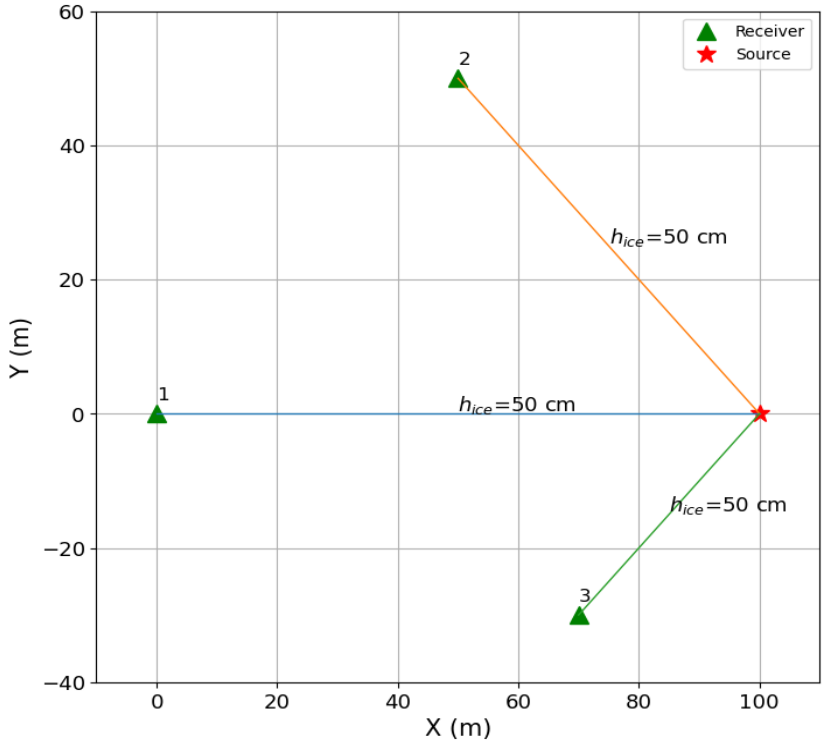

(a)

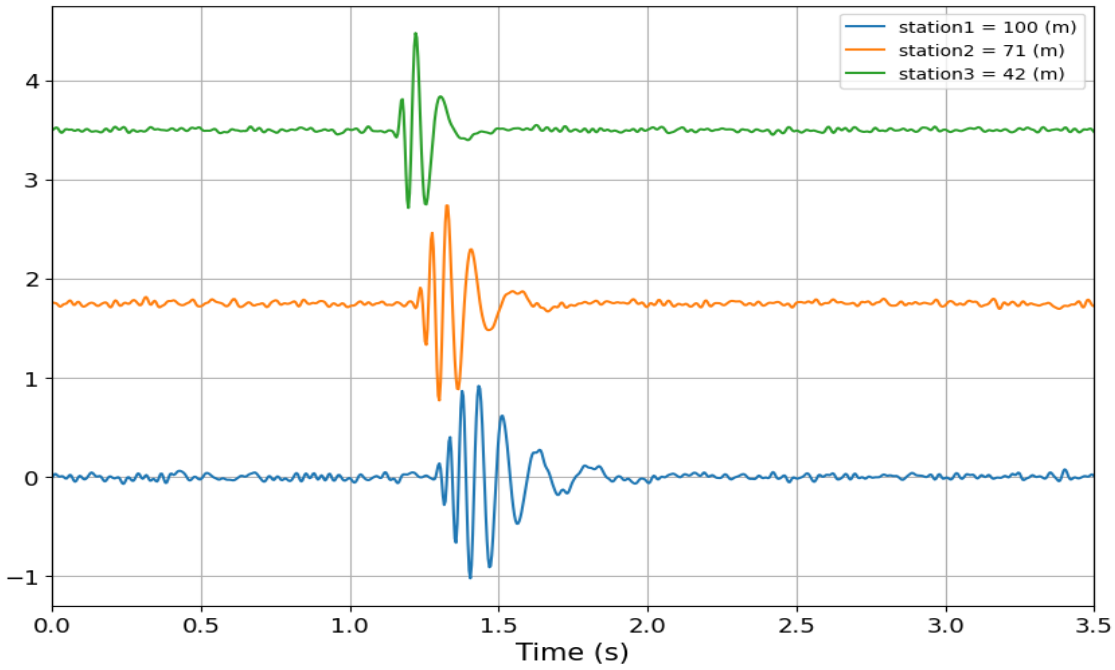

(b)

Figure 3.5: Example 2: (a) Three stations at $(0, 0)$ m, $(50, 50)$ m, and $(70, -30)$ m with a source located at $(100, 0)$ m. (b) Corresponding recorded waveforms of the flexural wave.

Given true time lag and ice thickness ($t_0 = 1$ s and $h_{\text{ice}} = 0.5$ m), we perform a grid search over the x–y plane. The results are shown below for different cost functions.

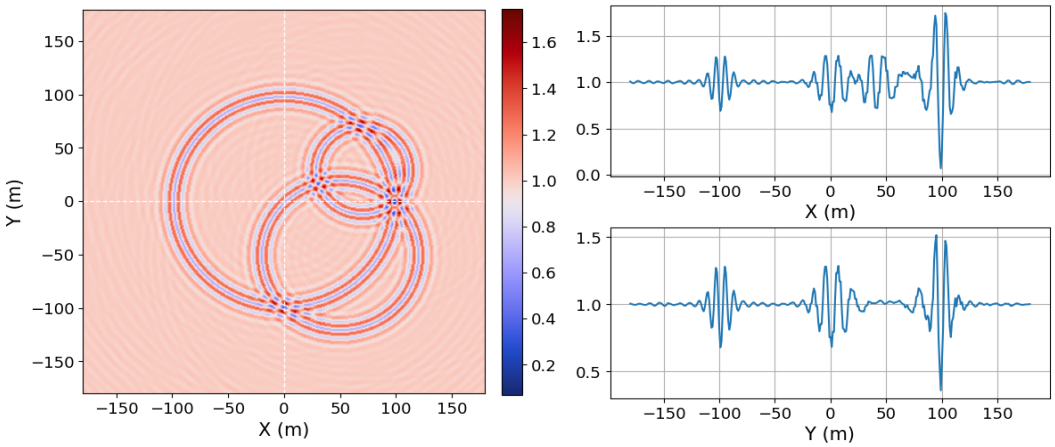

(a) Zero-lag correlation cost function

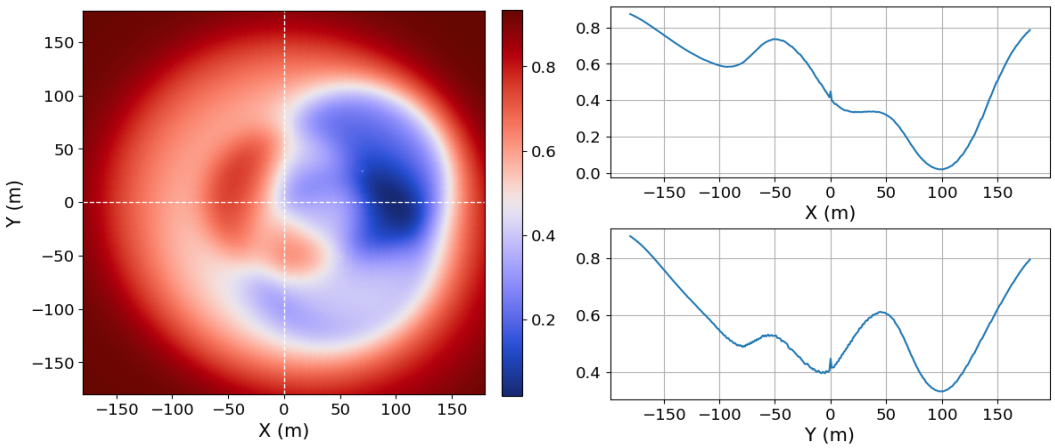

(b) STFT-based cost function

Figure 3.6: 2D view of the cost functions with horizontal and vertical cross-sections. Here, with the true ice thickness and time lag ($t_0 = 1$ s), the grid search is performed over the x and y dimensions.

Given the true source location ($x = 100$ m and $y = 0$ m), we perform a grid search over ice thickness (h_{ice}) and time lag (t_0). The results are shown below for different cost functions.

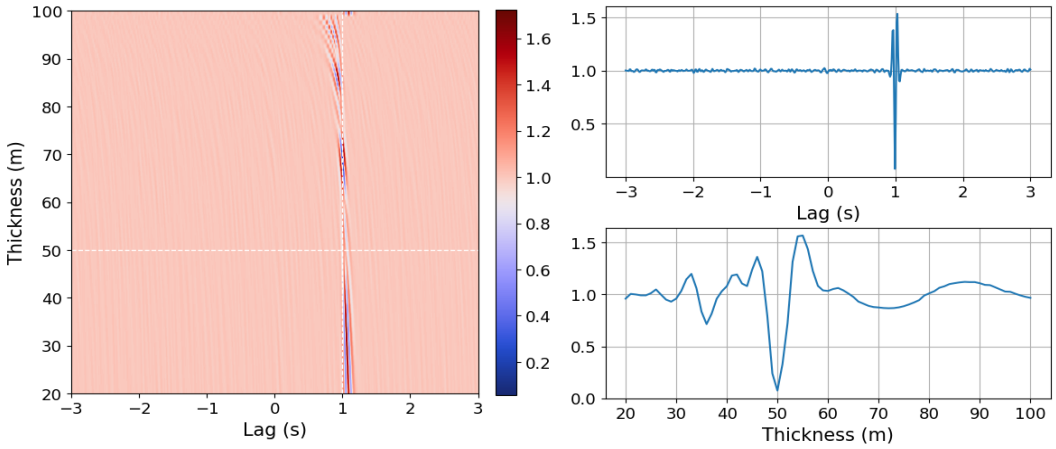

(a) Zero-lag correlation cost function

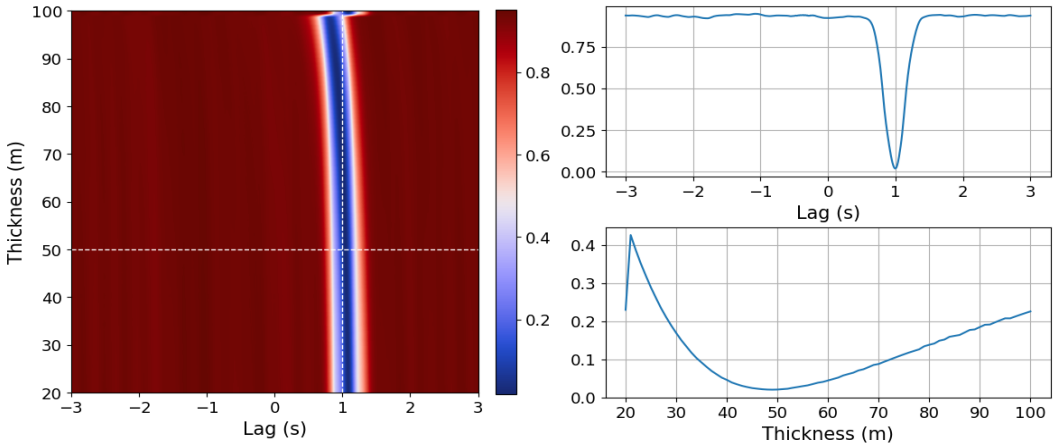

(b) STFT-based cost function

Figure 3.7: 2D view of the cost functions with horizontal and vertical cross-sections. Here, with the true source location fixed, the grid search is performed over ice thickness and time lag.

Visualization of the cost functions (Figures 3.6 and 3.7) highlights a clear contrast in their behavior. The zero-lag correlation cost (Figures 3.6(a) and 3.7(a)) is highly oscillatory, reflecting the sensitivity of flexural waveforms to small shifts in arrival time. Because flexural waves are dispersive, their different frequency components travel at different speeds, so even minor changes in source location, ice thickness, or activation time cause the waveform to go in and out of phase, producing rapid oscillations in the correlation.

In contrast, the STFT-based cost function (Figures 3.6(b) and 3.7(b)) is much smoother. This smoothness arises because the STFT decomposes the waveform into overlapping time windows and transforms each window into the frequency domain. By considering only the magnitude of the STFT—i.e., the spectral envelope, which represents the slowly varying distribution of energy across frequencies—the

cost function discards the rapidly oscillating phase information. Physically, this corresponds to comparing the energy distribution across frequencies within each time window (columns of the STFT). Mathematically, small parameter variations primarily affect the phase of each frequency component, while the magnitude (energy) changes only gradually. As a result, the STFT-based cost landscape varies smoothly across the parameter space.

These differences have practical implications for inversion. The smoothness of the STFT-based cost function allows global optimization algorithms (e.g., SA) to efficiently explore the parameter space without becoming trapped in local minima. The STFT-based cost displays a single dominant valley that reliably guides the search, enabling faster and more robust convergence. However, STFT-based costs are fundamentally constrained by the time–frequency trade-off: narrow windows provide high time resolution but poor frequency resolution (limiting the capture of low-frequency content), whereas wide windows offer good frequency resolution but smear temporal information, producing broader valleys in the misfit landscape.

In contrast, the oscillatory zero-lag correlation cost contains many local maxima and minima, which can trap the inversion in local minima and make the search for the best-fitting model highly sensitive to model parameters. Meanwhile, the oscillatory zero-lag correlation cost, by directly comparing raw waveforms, is highly sensitive to precise waveform alignment. This can yield greater accuracy for exact localization and ice-thickness estimation but comes at the cost of numerous local minima, which complicate global optimization.

Based on this analysis, we propose a **three-step inversion strategy** that takes advantage of the strengths of both cost functions:

1. **Step 1:** SA is applied over the full parameter space $(x, y, h_{\text{ice}}, t_0)$ using the **STFT-based** cost function. The smoothness of this cost landscape enables efficient global exploration of the parameter space and identifies a region of interest.

2. **Step 2:** SA is repeated over all parameters, but now restricted to the region identified in Step 1 and using the **zero-lag correlation** cost function. This step exploits waveform sensitivity to refine the source location and ice thickness. In Step 1 and 2, the ice thickness is assumed constant for all paths.

3. **Step 3:** A grid search is performed within a narrow window around the best (x, y, t_0) from Step 2 using the **zero-lag correlation** cost function. For each candidate (x, y, t_0), ice-thickness values are swept for each receiver over a predefined range (centered on the Step 2 estimate of ice thickness). For each receiver we select the thickness that minimizes that receiver's cost, and the total cost for the candidate is the sum of these per-receiver minima. This procedure refines the source location and time shift while allowing receiver-specific ice-thickness estimates (i.e., no uniform-thickness assumption).

This hybrid approach combines the robust convergence of the STFT-based cost with the high accuracy of the zero-lag correlation, ensuring both efficiency and reliability in the inversion process.

3.3 Validation of the Inversion Strategy Using Synthetic Test

To assess the effectiveness of the proposed three-step inversion strategy, we validate it using a synthetic example (Figure 3.5). In particular, we examine how the SA sampling behaves in Step 1 by plotting its candidate solutions directly onto the STFT-based cost landscape. This allows us to visualize how efficiently the algorithm explores the search space and whether it is guided toward the global minimum.

Step 1

Given the example in Figure 3.5, we perform SA to find the best model parameters. Here, the ice thickness is assumed constant for all source–receiver paths.

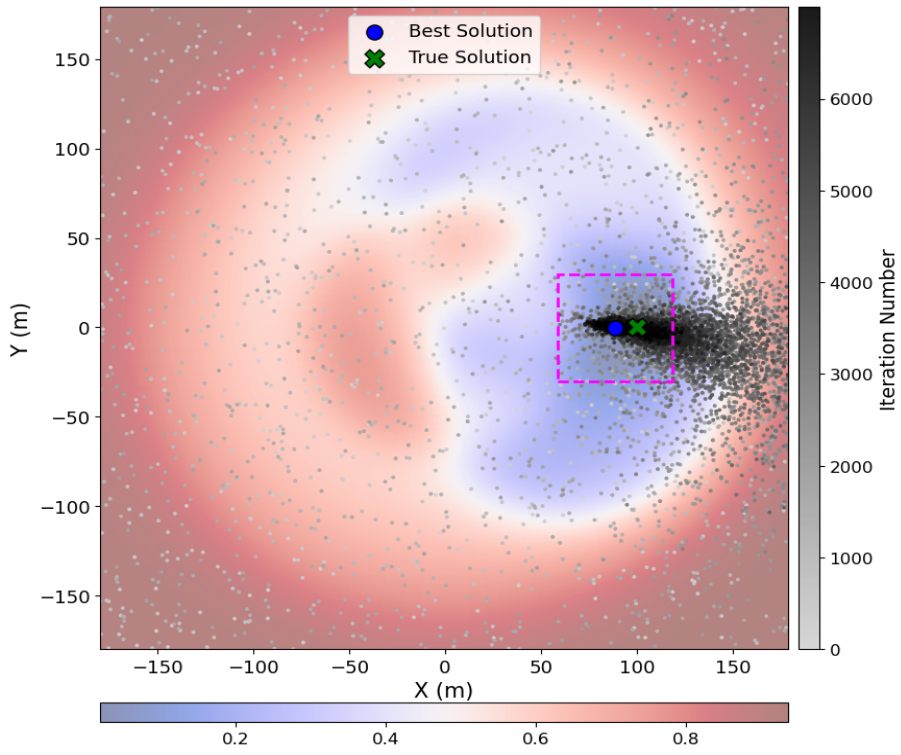

(a) Samples in the X–Y plane

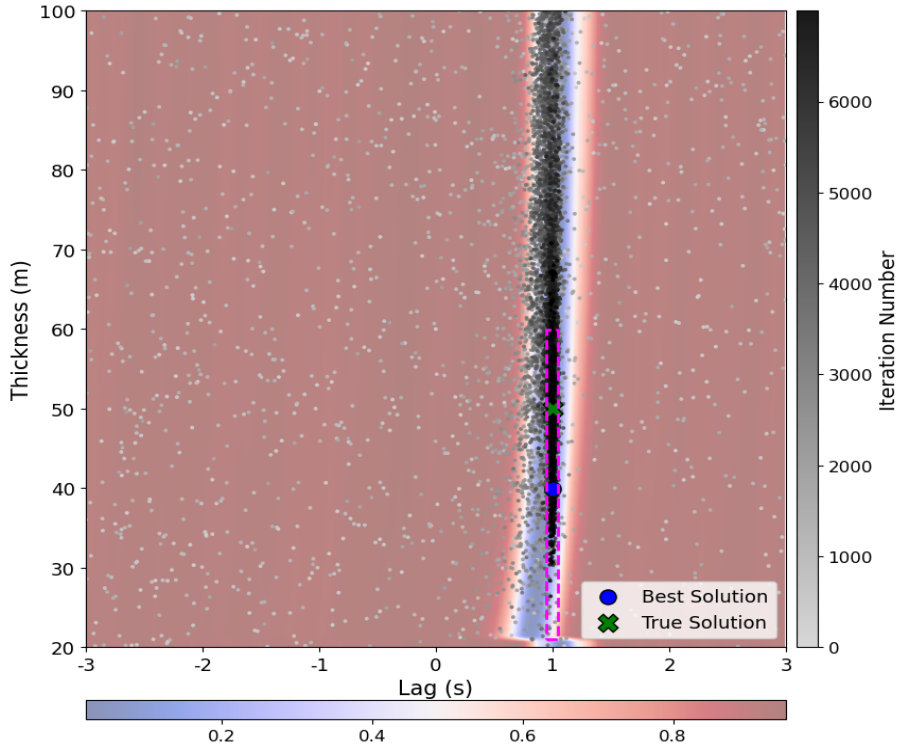

(b) Samples in the h_{ice}–t_0 plane

Figure 3.8: 2D view of the cost function. The true source location and the best solution found in **Step 1** are shown. The particles indicate the track of SA accepted candidates. The magenta dashed boxes in (a) and (b) show the search area in **Step 2**.

The trace plots of the accepted candidates are shown in Figure 3.9, displaying the evolution of all model parameters alongside the corresponding cost values.

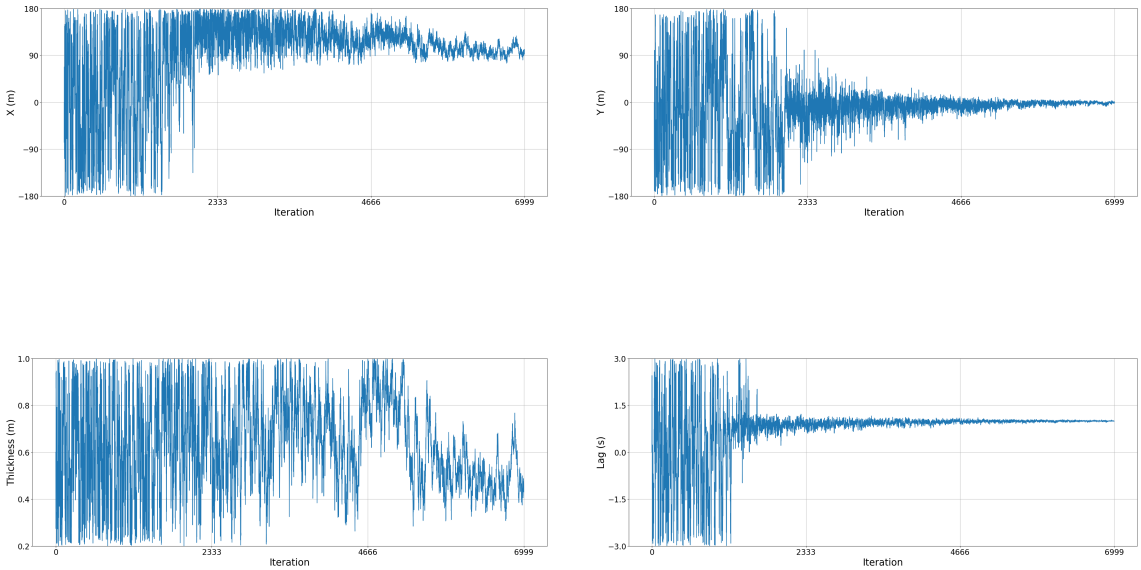

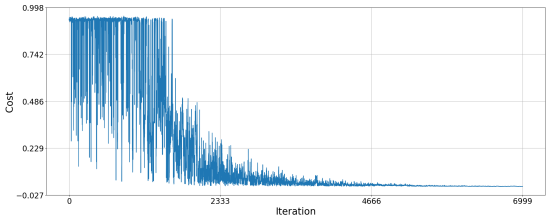

Figure 3.9: Trace plots of the accepted candidates of SA along with the STFT-based cost.

The waveform fit between the observed data and the synthetic data generated from the best solution obtained in Step 1 is shown in Figure 3.10.

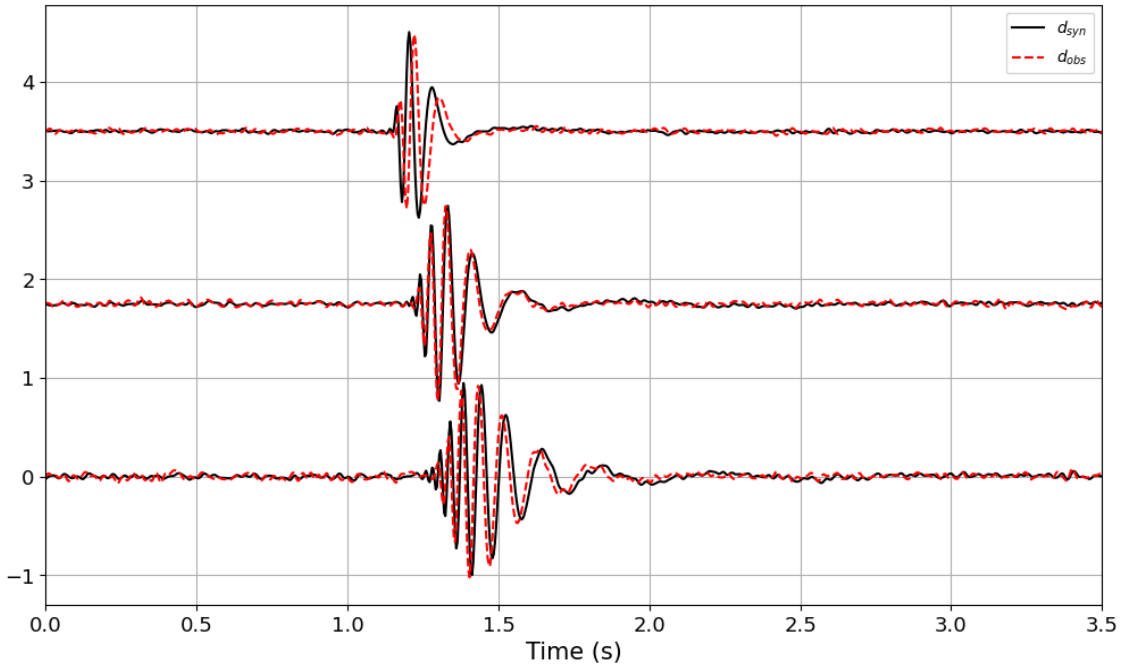

(b)

Figure 3.10: Fit between observed data and synthetics obtained from the best solution. The best solution is $X = 88.86$ m, $Y = 0.64$ m, $h_{ice} = 0.4$ m, and $t_0 = 1.0037$ s.

Step 2

From Figure 3.8, we see that t_0, X, and Y converge quickly, while h_{ice} (ice thickness) does not exhibit this rapid convergence. In **Step 2**, we use the zero-lag correlation cost function and restrict the search to the new area shown in Figure 3.8.

We heavily sample this reduced region (60,000 iterations). As shown, the results improve and yield a solution very close to the true one. The region shown in the magenta dashed box in Figure 3.8 is a spatial area of 60 by 60 m around the best solution, and a box of 40 cm by 0.1 s in ice thickness and time lag.

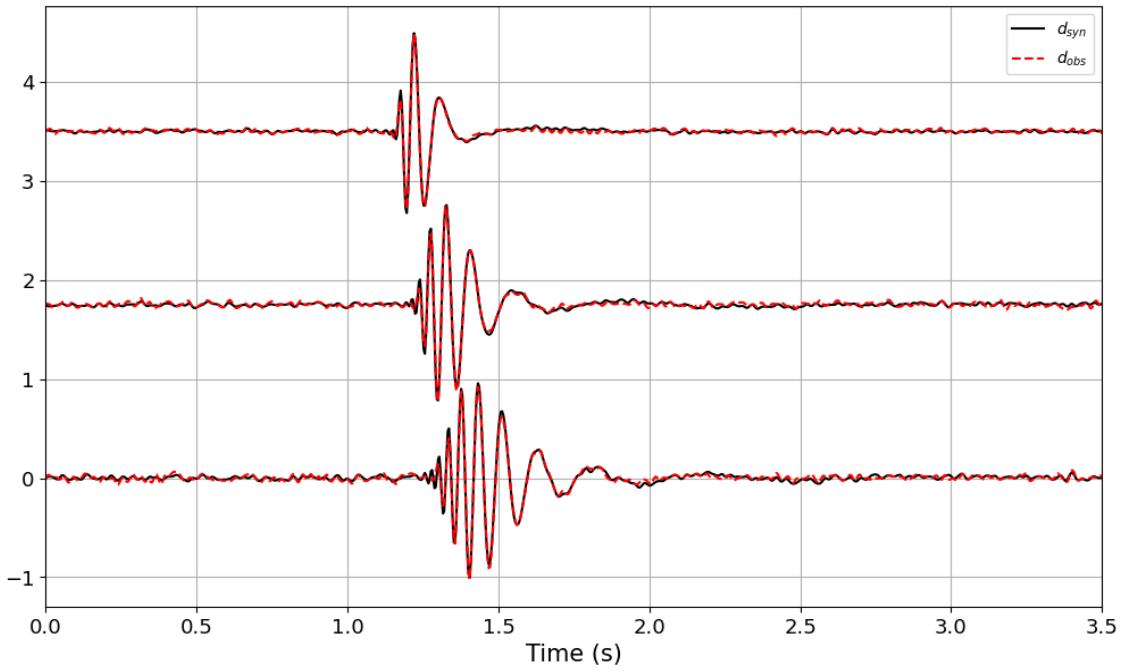

(b)

Figure 3.11: Fit between observed data and synthetics obtained from the best solution. The best solution is $X = 99.69$ m, $Y = -0.63$ m, $h_{ice} = 0.5$ m, and $t_0 = 1.00$ s. The cost value is 0.03391.

The waveform fit between the observed data and the synthetic data generated from the optimal solution obtained in Step 2 is presented in Figure 3.11, demonstrating a clear improvement compared to Step 1.

Step 3

Finally, a grid search is performed based on zero-lag correlation cost function as a complementary refinement. Here, t_0 is varied only within a range of $\frac{1}{f_s}$ s (f_s is sampling frequency), X and Y vary within ± 10 m, and h_{ice} varies within ± 15 cm of the best solution from **Step 2**. This step primarily improves the estimate of ice thickness.

The solution yields a marginal improvement, reducing the cost to 0.03368 (see Figure 3.12). The source locations obtained in Steps 2 and 3 correspond to source–receiver distances of 100 m, 71 m, and 42 m for stations 1–3, respectively, which match the true source–receiver distances (see Figure 3.5).

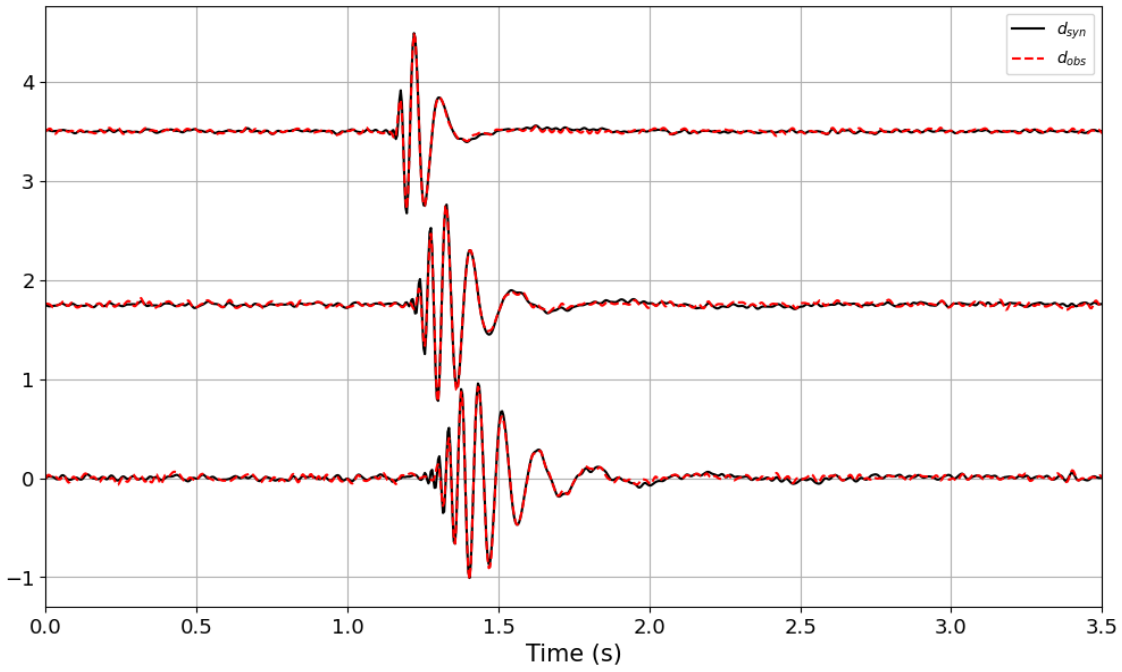

(b)

Figure 3.12: Fit between observed data and synthetics obtained from the best solution. The best solution is $X = 99.61$ m, $Y = -0.15$ m, $h_{ice}^{(1)} = 0.5$ m, $h_{ice}^{(2)} = 0.5$ m, $h_{ice}^{(3)} = 0.5$ m, and $t_0 = 1.0$ s. The superscripts denote the ice thickness for the corresponding stations (1 to 3). The cost value is 0.03368.

3.4 Field Data Application

In the following, we present an example of the application of the three-step inversion process to field data using a subset of five stations. Although three stations are theoretically sufficient for triangulation, five stations (Figure 3.14) are selected from the array in Figure 1.6 to provide optimal azimuthal and spatial coverage—four from the outer arrays and one within the dense inner array. Using five instead of three stations only modestly increases the computational cost in Steps 1 and 2, as each additional station adds one more cost evaluation. The main computational burden arises in Step 3, the final refinement, where each added station requires about 30 additional cost evaluations within the grid search loop. Consequently, using more than five stations would become computationally expensive while yielding only marginal improvements in localization accuracy. Once source locations are determined with this five-station configuration, they can be used to estimate ice thickness for the remaining stations without repeating the full three-step inversion.

Example Application of the Three-Step Inversion

In this section, we apply the three-step inversion strategy described above to icequakes recorded in Svalbard, using a subset of five selected stations. This sub-

set allows simultaneous estimation of source locations and ice thickness along the source–receiver paths. For illustration, we present one representative example.

We consider an icequake recorded on 1 March at Vellunden Lake, Svalbard. Figure 3.13 shows the trace plots of the model parameters and the corresponding cost values during Step 1, illustrating how the candidates evolve throughout the SA process.

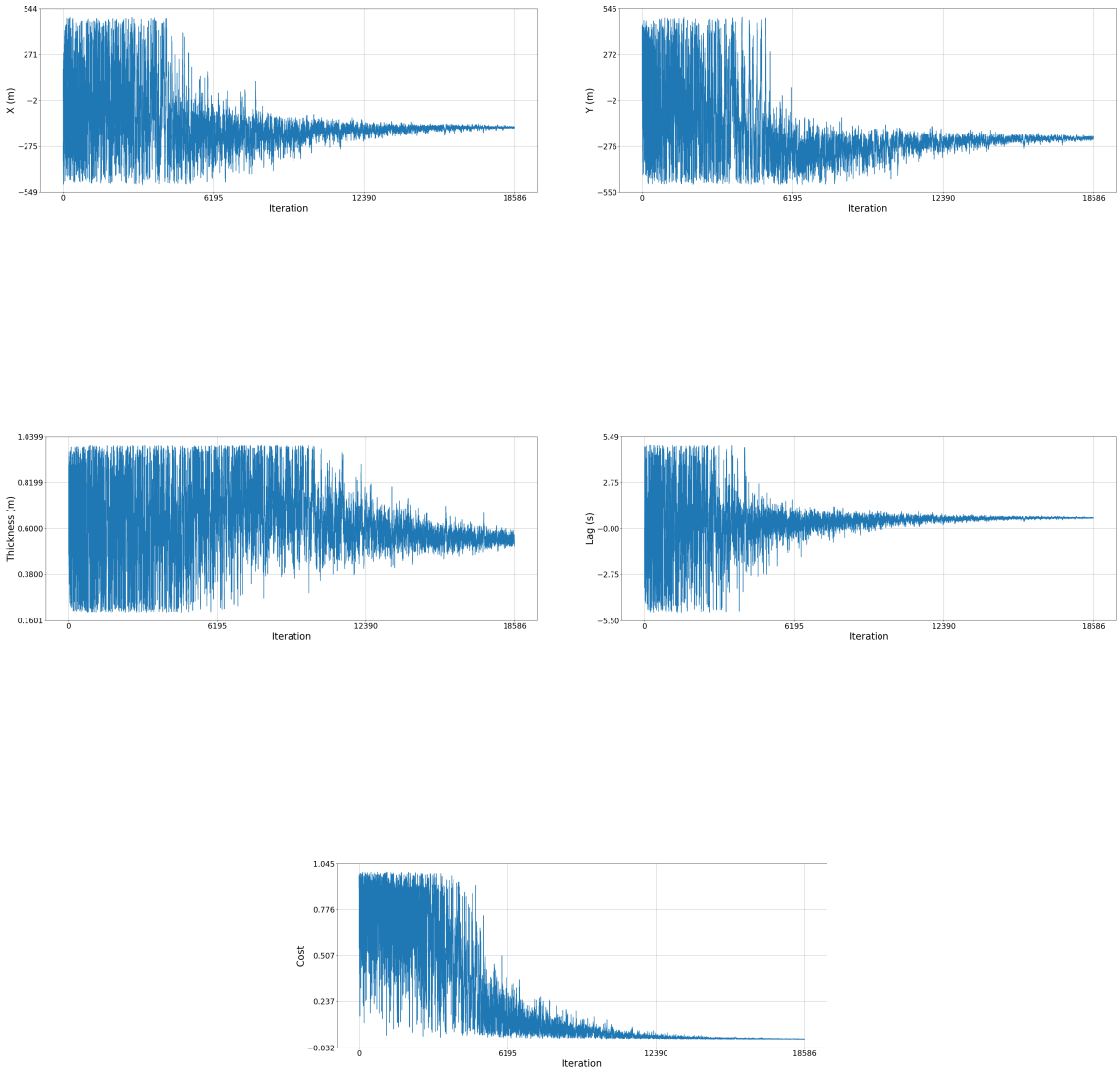

Figure 3.13: Trace plots of the accepted candidates from Step 1.

Figure 3.14 shows the accepted candidates of longitude and latitude from Step 1 (particles) along with the best-estimated icequake location obtained after Step 3 (blue star). Finally, Figure 4.18 presents the waveform fit corresponding to the best solution from Step 3.

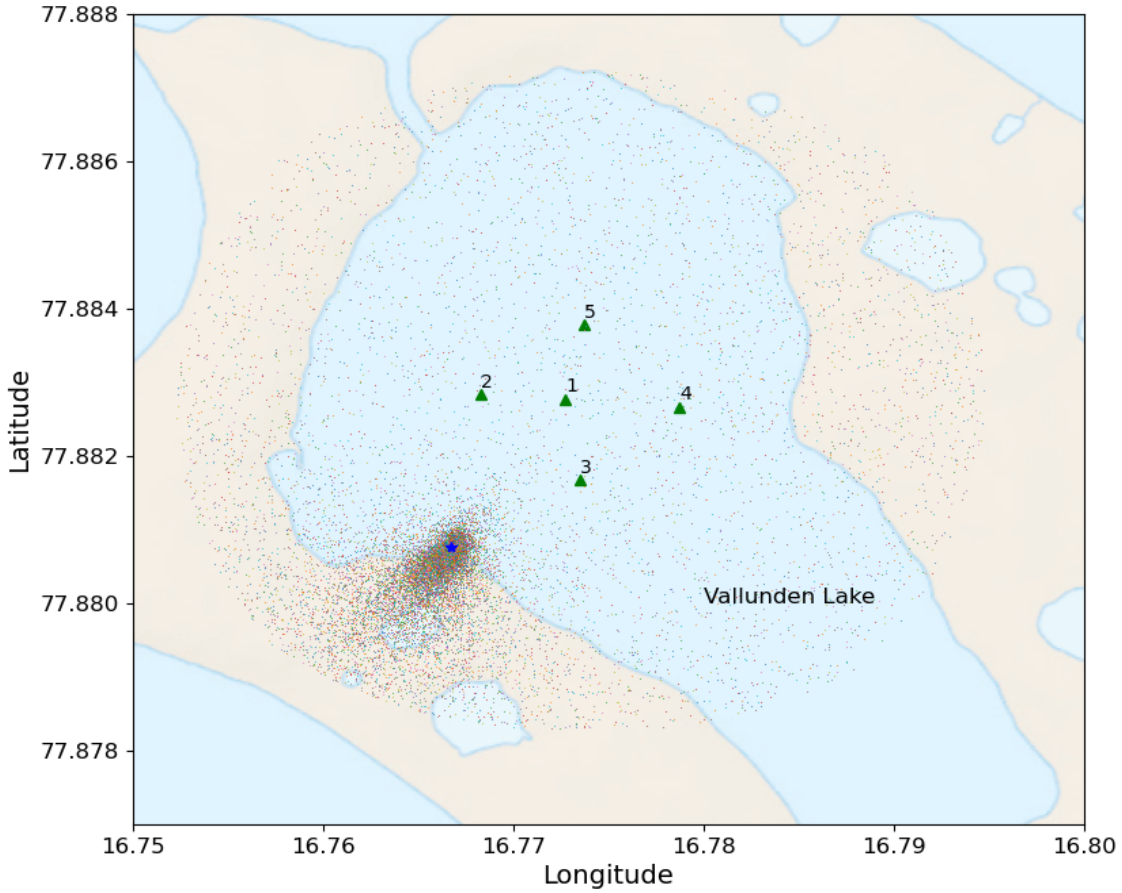

Figure 3.14: Locations of stations (green triangles), accepted candidates from Step 1 of the inversion, and the best-estimated location after Step 3 (blue star).

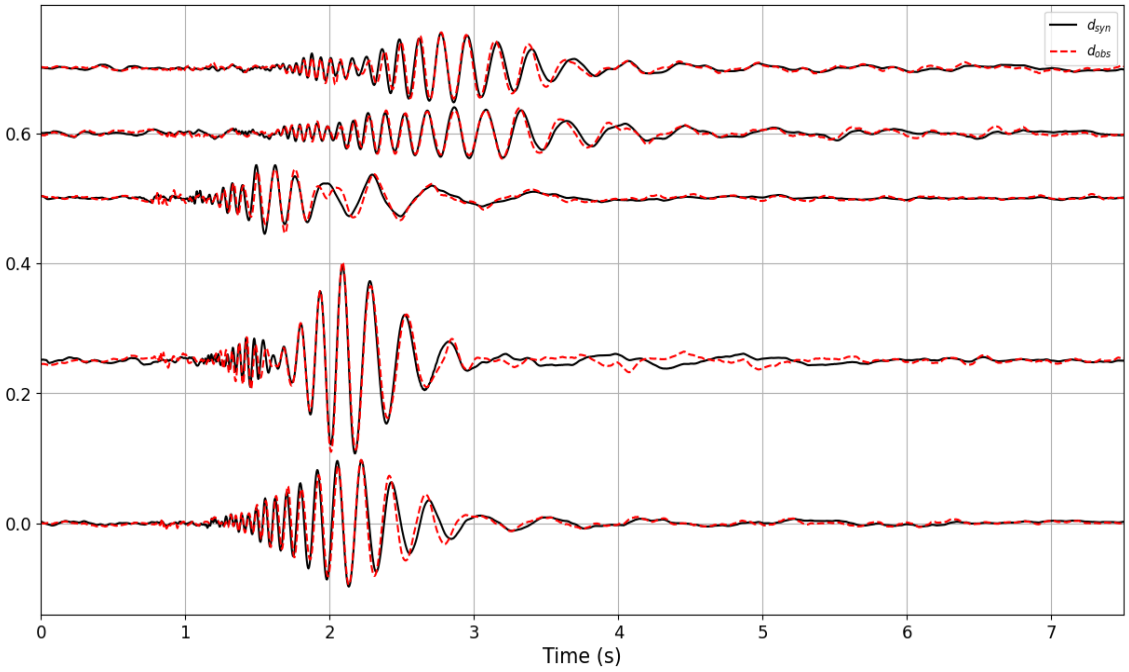

Figure 3.15: Waveform fitting between observed data (d_{obs}) and synthetic data (d_{syn}) generated from the best solution at Step 3 of the inversion. The estimated ice thicknesses along the five paths are 0.58, 0.51, 0.55, 0.54, and 0.55 m for stations 1–5, respectively.

The passive dataset from Svalbard consists of over 5,000 icequakes, which require source localization and ice thickness estimation along their paths. Here, we apply the three-step inversion using only five stations. Once the source locations for all events are determined, they can later be used to estimate ice thickness for the remaining receivers, as discussed in Chapter 4. In that scenario, since the event locations are already known, a simple grid search over ice thickness—similar to the approach used for active-source data—is sufficient.

Figures 3.16 and 3.17 provide an overview of the spatiotemporal characteristics of the dataset: Figure 3.16 displays the locations of 5,320 icequakes recorded between 28 February and 24 March at Vellunden Lake, while Figure 3.17 shows the corresponding daily occurrence rates over the same period, superimposed with ice-surface temperature measurements recorded between 5 and 15 March.

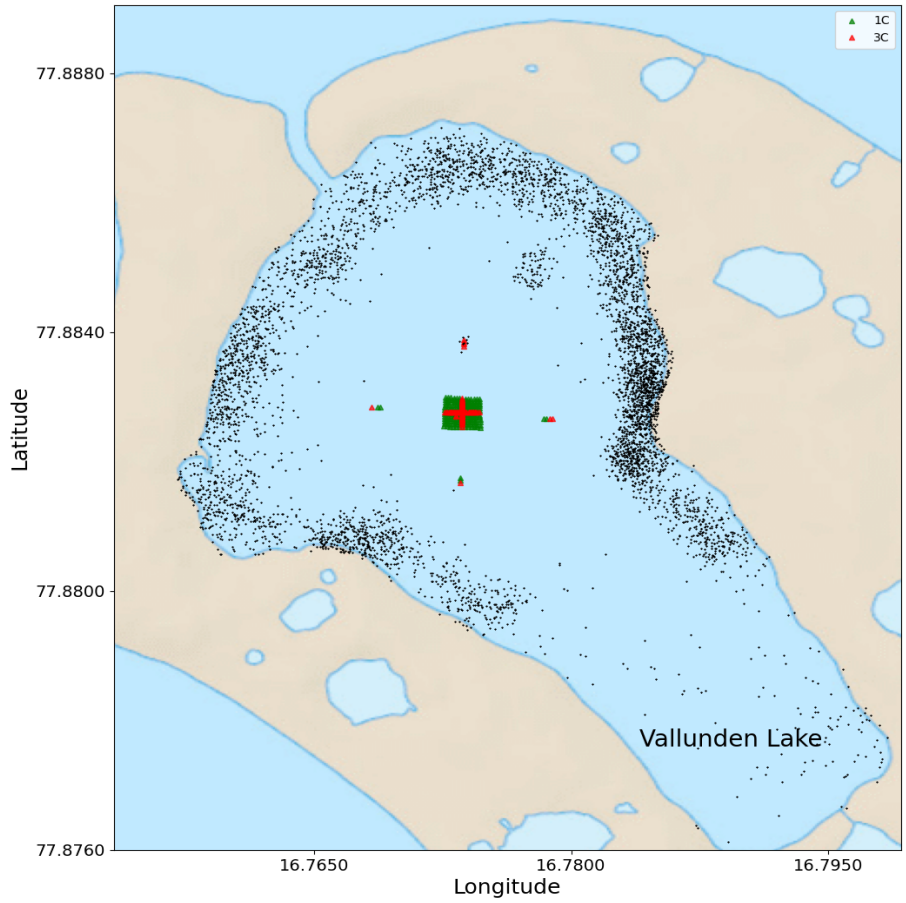

Figure 3.16: Locations of 247 seismic stations (red and green triangles) and 5,320 icequakes (black stars) recorded from 28 February to 24 March at Vellunden Lake, Svalbard.

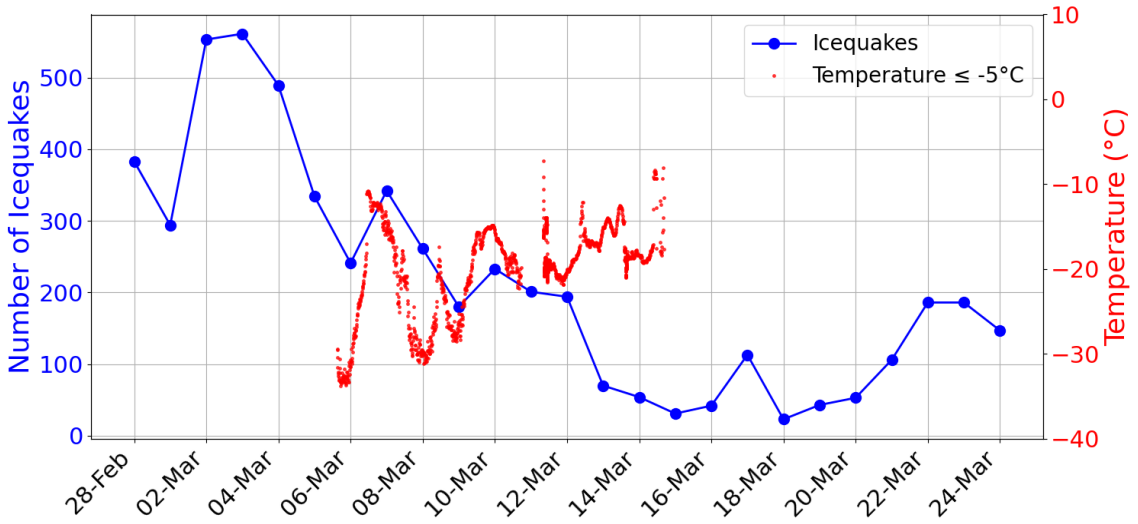

Figure 3.17: Daily number of icequakes (blue) from 28 February to 24 March, with ice-surface temperature measurements (red points) between 5 and 15 March. Lower temperatures coincide with higher icequake activity.

In summary, the vast majority of icequake sources are located along the shoreline, where mechanical stress accumulates due to thermal expansion/contraction and tidal forcing. As shown in Figure 3.17 and previously reported by Moreau et al. (2023), icequake activity is temperature-dependent, with a marked increase during colder periods. These shoreline icequakes are characterized by dominant horizontal energy, consistent with traction/compression source mechanisms driven by thermo-mechanical forcing rather than anthropogenic or tectonic processes. Furthermore, the progressive increase in ice thickness over the four-week period follows the same temperature trend. Overall, icequake occurrence appears to be primarily controlled by thermally induced stress variations, decreasing as temperatures rise.

In the next chapter, the ice thickness estimates retrieved along source–receiver paths are used to perform two-dimensional ice-thickness tomography. This allows reconstruction of both the spatial distribution and temporal evolution of ice thickness across the lake. These results are then combined with temperature and icequake activity to further explore the relationship between thermal forcing, icequake occurrence, and ice growth.

3.5 Perspectives

3.5.1 Particle Swarm Optimization

Particle Swarm Optimization (PSO) is a population-based algorithm inspired by the social behavior of birds and fish. Each particle represents a candidate solution and updates its position based on its own best experience (pbest) and the swarm's best experience (gbest). This combination of individual exploration and collective learning allows PSO to efficiently search large parameter spaces (Engelbrecht, 2007).

Mathematical Representation:

$$v_i^{t+1} = v_i^t + c_1 r_1 (pbest_i^t - p_i^t) + c_2 r_2 (gbest^t - p_i^t), \tag{3.6}$$

$$p_i^{t+1} = p_i^t + v_i^{t+1}, \tag{3.7}$$

- v_i^{t+1}: New velocity; v_i^t: Current velocity (inertia) c_1, c_2: Acceleration coefficients; r_1, r_2: Random numbers (0-1) $pbest_i^t$: Personal best; $gbest^t$: Global best; p_i^t: Current position

Figure 3.18 illustrates particle movement in the search space. The top panel shows 2D and 3D views of the swarm, while the bottom panel demonstrates how each particle updates its position considering inertia, personal best, and global best.

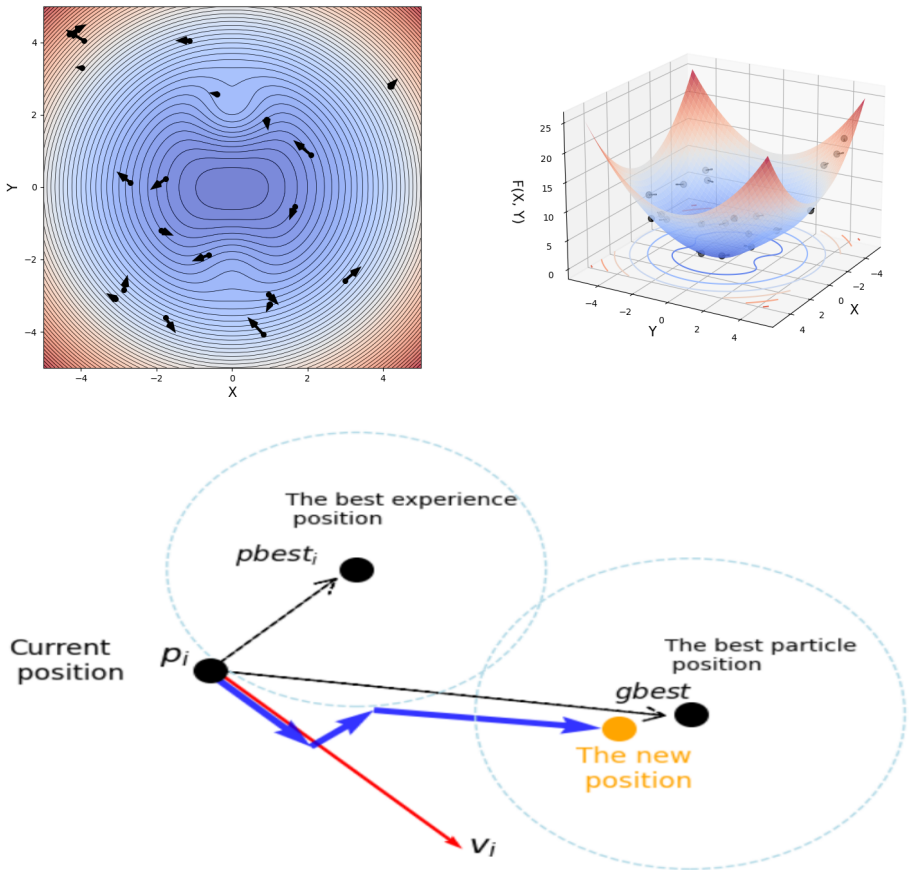

Figure 3.18: (Top) 2D and 3D plots of particle swarms. (Bottom) Example of position updates based on inertia, personal best, and global best.

PSO is a promising alternative optimization method that is computationally efficient, capable of effectively exploring high-dimensional parameter spaces with fast convergence, and can be applied in future work for parameter estimation.

3.5.2 Sensitivity of Inversion to the Choice of Forward Model, Heterogeneity, and Layer Geometry

As discussed in the previous chapter, we compared SEM simulations with both analytical and asymptotic solutions. While asymptotic solutions are widely used in practice, their dispersion curves deviate significantly from SEM and analytical solutions at higher frequencies and for increasing ice thickness (Figures 2.8 and 2.19).

To illustrate this effect, consider the synthetic setup shown in Figure 3.19, where no noise has been added. The observed data consist of four recordings of flexural waves at distances of 50, 150, 200, and 250 m from the source, in an ice layer of 90 cm thickness. Synthetic waveforms are generated using the Ewing model (Equation 2.27).

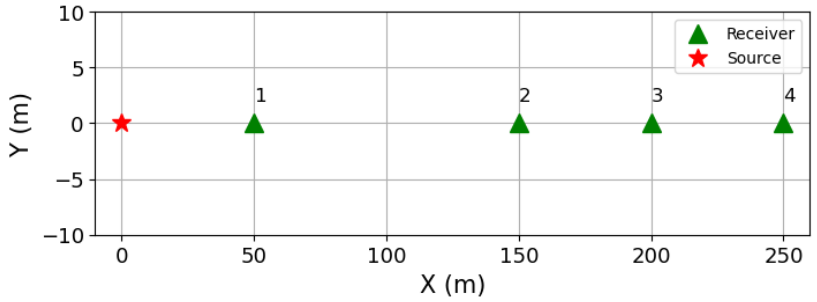

Figure 3.19: Geometry of the synthetic test, showing station and source locations.

We perform four separate inversions, each using a Ricker wavelet with a different central frequency. The results, summarized in Figure 3.20, show that as the central frequency of the source increases, the errors in both ice thickness and source location also increase. This systematic overestimation is expected: asymptotic solutions predict higher phase velocities, which are interpreted in the inversion as thicker ice layers. This trend is consistent with the dispersion curves shown in Figure 2.16, where larger phase velocities correspond to thicker ice.

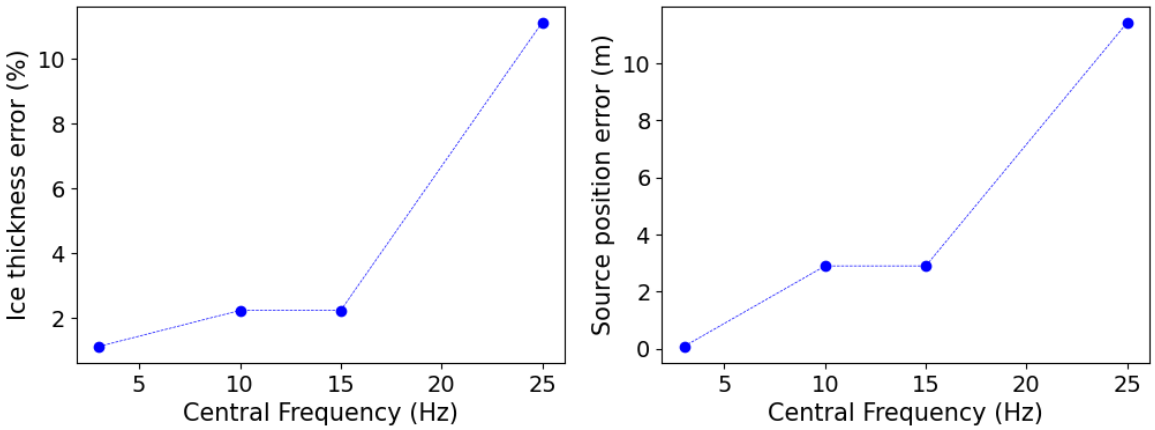

Figure 3.20: Sensitivity analysis showing errors in ice thickness and source location for the Ewing model.

These results emphasize the critical importance of selecting an appropriate forward modeling approach.

Other factors may also influence the estimation accuracy. For instance, Figure 2.22 shows the effect of snow cover, while Figure 2.24 illustrates that a thickness profile with increasing or decreasing trends does not necessarily yield the same result as a uniform thickness equal to the average of that profile. These findings highlight the need for further investigation into the impact of homogeneous versus evolved snow, as well as varying ice thickness profiles, and more complex geometries on inversion results.

CHAPTER 4

ICE THICKNESS RECONSTRUCTION USING TOMOGRAPHY: METHODS AND APPLICATIONS

Contents

4.1 Introduction 81

4.2 Methodology 82

4.3 Synthetic Test 87

4.3.1 Uncertainty Analysis 89

4.3.2 Checkerboard Test 92

4.4 Field Data Application 94

4.4.1 Tomographic Inversion of Sea Ice in the St. Lawrence Estuary, Quebec, Canada 94

4.4.2 Tomographic Inversion of Sea Ice in Svalbard 104

4.5 Perspectives 115

4.5.1 Impacts of the Number and Configuration of Stations . . 115

4.5.2 Adaptive Mesh Stratgey 118

4.1 Introduction

In Chapter 3, we developed a three-step inversion strategy to jointly estimate icequake source locations and path-averaged ice thicknesses using waveforms recorded on a sparse network of seismic stations. While this approach successfully recovers ice thickness along individual source–receiver paths, it does not provide a continuous spatial map of thickness across the study area. The methodology is therefore extended toward thickness imaging through tomographic inversion.

Tomographic inversion offers a natural framework for interpolating path-averaged measurements into a spatially continuous model. By discretizing the domain into cells and relating each path-averaged thickness to the sum of weighted cell-wise

thicknesses, we can formulate the problem as a linear inverse system. This approach, analogous to classical travel-time tomography in seismology, allows us to reconstruct two-dimensional ice thickness maps from a set of path-integrated observations.

This chapter presents the development and application of such a tomographic inversion framework. We begin by formulating the ice thickness tomography problem within the framework of linear inverse theory, establishing the relationship between observations, model parameters, and regularization constraints. We then validate the methodology using synthetic tests designed to assess resolution, stability, and sensitivity to noise. These tests include checkerboard analyses to quantify the resolving power of different acquisition geometries and uncertainty quantification via posterior covariance and resolution matrices.

Following validation, we apply the method to two distinct field datasets introduced in Chapter 1. The first application involves active-source experiments conducted on the St. Lawrence Estuary in Quebec, Canada, where human-generated sources and dense receiver arrays enable high-resolution mapping of ice thickness. The second application focuses on passive seismic monitoring at Vellunden Lake, Svalbard, where naturally occurring icequakes serve as sources over a 25-day period. This dataset allows us to reconstruct not only the spatial distribution of ice thickness but also its temporal evolution, capturing ice growth in response to temperature variations. Together, these applications demonstrate the versatility of the proposed method across different environmental conditions, source types, and spatial scales.

Beyond the core tomographic results, this chapter also explores practical considerations for implementing ice thickness tomography in field campaigns. We investigate how the number and spatial configuration of stations affect resolution, providing guidance for designing efficient monitoring networks in logistically challenging polar environments. Additionally, we explore the potential of adaptive mesh strategies, where cell sizes are refined in regions with dense ray coverage and coarsened in sparsely sampled areas, to optimize the trade-off between resolution and computational efficiency.

The main contributions of this chapter are threefold: (1) the development of a linear tomographic framework for reconstructing ice thickness maps from path-averaged seismic observations; (2) validation of the method through synthetic tests that quantify resolution and uncertainty; and (3) application to both active- and passive-source field datasets, demonstrating the method's ability to capture spatial and temporal ice thickness variability in real-world conditions. These results pave the way for using passive seismic monitoring as a cost-effective, long-term tool for sea ice characterization.

4.2 Methodology

Seismic tomography, which provides models of Earth's properties, such as velocity and density, is a vital tool for probing its structure and understanding dynamic processes, from planetary-scale convection to kilometer-scale features such as lithology, fracturing, temperature, and fluid content. Accurate model parameterization, solution, and assessment are crucial to ensure that the resulting models closely resemble the true Earth (Thurber and Ritsema, 2007).

The forward problem involves predicting seismic data for a given Earth model using the physics of wave propagation. Mathematically, this is expressed as

$$\mathbf{d} = \mathbf{G}(\mathbf{m}),$$

where $\mathbf{d}$ is the predicted data, $\mathbf{m}$ the model, and $\mathbf{G}$ the forward operator incorporating wave propagation physics. In a linear case, $\mathbf{G}$ can be represented as a matrix, leading to

$$\mathbf{Gm} = \mathbf{d}.$$

In practice, we measure $\mathbf{d}$ at seismic receivers and seek the model $\mathbf{m}$ that best reproduces the observed data. This inverse problem uses assumptions about physics, source characteristics, and Earth complexity to minimize the difference between predicted and observed data, whereas the forward problem simply maps a given model to data.

Seismic tomography is an inverse method that images Earth's interior by inferring subsurface properties from seismic waves. It began with P-wave travel times and later incorporated other wave types, improving structural resolution. Advances in forward modeling, data acquisition, and computational power now enable larger, more detailed Earth models from seismic recordings (Thurber and Ritsema, 2007).

In our study, we adopt a framework similar to classical travel-time tomography to reconstruct ice-thickness maps. Here, instead of travel times, each path is associated with an average ice thickness, obtained through a prior inversion process described in Chapter 3. This yields a constant thickness value for each source–receiver path. By assuming a linear relationship between these path-averaged thickness observations and the underlying ice-thickness model, we formulate the problem as a linear system where each ray path samples contributions from the intersected cells. In this way, the principles of tomography are reinterpreted to estimate a spatially varying ice-thickness map.

Tomographic Inversion for Deriving Ice Thickness Map

The goal of tomography is to reconstruct ice thickness maps using ice thickness estimates obtained along various paths connecting sources and receivers.

Each observation represents a path-averaged ice thickness estimated along a source–receiver path. Physically, this corresponds to integrating the local ice-thickness field, $h(x, y)$, along the ray path L_i, and then normalizing by the total path length:

$$h_{\text{obs},i} = \frac{1}{L_i} \int_{L_i} h(x, y)\, \mathrm{d}\ell. \tag{4.1}$$

Discretizing the domain into $N_x \times N_y$ cells, each with a constant ice-thickness value $\hat{h}_j$, the integral can be approximated as a weighted sum:

$$h_{\text{obs},i} = \sum_{j=1}^{N_x N_y} w_{ij} \hat{h}_j, \tag{4.2}$$

where $w_{ij} = \frac{\ell_{ij}}{L_i}$ represents the normalized contribution of cell j to path i, i.e., the fraction of the total ray length that crosses that cell.

In matrix form, this discrete relationship can be compactly written as:

$$\mathbf{h}_{\text{obs}} = \mathbf{A}\hat{\mathbf{h}}, \tag{4.3}$$

where the matrix $\mathbf{A}$ collects all weights w_{ij}. Each row of $\mathbf{A}$ corresponds to one ray path and represents a normalized linear averaging operator over the intersected cells. This formulation directly connects the physical process of path-averaged measurement with the discrete linear forward model used in tomography.

Given our observations, we aim to retrieve a pixel-wise ice thickness model, $\hat{\mathbf{h}}$, through an inversion process. A simple approach to this problem is by minimizing the residual vector, i.e., $\mathbf{e} = \mathbf{h}_{\text{obs}} - \mathbf{A}\hat{\mathbf{h}}$. A common approach is to minimize the squared 2-norm of the residual vector:

$$\min_{\hat{\mathbf{h}}} \|\mathbf{e}\|_2^2 = \min_{\hat{\mathbf{h}}} \|\mathbf{h}_{\text{obs}} - \mathbf{A}\hat{\mathbf{h}}\|_2^2. \tag{4.4}$$

Expanding the 2-norm, we have:

$$\|\mathbf{h}_{\text{obs}} - \mathbf{A}\hat{\mathbf{h}}\|_2^2 = (\mathbf{h}_{\text{obs}} - \mathbf{A}\hat{\mathbf{h}})^T(\mathbf{h}_{\text{obs}} - \mathbf{A}\hat{\mathbf{h}}). \tag{4.5}$$

Differentiating with respect to $\hat{\mathbf{h}}$ and setting the derivative to zero gives:

$$-2\mathbf{A}^T(\mathbf{h}_{\text{obs}} - \mathbf{A}\hat{\mathbf{h}}) = 0, \tag{4.6}$$

which simplifies to:

$$\mathbf{A}^T\mathbf{A}\hat{\mathbf{h}} = \mathbf{A}^T\mathbf{h}_{\text{obs}}. \tag{4.7}$$

Solving for $\hat{\mathbf{h}}$ yields the familiar least-squares solution:

$$\hat{\mathbf{h}}_{\text{L}_2} = (\mathbf{A}^T\mathbf{A})^{-1}\mathbf{A}^T\mathbf{h}_{\text{obs}}, \tag{4.8}$$

$\hat{\mathbf{h}}$ has dimensions (N_y, N_x), where N_x and N_y represent the number of cells in the x- and y-directions, respectively, while $\mathbf{h}_{\text{obs}}$ has dimension N_{path}, corresponding to the number of source–receiver paths. In Equation 4.8, the vector form is used, where $\hat{\mathbf{h}}$ has a dimension of $N_y \times N_x$. Similarly, the matrix A has rows corresponding to the number of paths and columns equal to $N_y \times N_x$, with each row representing the contribution of one path across all cells. As an example, in the following medium (see Figure 4.1), the contribution of a single path in each cell, normalized by the length of the path, is shown.

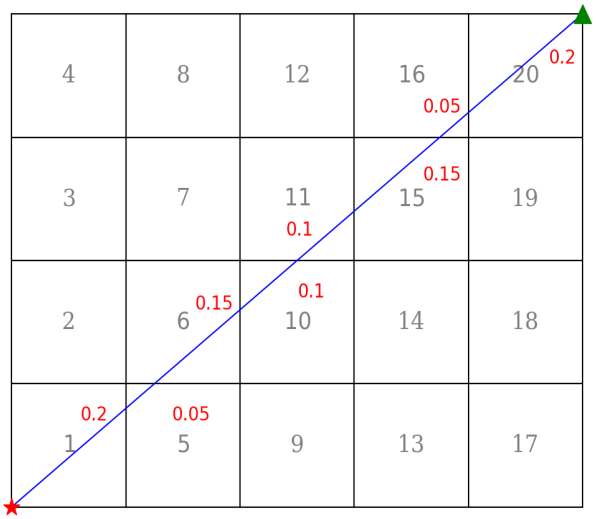

Figure 4.1: Example of one ray crossing the medium. Red star is the source, and blue circle is the receiver. Each cell's contribution is normalized by dividing the ray length within that cell by the total ray length, ensuring that all rays sum to one and carry equal weight in the inversion.

For example, in the case of Figure 4.1, path 1 can be represented as the following matrix $\mathbf{P}_1$:

$$\mathbf{P}_1 = \begin{bmatrix} 0 & 0 & 0 & 0.05 & 0.2 \\ 0 & 0 & 0.1 & 0.15 & 0 \\ 0 & 0.15 & 0.1 & 0 & 0 \\ 0.2 & 0.05 & 0 & 0 & 0 \end{bmatrix}.$$

We then vectorize this matrix column by column, following the numbering of the cells as shown. The resulting vector forms the first row of the system matrix $\mathbf{A}$, representing the contribution of path 1 to each cell.

The cell contributions sum to 1, as each path segment is normalized by the total path length between the source and receiver.

Rank deficiency and ill-conditioning in the matrix $\mathbf{A}$ arise because some model parameters (cells) are poorly sampled or unsampled by rays. As a results, solving an inverse problem faces challenges including lack of solution existence (no exact fit due to noisy data or model approximations), non-uniqueness (multiple models may fit the data), and instability (small changes in data can lead to large variations in solutions). To address these issues, regularization techniques are often essential for stabilizing the process and producing physically plausible, interpretable solutions (Aster et al., 2019, Chapter 1).

The objective function can incorporate zeroth-order or first-order Tikhonov regularization. In our case, the objective function is expressed as:

$$\hat{\mathbf{h}}_{\text{opt}} = \underset{\hat{\mathbf{h}}}{\text{argmin}} \left(\|\mathbf{W}_d(\mathbf{A}\hat{\mathbf{h}} - \mathbf{h}_{\text{obs}})\|_2^2 + \alpha^2 \|\mathbf{W}_m(\hat{\mathbf{h}} - \hat{\mathbf{h}}_{\text{prior}})\|_2^2 + \beta^2 \|\mathbf{L}\hat{\mathbf{h}}\|_2^2 \right), \quad (4.9)$$

The term $\|\mathbf{A}\hat{\mathbf{h}} - \mathbf{h}_{\text{obs}}\|^2$ represents the data misfit, measuring how well the model explains the observed data. The second term, corresponding to zeroth-order reg-

ularization, penalizes large deviations of the model from the prior model ($\hat{\mathbf{h}}_{\text{prior}}$), stabilizing the inversion. The third term, associated with first-order regularization, ensures smoothness in the solution by penalizing sharp variations. Both regularization terms improve the conditioning of the system matrix to be inverted. Optimal values for α and β can be determined using methods like cross-validation or L-curve analysis (Aster et al., 2019, Chapter 4).

In equation 4.9, the data misfit term $\|\mathbf{W}_d(\mathbf{A}\hat{\mathbf{h}} - \mathbf{h}_{\text{obs}})\|_2^2$ usually assumes no prior knowledge of data noise. Assuming independent data with unknown covariance, we take $\mathbf{W}_d = \mathbf{C}_d^{-1/2} = \mathbf{I}$, treating all observations equally.

Similarly, in the regularization term $\alpha^2\|\mathbf{W}_m(\hat{\mathbf{h}} - \hat{\mathbf{h}}_{\text{prior}})\|_2^2$, if the prior model covariance $\mathbf{C}_m$ is unknown, we set $\mathbf{W}_m = \mathbf{C}_m^{-1/2} = \mathbf{I}$. In this case, the prior weighting is omitted, though for daily real data (see next sections) it can be included when prior uncertainties are available.

Since the medium is 2D, the gradient term, represented by the matrix $\mathbf{L}$, should compute the gradient in both x and y directions. In this case, the gradient regularization can be expressed as:

$$\|\mathbf{L}\hat{\mathbf{h}}\|_2^2 = \|\mathbf{D}_x\hat{\mathbf{h}}\|_2^2 + \|\mathbf{D}_y\hat{\mathbf{h}}\|_2^2.$$

Expanding the terms:

$$\|\mathbf{L}\hat{\mathbf{h}}\|_2^2 = \hat{\mathbf{h}}^T\mathbf{D}_x^T\mathbf{D}_x\hat{\mathbf{h}} + \hat{\mathbf{h}}^T\mathbf{D}_y^T\mathbf{D}_y\hat{\mathbf{h}}.$$

Using a simple forward Euler method, the gradient can be computed. For the boundaries, a backward Euler method is employed. As an example, the first element resulting from the multiplication of the gradient matrix with the thickness model vector is (see Figure 4.1):

$$(\mathbf{D}_x\,\hat{\mathbf{h}})_1 = \frac{\hat{h}_5 - \hat{h}_1}{\Delta x}, \qquad (\mathbf{D}_y\,\hat{\mathbf{h}})_1 = \frac{\hat{h}_2 - \hat{h}_1}{\Delta y}.$$

In Figure 4.2, the matrices $\mathbf{D}_x$ (right) and $\mathbf{D}_y$ (left) are shown for a simple 4 by 5 cell medium.

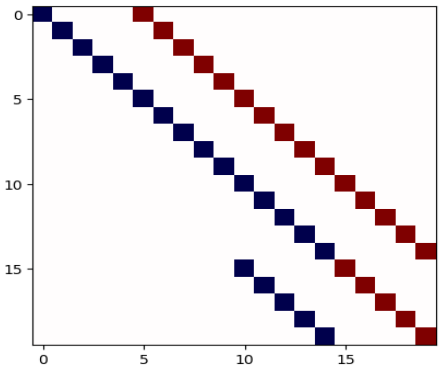

(a) $\mathbf{D}_x$ Matrix

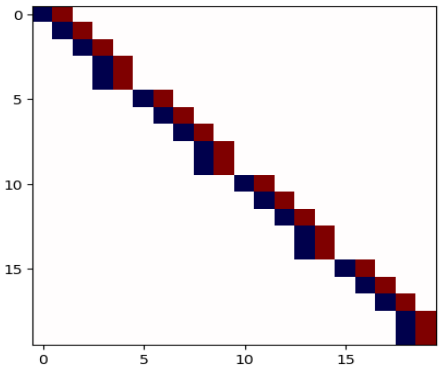

(b) $\mathbf{D}_y$ Matrix

Figure 4.2: In this example, the medium consists of 4×5 cells, resulting in 20×20 matrices for $\mathbf{D}_x$ and $\mathbf{D}_y$. In (a), red cells represent $\frac{1}{\Delta x}$ and blue cells represent $\frac{-1}{\Delta x}$, while in (b), red cells represent $\frac{1}{\Delta y}$ and blue cells represent $\frac{-1}{\Delta y}$.

Now that all the ingredients are in place, we can solve Equation 4.9 using a least-squares solution. The least-squares solution can be expressed as:

$$\hat{\mathbf{h}}_{\text{opt}} = \left(\frac{1}{N_p} \mathbf{A}^T \mathbf{A} + \alpha^2 \mathbf{I} + \beta^2 \mathbf{L}^T \mathbf{L} \right)^{-1} \left(\frac{1}{N_p} \mathbf{A}^T \mathbf{h}_{\text{obs}} + \alpha^2 \hat{\mathbf{h}}_{\text{prior}} \right). \tag{4.10}$$

The least-squares problem defined in Equation 4.10 is solved using a direct sparse solver, specifically a sparse LU factorization. Thanks to our choice of parameters and problem size, the matrices can be built and factorized efficiently, providing robust and accurate convergence. This direct approach is, however, memory-intensive, and for larger problems—where the number of observations and model parameters grows significantly—iterative methods such as Conjugate Gradient become preferable. Iterative solvers avoid explicit matrix factorization, reducing memory usage, although they may converge more slowly and can be sensitive to matrix conditioning (Menke, 2012; Aster et al., 2019).

The regularization parameters, α and β, can be determined using L-curve analysis. For various values of α and β within specified ranges, we compute the least-squares solutions, $\hat{\mathbf{h}}_{\text{opt}}$, and calculate the three terms of Equation 4.9: the data misfit term ($\|\mathbf{A}\hat{\mathbf{h}} - \mathbf{h}_{\text{obs}}\|_2^2$), the first regularization term ($\|\hat{\mathbf{h}} - \hat{\mathbf{h}}_{\text{prior}}\|_2^2$), and the second regularization term ($\|\mathbf{L}\hat{\mathbf{h}}\|_2^2$).

4.3 Synthetic Test

Consider the source–receiver configuration shown in Figure 4.3(a), taken from an active-source experiment dataset (see Section 1.3.1, survey S1 in Figure 1.4). This experiment was conducted on 2024-03-06 in the St. Lawrence Estuary, Quebec, Canada, and includes 21 active sources and 16 3C stations.

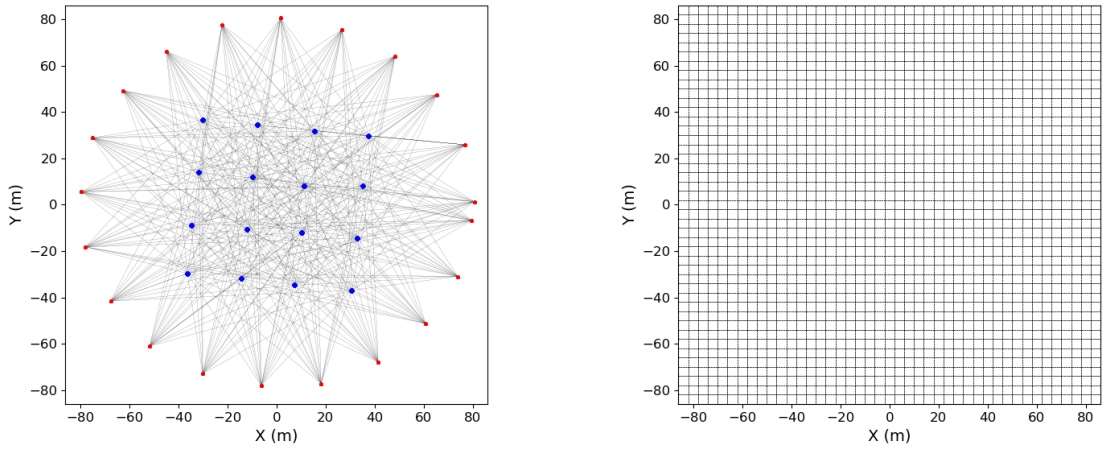

(a) (b)

Figure 4.3: (a) Array geometry showing the locations of sources (red stars) and receivers (blue circles). (b) Mesh used for tomography.

The area shown in Figure 4.3 is square (172 m × 172 m), with the origin $(0, 0)$ located at the center of the array in a Cartesian coordinate system. The domain is discretized into square cells of size 4 m × 4 m, resulting in a total of 1849 cells arranged in a 43 × 43 regular grid (see Figure 4.3(b)).

Figure 4.5(a) shows the synthetic true model, $\hat{\mathbf{h}}_{\text{true}}$, used for the test. The model features two ice thickness anomalies: a smaller anomaly located within the array, with a minimum thickness of 0.45 m at its center, and a larger anomaly extending toward the edge of the domain, with a maximum thickness of 0.55 m at its center. The contrasting thicknesses provide a controlled scenario to evaluate the inversion's ability to resolve both small- and large-scale features.

This synthetic model is used to generate the observed data, $\mathbf{h}_{\text{obs}}$. Using the source–receiver geometry in Figure 4.3(a), we construct the forward operator matrix, $\mathbf{A}$. The synthetic observations are then obtained simply as

$$\mathbf{h}_{\text{obs}} = \mathbf{A}\hat{\mathbf{h}}_{\text{true}}.$$

Solving Equation 4.10 yields the inversion results shown in Figure 4.5(b). The tomography successfully recovers the two primary anomalies, capturing their general shapes well. However, the amplitudes are slightly underestimated, and the smaller anomaly appears somewhat smoothed compared to the true model. Additionally, in regions near the edges where ray coverage is sparse or zero, the larger, high-thickness anomaly is also smoothed and smeared, as the inversion interpolates values from neighboring cells in areas with few or no rays.

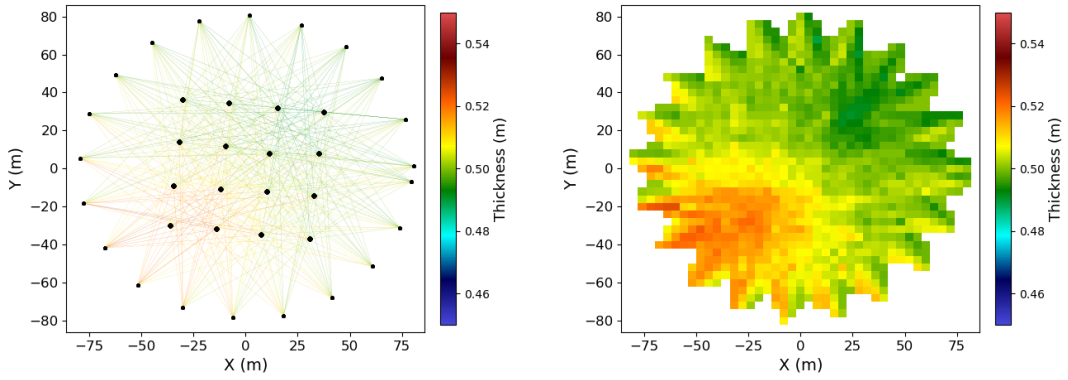

(a) (b)

Figure 4.4: (a) Ray paths, and (b) ray density map.

Figure 4.4(a) shows the ray paths: individual ray paths are plotted and each ray is colored according to its associated thickness. Figure 4.4(b) presents the mesh-based ray density map: individual rays are not shown here; instead, each mesh cell contains the average of the thicknesses of all rays that pass through that cell. In subsequent examples using field data, where the number of rays is smaller—as in this case—the individual ray paths are displayed. Conversely, when the number of rays is very large, ray density maps are used instead.

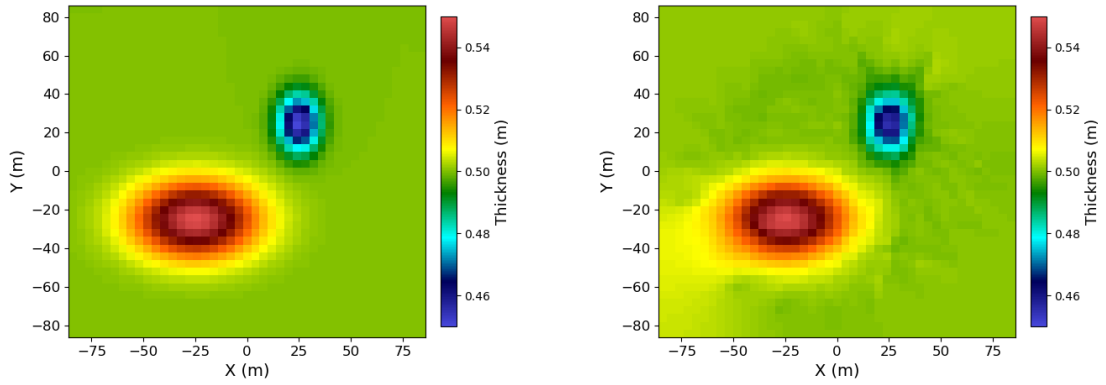

(a) (b)

Figure 4.5: (a) True model showing the two primary anomalies. (b) Tomography results obtained using regularization parameters $\beta = 1 \times 10^{-4}$ and $\alpha = 0$, meaning no prior model is included in the inversion.

To account for potential measurement errors, a small amount of random noise was added to the observation vector $\mathbf{h}_{\text{obs}}$. The noise follows a normal distribution with zero mean and a magnitude of approximately 2% of the maximum observed thickness variation, allowing us to assess the robustness of the inversion. As shown in Figure 4.6, the inversion reliably recovers both anomalies. A slightly larger smoothing parameter was applied to prevent overfitting of the added noise. The maximum amplitude of the larger anomaly is nearly recovered, while the smaller anomaly is also retrieved, though its peak is underestimated by about 1 cm.

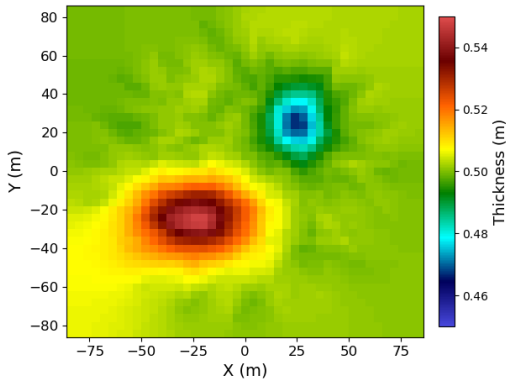

Figure 4.6: Tomography results obtained using regularization parameters $\beta = 5 \times 10^{-2}$ and $\alpha = 0$.

4.3.1 Uncertainty Analysis

To evaluate uncertainty in linear inverse problems, several matrix-based tools can be used, including:

- **Posterior Covariance Matrix**

- **Model Resolution Matrix**
- **Correlation Matrix**

An important concept is the **posterior covariance matrix**, $\mathbf{C}_M$, which quantifies the uncertainty in the recovered model parameters. It is defined as:

$$\mathbf{C}_M = \left(\frac{1}{N_p}\mathbf{A}^T\mathbf{A} + \alpha^2\mathbf{I} + \beta^2\mathbf{L}^T\mathbf{L}\right)^{-1}.$$

For a model with n parameters, $\mathbf{C}_M$ is an $n \times n$ matrix: the diagonal entries give the variance of each parameter, showing how uncertain the inversion is for that cell (see Figure 4.7:(a)), while the off-diagonal entries indicate covariances, i.e., how uncertainties in different cells are linked (see Figure 4.8:(b)). $\mathbf{C}_M$ has units of squared model parameters and directly reflects the scale of uncertainty in the inversion (Aster et al., 2019). Visualizing $\mathbf{C}_M$ can therefore help identify regions where the model is well-resolved versus areas of higher uncertainty, guiding interpretation of the inversion results.

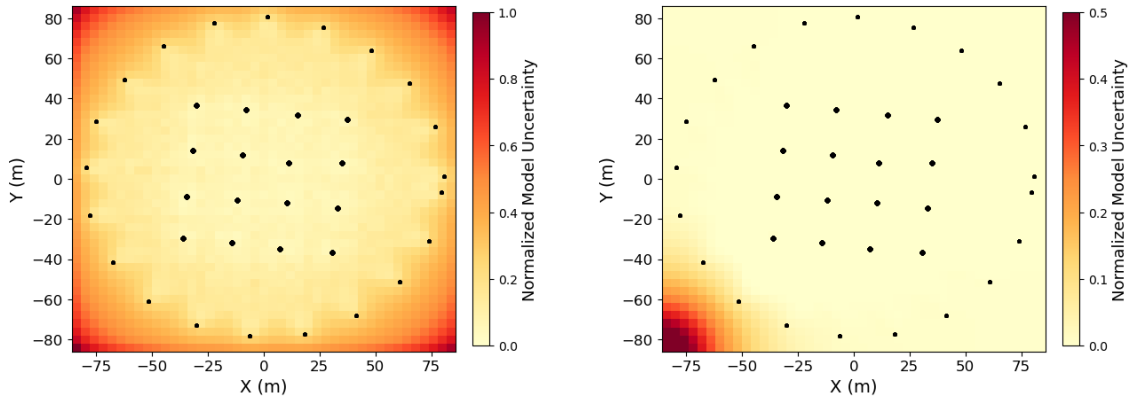

(a) (b)

Figure 4.7: (a) The diagonal entries of the posterior covariance matrix, representing the variance of each pixel. (b) Mapping a column corresponding to the cell with no rays (bottom-left corner cell), showing how the reconstruction of that pixel is correlated with all other pixels. Stations and receivers are shown as black stars and circles. Here $\beta = 1 \times 10^{-4}$ and $\alpha = 0$.

In the case of a linear inverse problem, as in our study, another commonly used metric is the **model resolution matrix**, $\mathbf{R}_m$, which describes the resolving power of the inversion. It can be viewed as a linear filter relating the true and estimated models ($\hat{\mathbf{h}}_{\text{est}} = \mathbf{R}_m\hat{\mathbf{h}}_{\text{true}}$). Diagonal values close to unity indicate well-resolved parameters, while significant off-diagonal terms represent parameter trade-offs or smearing. Thus, $\mathbf{R}_m$ reflects how faithfully the inversion recovers the underlying model structure (Aster et al., 2019). It is defined as:

$$\mathbf{R}_m = \left(\frac{1}{N_p}\mathbf{A}^T\mathbf{A} + \alpha^2\mathbf{I} + \beta^2\mathbf{L}^T\mathbf{L}\right)^{-1}\left(\frac{1}{N_p}\mathbf{A}^T\mathbf{A}\right).$$

The model resolution matrix, $\mathbf{R}_m$, describes how well the inversion can recover each model parameter. For a model vector with n parameters, $\mathbf{R}_m$ is an $n \times n$ square matrix, where each element $R_{m,ij}$ quantifies how much the recovered value of parameter i is influenced by the true value of parameter j. The diagonal entries $R_{m,ii}$ indicate the contribution of the true parameter i to its own recovered value, with values close to 1 corresponding to well-resolved parameters and values near 0 indicating poorly resolved ones (see Figure 4.8:(a)), while the off-diagonal entries $R_{m,ij}$ $(i \neq j)$ represent the leakage of information between different parameters (see Figure 4.8:(b)). In fact, each column of the resolution matrix, which includes the off-diagonal entries, is equivalent to the resolution kernel obtained from a traditional spike test, showing how a spike in one parameter spreads into neighboring ones (Aster et al., 2019).

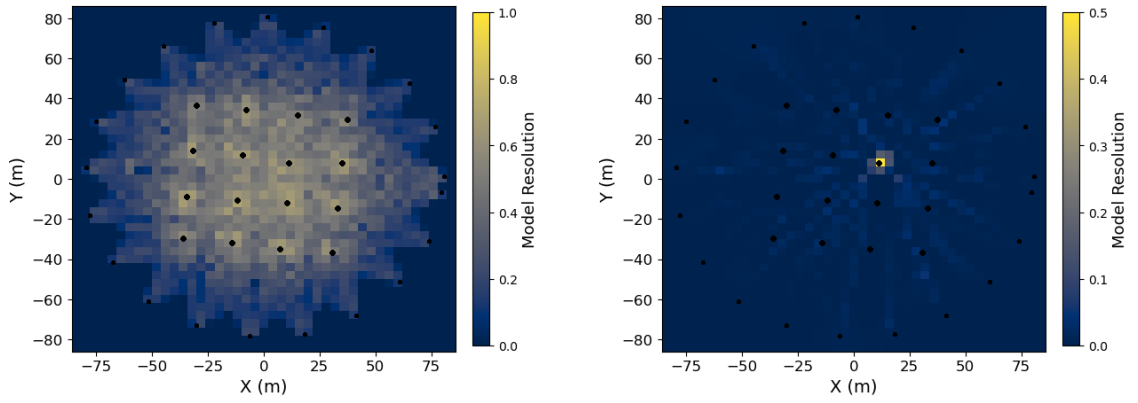

(a) (b)

Figure 4.8: (a) Mapping model resolution using diagonal entries. (b) Mapping a column corresponding to the cell with the maximum number of rays. Stations and receivers are shown as black stars and circles. Here $\beta = 1 \times 10^{-4}$ and $\alpha = 0$.

A third metric is the **correlation matrix**, a normalized form of $\mathbf{C}_M$ that measures parameter dependence. It is defined as:

$$\rho^{ij} = \frac{C_M^{ij}}{\left(C_M^{ii}\right)^{1/2} \left(C_M^{jj}\right)^{1/2}}, \tag{4.11}$$

with values ranging from -1 to 1. Strong correlations imply parameters are not independently resolved by the data (Tarantola, 2005).

Together, $\mathbf{R}_m$, $\mathbf{C}_M$, and $\boldsymbol{\rho}$ provide complementary measures of model quality: $\mathbf{R}_m$ describes resolution, $\mathbf{C}_M$ uncertainty, and $\boldsymbol{\rho}$ parameter dependence. These measures of uncertainty are most useful for linear problems.

A trade-off exists between the model covariance matrix and the resolution matrix, which is primarily controlled by the acquisition geometry, cell size, and regularization parameters, including smoothing and prior model constraints. The covariance matrix quantifies the uncertainty and correlation between model parameters, whereas the resolution matrix describes how well the true model can be recovered, effectively reflecting how true features are averaged or smeared in the estimated model. The

influence of acquisition geometry, cell size, and regularization parameters on the inversion results can be summarized as follows:

- ✓ Acquisition geometry—such as the distribution of sources and receivers—directly affects the path coverage and azimuthal coverage of rays, which in turn determines the ability to resolve structures: poor or uneven coverage leads to high covariance and low resolution, as some regions may be poorly constrained.

- ✓ The choice of cell size is also crucial: smaller cells can improve the potential resolution but may increase parameter covariance if the data cannot independently constrain them, whereas larger cells reduce variance but at the cost of resolution.

- ✓ Regularization parameters, including damping and smoothing, are used to stabilize the ill-posed inverse problem. However, these introduce a trade-off: stronger damping or smoothing reduces covariance and suppresses noise but also degrades resolution by overly smoothing or biasing the solution toward the prior, potentially masking real structures. In general, the optimal values of the regularization parameters can be estimated using methods such as L-curve analysis or cross-validation. For the L-curve, the point of maximum curvature defines the optimal regularization. When both α and β are considered simultaneously, this approach extends naturally to a two-dimensional L-curve, where the optimal parameters are identified by the point of maximum curvature on the surface.

In linear inverse problems, key challenges include the computational expense of explicitly computing covariance and resolution matrices for large-scale problems, the difficulty in accurately quantifying prior data and model uncertainties, the subjective choice of regularization parameters which may not reflect true Earth properties. Thus, while covariance and resolution analyses provide insight into solution reliability, their practical utility is limited by these interdependencies and assumptions (Rawlinson et al., 2014).

4.3.2 Checkerboard Test

As an alternative, checkerboard tests offer a practical way to assess the resolving power of the inversion under realistic conditions. In this approach, a synthetic model with alternating high and low values is constructed, and noise-free data are generated using the same acquisition geometry, model parametrization, and forward operator as the real experiment. The inversion is then performed with the same algorithm and regularization settings as for the real experiment. Comparing the recovered model to the input checkerboard pattern highlights where anomalies are well-resolved and where smearing or loss of resolution occurs, providing an intuitive and visual assessment of the inversion's capabilities.

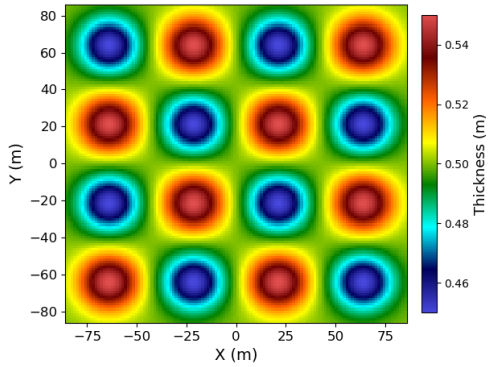

(a) True Model, 4×4 Checkerboard

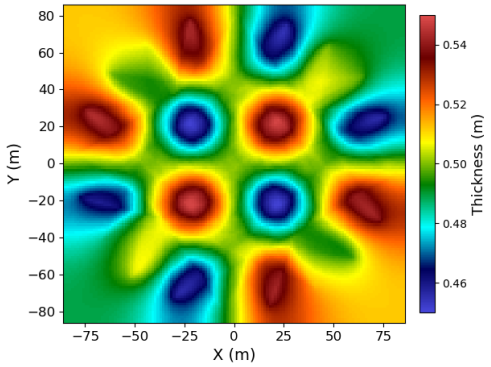

(b) Inverted Model

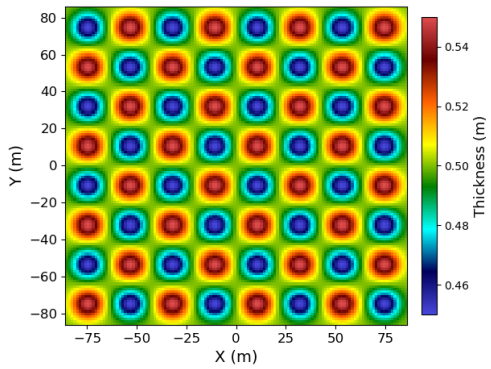

(c) True Model, 8×8 Checkerboard

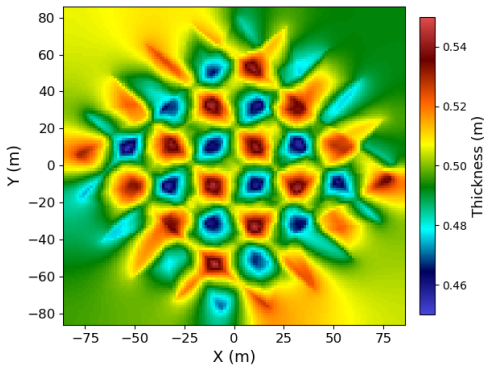

(d) Inverted Model

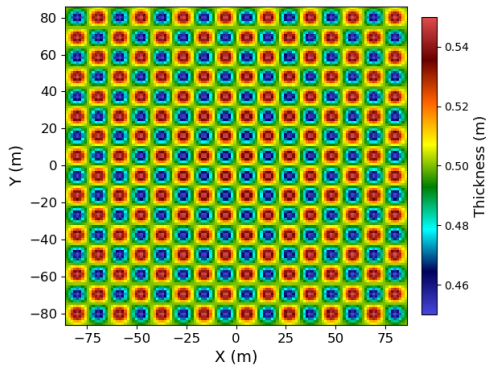

(e) True Model, 16×16 Checkerboard

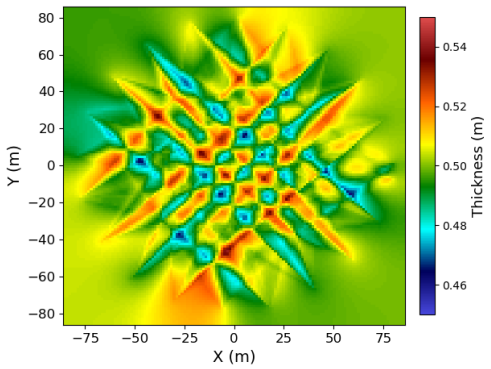

(f) Inverted Model

Figure 4.9: True and inverted models for three checkerboard patterns. Regions with dense ray and azimuthal coverage are well recovered, those with limited coverage show smearing, and areas without rays are interpolated from neighbors, as illustrated by the true and inverted checkerboard models. In all cases $\alpha = 0$ and $\beta = 1 \times 10^{-4}$.

As shown in Figure 4.9, the same acquisition geometry used in Figure 4.3 is applied to construct three checkerboard models. The grid is regular, with a cell size of 1.34375 m (giving a 128×128 grid of cells), chosen as a multiple of 2 and small

enough to generate smooth, fine-scale patterns (e.g., in Figure 4.9(e)).

The checkerboard pattern sizes are 43 m, 21.5 m, and 10.75 m, respectively. In each case, the true model is shown on the left panels ((a), (c), and (e) in Figure 4.9), while the corresponding inversion results are shown on the right ((b), (d), and (f) in Figure 4.9). Similar to the previous synthetic test, the synthetic observations are generated using:

$$\mathbf{h}_{\text{obs}} = \mathbf{A}\hat{\mathbf{h}}_{\text{ch}},$$

The checkerboard tests demonstrate that the inversion reliably recovers anomalies in regions with dense ray coverage and high azimuthal diversity, whereas areas with sparse or poorly intersecting rays exhibit smearing and spatial averaging. Smaller-scale features are resolved only where sufficient rays cross the corresponding cells, underscoring the importance of ray density and azimuthal coverage in controlling spatial resolution.

In the following examples, tomography inversions of field data are presented. For each case, a checkerboard test is conducted, regularization parameters are determined through trial and error, and the cell sizes are selected to be small enough to produce smooth, physically plausible models without making the inversion computationally intractable.

4.4 Field Data Application

In the following sections, two datasets from different regions are presented: St. Lawrence Estuary, Quebec, Canada and Svalbard. The St. Lawrence dataset consists of controlled-source data and serves as validation for our methodology, followed by the Svalbard case. We apply tomographic inversion to derive sea ice thickness maps for each dataset. The regularization and quality control parameters are tailored to each case. For the St. Lawrence dataset, fewer paths are available and the average misfit is higher, requiring a more lenient misfit threshold (i.e., data with misfit above this threshold are excluded). For Svalbard, the larger number of paths and lower average misfit allow a stricter misfit threshold. In both cases, thickness values inconsistent with field observations are excluded to remove outliers. Additionally, cell size and problem formulation differ between the two cases, leading to distinct regularization parameters determined through trial and error.

4.4.1 Tomographic Inversion of Sea Ice in the St. Lawrence Estuary, Quebec, Canada

We use four datasets from surveys conducted in this region (see Section 1.3.1) and apply tomography to generate ice thickness maps for each case. For all datasets, only the vertical component of the waveforms is considered. Since the source locations are known, ice thicknesses along each path are first estimated using a grid search approach, which then serves as input for the tomographic inversion.

The tomography results are based on a regular mesh of $2\,\text{m} \times 2\,\text{m}$ cells, with the parameter $\beta = 0.12 - 0.15$ selected through trial and error (here $\alpha = 0$, as no prior model is used). For each of the four cases, checkerboard tests were performed

following the same procedure as in Figure 4.9. In all cases, the tests were conducted using a subset of ray paths, filtered based on their cost values and by removing outliers in the observed thickness data. The checkerboard results consistently show that patterns with sizes approximately 20 m are well recovered in the regions between the sources and the receiver array.

2024-03-06 Dateset

The first dataset consists of 21 active sources generated by human jumps and 16 three-component (3C) stations (the same array shown in Figure 4.3 used for the synthetic tests). Figure 4.10 shows the source–receiver configuration and the mesh used for tomography. The mesh coordinates are given in meters, showing the spatial extent of the survey area.

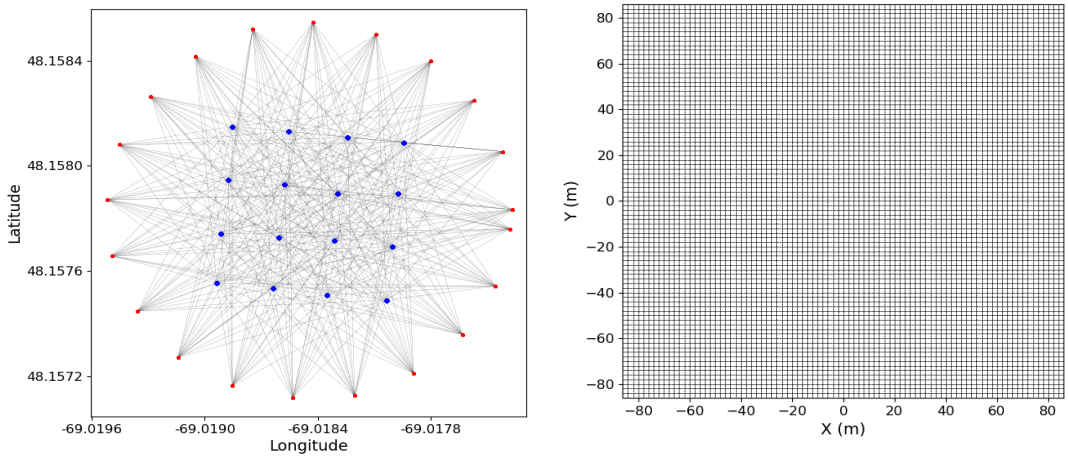

Figure 4.10: Array geometry showing the locations of sources (red stars) and receivers (blue filled circles) (left), and the mesh used for the tomography (right).

A synthetic database was generated using SEM, based on the parameters summarized in Table 4.1. This database is subsequently employed to estimate ice thicknesses along the source–receiver paths.

Table 4.1: Ice and water properties used in the synthetic database generation for different dates.

Parameter	**Symbol**	**2024-03-06**	**2025-02-06**	**2025-02-10**	**2025-02-24**
Ice density	ρ_{ice}	$900\,\text{kg/m}^3$	$910\,\text{kg/m}^3$	$910\,\text{kg/m}^3$	$910\,\text{kg/m}^3$
Ice Poisson's ratio	ν_{ice}	0.38	0.24	0.30	0.30
Water density	ρ_{w}	$1000\,\text{kg/m}^3$	$1000\,\text{kg/m}^3$	$1000\,\text{kg/m}^3$	$1000\,\text{kg/m}^3$
Water sound speed	c_{w}	$1440\,\text{m/s}$	$1480\,\text{m/s}$	$1480\,\text{m/s}$	$1480\,\text{m/s}$
Ice Young's modulus	E	$7 \times 10^9\,\text{Pa}$	$3.4 \times 10^9\,\text{Pa}$	$4.2 \times 10^9\,\text{Pa}$	$4 \times 10^9\,\text{Pa}$

The inversion procedure consists of three steps:

1. **Grid search over ice thicknesses:** Knowing the source locations, we perform a grid search using a zero-correlation cost function to estimate ice thicknesses along each path. An example of the fit between observed and synthetic waveforms, along with the corresponding estimated ice thickness for the given source–receiver distance, is shown in Figure 4.11.

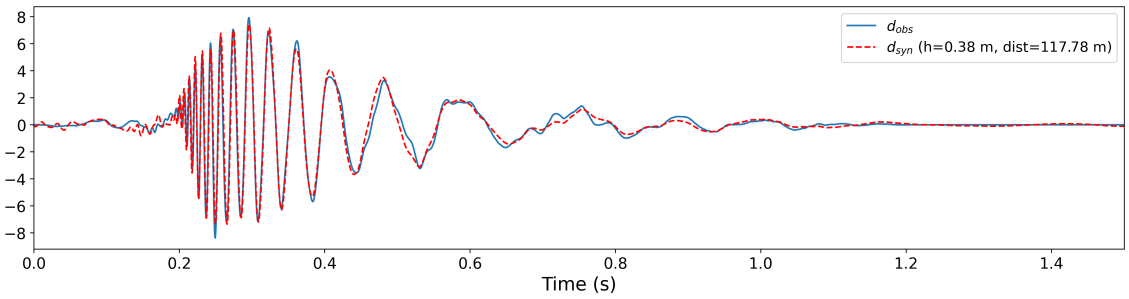

Figure 4.11: Example of the fit between synthetic and observed waveforms.

2. **Quality control:** We retain only solutions with a misfit value below 0.15 (i.e., a correlation above 0.85). Outliers are also removed, those with thicknesses less than 0.2 m or greater than 0.9 m. Figure 4.12(a) shows the selected paths retained after quality control, which are used in the inversion.

3. **Tomography:** Using the filtered set of source–receiver path estimates, we perform the tomographic inversion to obtain the final ice thickness map, which is shown in Figure 4.12(b).

After applying Step 1 and Step 2, 319 paths remained out of 336. Ray paths and tomography results for the field data are shown below. The results are shown in Figure 4.12.

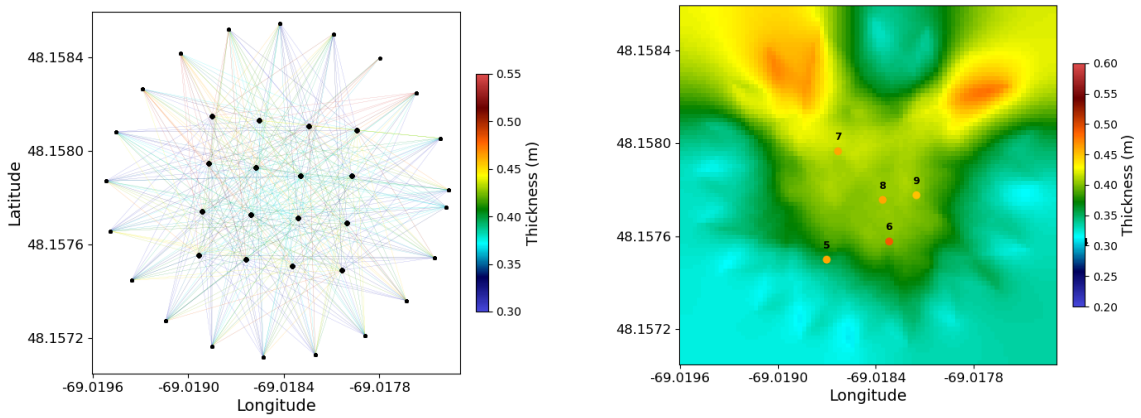

(a) (b)

Figure 4.12: (a) Selected paths (319), along with the 21 sources and 16 receivers. (b) Tomographic inversion result. Filled circles indicate drilling observations.

For the remaining datasets, the same three-step procedure is applied: a grid search to estimate ice thicknesses along each path, quality control, and tomographic inversion. For each case, the synthetic database is generated using the corresponding material properties from Table 4.1. The only variation between cases is the misfit threshold used during quality control, which is adjusted according to the data quality of each survey. Additionally, the number of paths retained after filtering and the spatial extent of the survey area differ across the four datasets.

2025-02-06 Dateset

The second dataset consists of 33 active sources generated by human jumps and 16 three-component (3C) stations. Figure 4.13 shows the source–receiver configuration and the mesh used for tomography.

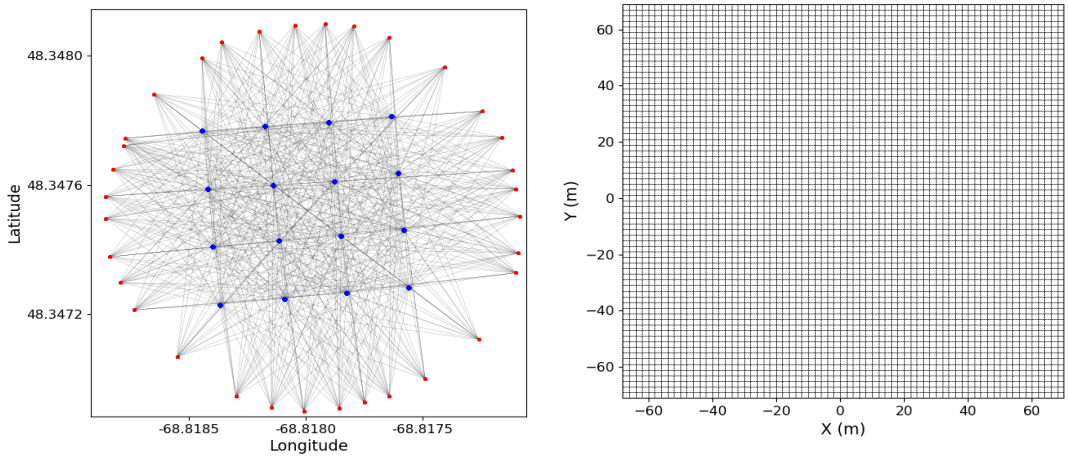

Figure 4.13: Array geometry showing the locations of sources (red stars) and receivers (blue filled circles) (left), and the mesh used for the tomography (right).

An example of the fit between observed and synthetic waveforms, along with the corresponding estimated ice thickness for the given source–receiver distance, is shown in Figure 4.14.

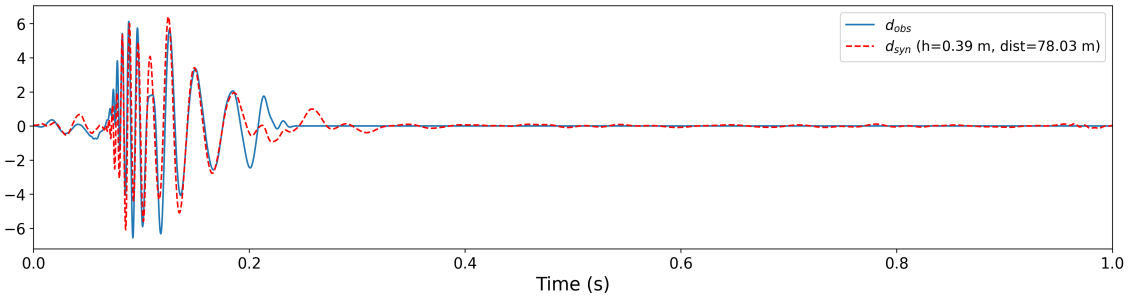

Figure 4.14: Example of the fit between synthetic and observed waveforms.

Here we retain only solutions with a misfit value below 0.3 (i.e., a correlation above 0.7). After applying the grid search and quality control, 296 paths remained

out of 528. The selected paths are shown in Figure 4.15(a), and the final ice thickness map obtained from the tomographic inversion is presented in Figure 4.15(b).

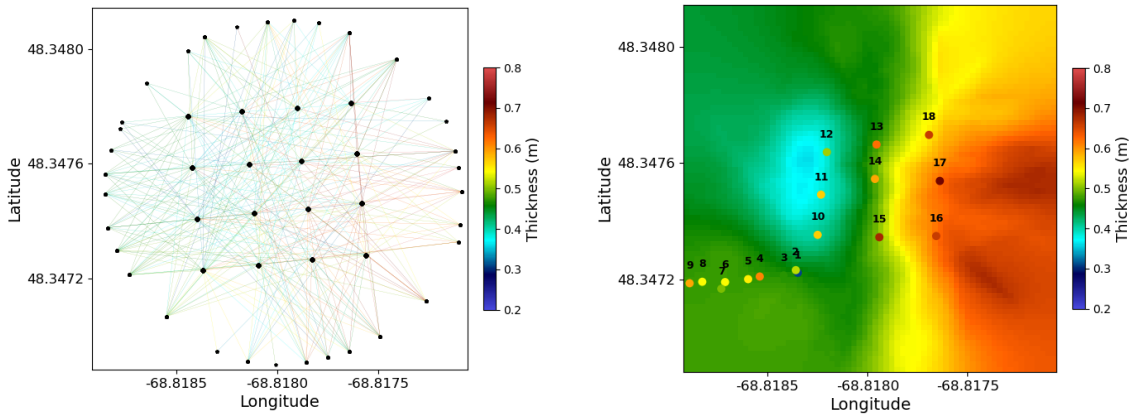

(a) (b)

Figure 4.15: (a) Selected paths (391), along with the 33 sources and 16 receivers. (b) Tomographic inversion result. Filled circles indicate drilling observations.

As illustrated in Figure 4.16, the receiver array corresponding to the configuration in Figure 4.15(a) was deployed across a boundary separating two visually distinct ice types.

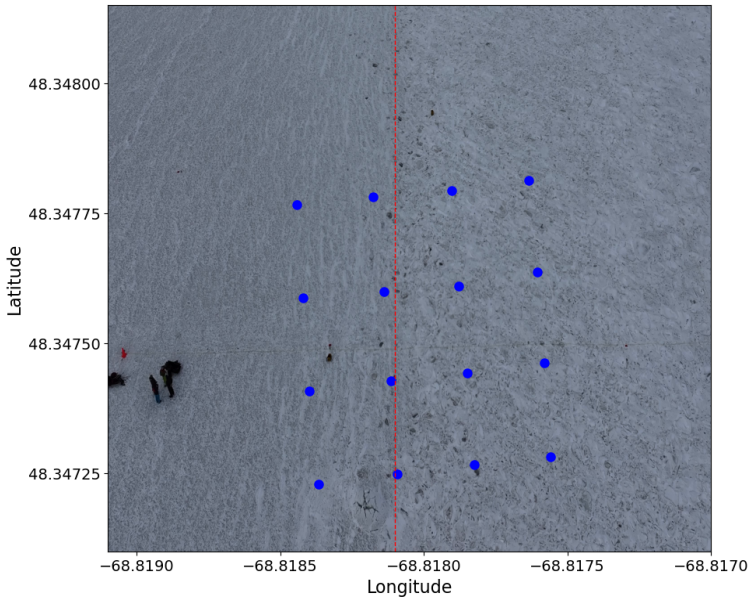

Figure 4.16: Field photograph of the array of receivers corresponding to the configuration shown in Figure 4.15(a). The dashed red line approximately marks the boundary between two visually distinct ice types observed in the field on 6 February 2025.

2025-02-10 Dateset

The third dataset consists of 21 active sources generated by human jumps and 16 three-component (3C) stations. Figure 4.17 shows the source–receiver configuration and the mesh used for tomography.

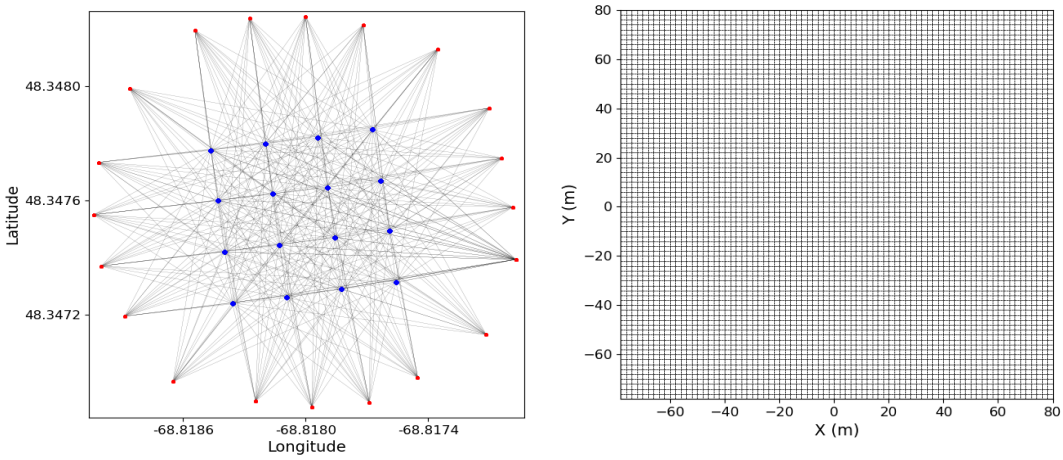

Figure 4.17: Array geometry showing the locations of sources (red stars) and receivers (blue filled circles) (left), and the mesh used for the tomography (right).

An example of the fit between observed and synthetic waveforms, along with the corresponding estimated ice thickness for the given source–receiver distance, is shown in Figure 4.18.

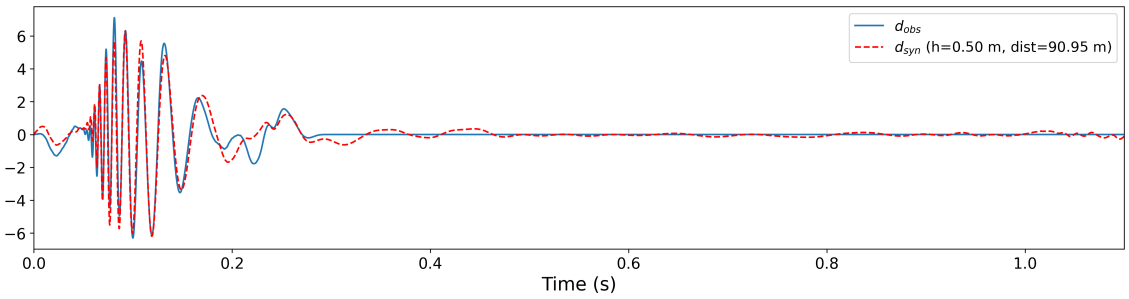

Figure 4.18: Example of the fit between synthetic and observed waveforms.

Here we retain only solutions with a misfit value below 0.25 (i.e., a correlation above 0.75). After applying the grid search and quality control, 313 paths remained out of 336. The selected paths are shown in Figure 4.19(a), and the final ice thickness map obtained from the tomographic inversion is presented in Figure 4.19(b).

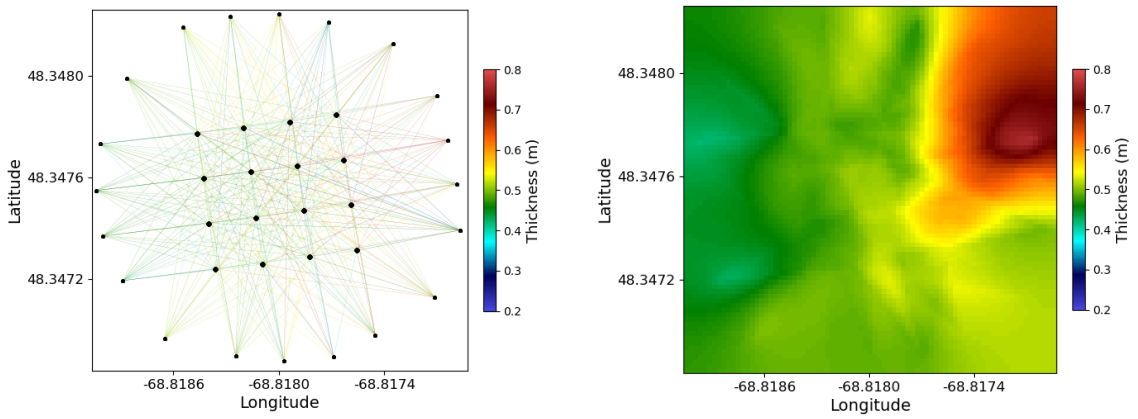

(a) (b)

Figure 4.19: (a) Selected paths (313), along with the 21 sources and 16 receivers. (b) Tomographic inversion result.

2025-02-24 Dateset

The third dataset consists of 20 active sources generated by human jumps and 16 three-component (3C) stations. Figure 4.20 shows the source–receiver configuration and the mesh used for tomography.

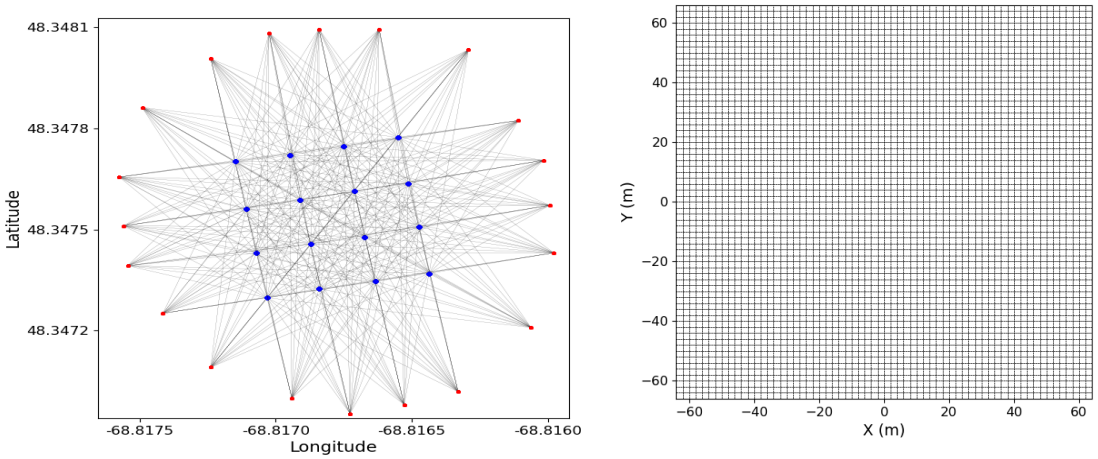

Figure 4.20: Array geometry showing the locations of sources (red stars) and receivers (blue filled circles) (left), and the mesh used for the tomography (right).

An example of the fit between observed and synthetic waveforms, along with the corresponding estimated ice thickness for the given source–receiver distance, is shown in Figure 4.21.

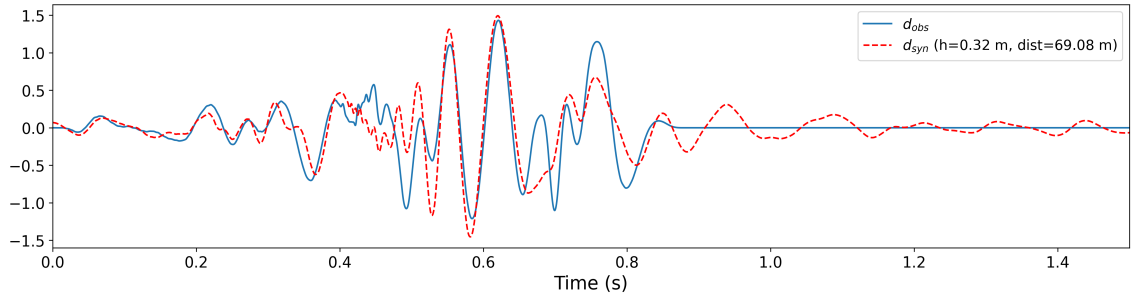

Figure 4.21: Example of the fit between synthetic and observed waveforms.

Here we retain only solutions with a misfit value below 0.4 (i.e., a correlation above 0.6). After applying the grid search and quality control, 135 paths remained out of 320. The selected paths are shown in Figure 4.19(a), and the final ice thickness map obtained from the tomographic inversion is presented in Figure 4.19(b).

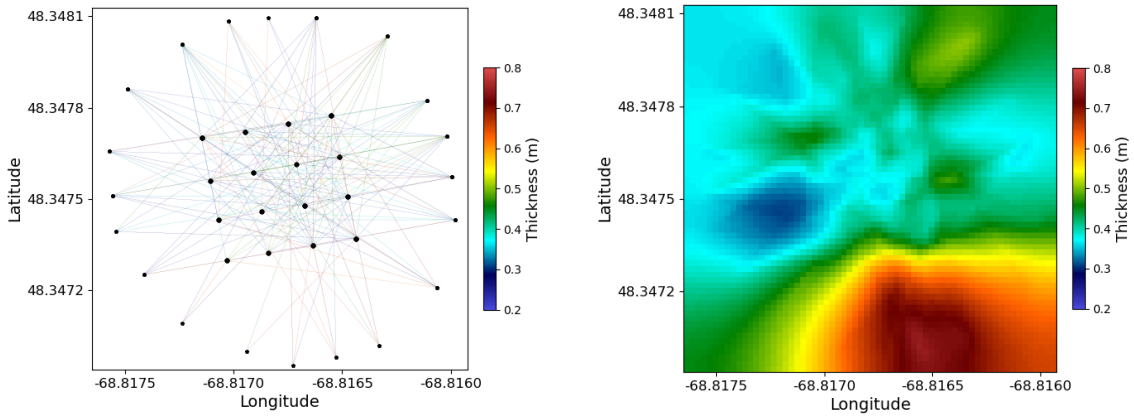

(a) (b)

Figure 4.22: (a) Selected paths (135), along with the 20 sources and 16 receivers. (b) Tomographic inversion result.

Results and Discussion

We consider four datasets in this study. One dataset was acquired on 6 March 2024, while the other three were collected on 6, 10, and 24 February 2025, respectively (see Figure 1.4). The 2024 dataset corresponds to a small inland lake located approximately 25 km from the 2025 survey sites, whereas the 2025 datasets were acquired on the Saint Lawrence River. This geographic distinction is important, as the two environments exhibit different ice formation processes: the inland lake experiences primarily static freezing with limited currents, while the river environment is subject to tidal flows and more dynamic ice conditions.

Checkerboard tests were performed for all four cases using the selected ice thickness estimates shown in Figures 4.12(a), 4.15(a), 4.19(a), and 4.22(a). These tests indicate that patterns with a spatial scale of approximately 20 m are well recovered in regions with adequate ray coverage, while areas with denser ray coverage show resolution down to about 10 m. The resolution is primarily controlled by the

source–receiver geometry: regions between the active sources and the receiver array are best resolved, while areas outside this zone exhibit increased smoothing due to limited ray crossings. This highlights the importance of survey design in achieving desired resolution targets.

Regarding the 2024 dataset, shown in Figure 4.12(b) (area 172 m by 172 m; see mesh in Figure 4.10), field drilling measurements at points 5–9 indicate ice thicknesses of 46, 49, 46, 46, and 45 cm, respectively. The thicknesses obtained from the tomographic inversion are systematically 4–5 cm smaller for points 7–9, and approximately 9 cm smaller for points 5 and 6. The discrepancies are smallest in regions with the highest ray density, suggesting that residual errors are partly attributable to limited spatial sampling rather than systematic bias.

Several factors may contribute to these differences. Drilling measurements may slightly overestimate ice thickness by approximately 5 cm because the porous, slushy bottom layer is included in the measurement but is too soft to guide flexural waves. Additionally, the inversion assumes a homogeneous ice density and elastic moduli, whereas real ice may exhibit vertical gradients in properties due to temperature variations and brine content. Despite these discrepancies, the tomography successfully captures the thicker ice in the central region, producing physically consistent results.

The three datasets acquired in February 2025 are located close to one another (Figure 4.23), enabling comparison of ice conditions over time and space. Notably, the array deployed on 6 February 2025 is nearly at the same location as the array from 10 February 2025, with a four-day interval between surveys. This temporal proximity allows us to examine short-term ice evolution under stable cold conditions.

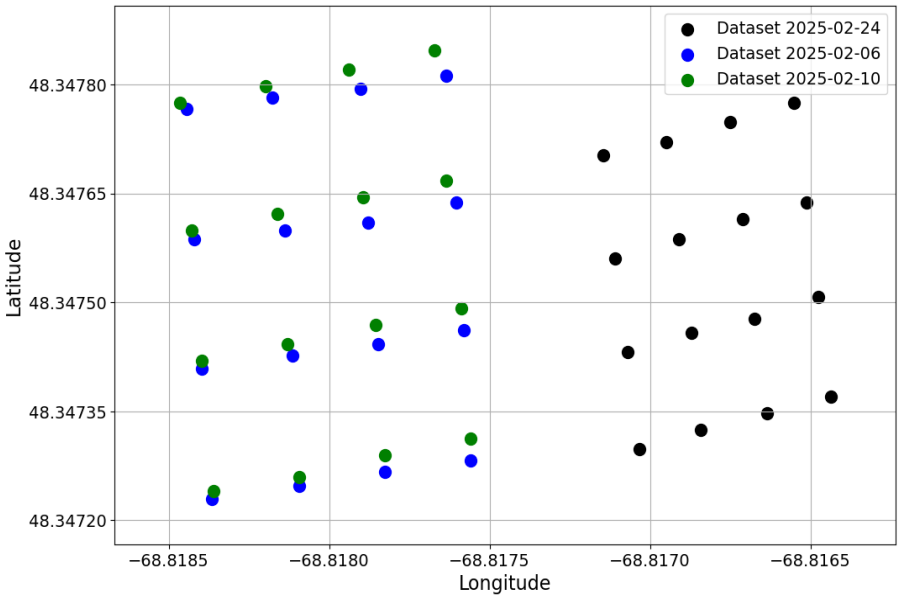

Figure 4.23: Positions of the three seismic receiver arrays deployed in February 2025.

The 6 February dataset (area 138 m by 140 m; see mesh in Figure 4.13) was acquired across a boundary between two distinct ice regimes (Figure 4.16). In the results shown in Figure 4.15(b), red points indicate field drilling measurements col-

lected during the survey. The tomographic inversion clearly reveals a transition from thicker to thinner ice across the array, consistent with the observed ice ridge separating the two ice types in the field. On the eastern side, drilling measurements indicate ice thicknesses of approximately 70–80 cm, whereas on the western side, thicknesses are around 35–40 cm. The tomography reproduces this sharp contrast well, although inverted values are generally slightly lower than the field measurements. As noted, drillings may overestimate by approximately 5 cm due to the unconsolidated basal layer. In regions of dense ray coverage, inversion results match drilling data within a few centimeters, while areas with sparser coverage show deviations up to 10–15 cm. Notably, the transition zone itself is captured with good fidelity, demonstrating the method's ability to resolve sharp lateral gradients when adequately sampled by rays.

For the 10 February dataset (area 158 m by 158 m; see mesh in Figure 4.17), shown in Figure 4.19(b), the same ice thickness contrast is observed in nearly the same location, confirming the persistence of the ice ridge over the four-day interval. The overall pattern remains consistent with the 6 February results, although slight differences are visible. The thicker eastern region shows a modest increase of approximately 5 cm compared to the earlier survey, consistent with ongoing thermal growth under sustained cold conditions.

The results for the 24 February dataset, shown in Figure 4.22(b) (area 128 m by 132 m; see mesh in Figure 4.20), present more complex conditions. This survey occurred following a storm event that significantly altered the ice cover. Data quality is notably lower than in the other surveys, reflected in the higher misfit threshold of 0.4 used for quality control (compared to 0.15–0.3 for other datasets). The ice cover appears highly heterogeneous due to fracturing and displacement caused by wind and wave action, producing a pancake-like structure with significant spatial variability.

The tomographic inversion captures this complexity, revealing pronounced thickness variability across the array. The most consistent feature is a markedly thicker ice zone in the southern part of the survey area, which may correspond to ice accumulation through rafting or compression during the storm event. Unlike the sharp, linear gradient observed in the previous surveys, the thickness distribution here is more chaotic, with variations of 10–20 cm occurring over distances of 10–20 m. This pattern is consistent with mechanical breakup and redistribution rather than thermal growth, highlighting the method's ability to distinguish between different ice formation and deformation processes.

Across all four datasets, several consistent observations emerge. First, the tomographic inversion successfully recovers ice thickness patterns that are consistent with independent drilling measurements and field observations, with discrepancies generally within 5–10 cm in well-sampled regions. Second, the method captures both gradual spatial variations (as in the inland lake) and sharp gradients (as in the river surveys), demonstrating its versatility across different ice environments. Third, the temporal consistency between the 6 and 10 February surveys, and the distinct pattern observed after the storm on 24 February, indicates that the method can track ice evolution over timescales of days to weeks.

4.4.2 Tomographic Inversion of Sea Ice in Svalbard

As explained in Section 1.3.2, this dataset comprises 27 days of seismic ambient noise recorded by 247 stations from 28 February to 26 March 2019, including 2 days of active-source acquisition (1 and 26 March) at Vallunden Lake, Van Mijen Fjord, Svalbard.

The main dataset in this study is the passive icequake recordings, covering the period from 28 February to 24 March. We apply the three-step inversion method described in Chapter 3. First, we locate all icequake events and estimate ice thickness along paths connecting these events to a subset of five stations from the 247-station array. Once the event locations are determined (refer to Figure 3.16), we extend the ice thickness estimates to the remaining 242 stations using a grid search. This provides thickness measurements for all paths in the array. Using this dataset, tomography allows us to analyze both the spatial variations and temporal changes in ice thickness over the 25-day period.

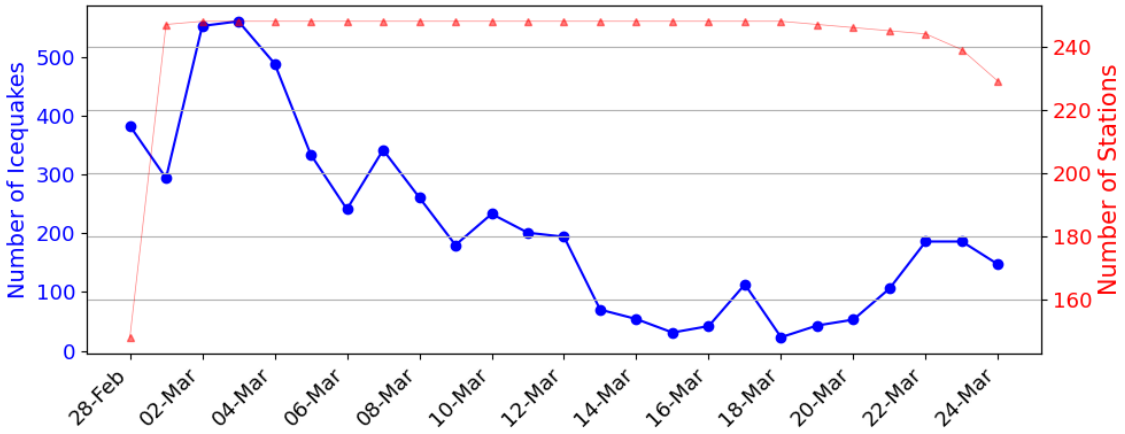

Figure 4.24: Number of events and stations available each day.

The inversion procedure consists of three main steps:

1. **Grid search over ice thicknesses:** Given the known source and receiver locations, a grid search is performed to estimate ice thickness along each path by minimizing a zero-lag correlation cost function. A synthetic database, generated using SEM and based on the parameters in Table 2.1 is used in the inversion. An example of the fit between observed and synthetic waveforms, along with the corresponding estimated ice thickness for the given source–receiver distance, is shown in Figure 4.25.

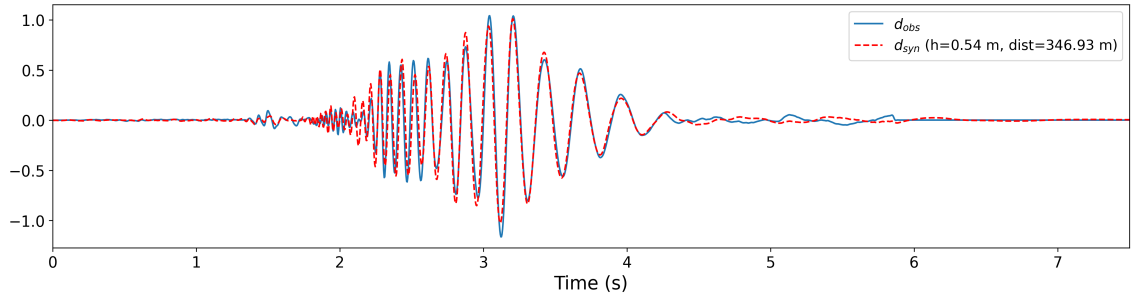

Figure 4.25: Example of the fit between synthetic and observed waveforms for the first event on 28 February.

2. **Quality control:** Only solutions with a misfit below 0.1 (correlation above 0.9) are retained. Figure 4.26 shows the total number of source–receiver paths per day. Paths are filtered based on a maximum cost-value criterion (0.1), and the final number of paths used for tomography is also indicated.

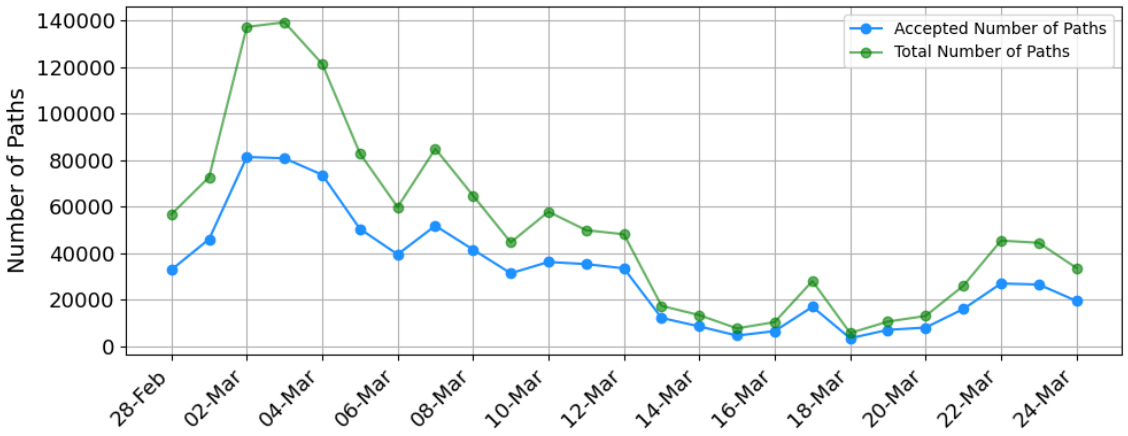

Figure 4.26: Number of source–receiver paths before and after filtering based on cost value.

3. **Tomography:** Using the filtered set of thickness estimates, a daily tomographic inversion is performed to obtain the final ice thickness map.

For the tomography, we generated a regular mesh with a spacing of 6 m × 6 m, which is applied in all subsequent examples. This cell size is small enough to produce smooth and spatially detailed ice thickness maps while remaining consistent with the resolution power of our dataset, making finer discretization unnecessary. The mesh is shown in Figure 4.27. The survey area displayed here covers approximately 900 m × 1,200 m.

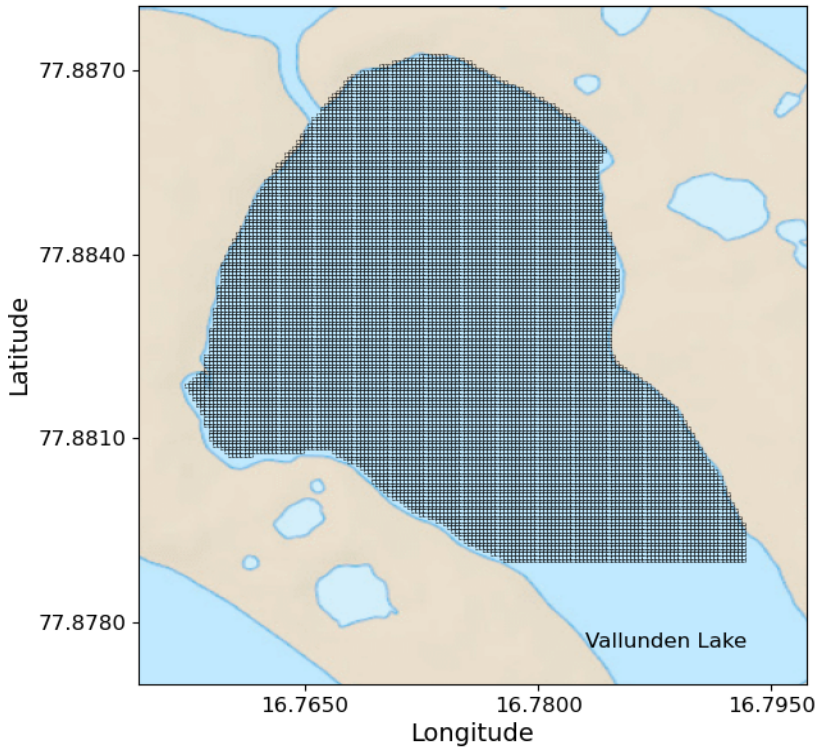

Figure 4.27: Regular 6 m × 6 m mesh used in the tomography.

The checkerboard tests show that patterns with a characteristic size of about 200 m are well recovered. For smaller features (around 100 m), some smearing appears, particularly in sparsely sampled areas. However, in the central region—where station density is highest—the inversion can still resolve smaller-scale structures (see Appendix B).

For daily data, in order to incorporate the previous day's model as a prior, one must account for the fact that ray coverage varies across cells. To address this, different weights are assigned to each cell based on its ray coverage. In the following approach, the posterior model covariance matrix from the previous day is used to weight the regularization term associated with the prior model.
The posterior covariance matrix is given by:

$$\mathbf{C}_{\text{post}}^{\text{prev}} = \frac{1}{N_p^{\text{prev}}} \mathbf{A}^{\text{prev}\,\top} \mathbf{A}^{\text{prev}} + \alpha_0^2 \mathbf{C}_{\text{post}}^{0} + \beta_0^2 \mathbf{L}^{\text{prev}\,\top} \mathbf{L}^{\text{prev}}. \tag{4.12}$$

Here, $\mathbf{C}_{\text{post}}^{0}$ is the posterior covariance matrix from the previous day if it exists; otherwise, as on the first day, it is set to $\mathbf{I}$. The subscript 'prev' denotes matrices and parameters from the previous day's tomography, and β_0 is regularzation parameter used for the previous day.
To incorporate uncertainty-based weighting, we use the normalized form: $\overline{\mathbf{C}}_{\text{post}}^{\text{prev}} = \frac{\mathbf{C}_{\text{post}}^{\text{prev}}}{max(\mathbf{C}_{\text{post}}^{\text{prev}})}$. The weighted least-squares solution for the current day is then expressed as:

$$\hat{\mathbf{h}}_{\text{opt}} = \left(\frac{1}{N_p} \mathbf{A}^\top \mathbf{A} + \alpha^2 \overline{\mathbf{C}}_{\text{post}}^{\text{prev}} \mathbf{I} + \beta^2 \mathbf{L}^\top \mathbf{L} \right)^{-1} \left(\frac{1}{N_p} \mathbf{A}^\top \mathbf{h}_{\text{obs}} + \alpha^2 \overline{\mathbf{C}}_{\text{post}}^{\text{prev}} \hat{\mathbf{h}}_{\text{prior}} \right). \tag{4.13}$$

Figure 4.28 shows the ray density maps from 28 February to 24 March, illustrating the ray coverage and, consequently, the resolving power for each day. The corresponding tomographic inversion results are presented in Figure 4.29, and a detailed analysis of these results is provided afterward.

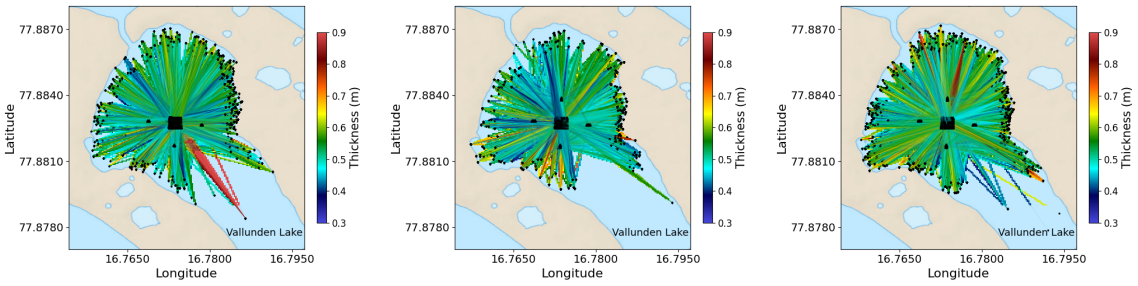

28 Feb 1 Mar 2 Mar

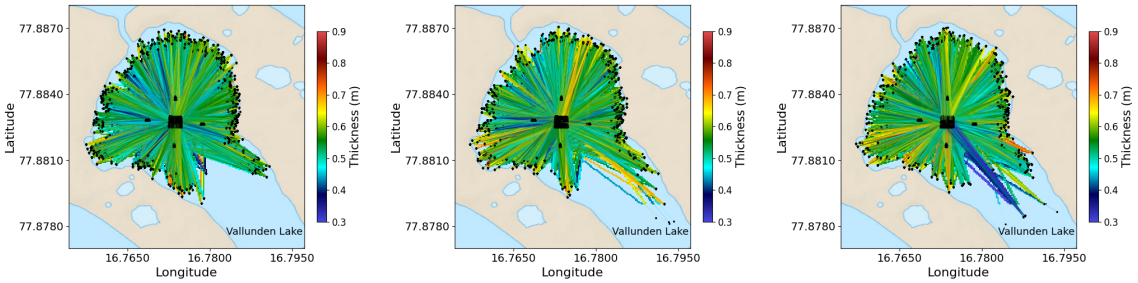

3 Mar 4 Mar 5 Mar

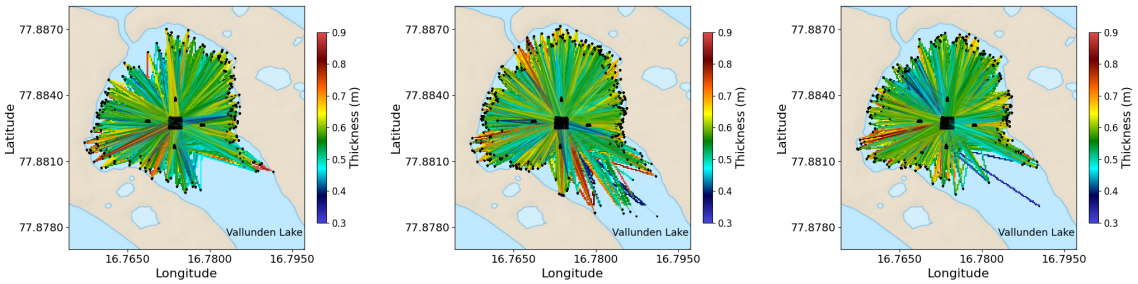

6 Mar 7 Mar 8 Mar

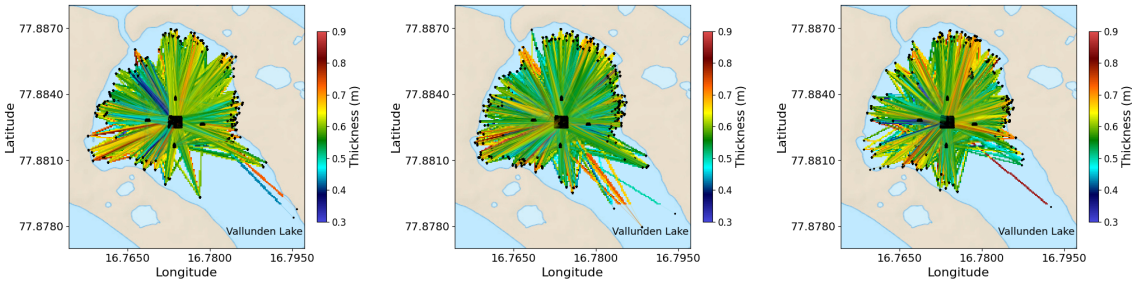

9 Mar 10 Mar 11 Mar

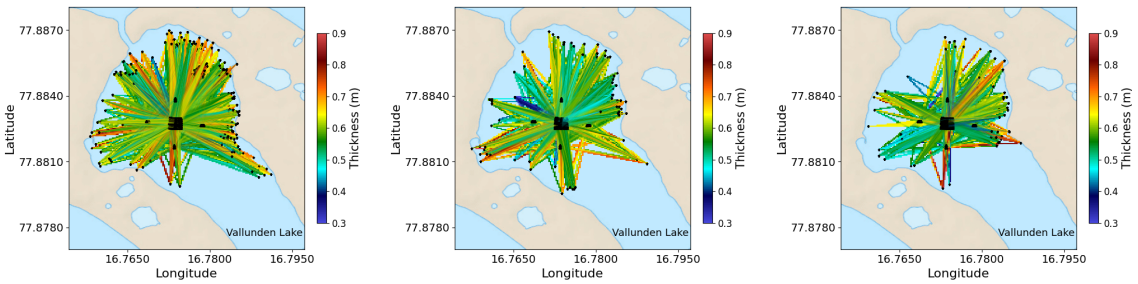

12 Mar 13 Mar 14 Mar

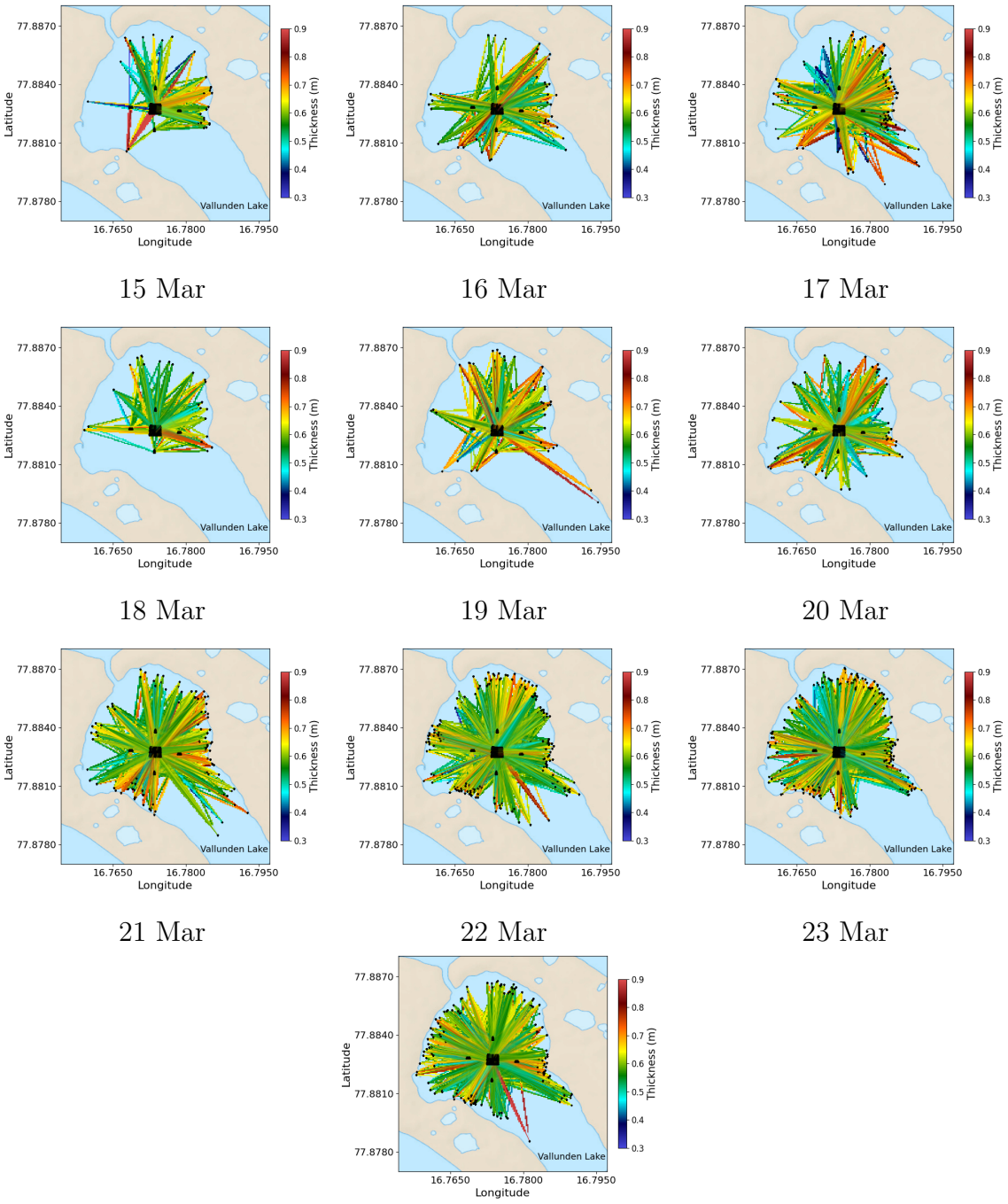

Figure 4.28: Path density maps for different days.

Figure 4.29 represents the tomography results obtained between 28 February and 24 March, using regularization parameters $\alpha = 0.015$ and $\beta = 0.12$.

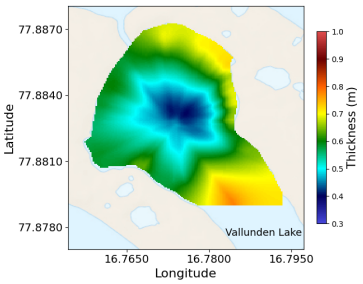

28 Feb

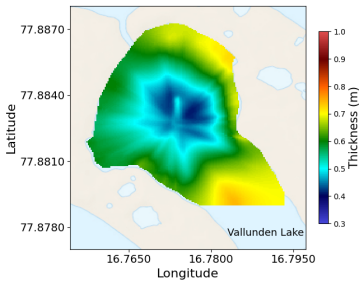

1 Mar

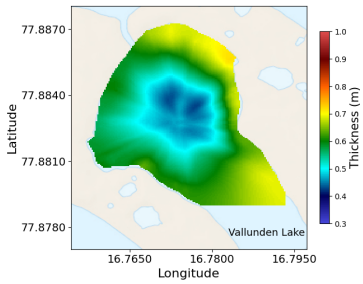

2 Mar

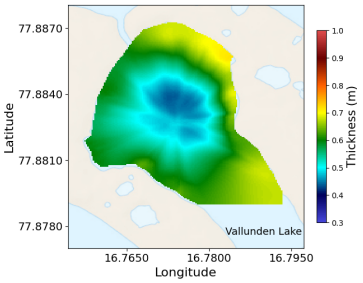

3 Mar

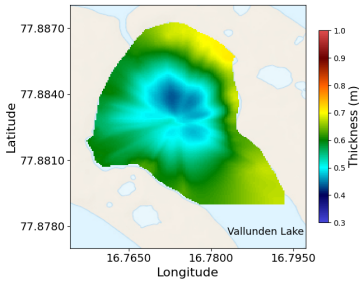

4 Mar

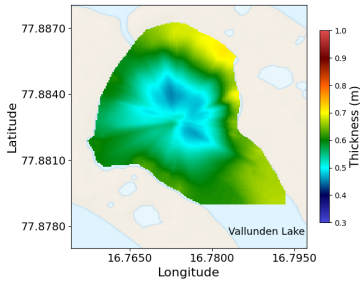

5 Mar

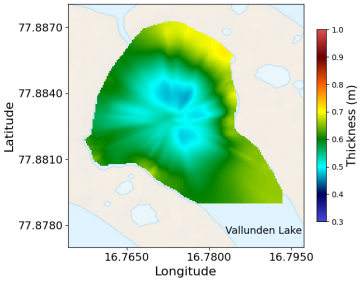

6 Mar

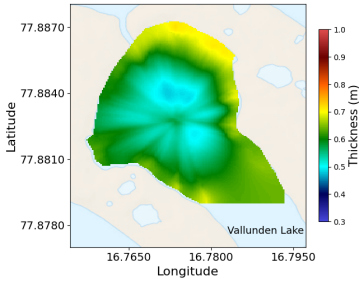

7 Mar

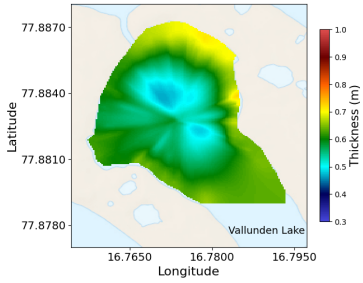

8 Mar

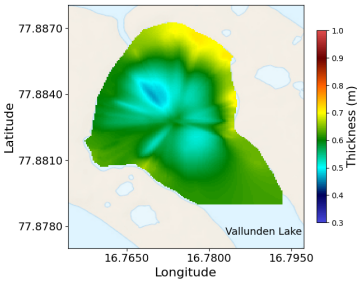

9 Mar

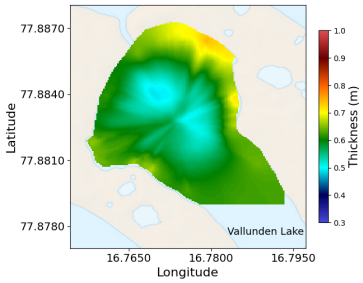

10 Mar

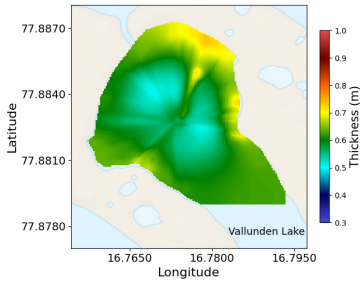

11 Mar

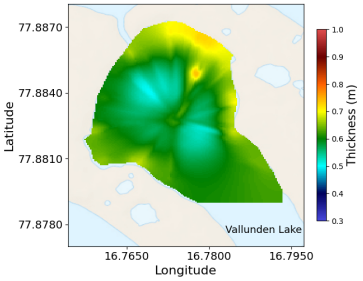

12 Mar

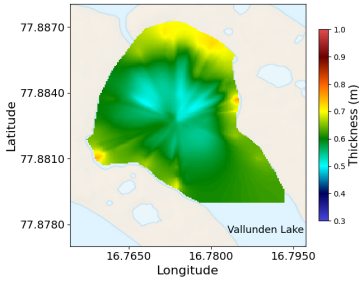

13 Mar

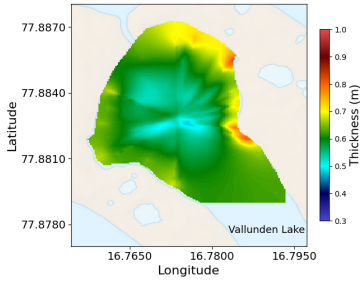

14 Mar

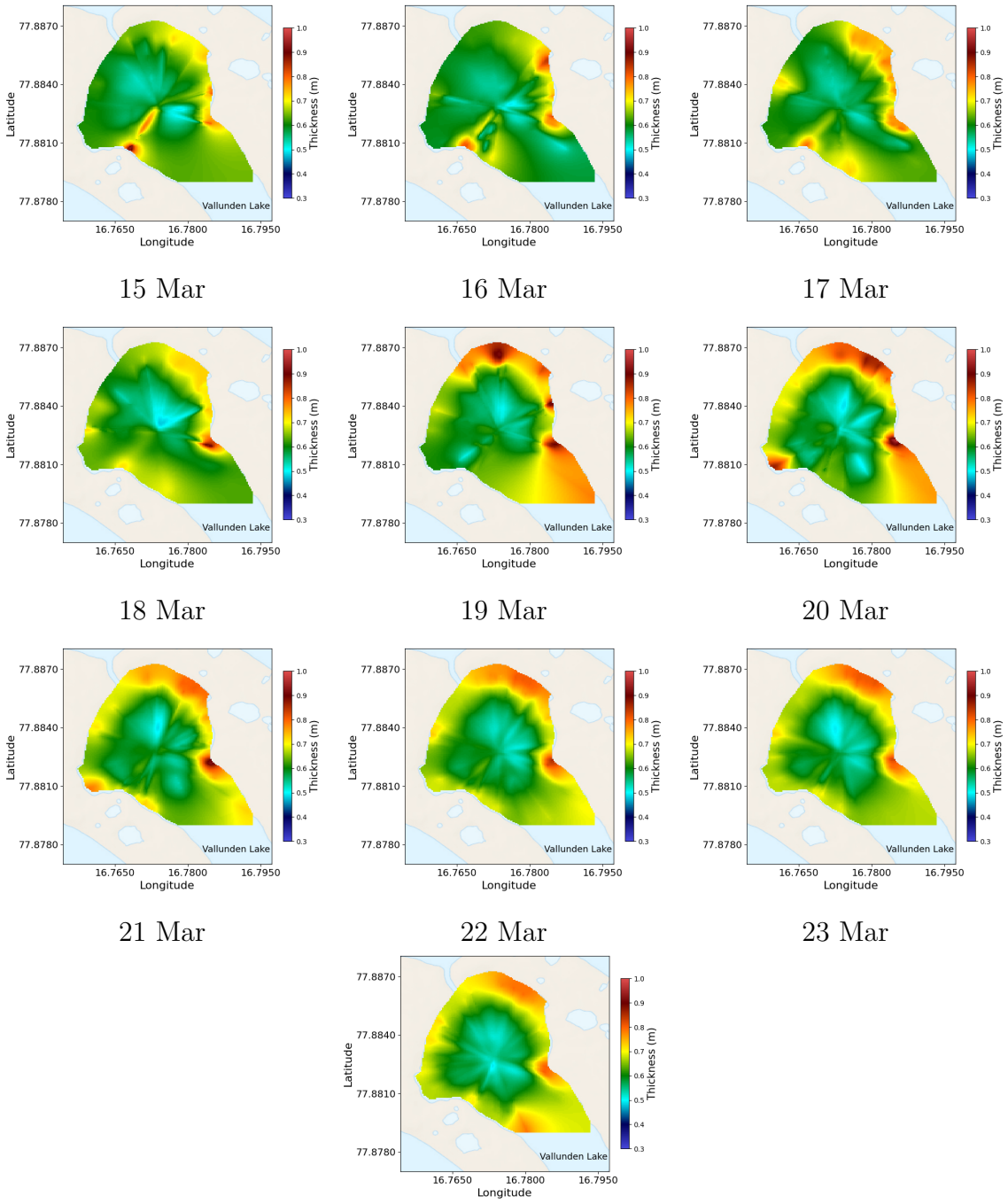

Figure 4.29: Tomography results for different days.

Results and Discussion

This dataset has been extensively used in previous studies focusing on passive seismic monitoring of sea ice. In Moreau et al. (2020a), passive seismology and array processing were applied to retrieve multimodal dispersion curves, which yielded ice thickness estimates of 54–58 cm for 1 and 5 March, in agreement with field measurements. In a subsequent study, Moreau et al. (2020b) demonstrated that instrumen-

tation requirements could be drastically reduced by using only 3–5 geophones. By combining noise interferometry with Bayesian inversion of icequake waveforms, they reported an increase in ice thickness from approximately 55 cm at the beginning of March to about 65 cm near the end of the month. Building on these findings, Serripierri et al. (2021) analyzed 24 days of continuous recordings from the same array and developed a passive seismic method for daily monitoring of ice properties. Their results, obtained through interferometry, array processing, and Bayesian inversion, revealed elastic properties and a progressive increase in ice thickness from ∼55 cm to ∼66 cm, once again matching in-situ observations. More recently, Moreau et al. (2023) proposed an automated workflow based on deep learning and Bayesian inversion of icequakes, showing a 15 cm increase in ice thickness over four weeks and capturing both temporal and spatial thickness variability.

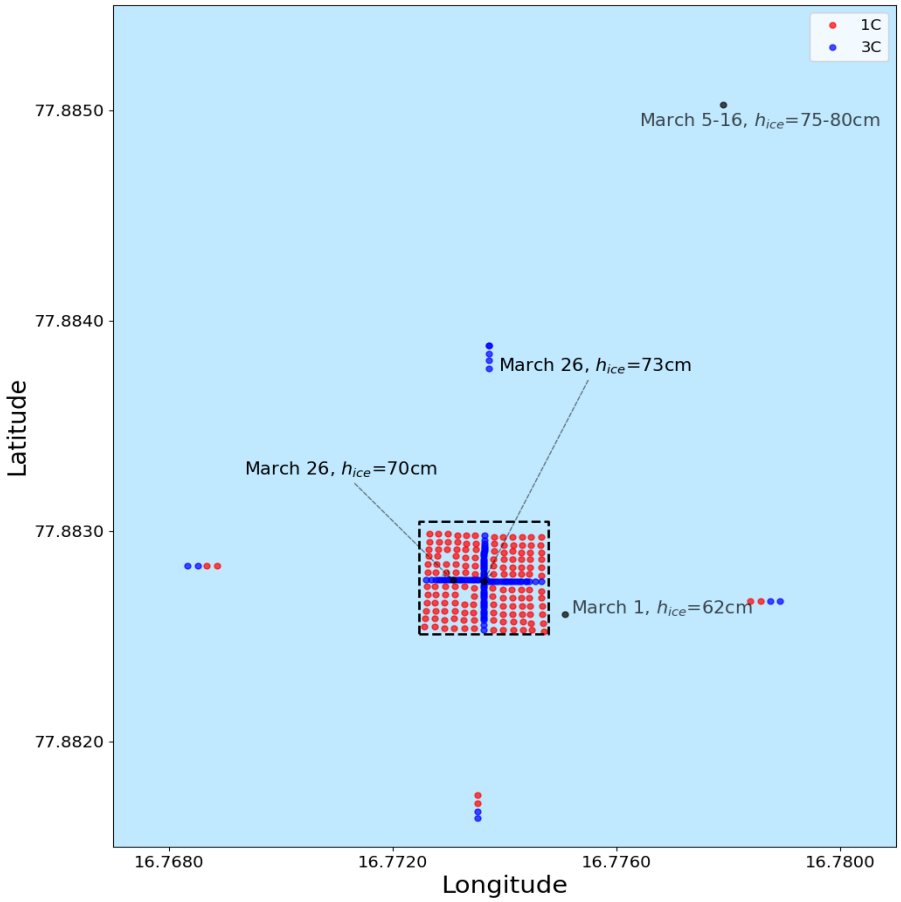

Figure 4.30: Map of receivers and selected field observations from Moreau et al. (2020a) and Marchenko et al. (2021). The dashed box indicates the area used to compute the average ice thickness for comparison with previous studies. Black filled circles show the field observations.

Examining the daily thickness maps shown in Figure 4.29, the first key observation is a consistent spatial pattern: ice thickness is greater near the shorelines and thinner toward the lake center. This pattern, which varies on the order of several tens of centimeters, remains stable throughout the observation period. It aligns well

with the lake's bathymetry and expected thermodynamic processes, as shallower water near the shore limits convective heat transfer from the water column, promoting more efficient cooling and enhanced ice growth.

A second key observation concerns temporal variations in ice thickness over the 25-day period. These changes are primarily driven by local temperature fluctuations. Early March experienced particularly low surface temperatures, dropping below $-30°C$ on 6 and 8 March, which promoted active ice growth. This period coincided with a peak in shoreline icequake activity, driven by mechanical stress from thermal expansion/contraction and tidal forcing. As shown in Figure 3.17 and reported by Moreau et al. (2023), these icequakes are temperature-dependent and exhibit dominant horizontal energy, consistent with traction and compression mechanisms induced by thermomechanical forcing. Later in the month, as temperatures increased, both icequake activity and ice thickening rates decreased, underscoring the dominant role of thermal stress in controlling ice growth and icequake activity.

A secondary but noteworthy effect relates to the influence of tidal currents. As discussed by Marchenko et al. (2021), the transport of frazil ice and slush beneath the ice cover can lead to preferential ice accretion along the margins. This mechanism is especially evident in the northern channel, where Vallunden Lake connects to Van Mijenfjorden via a narrow (10 m wide) tidal passage. In this region, we consistently observe higher ice thicknesses, likely resulting from tidal currents enhancing ice accretion—an effect that supplements the primary thermodynamic growth. By mid-March, however, this channel closes, eliminating current-driven accretion. Notably, this closure also contributes to reduced icequake activity, as tidal forcing is one of the key mechanisms generating seismic events, alongside other sources such as wind and thermal stress. Thus, the combined effects of rising temperatures and the cessation of tidal currents explain the observed decrease in both ice growth and icequake activity later in the observation period. In contrast, the southern region of the lake is characterized by sparser ray coverage, leading to higher inversion uncertainty and limiting the resolution of small-scale features there.

We now turn to a quantitative comparison with independent field measurements and previous studies to assess the reliability of our thickness estimates. From Figure 4.30, we can see that on 1 March, tomography estimates a thickness of approximately 48 cm within the array, whereas field measurements report around 62 cm near the same area. On 26 March, tomography indicates a thickness of about 58 cm inside the array, compared to field observations of roughly 70 cm. This consistent offset reflects a systematic bias: drillings capture the full physical ice column, including the porous, slushy basal layer, whereas tomography resolves only the effective elastic thickness that governs flexural wave propagation. Additionally, field observations (see Marchenko et al. (2021)) for the period 5–16 March indicate ice thicknesses of 75–80 cm in the northeastern part of the lake. Our analysis indicates a gradual increase from approximately 60 to 70 cm in this region, except on 11 and 12 March, when thickness estimates reach 75 cm, respectively. These two days correspond to 75 icequakes likely induced by the presence and activities of the research team in this area, producing denser ray coverage and consequently higher-resolution thickness estimates that closely match the field observations (Marchenko et al., 2021).

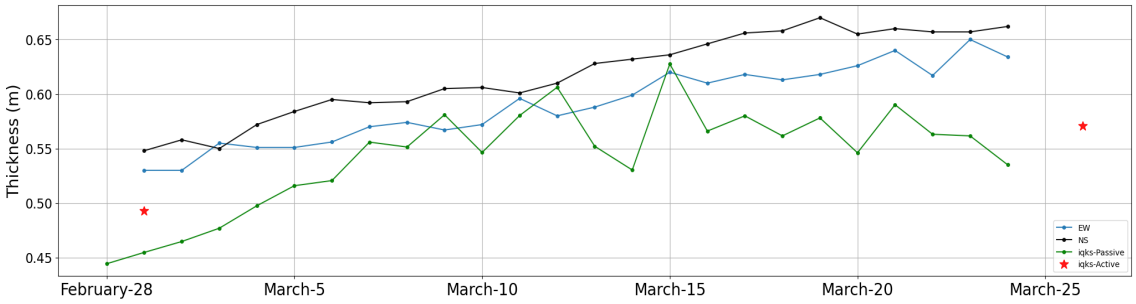

Figure 4.31: Evolution of ice thickness in the dense array area. Red stars indicate results from two active-source experiments. Black and blue lines show the results from Serripierri et al. (2021) along the east–west (ES) and north–south (NS) directions of the 3C receivers in the dense array, while our results represent the average ice thickness of all cells within this region (see Figure 4.30).

To illustrate variations in ice thickness and the previously reported increasing trend, we computed the average ice thickness within the dense array region (dashed box in Figure 4.30) for different days and compared these values with independent measurements. The temporal evolution of ice thickness in this region is summarized in Figure 4.31, which also includes two active-source measurements for reference. For further comparison, estimates from Serripierri et al. (2021), derived from multimodal dispersion curves using noise interferometry within the same area, are overlaid.

Both Serripieri's estimates and our inversion results indicate a clear increase in ice thickness during the low-temperature period at the beginning of March, followed by a marked reduction in growth as temperatures rise. This temporal evolution is consistent with the broader patterns observed in the tomographic maps (Figure 4.29), where ice thickening of around 10-15 centimeters is observed between late February and mid-March, before stabilizing during the second half of the month. The decrease in growth coincides with increasing air temperatures, which reduce the thermal gradient driving ice formation.

Despite the overall agreement in temporal trends, our inversion results generally yield lower thickness values at the beginning and end of the survey period, while converging toward similar values in mid-March. This discrepancy can be attributed in part to methodological differences: we use spectral-element method (SEM) simulations for forward modeling, whereas Serripierri et al. (2021) relied on asymptotic solutions. In addition, the spatial sensitivity of the two approaches differs. Our inversion primarily samples wave paths that originate near the lake margins and propagate over longer distances, whereas their estimates are mainly constrained by wavefields traveling within the central array. As a result, our measurements may be more strongly influenced by the paths, though the impact of this spatial sensitivity is not yet fully understood and requires further study.

The impact of data coverage is also evident in the temporal fluctuations of our estimates. Days with fewer detected icequakes—and consequently lower ray-path density—exhibit larger apparent variations in thickness (see Figure 4.28). These fluctuations likely reflect reduced spatial sampling. Conversely, periods with high seismic activity, such as early March, provide dense ray coverage and more robust, spatially resolved thickness estimates. The incorporation of prior information from

previous days further helps stabilize the inversion and maintain temporal consistency during periods of sparse data.

Overall, the tomographic results successfully reproduce both the temporal evolution and spatial variability of ice thickness reported in previous studies. Although the absolute thickness values are slightly lower than those obtained from field observations, the method captures the key physical patterns. These findings highlight the robustness of passive-source tomography and reinforce its potential as a reliable tool for long-term monitoring of sea ice evolution, particularly in environments where conventional measurements are sparse or logistically challenging.

4.5 Perspectives

In this section, we explore two cases. The first examines ice thickness tomography under practical constraints, focusing on how reducing the number of stations impacts tomographic resolution. We then investigate how an optimized spatial configuration of these stations can improve resolution. This analysis uses the source–receiver configuration from Svalbard. The second case considers the applicability of adaptive meshes for thickness tomography. Here, we explore adaptive mesh strategies for model parameterization that account for data coverage, aiming to improve stability and resolution while maintaining computational efficiency. For this part, we employ the source–receiver configuration from the 2024 dataset in Quebec, Canada.

4.5.1 Impacts of the Number and Configuration of Stations

We explore the feasibility of performing sea ice tomography with a limited number of stations. In our case, we use five stations—the same ones employed for icequake localization in Section 3.4—and consider all possible source–receiver paths.

For 383 events recorded on 28 February, this configuration yields 1888 valid paths (out of 1915 total). A few paths are excluded because the source–receiver distances exceed 620 m, which is the maximum distance existed in our SEM database.

We perform a checkerboard test using an 8×8 pattern, with each cell approximately 108 m in size. The regularization parameters are set to $\alpha = 0$ and $\beta = 0.01$. The synthetic model and corresponding ray paths are shown in Figures 4.32(a) and (b), respectively.

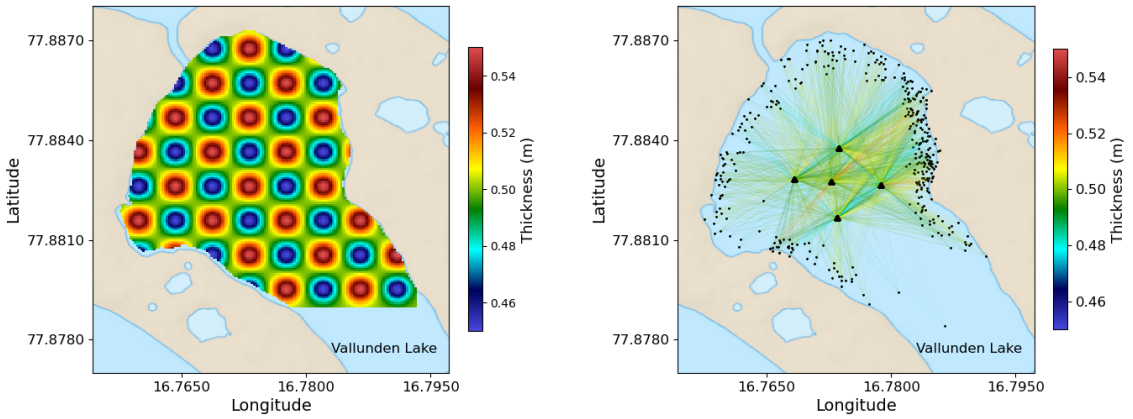

(a) (b)

Figure 4.32: Checkerboard test with an 8×8 pattern (cell size $\sim$ 108 m): (a) synthetic model and (b) corresponding ray paths.

The tomographic reconstruction for this configuration is presented in Figure 4.33(b). As shown, the resulting model closely resembles the one obtained using all available stations for the same day (Figure 4.33(a)), demonstrating that tomography can be effectively performed with a reduced number of stations.

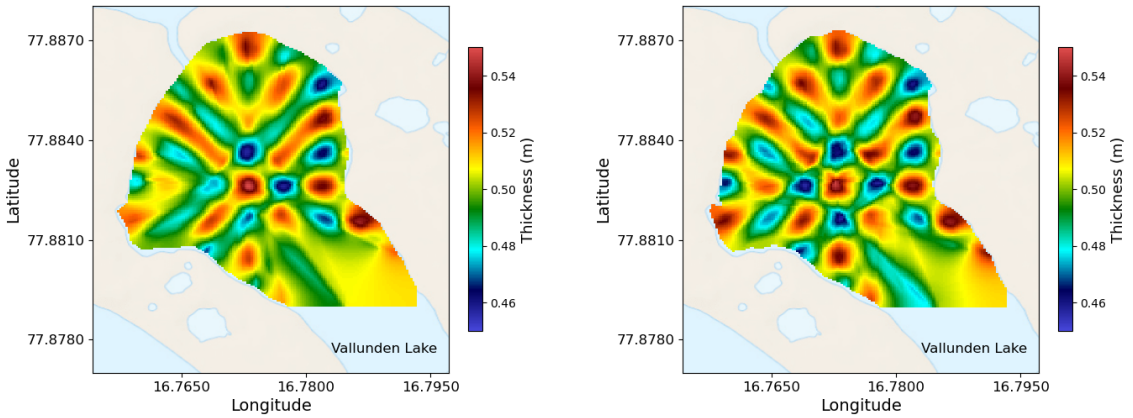

(a) (b)

Figure 4.33: Tomographic results of the checkerboard test: (a) using all stations on 28 February (see Figure 4.28), and (b) using five stations (Figure 4.32(b)).

Next, we investigate how station configuration affects the tomographic results. In this test, we keep the central station fixed and move the remaining stations toward the shoreline of the lake, which increases the number of ray crossings and overall coverage. Here there are 1743 paths (Figure 4.34(a)), and the corresponding tomographic reconstruction (Figure 4.34(b)) shows a clear improvement in resolution, particularly near the lake edges. These findings highlight the importance of station layout and have practical implications for designing future tomographic experiments.

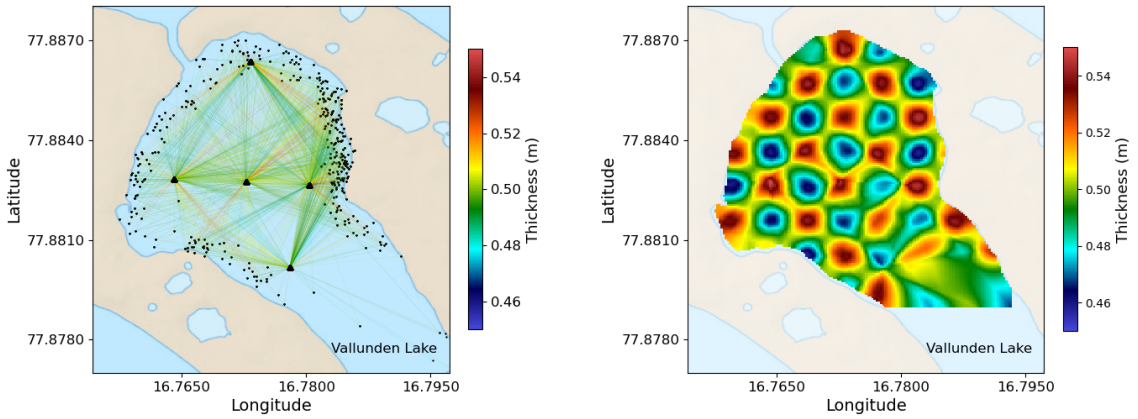

(a) (b)

Figure 4.34: (a) Ray paths for the optimized station configuration. (b) Tomographic result obtained using the optimized configuration.

As observed in Figure 4.29, the tomographic models generally show an increase in ice thickness toward the shoreline. To test whether our ray coverage can reproduce this pattern, we conduct another synthetic experiment in which the tomographic model from 10 March serves as the true model (Figure 4.35). We then perform inversions using (i) the five-station configuration shown in Figure 4.33(b), and (ii) the optimized configuration shown in Figure 4.34(a).

In both cases, we use the ice thickness data from 28 February. Here $\beta = 0.12$, consistent with the inversion results shown in Figure 4.29, while no prior model is applied ($\alpha = 0$).

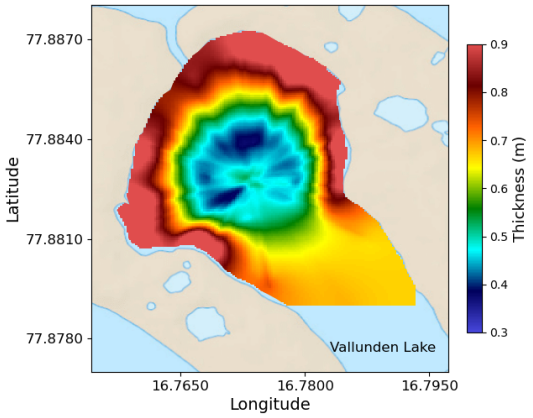

Figure 4.35: True model used in the synthetic test, based on the 10 March tomographic result.

Figure 4.36 compares the results. The inversion using five stations (Figure 4.36(a)) successfully recovers the main ice-thickness pattern, albeit with smoother variations. In contrast, the optimized configuration (Figure 4.36(b)) yields a noticeably improved result, further emphasizing the importance of station configuration in enhancing tomographic resolution.

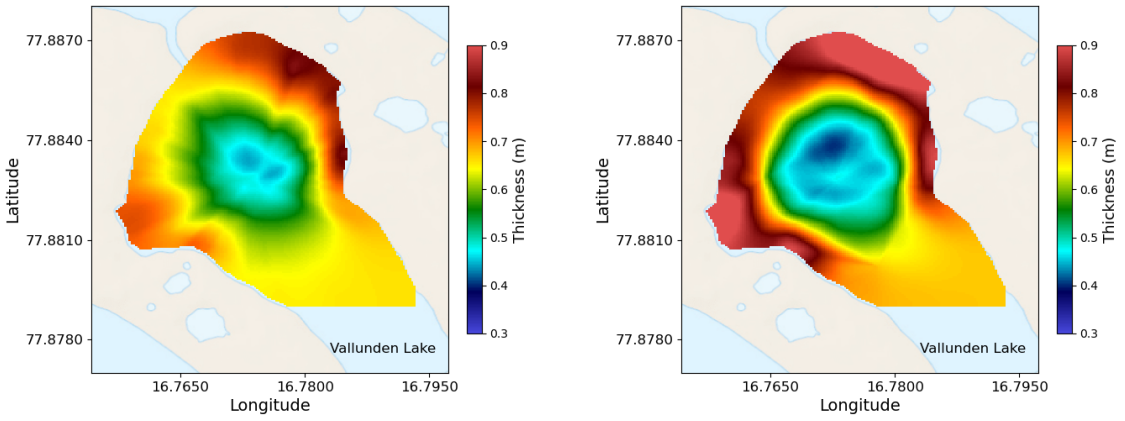

(a) (b)

Figure 4.36: (a) Tomography result for the five-station configuration shown in Figure 4.33(b), and (b) tomography result for the optimized configuration shown in Figure 4.34(a).

4.5.2 Adaptive Mesh Stratgey

In seismic tomography, the inverse problem is often unstable and rank-deficient because data coverage is uneven, leaving some model parameters unsampled (condition number of matrix **A** can be large as some cells do not have hits). To address this, adaptive techniques such as irregular meshes, tetrahedral or Voronoi-based cells, and multiscale (nested or overlapping) grids are used. These methods align model parameterization with data density, improving stability, conditioning, and spatial resolution while reducing the number of unknowns. Irregular meshes allow nodes to cluster in regions of rapid velocity change, tetrahedral cells can automatically adjust to match ray coverage, and multiscale grids provide fine detail where needed without overparameterizing the entire model. However, all three approaches have limitations: irregular meshes can complicate resolution testing, tetrahedral or adaptive methods can be computationally intensive, and multiscale grids may require careful integration of results from different scales. Overall, these techniques help produce more stable, data-consistent models but must be carefully designed and validated to avoid artifacts or unresolved features (Thurber; section 1.10.3.2)

In a tomography problem, due to the heterogeneous configuration of seismic sources and stations, some areas are over-sampled while others are under-sampled. Using a regular mesh, choosing a large grid reduces the resolving power in regions with dense ray coverage. Conversely, using a small mesh to enhance resolution in well-sampled areas leads to over-parameterization in sparsely sampled regions, which requires strong regularization. To mitigate over-parameterization while preserving the ability to resolve small-scale structures, we can use irregular cells for the inverse problem (Bijwaard et al., 1998). By considering the hit count (the number of rays in each cell) and the azimuthal coverage of rays, an adaptive mesh can be created based on the data (Schaefer et al., 2011).

Both in regular and adaptive formulations, the gradients of the model parameters in the x- and y-directions are computed using a forward difference scheme. The

discrete operator can be interpreted as a generalization of the simple forward–Euler approximation of a first–order derivative. In the adaptive case, where a cell may have multiple neighbours, the contribution of each neighbour is weighted by its shared length with the cell and normalized by the average distance.

In the classical case, the derivative at a cell i is approximated by subtracting the value of the right neighbour from the value at i and dividing by the grid spacing. Here, this idea is extended to irregular grids with multiple right–hand neighbours. Instead of a single neighbour, a weighted average of all neighbours in the forward stencil is taken. The weights are proportional to the shared interface length s_{ij} between cell i and neighbour j, normalized by the total interface length $S_i = \sum_{k\in\mathcal{N}(i)} s_{ik}$. Thus the numerator replaces the classical "$h_j - h_i$" with $\sum_{j\in\mathcal{N}(i)} w_{ij}\hat{h}_j - \hat{h}_i$, where $w_{ij} = s_{ij}/S_i$. Finally, the result is normalized by the mean distance between cell i and its neighbours, so that the denominator reflects the average spacing in the irregular grid.

$$\mathbf{D}_x\hat{\mathbf{h}} \;=\; C^{(x)}\big(W^{(x)} - I\big)\,\hat{\mathbf{h}}, \qquad \mathbf{D}_x\hat{\mathbf{h}} \;=\; C^{(y)}\big(W^{(y)} - I\big)\,\hat{\mathbf{h}}, \tag{4.14}$$

$$(\mathbf{D}_x)_{ij} = c_i^{(x)}\big(W_{ij}^{(x)} - \delta_{ij}\big), \qquad (\mathbf{D}_y)_{ij} = c_i^{(y)}\big(W_{ij}^{(y)} - \delta_{ij}\big), \tag{4.15}$$

$$c_i^{(x)} = \frac{n_i^{(x)}}{\sum\limits_{k\in\mathcal{N}_x(i)} \Delta x_{ik}}, \qquad c_i^{(y)} = \frac{n_i^{(y)}}{\sum\limits_{k\in\mathcal{N}_y(i)} \Delta y_{ik}}, \tag{4.16}$$

$$W_{ij}^{(x)} = \begin{cases} \dfrac{s_{ij}^{(x)}}{\sum\limits_{k\in\mathcal{N}_x(i)} s_{ik}^{(x)}}, & j \in \mathcal{N}_x(i), \\ 0, & \text{otherwise}, \end{cases} \qquad W_{ij}^{(y)} = \begin{cases} \dfrac{s_{ij}^{(y)}}{\sum\limits_{k\in\mathcal{N}_y(i)} s_{ik}^{(y)}}, & j \in \mathcal{N}_y(i), \\ 0, & \text{otherwise}. \end{cases} \tag{4.17}$$

Here, $\hat{\mathbf{h}}$ is the vector of unknowns, $W^{(x)}$ and $W^{(y)}$ are the neighbour weight matrices, and I is the identity matrix. The diagonal matrices $C^{(x)}$ and $C^{(y)}$ contain the row–wise scaling factors $c_i^{(x)}$, $c_i^{(y)}$, which normalize by the mean neighbour distances. The weights W_{ij} are defined from the interface lengths s_{ij} so that each neighbour contributes proportionally to its contact with cell i. The Kronecker delta δ_{ij} subtracts the self–term $\hat{h}_i$. This construction reduces to the standard forward–Euler difference on a uniform grid with a single neighbour, while remaining consistent for irregular grids with multiple neighbours of different sizes.

While Equation 4.14 provides a general formulation for computing derivatives on rectangular grids, we illustrate it below using the simple case of square cells.

In Example 1, the central cell (where the derivative is computed) has a right-hand neighbour of the same size, so the shared length between them equals the cell size. Consequently, the weight assigned to this neighbour is 1.

In Example 2, the smallest cell has a size equal to one-fourth of the largest cells. Therefore, the shared length between the smallest cell and its right-hand neighbour is 1/4 of the full cell size, giving it a weight of 1/4. The medium-size neighbour (the second smallest cell) shares half the length with the central cell and thus receives a weight of 1/2.

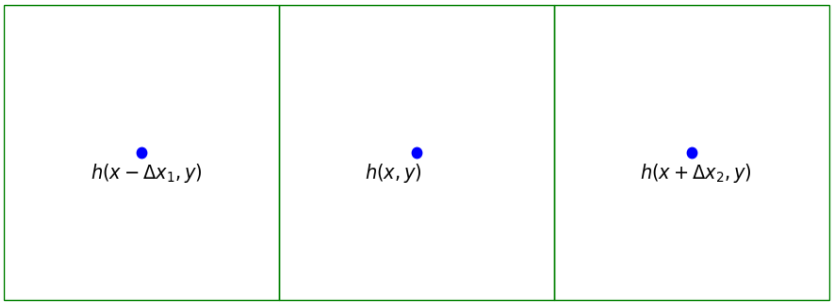

Figure 4.37: Example 1.

In Example 1, the gradient of model with respect to x is obtained as follows:

$$\nabla_x \hat{h}(x,y) = \frac{\hat{h}(x+\Delta x_2, y) - \hat{h}(x,y)}{\Delta x_2},$$

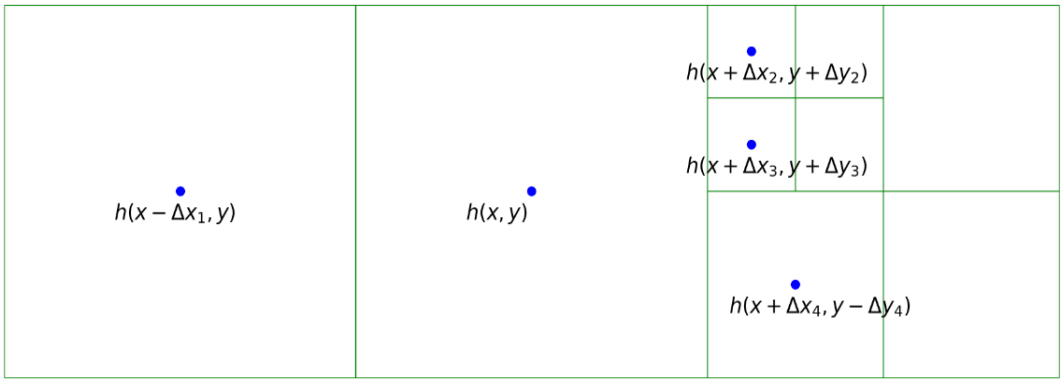

Figure 4.38: Example 2.

In Example 2, the gradient of model with respect to x is obtained as follows:

$$\nabla_x \hat{h}(x,y) = \frac{\frac{1}{4}\,\hat{h}(x+\Delta x_2, y+\Delta y_2) + \frac{1}{4}\,\hat{h}(x+\Delta x_3, y+\Delta y_3) + \frac{1}{2}\,\hat{h}(x+\Delta x_4, y-\Delta y_4) - \hat{h}(x,y)}{\frac{\Delta x_2+\Delta x_3+\Delta x_4}{3}}.$$

Example

Given the dataset shown in Figure 4.10 (left), which includes 336 source–receiver paths, we present three examples to compare the grids and tomography results for a simple case of a 4×4 checkerboard model. In the following examples, the regularization parameters are identical to those used in Figure 4.9.

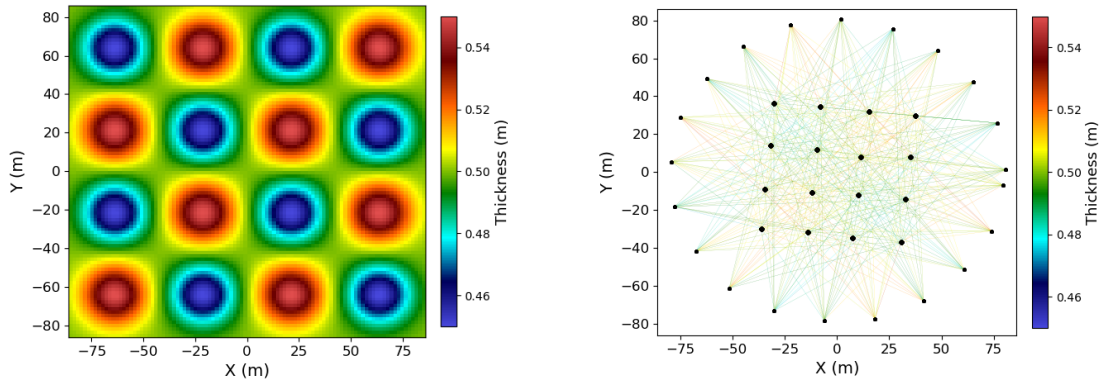

(a) 4×4 checkerboard model (b) Ray Paths

Figure 4.39: The checkerboard model (a) and ray paths (b).

The checkerboard model, projected onto the regular mesh in Figure 4.39:(a), is used to generate observed data (thicknesses along different paths), as shown in Figure 4.39:(b). These observations are employed in all the following examples, which include both regular and adaptive meshes. In all cases, we set $\alpha = 0$ and $\beta = 1 \times 10^{-4}$.

For the regular case, the grid consists of cells of size 1.72 m, resulting in a total of 10,000 cells. Figure 4.40(a) illustrates the mesh, while Figure 4.40(b) presents the corresponding tomographic inversion. These results are shown for comparison with those obtained using the adaptive mesh strategy.

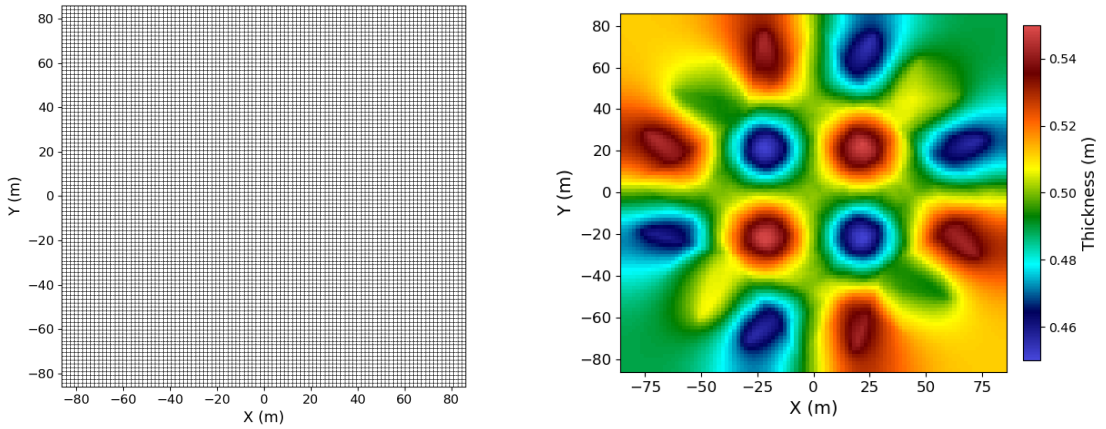

(a) Regular Mesh (b) Inverted Model

Figure 4.40: Regular grid case.

Next, we provide two examples of adaptive meshing. In both cases, we start with a 10 × 10 grid and set a minimum cell size of 1.72 m. Cells are not further divided if they are already at this minimum size; otherwise, subdivision continues until the refinement criteria are no longer satisfied.

In the first adaptive case, only hit count is considered: cells are subdivided if at least 10 rays pass through them. This produces cells as small as 1.075 m (see Figure 4.41). Here the number of cells is 2638.

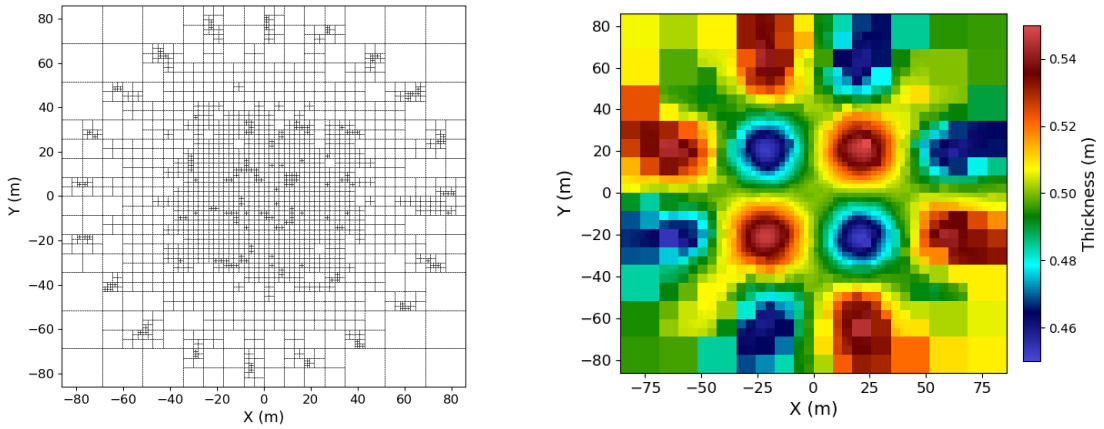

(a) Adaptive Mesh (b) Inverted Model

Figure 4.41: Adaptive grid based on hit count only.

In the second adaptive case, both hit count (again set to 10) and azimuthal coverage are considered. Here, a cell is subdivided only if hit count is at least 10 and rays pass through at least three out of four azimuthal quadrants. This results in even fewer subdivided cells (see Figure 4.42). Here the number of cells is 2167.

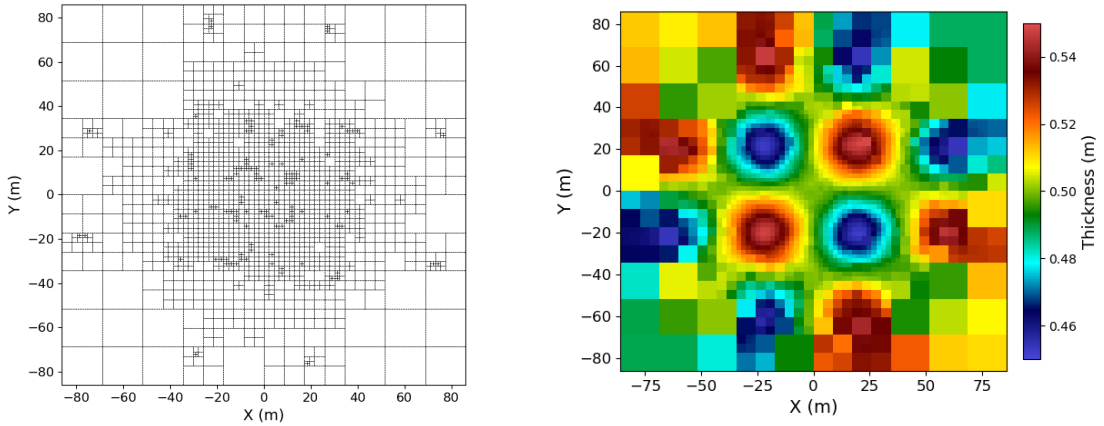

(a) Adaptive Mesh (b) Inverted Model

Figure 4.42: Adaptive grid based on hit count and azimuthal coverage.

As shown in Figures 4.41(a) and 4.42(a), adaptive meshing greatly reduces the number of cells, preventing over-parameterization in regions with sparse ray coverage. However, boundary effects in the inversion results of Figures 4.41(b) and 4.42(b) appear at the interfaces between small and large cells. These artifacts become more pronounced when the difference in cell size is large. To avoid such artificial effects,

we opted to use regular cells for our inversions. Nevertheless, exploring strategies to mitigate these boundary effects and determining the optimal ratio between the largest and smallest cell sizes remain subjects for future work.

CHAPTER 5

CONCLUSIONS AND PERSPECTIVES

Contents

5.1 Conclusions 125

5.2 Perspectives 126

5.2.1 Technical Refinements and Expanded Inversions 126

5.2.2 Applications and Integration 127

This thesis has developed and validated a comprehensive framework for reconstructing sea ice thickness with high spatial and temporal resolution. By integrating numerical modeling with robust inversion and tomographic techniques, this work provides a novel tool for monitoring climate-driven changes in sea ice. This chapter summarizes the key conclusions and outlines promising directions for future research.

5.1 Conclusions

Chapter 1 highlights the importance of sea ice for climate, ecosystems, and human activities, reviewing its recent decline in extent and thickness and the resulting environmental impacts. It presents methods for measuring and monitoring ice, from satellites and field campaigns to high-resolution seismic techniques. Special emphasis is placed on seismic approaches as an efficient alternative for small-scale monitoring, supported through a literature review. The chapter also underscores the importance of passive seismic monitoring for long-term, continuous observation, offering a cost-effective and low-impact approach that enables tracking temporal changes and spatial variability without the need for expensive active-source campaigns.

Chapter 2 addressed the fundamental need for an accurate forward model of seismic wave propagation in sea ice. It demonstrated that while asymptotic solutions are computationally efficient, they systematically deviate from true solutions at higher frequencies and for thicker ice, introducing significant biases in subsequent inversions. The Spectral Element Method (SEM) was successfully implemented

and validated against analytical solutions, proving its high accuracy in reproducing flexural wave dispersion curves. Beyond homogeneous media, SEM showcased its capability to handle realistic complexities such as snow cover and spatially varying ice thickness, establishing it as an efficient forward modeling tool for this study and future investigations.

Chapter 3 focused on the key challenge of estimating unknown parameters—specifically, icequake locations and ice thickness along source–receiver paths—using passive seismic data. To address this, we developed a novel three-step inversion strategy that leverages the strengths of two cost functions. The STFT-based cost provides a smooth misfit landscape, enabling efficient global exploration via simulated annealing (SA), while the zero-lag correlation cost is highly sensitive to waveform alignment, allowing precise local refinement of parameter estimates. Validated with synthetic tests, the method was successfully applied to the Svalbard dataset, locating icequakes and revealing their concentration along the shoreline—a pattern consistent with thermomechanical forcing from tidal and temperature variations.

Chapter 4 developed a comprehensive framework for tomographic reconstruction of sea ice thickness, validated through synthetic tests including resolution and uncertainty analysis. The methodology was then applied to field datasets from two distinct regions. For the active-source experiments in Québec, the resulting ice thickness maps showed good agreement with field and drilling observations. In Svalbard, the passive-source dataset enabled reconstruction of both the spatial pattern of ice thickness—showing thinner ice in the center and thicker ice at the edges—and its daily temporal evolution over a 25-day period. The observed patterns are consistent with hydro-thermodynamic processes, including tidal forcing and temperature variations.

Additional synthetic tests explored the use of a reduced number of stations in optimal configurations, as well as the implementation of adaptive mesh refinement. These experiments showed that even with a limited number of optimally positioned stations, high-quality reconstructions of ice thickness can be achieved. Adaptive mesh refinement also shows promise for improving computational efficiency, though further investigation is needed to fully optimize its use—particularly to address boundary effects that arise when very large cells meet much smaller ones.

5.2 Perspectives

The methodologies developed in this thesis open numerous avenues for future research, through technical refinements, expanded applications, and contributions to major scientific projects.

5.2.1 Technical Refinements and Expanded Inversions

- The SEM framework can be extended to incorporate more realistic physics, including viscoelasticity and anisotropy, which will more accurately represent the true mechanical behavior of sea ice, especially in deformed or partially consolidated ice. Heterogeneities such as evolved snow layers, which can affect waveform dispersion, can also be incorporated.

- SEM databases can be expanded to include not only ice thickness but also elastic parameters, such as Young's modulus and Poisson's ratio, allowing the inversion to simultaneously retrieve spatial maps of both thickness and mechanical properties. This is a critical step toward a more complete mechanical characterization of the ice sheet.

- The icequake catalog and synthetic database generated in this thesis are ideal for applications such as training Convolutional Neural Networks (CNNs). A CNN could learn to directly map seismic waveforms to source location, ice thickness, and elastic constants, potentially enhancing inversion speed and enabling real-time monitoring.

- The promising results with reduced station networks in optimal configurations and adaptive meshing require further investigation.

- One possible next step in methodological evolution is 3D FWI. Using 3C recordings and 3D SEM modeling, FWI could exploit the full information content of seismic waveforms (amplitudes and phases) to jointly invert for source parameters, 3D ice thickness with more realistic ice profiles, and 3D elastic parameters. While computationally demanding, this approach could be pursued in future seismic imaging studies.

5.2.2 Applications and Integration

- The proposed extension to simultaneous thickness and Young's modulus tomography aligns with the goals of the ANR project MSIM (see Section 1.3.1). By providing high-resolution maps of mechanical properties, this methodology can help answer key questions: Where does the ice break first under ocean wave forcing? What is the critical wave amplitude required for break-up? These insights are crucial for validating and improving wave–ice interaction models.

- The capability to provide dense, spatially resolved maps of ice thickness and mechanical properties is crucial for large-scale initiatives such as the SASIP project (The Scale-Aware Sea Ice Project). These high-resolution datasets enable testing and validation of new dynamic–thermodynamic sea ice models, linking local measurements of ice structure and mechanical behavior to broader pan-Arctic simulations.

- The tomographic method is not limited to sea ice but can also be applied to lake ice and different types of datasets, including geophones, Distributed Acoustic Sensing (DAS), and microphones. DAS, with its dense spatial sampling, could revolutionize the resolution of ice thickness maps.

APPENDIX A

ZERO-LAG CORRELATION IN THE FREQUENCY DOMAIN

We use the Fourier transform:

$$X(\omega) = \int_{-\infty}^{\infty} x(t)\, e^{-j\omega t}\, dt, \qquad x(t) = \frac{1}{2\pi} \int_{-\infty}^{\infty} X(\omega)\, e^{j\omega t}\, d\omega$$

Let the cross-correlation be:

$$r_{xy}(\tau) \;=\; \int_{-\infty}^{\infty} x(t)\, y^*(t-\tau)\, dt$$

The correlation theorem states:

$$r_{xy}(\tau) \;=\; \frac{1}{2\pi} \int_{-\infty}^{\infty} X(\omega)\, Y^*(\omega)\, e^{j\omega\tau}\, d\omega$$

Setting $\tau = 0$ gives the zero-lag value:

$$r_{xy}(0) \;=\; \frac{1}{2\pi} \int_{-\infty}^{\infty} X(\omega)\, Y^*(\omega)\, d\omega$$

In particular, for frequency-domain data $\tilde{D}_{\text{syn}}(\omega)$ and $D_{\text{obs}}(\omega)$ over a band Ω:

$$r(0) \;=\; \frac{1}{2\pi} \int_{\Omega} \tilde{D}_{\text{syn}}(\omega)\, \big(D_{\text{obs}}(\omega)\big)^*\, d\omega$$

and the normalized zero-lag correlation is written as:

$$\rho_0\Big(\tilde{D}_{\text{syn}}, D_{\text{obs}}\Big) = \frac{\displaystyle\int_{\Omega} \tilde{D}_{\text{syn}}(\omega)\, \big(D_{\text{obs}}(\omega)\big)^*\, d\omega}{\displaystyle\sqrt{\int_{\Omega} \Big|\tilde{D}_{\text{syn}}(\omega)\Big|^2\, d\omega}\, \sqrt{\int_{\Omega} |D_{\text{obs}}(\omega)|^2\, d\omega}}$$

For discrete frequencies, replace $\int_{\Omega}(\cdot)\, d\omega$ by $\sum_{\omega\in\Omega}(\cdot)\, \Delta\omega$.

The normalized zero-lag correlation between the spectrally weighted synthetic data and the observed data is real, as shown below. Let $D_{\text{obs}}(\omega) = A(\omega)e^{j\phi(\omega)}$ and $D_{\text{syn}}(\omega) = B(\omega)e^{j\psi(\omega)}$ with $A(\omega), B(\omega) \geq 0$. With the spectral weighting:

$$\tilde{D}_{\text{syn}}(\omega) = \frac{D_{\text{syn}}(\omega)\,|D_{\text{obs}}(\omega)|}{|D_{\text{syn}}(\omega)|} = A(\omega)e^{j\psi(\omega)}$$

the zero-lag correlation numerator becomes:

$$\mathcal{N} = \int_{\Omega} \tilde{D}_{\text{syn}}(\omega)\, D^{*}_{\text{obs}}(\omega)\, d\omega = \int_{\Omega} A(\omega)^2 e^{j(\psi(\omega)-\phi(\omega))}\, d\omega$$

For real time-domain signals, spectra are Hermitian: $A(-\omega) = A(\omega)$, $\psi(-\omega) = -\psi(\omega)$, $\phi(-\omega) = -\phi(\omega)$. Pairing ω and $-\omega$ over the symmetric band Ω yields:

$$A(\omega)^2 e^{j(\psi-\phi)} + A(\omega)^2 e^{-j(\psi-\phi)} = 2A(\omega)^2 \cos(\psi(\omega) - \phi(\omega)) \in \mathbb{R}$$

so all imaginary parts cancel and $\mathcal{N} \in \mathbb{R}$. The denominator of the normalized correlation is positive real, hence the normalized zero-lag correlation is also real.

APPENDIX B

SYNTHETIC TESTS IN SVALBARD

First, we perform a **checkerboard resolution test**. Starting from a synthetic model, we generate the observed data by applying the forward operator $\mathbf{A}$ to the model:

$$\mathbf{h}_{\text{obs}} = \mathbf{A}\hat{\mathbf{h}}_{\text{syn}}.$$

For this test, we use the ice thickness estimates from 28 February. The regularization parameters are set to $\alpha = 0$ and $\beta = 0.12$.

We begin with a 2×2 checkerboard pattern, where each cell has a size of approximately 432 m. The synthetic model $\hat{\mathbf{h}}_{\text{syn}}$ is shown in Figure B.1(a), while the corresponding ray paths generated from this model are presented in Figure B.1(b).

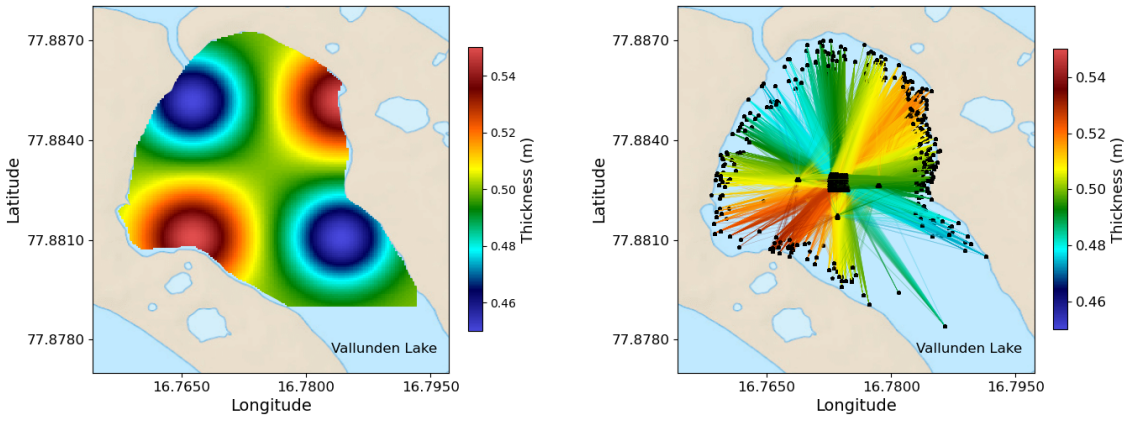

(a) (b)

Figure B.1: Checkerboard test with a 2×2 pattern (cell size $\sim$ 432 m): (a) synthetic model, (b) corresponding ray paths.

The result of the tomographic inversion for this case is shown in Figure B.2.

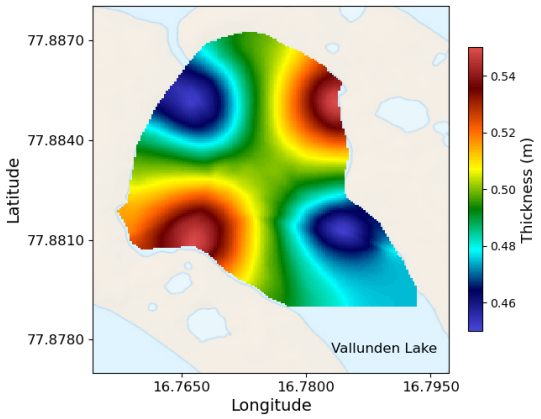

Figure B.2: Tomographic result of the checkerboard test with a 2×2 pattern (pattern size ∼ 432 m).

Second, we use a 4×4 checkerboard pattern, where each cell measures approximately 216 m. The synthetic model and the corresponding ray paths are shown in Figures B.3(a) and B.3(b), respectively.

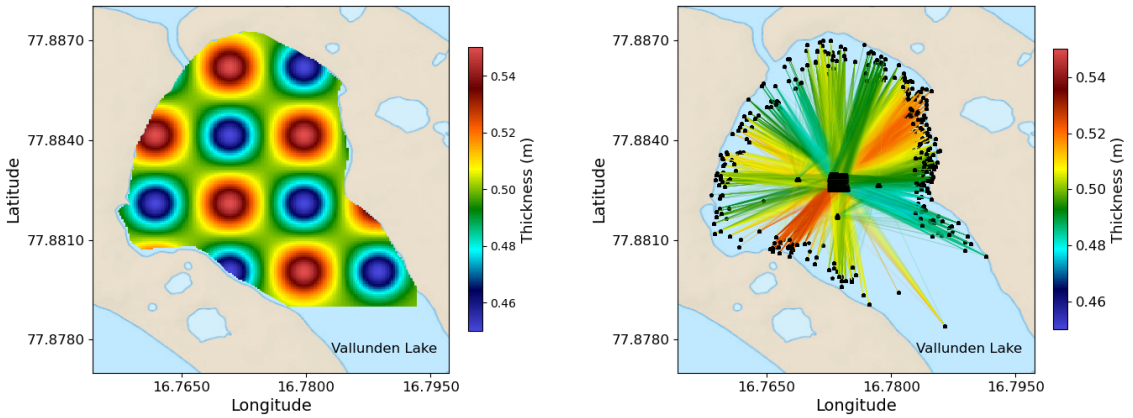

(a) (b)

Figure B.3: Checkerboard test with a 4×4 pattern (pattern size ∼ 216 m): (a) synthetic model, (b) corresponding ray paths.

The tomographic result for this case is presented in Figure B.4.

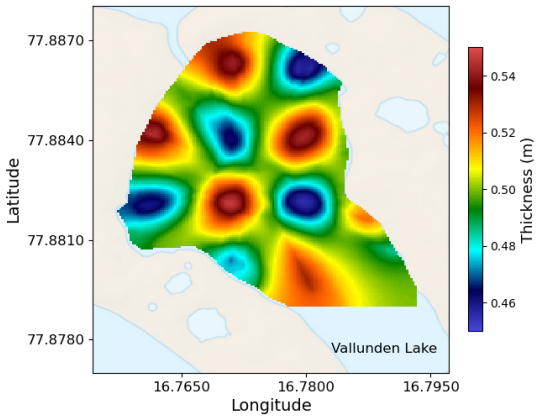

(b)

Figure B.4: Tomographic result of the checkerboard test with a 4×4 pattern (cell size $\sim$ 216 m).

Third, we use an 8×8 checkerboard pattern, where each cell measures approximately 108 m. The synthetic model and the corresponding ray paths are shown in Figures B.5(a) and B.5(b), respectively.

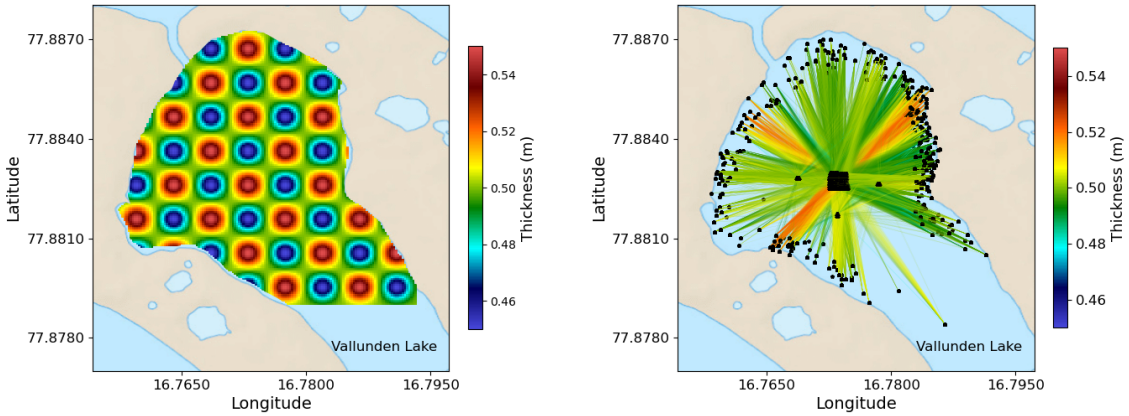

(a) (b)

Figure B.5: Checkerboard test with a 8×8 pattern (pattern size $\sim$ 108 m): (a) synthetic model, (b) corresponding ray paths.

The tomographic result for this case is presented in Figure B.6.

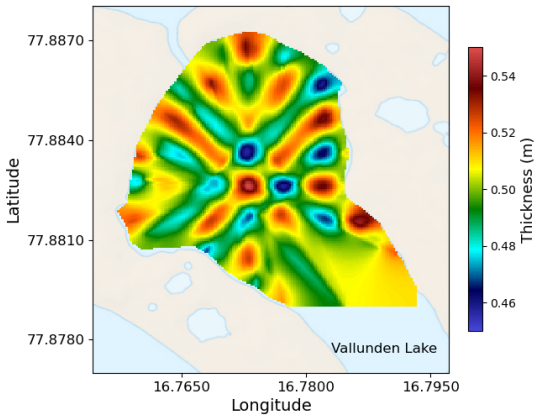

(b)

Figure B.6: Tomographic result of the checkerboard test with a 8×8 pattern (cell size $\sim$ 108 m).

The results of the checkerboard resolution tests highlight how spatial resolution depends on both the pattern size and the distribution of ray paths.

In the first case, using a 2×2 checkerboard pattern (cell size $\sim$ 432 m), the inversion successfully recovers the synthetic model across the study area (Figure B.2). The pattern is well resolved and well covered, with minimal smearing, demonstrating that under these conditions, the tomographic setup is capable of accurately recovering large-scale variations in ice thickness.

For the second case, a 4×4 checkerboard pattern (cell size $\sim$ 216 m), the model is still largely recovered (Figure B.4), but the resolution is slightly reduced compared to the first case. Overall, the inversion is still effective, and most of the synthetic pattern is clearly visible.

In the third case, the 8×8 checkerboard pattern (cell size $\sim$ 108 m), the inversion begins to smear along the ray paths (Figure B.6). Fine-scale features are only recovered in regions with large ray crossings, typically near the central part of the array, while the edges and sparsely sampled regions exhibit noticeable smoothing. This illustrates that the achievable resolution is strongly limited by ray coverage, and very fine patterns cannot be fully resolved with the current station configuration.

BIBLIOGRAPHY

Andrieu, C. and Moulines, É.: On the ergodicity properties of some adaptive MCMC algorithms, Ann. Appl. Probab., 16, 1462–1505, doi:10.1214/105051606000000286, URL https://doi.org/10.1214/105051606000000286, 2006.

Ardyna, M., Babin, M., Gosselin, M., Devred, E., Rainville, L., and Tremblay, J.- Recent Arctic Ocean sea ice loss triggers novel fall phytoplankton blooms, Geophysical Research Letters, 41, 6207–6212, doi:https://doi.org/10.1002/2014GL061047, URL https://agupubs.onlinelibrary.wiley.com/doi/abs/10.1002/2014GL061047, 2014.

Aster, R. C., Borchers, B., and Thurber, C. H.: Parameter Estimation and Inverse Problems (Third Edition), Elsevier, third edition edn., doi:https://doi.org/10.1016/B978-0-12-804651-7, URL https://www.sciencedirect.com/science/book/9780128046517, 2019.

Bijwaard, H., Spakman, W., and Engdahl, E. R.: Closing the gap between regional and global travel time tomography, Journal of Geophysical Research: Solid Earth, 103, 30 055–30 078, doi:https://doi.org/10.1029/98JB02467, URL https://agupubs.onlinelibrary.wiley.com/doi/abs/10.1029/98JB02467, 1998.

Boutin, G., Williams, T., Rampal, P., Olason, E., and Lique, C.: Wave–sea-ice interactions in a brittle rheological framework, The Cryosphere, 15, 431–457, doi:10.5194/tc-15-431-2021, URL https://tc.copernicus.org/articles/15/431/2021/, 2021.

Cao, J., Brossier, R., Górszczyk, A., Métivier, L., and Virieux, J.: 3-D multiparameter full-waveform inversion for ocean-bottom seismic data using an efficient fluid–solid coupled spectral-element solver, Geophys. J. Int., 229, 671–703, doi:10.1093/gji/ggab484, URL https://doi.org/10.1093/gji/ggab484, 2021.

Carmagnola, C. M.: Mesure, analyse et modélisation des processus physiques du manteau neigeux sec, Phd thesis, Université de Grenoble, URL https://theses.hal.science/tel-01070005, 2014.

Cerjan, C., Kosloff, D., Kosloff, R., and Reshef, M.: A Nonreflecting boundary-condition for discrete acoustic and elastic wave-equations, Geophysics, 50, 705–708, doi:10.1190/1.1441945, 1985.

Chaljub, E., Komatitsch, D., Vilotte, J.-P., Capdeville, Y., Valette, B., and Festa, G.: Spectral-element Analysis in Seismology, Advances in Geophysics, 48, 365–419, doi:10.1016/S0065-2697(06)48007-9, 2007.

Comiso, J. C., Meier, W. N., and Gersten, R.: Variability and trends in the Arctic Sea ice cover: Results from different techniques, Journal of Geophysical Research: Oceans, 122, 6883–6900, doi:https://doi.org/10.1002/2017JC012768, URL https://agupubs.onlinelibrary.wiley.com/doi/abs/10.1002/2017JC012768, 2017.

Crabeck, O., Galley, R., Delille, B., Else, B., Geilfus, N.-X., Lemes, M., Des Roches, M., Francus, P., Tison, J.-L., and Rysgaard, S.: Imaging air volume fraction in sea ice using
non-destructive X-ray tomography, The Cryosphere, 10, 1125–1145, doi:10.5194/tc-10-1125-2016, URL https://tc.copernicus.org/articles/10/1125/2016/, 2016.

Dai, A., Luo, D., Song, M., and Liu, J.: Arctic amplification is caused by sea-ice loss under increasing CO2, Nature Communications, 10, doi:10.1038/s41467-018-07954-9, URL https://par.nsf.gov/biblio/10100380, 2019.

Dugan, J. P., DiMarco, R. L., and Martin, W. W.: Low-frequency vibrational motion of Arctic pack ice, Journal of Geophysical Research: Oceans, 97, 5381–5388, doi:https://doi.org/10.1029/92JC00151, URL https://agupubs.onlinelibrary.wiley.com/doi/abs/10.1029/92JC00151, 1992.

Engelbrecht, A.: Particle Swarm Optimization, chap. 16, pp. 289–358, John Wiley & Sons, Ltd, doi:10.1002/9780470512517.ch16, URL https://onlinelibrary.wiley.com/doi/abs/10.1002/9780470512517.ch16, 2007.

Ewing, M. and Crary, A. P.: Propagation of Elastic Waves in Ice. Part II, Physics, 5, 181–184, doi:10.1063/1.1745249, URL https://doi.org/10.1063/1.1745249, 1934.

Ewing, M., Crary, A. P., and Thorne, A. M.: Propagation of Elastic Waves in Ice. Part I, Physics, 5, 165–168, doi:10.1063/1.1745245, URL https://doi.org/10.1063/1.1745245, 1934.

Feltham, D. L., Untersteiner, N., Wettlaufer, J. S., and Worster, M. G.: Sea ice is a mushy layer, Geophysical Research Letters, 33, doi:https://doi.org/10.1029/2006GL026290, URL https://agupubs.onlinelibrary.wiley.com/doi/abs/10.1029/2006GL026290, 2006.

Fissel, D., Marko, J., and Melling, H.: Advances in upward looking sonar technology for studying the processes of change in Arctic Ocean ice climate, Journal of Operational Oceanography, 1, 9–18, doi:10.1080/1755876X.2008.11081884, 2008.

Ford, J. D., Pearce, T., Canosa, I. V., and Harper, S.: The rapidly changing Arctic and its societal implications, WIREs Climate Change, 12, e735, doi: https://doi.org/10.1002/wcc.735, URL https://wires.onlinelibrary.wiley.com/doi/abs/10.1002/wcc.735, 2021.

Geiger, L.: Probability Method for Determination of Earthquake Epicenters from Arrival Time Only, Bulletin of Saint Louis University, 8, 60–71, 1912.

Gong, J. and Chen, H.: Local Peaks Search Method for Solving Lamb Waves' Dispersion Equation of Laminated Structures and the Application, Sensors, 23, doi:10.3390/s23239359, URL https://www.mdpi.com/1424-8220/23/23/9359, 2023.

Greenhill, A. G.: Wave Motion in Hydrodynamics, American Journal of Mathematics, 9, 62–96, doi:10.2307/2369499, URL https://doi.org/10.2307/2369499, 1886.

Guerreiro, K., Fleury, S., Zakharova, E., Kouraev, A., Rémy, F., and Maisongrande, P.: Comparison of CryoSat-2 and ENVISAT radar freeboard over Arctic sea ice: toward an improved Envisat freeboard retrieval, The Cryosphere, 11, 2059–2073, doi:10.5194/tc-11-2059-2017, URL https://tc.copernicus.org/articles/11/2059/2017/, 2017.

Haskell, N. A.: The dispersion of surface waves on multilayered media, Bulletin of the Seismological Society of America, 43, 17–34, 1953.

Hills, D., Lawless, B., Khangerey, R., Wilkinson, J., and Marsh, L. A.: Towards the Measurement of Sea-Ice Thickness Using a Time-Domain Inductive Measurement System, Sensors, 25, doi:10.3390/s25020510, URL https://www.mdpi.com/1424-8220/25/2/510, 2025.

Hunkins, K.: Seismic studies of sea ice, J. Geophys. Res. (1896-1977), 65, 3459–3472, doi:https://doi.org/10.1029/JZ065i010p03459, 1960.

Jensen, F., Kuperman, W., Porter, M., and Schmidt, H.: Computational Ocean Acoustics, vol. 47, doi:10.1063/1.2808704, 2000.

Johansen, T. A., Ruud, B. O., and Hope, G.: Seismic on floating ice on shallow water: Observations and modeling of guided wave modes, GEOPHYSICS, 84, P1–P13, doi:10.1190/geo2018-0211.1, URL https://doi.org/10.1190/geo2018-0211.1, 2019.

Karvonen, J. and Cheng, B.: Baltic sea ice thickness estimation based on X-band SAR data and background information, Annals of Glaciology, 65, 1–11, doi:10.1017/aog.2024.24, 2024.

Kawamura, T.: Observations of the internal structure of sea ice by X ray computed tomography, Journal of Geophysical Research: Oceans, 93, 2343–2350, doi:https://doi.org/10.1029/JC093iC03p02343, URL https://agupubs.onlinelibrary.wiley.com/doi/abs/10.1029/JC093iC03p02343, 1988.

Kirkpatrick, S., Gelatt Jr, C. D., and Vecchi, M.: Optimization by Simulated Annealing, Science, 220, 671–680, doi:https://doi.org/10.1142/9789812799371_0035, 1983.

Kissling, E., Kradolfer, U., and Maurer, H.: Velest User's Guide, Int. Inst. Geophys., pp. 1–26, 1995.

Klein, F.: User's guide to HYPOINVERSE-2000, a Fortran program to solve for earthquake locations and magnitudes, U.S. Geol. Surv. Open-File Rept, 2, 2002.

Komatitsch, D. and Tromp, J.: Introduction to the spectral element method for three-dimensional seismic wave propagation, Geophys. J. Int., 139, 806–822, doi:10.1046/j.1365-246x.1999.00967.x, URL https://doi.org/10.1046/j.1365-246x.1999.00967.x, 1999.

Kuchly, S., Auvity, B., Mokus, N., Bureau, M., Nicot, P., Fourgeaud, A., Dansereau, V., Eddi, A., Perrard, S., Dumont, D., and Moreau, L.: An integrated multi-instrument methodology for studying marginal ice zone dynamics and wave-ice interactions, EGUsphere, 2025, 1–23, doi:10.5194/egusphere-2025-3304, URL https://egusphere.copernicus.org/preprints/2025/egusphere-2025-3304/, 2025.

Lamb, H.: On Waves in an Elastic Plate, Proceedings of the Royal Society of London. Series A, Containing Papers of a Mathematical and Physical Character, 93, 114–128, URL http://www.jstor.org/stable/93792, 1917.

Landau, L. D. and Lifshitz, E. M.: Fluid Mechanics, vol. 6 of *Course of Theoretical Physics*, Pergamon Press, 2nd edn., 1987.

Landschulze, M.: Seismic wave propagation in floating ice sheets – a comparison of numerical approaches and forward modelling, Near Surface Geophysics, 16, 493–505, doi:https://doi.org/10.1002/nsg.12013, URL https://onlinelibrary.wiley.com/doi/abs/10.1002/nsg.12013, 2018.

Lienert, B. R. and Havskov, J.: A Computer Program for Locating Earthquakes Both Locally and Globally, Seismological Research Letters, 66, 26–36, doi:10.1785/gssrl.66.5.26, URL https://doi.org/10.1785/gssrl.66.5.26, 1995.

Liston, G. E., Itkin, P., Stroeve, J., Tschudi, M., Stewart, J. S., Pedersen, S. H., Reinking, A. K., and Elder, K.: A Lagrangian Snow-Evolution System for Sea-Ice Applications (SnowModel-LG): Part I—Model Description, Journal of Geophysical Research: Oceans, 125, e2019JC015 913, doi:https://doi.org/10.1029/2019JC015913, URL https://agupubs.onlinelibrary.wiley.com/doi/abs/10.1029/2019JC015913, e2019JC015913 2019JC015913, 2020.

Lohne, K. D., Lunde, P., and Vestrheim, M.: Ultrasonic signal transmission in plates – Study of a steel plate immersed in water, 2008.

Lomax, A., Virieux, J., Volant, P., and Berge-Thierry, C.: Probabilistic Earthquake Location in 3D and Layered Models, pp. 101–134, Springer Netherlands,

Dordrecht, doi:10.1007/978-94-015-9536-0_5, URL https://doi.org/10.1007/978-94-015-9536-0_5, 2000.

Lysmer, J. and Kuhlemeyer, R.: Finite Dynamic Model for Infinite Media, J Eng Mech, ASCE, 95, doi:10.1061/JMCEA3.0001144, 1969.

Marchenko, A., Morozov, E., Ivanov, A., Elizarova, T., and Frey, D.: Ice thickening caused by freezing of tidal jet, Russian Journal of Earth Sciences, 21, 1–8, doi:10.2205/2021ES000761, 2021.

Marsan, D., Weiss, J., Larose, E., and Métaxian, J.-P.: Sea-ice thickness measurement based on the dispersion of ice swell, The Journal of the Acoustical Society of America, 131, 80–91, doi:10.1121/1.3662051, URL https://doi.org/10.1121/1.3662051, 2012.

Marsan, D., Weiss, J., Moreau, L., Gimbert, F., Doble, M., Larose, E., and Grangeon, J.: Characterizing horizontally-polarized shear and infragravity vibrational modes in the Arctic sea ice cover using correlation methods, The Journal of the Acoustical Society of America, 145, doi:10.1121/1.5094343, 2019.

Matsumoto, M., Yoshimura, M., Naoki, K., Cho, K., and Wakabayashi, H.: GROUND PENETRATING RADAR DATA INTERPRETATION USING ELECTROMAGNETIC FIELD ANALYSIS FOR SEA ICE THICKNESS MEASUREMENT, ISPRS - International Archives of the Photogrammetry, Remote Sensing and Spatial Information Sciences, XLII-3/W7, 47–50, doi:10.5194/isprs-archives-XLII-3-W7-47-2019, 2019.

Menke, W.: Chapter 9 - Nonlinear Inverse Problems, in: Geophysical Data Analysis: Discrete Inverse Theory (Third Edition), edited by Menke, W., pp. 163–188, Academic Press, Boston, third edition edn., doi:https://doi.org/10.1016/B978-0-12-397160-9.00009-6, URL https://www.sciencedirect.com/science/article/pii/B9780123971609000096, 2012.

Miller, B. E. and Schmidt, H.: Observation and inversion of seismo-acoustic waves in a complex arctic ice environment, The Journal of the Acoustical Society of America, 89, 1668–1685, doi:10.1121/1.401000, URL https://doi.org/10.1121/1.401000, 1991.

Moreau, L., Minonzio, J.-G., Talmant, M., and Laugier, P.: Measuring the wavenumber of guided modes in waveguides with linearly varying thickness, The Journal of the Acoustical Society of America, 135, 2614–2623, doi:10.1121/1.4869691, 2014.

Moreau, L., Lachaud, C., Théry, R., Predoi, M., Marsan, D., Larose, E., Weiss, J., and Montagnat, M.: Monitoring ice thickness and elastic properties from the measurement of leaky guided waves: A laboratory experiment, The Journal of the Acoustical Society of America, 142, doi:10.1121/1.5009933, 2017.

Moreau, L., Boué, P., Serripierri, A., Weiss, J., Hollis, D., Pondaven, I., Vial, B., Garambois, S., Larose, É., Helmstetter, A., Stehly, L., Hillers, G., and Gilbert, O.: Sea Ice Thickness and Elastic Properties From the Analysis of Multimodal Guided Wave Propagation Measured With a Passive Seismic Array, J. Geophys. Res. Oceans, 125, doi:10.1029/2019JC015709, URL https://hal.archives-ouvertes.fr/hal-03014333, 2020a.

Moreau, L., Weiss, J., and Marsan, D.: Accurate estimations of sea-ice thickness and elastic properties from seismic noise recorded with a minimal number of geophones: from thin landfast ice to thick pack ice, J. Geophys. Res. Oceans, URL https://hal.archives-ouvertes.fr/hal-02986579, 2020b.

Moreau, L., Seydoux, L., Weiss, J., and Campillo, M.: Analysis of microseismicity in sea ice with deep learning and Bayesian inference: application to high-resolution thickness monitoring, The Cryosphere, 17, 1327–1341, doi:10.5194/tc-17-1327-2023, URL https://tc.copernicus.org/articles/17/1327/2023/, 2023.

Müller, G.: The reflectivity method: a tutorial, Journal of Geophysics, 58, 153–174, URL https://journal.geophysicsjournal.com/JofG/article/view/330, 1985.

Mäkynen, M., Jari, H., Giuseppe, A., Beena, B.-S., Magdalena, B., Alexandru, G., Fanny, A., Stefan, H., Georg, H., Larysa, I., Lars, K., Juha, K., Thomas, K., Mikko, L., Michael, M., Flavio, P., Robert, R., Eero, R., Amélie, S., Markku, S., Steffen, T., Rasmus, T., Peter, W., Mai, W., and Z., H.: Satellite Observations for Detecting and Forecasting Sea-Ice Conditions: A Summary of Advances Made in the SPICES Project by the EU's Horizon 2020 Programme, Remote Sensing, 12, 1214 (20p.), doi:https://doi.org/10.3390/rs12071214, URL https://archimer.ifremer.fr/doc/00622/73389/, 2020.

NASA Earth Observatory: World of Change: Arctic Sea Ice, URL https://earthobservatory.nasa.gov/world-of-change/sea-ice-arctic, accessed: October 8, 2025, 2025.

Notz, D. and Worster, M. G.: Desalination processes of sea ice revisited, Journal of Geophysical Research: Oceans, 114, doi:https://doi.org/10.1029/2008JC004885, URL https://agupubs.onlinelibrary.wiley.com/doi/abs/10.1029/2008JC004885, 2009.

Oliver, J., Crary, A. P., and Cotell, R.: Elastic waves in Arctic pack ice, Eos, Transactions American Geophysical Union, 35, 282–292, doi:https://doi.org/10.1029/TR035i002p00282, URL https://agupubs.onlinelibrary.wiley.com/doi/abs/10.1029/TR035i002p00282, 1954.

Olson, A. H., Orcutt, J. A., and Frazier, G. A.: The discrete wavenumber/finite element method for synthetic seismograms, Geophysical Journal International, 77, 421–460, doi:10.1111/j.1365-246X.1984.tb01942.x, URL https://doi.org/10.1111/j.1365-246X.1984.tb01942.x, 1984.

Osborne, M. F. M. and Hart, S. D.: Transmission, Reflection, and Guiding of an Exponential Pulse by a Steel Plate in Water. I. Theory, The Journal of the Acoustical Society of America, 17, 1–18, doi:10.1121/1.1916293, URL https://doi.org/10.1121/1.1916293, 1945.

Post, E., Bhatt, U., Bitz, C., Brodie, J., Fulton, T., Hebblewhite, M., Kerby, J., Stirling, I., and Walker, D.: Ecological Consequences of Sea-Ice Decline, Science (New York, N.Y.), 341, 519–24, doi:10.1126/science.1235225, 2013.

Press, F.: Propagation of elastic waves in a floating ice sheet, Eos, Transactions American Geophysical Union, 32, 673–678, doi:https://doi.org/10.1029/TR032i005p00673, URL https://agupubs.onlinelibrary.wiley.com/doi/abs/10.1029/TR032i005p00673, 1951.

Press, F. and Ewing, M.: Theory of Air-Coupled Flexural Waves, Journal of Applied Physics, 22, 892–899, doi:https://doi.org/10.1063/1.1700069, 1951.

Rajan, S. D., Frisk, G. V., Doutt, J. A., and Sellers, C. J.: Determination of compressional wave and shear wave speed profiles in sea ice by crosshole tomography—Theory and experiment, J. Acoust. Soc. Am., 93, 721–738, doi:10.1121/1.405436, URL https://doi.org/10.1121/1.405436, 1993.

Rampal, P., Weiss, J., Dubois, C., and Campin, J.-M.: IPCC climate models do not capture Arctic sea ice drift acceleration: Consequences in terms of projected sea ice thinning and decline, J. Geophys. Res. Oceans, 116, doi:https://doi.org/10.1029/2011JC007110, URL https://agupubs.onlinelibrary.wiley.com/doi/abs/10.1029/2011JC007110, 2011.

Rawlinson, N., Fichtner, A., Sambridge, M., and Young, M. K.: Chapter One - Seismic Tomography and the Assessment of Uncertainty, vol. 55 of *Advances in Geophysics*, pp. 1–76, Elsevier, doi:https://doi.org/10.1016/bs.agph.2014.08.001, URL https://www.sciencedirect.com/science/article/pii/S0065268714000028, 2014.

Reddy, J.: 3 - Classical Theory of Plates, in: Theory and Analysis of Elastic Plates and Shells, pp. 95–124, CRC Press, Texas, doi:https://doi.org/10.1201/9780849384165, 2006.

Ricker, R., Lavergne, T., Hendricks, S., Paul, S., Down, E., Killie, M. A., and Bocquet, M.: Drift-aware sea ice thickness maps from satellite remote sensing, EGUsphere, 2025, 1–27, doi:10.5194/egusphere-2025-359, URL https://egusphere.copernicus.org/preprints/2025/egusphere-2025-359/, 2025.

Romeyn, R. and Hanssen, A.: Microphone recording of flexural waves for estimation of lake ice thickness, Cold Regions Science and Technology, 211, 2023.

Romeyn, R., Hanssen, A., Ruud, B. O., and Johansen, T. A.: Sea ice thickness from air-coupled flexural waves, The Cryosphere, 15, 2939–2955, doi:10.5194/tc-15-2939-2021, URL https://tc.copernicus.org/articles/15/2939/2021/, 2021.

Rose, J. L.: Ultrasonic Guided Waves in Solid Media, Cambridge University Press, United Kingdom, doi:10.1017/CBO9781107273610, 2014.

Sabra, K., Gerstoft, P., Roux, P., Kuperman, W., and Fehler, M.: Extracting time-domain Greens function estimates from ambient seismic noise, 32, L03 310, 2005.

Schaefer, J. F., Boschi, L., and Kissling, E.: Adaptively parametrized surface wave tomography: methodology and a new model of the European upper mantle, Geophysical Journal International, 186, 1431–1453, doi:10.1111/j.1365-246X.2011.05135.x, URL https://doi.org/10.1111/j.1365-246X.2011.05135.x, 2011.

Schweiger, A. J., Wood, K. R., and Zhang, J.: Arctic Sea Ice Volume Variability over 1901â€“2010: A Model-Based Reconstruction, Journal of Climate, 32, 4731–4752, doi:10.1175/jcli-d-19-0008.1, 2019.

Serreze, M. C. and Barry, R. G.: Processes and impacts of Arctic amplification: A research synthesis, Global and Planetary Change, 77, 85–96, doi:https://doi.org/10.1016/j.gloplacha.2011.03.004, URL https://www.sciencedirect.com/science/article/pii/S0921818111000397, 2011.

Serripierri, A., Moreau, L., Boue, P., Weiss, J., and Roux, P.: Recovering and monitoring the thickness, density and elastic properties of sea ice from seismic noise recorded in Svalbard, The Cryosphere Discussions, 2021, 1–20, doi:10.5194/tc-2021-340, URL https://tc.copernicus.org/preprints/tc-2021-340/, 2021.

Shapiro, N. M. and Campillo, M.: Emergence of broadband Rayleigh waves from correlations of the ambient seismic noise, Geophys. Res. Lett., 31, doi:https://doi.org/10.1029/2004GL019491, URL https://agupubs.onlinelibrary.wiley.com/doi/abs/10.1029/2004GL019491, 2004.

Shuvalov, A., Poncelet, O., and Deschamps, M.: Analysis of the dispersion spectrum of fluid-loaded anisotropic plates: leaky-wave branches, Journal of Sound and Vibration, 296, 494–517, doi:https://doi.org/10.1016/j.jsv.2005.12.059, URL https://www.sciencedirect.com/science/article/pii/S0022460X06002197, 2006.

Sidler, R.: A porosity-based Biot model for acoustic waves in snow, Journal of Glaciology, 61, doi:10.3189/2015JoG15J040, 2015.

Squire, V. A., Hosking, R. J., Kerr, A. D., and Langhorne, P. J.: Moving Loads on Ice Platess, in: Moving Loads on Ice Platess, p. 236, Kluwer Academic Publishers, Dordrecht, first edition edn., doi:https://doi.org/10.1007/978-94-009-1649-4, 1996.

Stein, P., Euerie, S., and Parinella, J.: Inversion of pack ice elastic wave data to obtain ice physical properties, J. Geophys. Res. Oceans, 103, doi:https://doi.org/10.1029/98JC01269, URL https://agupubs.onlinelibrary.wiley.com/doi/abs/10.1029/98JC01269, 1998.

Stein, P. J.: Acoustic monopole in a floating ice plate, PhD dissertation, Mass. Inst. of Technol., Cambridge, 1986.

Stroeve, J. and Notz, D.: Changing state of Arctic sea ice across all seasons, Environmental Research Letters, 13, 103 001, doi:10.1088/1748-9326/aade56, URL https://doi.org/10.1088/1748-9326/aade56, 2018.

Stroeve, J. C., Kattsov, V., Barrett, A., Serreze, M., Pavlova, T., Holland, M., and Meier, W. N.: Trends in Arctic sea ice extent from CMIP5, CMIP3 and observations, Geophysical Research Letters, 39, doi:https://doi.org/10.1029/2012GL052676, URL https://agupubs.onlinelibrary.wiley.com/doi/abs/10.1029/2012GL052676, 2012.

Tarantola, A.: Inverse Problem Theory and Methods for Model Parameter Estimation, SIAM, doi:10.1137/1.9780898717921, URL https://epubs.siam.org/book/9780898717921, 2005.

Thomson, W. T.: Transmission of elastic waves through a stratified solid medium, Journal of Applied Physics, 21, 89–93, doi:10.1063/1.1699629, 1950.

Thurber, C. and Ritsema, J.: Theory and Observations – Seismic Tomography and Inverse Methods, vol. 1, pp. 323–360, Elsevier, Amsterdam, doi:10.1016/B978-044452748-6.00009-2, 2007.

Tromp, J., Komattisch, D., and Liu, Q.: Spectral-Element and Adjoint Methods in Seismology, Communications in Computational Physics, 3, 2008.

Virieux, J.: P-SV wave propagation in heterogeneous media: Velocity-stress finite-difference method, GEOPHYSICS, 51, 889–901, doi:10.1190/1.1442147, URL https://doi.org/10.1190/1.1442147, 1986.

Wang, F., Yang, D., Zhang, B., and Yang, L.: Can sea ice thickness be retrieved using GNSS-interferometric reflectometry?, GPS Solutions, 26, doi:10.1007/s10291-022-01309-0, 2022.

Wang, Q.: Wavelet-based inversion of seismic waves in Arctic ice, PhD dissertation, Mass. Inst. of Technol., Cambridge, 1995.

Williams, T. D., Bennetts, L. G., Squire, V. A., Dumont, D., and Bertino, L.: Wave–ice interactions in the marginal ice zone. Part 1: Theoretical foundations, Ocean Modelling, 71, 81–91, doi:https://doi.org/10.1016/j.ocemod.2013.05.010, URL https://www.sciencedirect.com/science/article/pii/S1463500313000954, arctic Ocean, 2013.

Xie, Y. and Farmer, D. M.: Seismic-acoustic sensing of sea ice wave mechanical properties, J. Geophys. Res. Oceans, 99, 7771–7786, doi:https://doi.org/10.1029/93JC03483, URL https://agupubs.onlinelibrary.wiley.com/doi/abs/10.1029/93JC03483, 1994.

Xing, J., Song, R., Zhen, S., and Jiang, X.: Construction of the Central Arctic Sea Ice Structure and Acoustic Velocity Model at the Short-Term Ice Station During N11 CHINARE, IEEE Transactions on Geoscience and Remote Sensing, 60, 1–7, doi:10.1109/TGRS.2021.3107363, 2022.

Xu, H., Xing, J., Zuo, G., and Wei, J.: Cross-hole acoustic tomography of Arctic sea ice: insights into temperature-driven velocity and attenuation variations, Intelligent Marine Technology and Systems, 3, doi:10.1007/s44295-025-00078-z, URL https://link.springer.com/article/10.1007/s44295-025-00078-z, open Access, 2025.

Yang, T. and Yates, T.: Flexural waves in a floating ice sheet: Modeling and comparison with data, Journal of The Acoustical Society of America - J ACOUST SOC AMER, 97, 971–977, doi:10.1121/1.412076, 1995.

Yang, T. C. and Giellis, G. R.: Experimental characterization of elastic waves in a floating ice sheet, The Journal of the Acoustical Society of America, 96, 2993–3009, doi:10.1121/1.411261, URL https://doi.org/10.1121/1.411261, 1994.

Yitayew, T. G., Ferro-Famil, L., and Eltoft, T.: 3-D imaging of sea ice using ground-based tomographic SAR data and comparison of the measurements with TerraSAR-X data, in: 2014 IEEE Geoscience and Remote Sensing Symposium, pp. 1329–1332, doi:10.1109/IGARSS.2014.6946679, 2014.

Yitayew, T. G., Ferro-Famil, L., and Eltoft, T.: Investigation of sea ice and lake ice using Ground-Based SAR tomography, in: 2015 IEEE International Geoscience and Remote Sensing Symposium (IGARSS), pp. 5276–5279, doi:10.1109/IGARSS.2015.7327025, 2015.

Zhang, J., Schweiger, A., Steele, M., and Stern, H.: Sea ice floe size distribution in the marginal ice zone: Theory and numerical experiments, Journal of Geophysical Research: Oceans, 120, 3484–3498, doi:https://doi.org/10.1002/2015JC010770, URL https://agupubs.onlinelibrary.wiley.com/doi/abs/10.1002/2015JC010770, 2015.